Magnetic Molecular-based Materials Assembled on Metallic Substrates : Experimental X-ray Absorption Spectroscopy and Ligand Field Multiplet Calculations

Luqiong Zhang

UNIVERSITÉ PARIS SUD
Comprendre le monde, construire l'avenir

Magnetic Molecular-based Materials Assembled on Metallic Substrates: Experimental X-ray Absorption Spectroscopy and Ligand Field Multiplet Calculations

Thèse de doctorat de l'Université Paris-Saclay
préparée à l'Université Paris Sud

École doctorale n°571 Sciences chimiques : molécules, matérieux, instrumentation et biosystèmes (2MIB)
Spécialité de doctorat: Chimie

Thèse présentée et soutenue à Orsay, le 18 Décembre 2019, par

Mme Luqiong ZHANG

Composition du Jury :

M. Ally AUKAULOO Professeur, ICMMO, Université Paris Sud	Président
Mme. Amélie JUHIN Chargé de recherche, IMPMC, Université de Sorbonne	Rapporteur
Mme. Valérie MARVAUD Directrice de Recherche, IPCM, Université de Sorbonne	Rapporteur
M. Rodrigue LESCOUEZEC Professeur, IPCM, Sorbonne Université	Examinateur
M. Talal MALLAH Professeur, ICMMO, Université Paris Sud	Directeur de thèse
M. Philippe SAINCTAVIT Directeur de Recherche, IMPMC, Université de Sorbonne	Co-Directeur de thèse

Table of Contents

Acknowledgments

Primarily, I would like to express my deep gratitude to my supervisors: Prof. Talal MALLAH and Dr. Philippe SAINCTAVIT. It is really a great honor and fortune for me have a chance to continue my graduate career under their supervisions, and to study and work in the Laboratoire Chimie Inorganique (LCI), Institut de Chimie Moléculaire et des Matériaux d'Orsay (ICMMO) and IMPMC (Institut de mineralogie, de physique des matériaux et de cosmochinie) of Sorbonne university. They both offer me abundant help in this new scientific field of magnetism. What they have done (invaluable guidance, support, encouragement, understanding and insight vision) and imparted to me (new knowledge, research skills, research experiences and critical thinking) are a tremendous treasure in my lifetime. Form my viewpoint, they are not only supervisors but also amiable elders. Again, I do really feel grateful and lucky to have my PhD study under their supervisions.

I appreciate Marie-Anne Arrio a lot, who is very nice, warm, patient and amiable. She leads me to mastering calculated skills and theories step by step, and also, she provides a lot of help in study and life. We get along well with each other in these three years. Besides, many deep thanks to great researchers for their help and preliminary preparation: 1) Marie-Laure BOILLOT, Laure CATALA, Riviére ERIC and Sandra MAZERAT in ICMMO; 2) Edwige OTRRO and Philippe OHRESSER in SOLEIL (DEIMOS beamline); 3) Amandine BELLEC, Vincent REPAIN and Yongfeng TONG in LMPQ of Paris-Diderot University. All of them help me to synthesize nanoparticles and compounds, to characterize magnetic/structural properties by SQUID and XAS measurements, and to take STM measurements. It is their work, support and aid that enriches my study, without them, my work cannot progress smoothly and nice. Their guidance, encouragement, knowledge and skills are the driving forces for my work during my PhD study period.

I would like to thank all group members of LCI (present and past) in ICMMO. Members in our group, especially Yiting, Fatima, Linh, Adama, Amanda, Khaled, Youngju, Asma, Philippe, Antonie, Laure, Marie, Axel, Tam, Bamjamine, Christian and so on (actually so many members), are very friendly, mutual helpful, dynamics and energetic, which makes the lab full of happiness and love. It is my pleasure and fortune to work with them throughout 3 years. Thanks to this group, this period of work is one unforgettable memory in my life. I am grateful to all permanent staffs, Sandra, Laure, Marie-Laure, Pei, Anne-Bleuzen, Amelie, Jean-Jacques, Ally, Jean-Noel, Eric and so on, for their help, guidance and advice. I also want to acknowledge colleagues in IMPMC lab of Sorbonne Université because of their kindness. I still remember the first time we went to a noodle bar together, and they introduced how they are working. Scientific atmosphere there is quite harmonious and warm. And a special gratitude to Gérald and Andrew in ISMO (Institue des sciences moléculaires d'Orsay) for

their kindly help and understanding.

This experience during my PhD study makes me realize clearly that teamwork and collaboration are the essential compositions of scientific research. The overall work of each researcher not only depends upon the subject and technical skills, but also upon the teamwork, collaborations and the surrounding atmosphere. Thanks to my colleagues in LCI and IMPMC, collaborators of DEIMOSE in SOLEIL and LMPQ.

In addition, I would like to express my gratitude to friends who are in China or abroad. They all are very kindhearted, hospitable and accommodating. On the way to chase my dream, my friends provide a lot of psychological and financial help to me. I do really appreciate them for their trust and help. And I would also express my acknowledgement to friends in France who gave me vast courage, support, understanding, comfort and help when I met one healthy problem in the first year of PhD study. During these four years, their words and behaviors facilitate me to keep optimistic and positive. Laughters, dinners, parties, short holidays we shared together are one of my precious memory in my life, impressive and unforgettable, which still plays out in my mind vividly as if it were yesterday.

A non-negligible gratitude I would show it to my previous supervisors and colleagues in master period: Asso.Prof. Wei Shen, Prof. Rongxin He, Dr. Cheng Huang, Meiyuan Guo, and Yulan Dai et.al. On the way to pursue my dream, my master supervisor (Asso.Prof. Wei Shen) and researcher in this group provide me with enormous guidance, help and financial support as well as their trust. Meiyuan, Yulan and Xiaorui are the guys we will share our scientific ideas and thoughts before and now.

I would acknowledge greatly to the financial support from the China Scholar Council (CSC) for providing me this opportunity to study and work abroad in France. It is thanks to the Collaborative Program between CSC and Université Paris-Sud that I won this opportunity to study abroad and be more closely to my idol (Curie Marie). Although there is a long-term laborious work I should persist on, I still believe firmly that one day I would become a better eligible researcher.

Last but not least, I would like to express my personal gratitude to my families, especially my beloved husband, Nicolas. Thanks a lot for your thoughtfulness, understanding, encouragement and your deep love. All the time you support me the best and now you give me a warm family.

My family, friends, colleagues and collaborators: this manuscript is for you.

ZHANG Luqiong

张露琼

2019-12-18

Abstract

The research work in this thesis is focused on the investigation of the magnetic properties of magnetic nanoparticles and spin crossover complexes assembled as monolayer or submonolayer on different substrates by X-ray Absorption Spectroscopy (XAS) at the $L_{2,3}$ edges of metallic atoms. We use X-ray Magnetic Circular Dichroism (XMCD) and X-ray Natural Linear Dichroism (XNLD) to do so. Simulations of the experimental data are carried out by Ligand Field Multiplet (LFM) Theory.

The thesis is divided into two parts. The first part aims at studying the magnetic anisotropy of Prussian blue analog magnetic coordination nanoparticles that were assembled as single layers on Highly Oriented Pyrolytic Graphite (HOPG). The sample was examined by XNLD measured with the light polarization vector at different angles to the normal to the substrate plane that evidences an electronic anisotropy at the Ni and Cr $L_{2,3}$ edges in line with a structural distortion of the coordination sphere of the atoms belonging to the surface of the particles. The structural distortion of the Ni(II) coordination sphere corresponds to an elongation along the axis perpendicular to the particles' surface and, therefore, is responsible of a zero-field splitting (ZFS) of the Ni(II) $S = 1$ magnetic moment, confirmed by LFM calculations. The presence of ZFS is responsible for a magnetic anisotropy when a magnetic field is applied corresponding to an easy plane of magnetization in the case of an elongated structural distortion. The examination of the magnetic properties of the single layer by XMCD at different values of the magnetic field and different orientations of the sample with respect to the applied field reveals the presence of a hysteresis loop when the magnetic field is at 60° to the normal to the substrate plane. This result is compatible with an easy plane of magnetization within the plane of the single layer in line with the results deduced from the electronic distortion.

The second part of the work is devoted to the investigation of the thermal and light-induced switching of spin crossover (SCO) Fe(II) containing molecules assembled as submonolayer on metallic substrates namely Au(111), Ag(111) and Cu(111). The analysis of the data is based on a comparison with those obtained for a thick film (7 microns). The XAS data at the Fe $L_{2,3}$ edges of the thick film show a complete spin crossover upon cooling from 300 to 80 K. While for the submonolayer samples an incomplete crossover occurs with residual high spin species whose percentage depends on the nature of the substrate. Complementary Scanning Tunnel Microscopy (STM) studies reveal that on Au(111) an ordered high spin/low spin phase is present with 2:1 ratio that was confirmed by the XAS study. The incomplete transition on Cu(111) does not reveal any ordered phase by STM, highlighting the effect of the molecules/substrate interface on the crossover phenomenon. We have checked that the crossover of an additional layer is complete confirming the major role of the interface. The dynamic of the crossover was studied by light irradiation (blue and green) at low temperature (4 K).

Abstract

An anomalous transformation from high spin to low spin is observed and was tentatively assigned to a plasmonic effect of the metallic substrates that excites some vibration modes of the high spin molecules inducing a population of the low spin state and therefore a high spin to low spin crossover.

Résumé

Les travaux de recherche de cette thèse focalisent sur l'étude des propriétés des deux nano-objets magnétiques différents: les nanocristaux appartenant à la famille des analogues du bleu de Prusse (PBA) et de complexes à transition de spin assemblés en monocouches sur substrats métalliques. Afin d'interpréter les propriétés magnétiques et les propriétés structurelles de ces nano-objets assemblés sur des substrats métalliques, des expériences de spectroscopie d'absorption des rayons X (XAS) aux bords L2,3 des atomes métalliques ont été menées en combinant avec le multiplicateur de champ de ligand (LFM) correspondant calculs. Les spectres pourraient contenir du XAS expérimental, du dichroïsme circulaire magnétique à rayons X (XMCD) et du dichroïsme linéaire naturel à rayons X (XNLD), ainsi que ceux simulés à partir de calculs LFM.

La thèse est divisée en deux parties. La première partie porte sur l'étude de l'anisotropie magnétique de nanoparticules de coordination qui sont des analogues du bleu de Prusse assemblées en monocouche sur du graphite pyrolytique orienté (HOPG). L'échantillon a été examiné par XNLD, et a été mesuré avec le vecteur de polarisation de la lumière à différents angles par rapport à la normale au plan du substrat, mettant en évidence une anisotropie électronique aux seuils de Ni et Cr due à une distorsion structurale de la sphère de coordination des atomes présents à la surface des particules. La distorsion structurale de la sphère de coordination du Ni(II) correspondant à un allongement le long de l'axe perpendiculaire à la surface des particules est donc responsable de la levée de dégénérescence en champ nul (ZFS) du moment magnétique $S = 1$ du Ni(II), confirmée par des calculs LFM. La présence de ZFS est responsable d'une anisotropie magnétique lorsqu'un champ magnétique est appliqué ceci correspondant à un plan de facile aimantation dans le cas d'une élongation. L'examen des propriétés magnétiques de la monocouche par XMCD à différentes valeurs du champ magnétique et à différentes orientations de l'échantillon par rapport au champ appliqué révèle la présence d'une boucle d'hystérèse lorsque le champ magnétique est à 60° de la normale au substrat. Ce résultat indique la présence d'un plan de facile aimantation dans le plan de la monocouche compatible avec les résultats déduits de la distorsion électronique.

La deuxième partie au Chapitre 4 du travail est consacrée à l'étude de la commutation induite thermiquement et par la lumière de complexes à transition de spin des molécules Fe(II)-SCO, ($Fe^{II}[HB(3,5\text{-}Me_2Pz)_3]_2$), assemblées en sous-monocouches sur des substrats métalliques (Au (111), Ag (111) et Cu (111). L'analyse des données est comparée à celle d'un film épais (7 microns). Les données XAS au seuil $L_{2,3}$ de Fe du film épais montrent une transition complète lors du refroidissement entre 300 et 80 K. Tandis que pour les échantillons en sous-monocouches, une transition incomplète se produit avec des espèces haut spin résiduelles dont le pourcentage dépend de

la nature du substrat. Des études complémentaires en microscopie tunnel à balayage (STM) révèlent que, sur Au (111), une phase ordonnée haut spin/bas spin est présente avec un rapport de 2:1 confirmée par l'étude XAS. La transition incomplète sur Cu (111) ne révèle aucune phase ordonnée par STM, mettant en évidence l'effet de l'interface molécules/substrat sur le phénomène de transition. Nous avons vérifié que la transition d'une couche supplémentaire était complète, confirmant ainsi le rôle majeur de l'interface. La dynamique de la transition a été étudiée par irradiation lumineuse (lumière bleue et verte) à basse température (4 K). Une transformation anormale de l'état haut spin vers l'état bas spin est observée et a été provisoirement attribuée à un effet plasmonique des substrats métalliques qui excite certains modes de vibration des molécules à spin élevé induisant une population de l'état bas spin et donc la transition haut spin vers bas spin.

Abbreviations

AFM	Atomic Force Microscopy
AFOM	Antiferromagnets
CF	Crystal Field
CN^-	Cyanide Anions
CTA	Cetyltrimethyllammonium
D_{4h}	Tetrahedron/Tetrahedral Group
DODA	dimethyl dioctadecyl ammonium
fcc	Face-centered cubic
FOM	Ferromagnets
FIM	Ferrimagnets
H_C	Coercive Field
H_{eff}	Effective magnetic field
H_{ext}	External magnetic field
HOPG	Highly Oriented Pyrolytic Graphite
HS	High Spin
HT	High Temperature
IR	Infrared-red
LFM	Ligand Field Multiplet
LIESST	Light Induced Excited Spin State Trapping (LS to HS)
LS	Low Spin
LT	Low temperature
M	Magnetization
ML	Molecular layer
M_{rem}	Remnant Magnetization
NCs	Nanocrystals
NEXAFS	Near-Edge X-rays Absorption Fine Structure
NPs	Nanoparticles
O_h	Octahedron/Octahedral group
PB	Prussian Blue
PBA	Prussian Blue Analogues
PVP	Organic Polymer Polyvinylpyrrolidone
QTM	Quantum Tunneling of Magnetization
Reverse-LIESST	Reverse-Light Induced Excited Spin State Trapping (HS to LS)

Reverse-SOXIESST	Reverse- Soft X-ray Induced Excited Spin State Trapping (HS to LS)
SAMs	Self-Assembled Molecules
SCO	Spin Crossover
SMMs	Single Molecular Magnets
SOC	Spin-Orbit Coupling
SO-SI	Spin-Orbit State-Interaction
SOXIESST	Soft X-ray Induced Excited Spin State Trapping (LS to HS)
SQUID	Superconducting Quantum Interference Device
ST	Spin Transition
STM	Scanning Tunnel Microscopy
T	Temperature
T_B	Blocking Temperature
T_C	Curie Temperature
TEY mode	Total Electron Field mode
$T_{1/2}$	Temperature at which 50 per cent of the "SCO-active" molecules have changed the spin state
$t_{exposure}$	Exposure time under an illumination with light (red, green and blue laser) and/or X-rays
UV-Vis	Ultra Violet-Visble
XAS	X-ray Absorption Spectroscopy
XMCD	X-ray Magnetic Circular Dichroism
XNLD	X-ray Natural Linear Dichroism
XRD	X-ray Diffraction
ZFS	Zero-Field Splitting
$\boldsymbol{D}$	Zero Field Splitting parameter
G	Gibbs Free Energy
γ_{HS}	HS fraction
$\gamma_{HS}(T)$	HS fraction as a function of temperature
H	Enthalpy
g	Landé factor
χ_M	Molar magnetic susceptibility
P	Pairing Energy
Δ	Splitting Energy
S	Entropy

Overview

The present PhD study is centered on molecular magnetism. I have mainly been working with two different systems: nanocrystals belonging to the family of the Prussian blue analogues (PBAs) and molecules belonging to the group of Iron spin cross-over (SCO). In both cases, the systems belong to the state-of-the-art chemistry and in both cases my work has been to bring a fine characterization of the electronic and magnetic structures by using experimental spectroscopic techniques and by applying theoretical methods in order to interpret the experimental features. This thesis is composed of five chapters.

Chapter 1 is a general brief introduction on magnetism, molecular magnetism including Prussain blue analogs and spin crossover materials that constitute the two systems investigated in this work.

Chapter 2 is devoted to the general methodology used to analyze the X-ray Absorption Spectra including Ligand Field Multiplet calculations.

In **Chapter 3**, a combinational study of XAS and LFM calculations is implemented for the PBAs $CsNi^{II}Cr^{III}$[6] nanoparticles (NPs) deposited monolayer on HOPG (highly oriented purely graphite). This chapter is to expound the electronic and structural information of Ni^{II} and Cr^{III} sites in NPs deposited on a solid surface of HOPG by using XAS technique. Then a series of sophisticated calculations being the ancillary technique are carried out by the multiplet program based on the ligand field theory, which favors to gaining a deeper insight of understanding the intrinsic structural properties at metal ions sites and the intermolecular interaction in the case of the self-assembled molecules (SAMs).

In **Chapter 4**, monolayer or submonolayer Fe (II) compounds directly contacting to different metallic substrates are investigated by XAS experiments to explore their SCO behaviors. It is of great significance and interest to investigate the SCO phenomenon among Fe (II) compounds since the applied metallic substrates would have interplay with Fe (II) compounds under the circumstance of external stimuli. Primarily, the thermal dependence of Fe (II)-SCO is recorded from 4.5 K to 300 K and then the light induced excited state effect is carried under the illumination with blue laser and red laser. A theoretically multiplet study is used to provide a fundamental reference for real-time spectra and to give a relatively accurate spin state at a quantitatively scale.

In **Chapter 5**, general conclusions are presented which I have obtained from the case of PBAs $CsNi^{II}Cr^{III}$[6] assembled monolayer on HOPG and the case of Fe(II) spin crossover compounds deposited submonolayer on different metallic substrates. Also, the challenges and emerging new thoughts are listed in this chapter.

Chapter 1 - General Introduction

1.1 Introduction

1.1.1 Magnetism

General history of magnetism. The first discovery of magnetism was found in lodestones which could attract iron naturally in antiquity from the ancient world.[1] The lodestone is composed of the magnetite that is an iron oxide. As for the terminology of magnet, it stemmed ultimately from "μαγνητιζ λιθοζ" (*magnetis lithos)* and "the Magnesian stone" (lodestone) in Greek *(seeing the link: http://languagehat.com/magnet/)*, while the concept of magnetism was firstly named by the philosopher Thales of Miletus in ancient Greece, during the 6th century BC (625-547 BC).[2] Due to magnetic interaction, lodestone minerals could be rotated and moved by other pieces of lodestone, the first magnetic devices have been invented by Chinese people and they were mainly used for divination purposes before military applications to orientation and early navigation.[1, 3-5] During Han dynasty of China, one special spoon, called "directional spoon", was invented by Wang Chong (in Lun Heng, 27-97).[5] This "directional spoon" was the first compass which always directs towards to the south when placing on a plate on the ground (seeing ***Figure 1-1***) due to the magnetic properties of lodestone. Compasses are still used in the 21st century based on this ancient use of magnets for orientation.

Figure 1-1*. The image of ancient compass "directional spoon" in China.*

Today magnetism is depicted as the response of a magnetic material to an external magnetic field. It originates from the intrinsic magnetic moments of ions and from electric currents. Except for the lodestone (i.e. Fe_3O_4: magnetite) found in ancient world, there are various natural minerals based on Fe possessing a permanent magnetization (for instance α-Fe_2O_3: hematite, γ-Fe_2O_3: maghemite). These iron oxides are either antiferromagnets, weak ferromagnets or ferrimagnets, which have a large enough magnetic anisotropy to present a net magnetization and form permanent magnets (at least for ferrimagnets such as γ-Fe_2O_3 and Fe_3O_4). There also exist other magnetic minerals, such as iron sulfiVacudes, or titanium, chromium, cobalt, or nickel oxides.

When a material is submitted to an external magnetic induction $\boldsymbol{B}$, its Helmotz free energy (F=U-TS, where U is the free energy, T the temperature and S the entropy) becomes a function of $\boldsymbol{B}$. By definition, the magnetization M ($\boldsymbol{B}$,T) of a material is given by

$$\mathrm{M}(\boldsymbol{B},\mathrm{T}) = -\frac{1}{V}.\frac{\partial F}{\partial B}\,, \qquad (1-1)$$

and the magnetic susceptibility is defined by

$$\chi(\boldsymbol{B},T) = \frac{\mu_0}{4\pi}.\frac{\partial M}{\partial B} = -\frac{\mu_0}{4\pi}.\frac{1}{V}\frac{\partial^2 F}{\partial^2 B}\,, \qquad (1-2)$$

where μ_0 is the magnetic permeability of vacuum. Classically magnetic materials are classified into two different groups according to the sign of the magnetic susceptibility:

--those for which the magnetic susceptibility is negative are called diamagnetic materials,

--those for which the magnetic susceptibility is positive are called paramagnetic materials.

On one hand, atoms with closed shells are diamagnetic so that most materials are diamagnetic (for instance rare gases in their solid phase are diamagnets). The related diamagnetic properties, called diamagnetism, appear in all materials since all atoms have closed. Diamagnetism tends to repel the external magnetic field. On the other hand, materials containing *3d*, *4d*, *5d* (transition metals), *4f* (lanthanides) and *5f* (actinides) may have open shells with unpaired electrons and most of them are paramagnetic materials.

For the materials containing paramagnetic atoms, there is a further classification depending on the existence or the absence of a long-range magnetic order where long range generally refers to lengths that are much larger than interatomic distances:

--materials for which there is no long-range magnetic order are called paramagnets (for instance metallic Ti or Cr);

--materials with a long-range magnetic order but no net magnetic moment are called antiferromagnets (AFOM);

--materials which possess a long-range magnetic order with a net magnetization are called ferromagnets (FOM) or ferrimagnets (FIM). FOM have only one magnetic lattice or sub-lattice (for instance metallic Fe or CrO_2). FIM have several magnetic sub-lattices and the contribution from each

sub-lattice does not cancel so that a net magnetization is observed (for instance maghemite or magnetite are ferrimagnets; hematite above 260 K is a ferrimagnet although it commonly receives the name of weak FOM)

A schematic representation of the various types of magnetic materials is provided in ***Figure 1-2.***

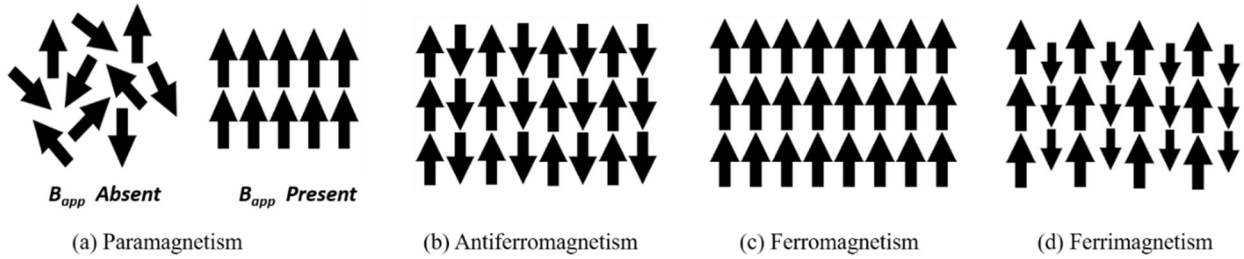

Figure 1-2. *Schematic types of magnetic systems depending upon the magnetic ordering.*

For ferro- or ferrimagnetic materials, one observes a Curie Temperature, T_C. Above T_C, there is no long-range magnetic order so that the material is a paramagnet, whereas below T_C one observes a long-range magnetic order and a net magnetic moment is generally observed. In addition to the existence of a long-range order, one also generally observes an opening of the magnetic hysteresis loops: when a ferromagnetic or ferrimagnetic material is submitted to an external magnetic field, its magnetization changes. One then observes that its magnetization depends on the history of the material: if the material is first submitted to a positive external magnetic field then its magnetization in zero external magnetic field is different from the one observed if the material is first magnetized in a negative magnetic field. This means that a magnetized ferrimagnet or ferromagnet is not in a thermodynamic state since its energy is not only a function of the thermodynamic parameters (temperature, external magnetic induction) but also a function of its history.

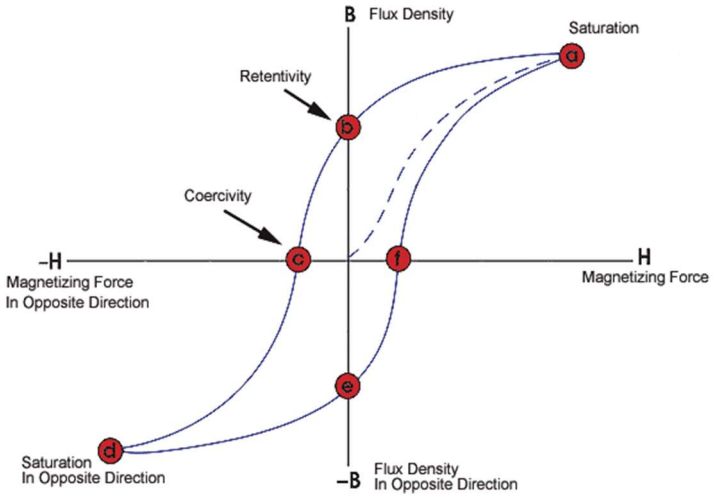

Figure 1-3*. The hysteresis Loop obtained from the induced magnetic flux density (B).* *https://www.nde-ed.org/EducationResources/CommunityCollege/MagParticle/Physics/HysteresisLoop.php*.

In a hysteresis loop (***Figure 1-3***), one records the magnetic moment of a sample as a function of the external magnetic induction. From a magnetization curve, one can extract two quantities that help

summarizing the shape of the hysteresis:

--the remnant magnetization, M_{rem}, is the magnetization that is observed in zero magnetic induction after the sample has been fully magnetized up to saturation in a given direction;

--the coercive field, H_C, is the field with direction opposite to the one of the saturating field, which is necessary to cancel any magnetization of the material.

1.1.2 Molecular Magnetism and Nano-Magnetism

The above description of magnetism holds for bulk materials such as large single crystals, powders with large grains or thick films. Beyond the usual description of magnetism for macro-crystals, the situation for nanoparticles, nanocrystals, ultra-thin films is a bit more subtle because the intrinsic absence of long-range crystallographic order in nanoparticles prevents the existence of any long-range magnetic order.[6-7] Then for paramagnetic nanoparticles (NPs), one observes another order temperature that is called the blocking temperature, T_B. When the temperature of a NP is below T_C of the associated bulk material, the whole magnetic ions of the NP are coupled so that one observes a magnetic order between the various magnetic ions and the NP presents an instantaneous, net magnetic moment. Because of thermal energy and the absence of long-range crystallographic order, the net magnetic moment keeps on changing between directions that are crystallographically equivalent so that on a "large" (i.e. several nanoseconds) time scale, the average net magnetic moment is zero. In this case the magnetic behavior of the NP is called superparamagnetic. When the temperature is lowered, the thermal energy lowers and can eventually become less that the magnetic anisotropy associated to the re-orientation of the NP net magnetic moment. Below T_B the NP presents a net magnetic moment and mostly behaves as a ferromagnet or a ferrimagnet.

1.1.2.1 Molecular Magnetism

Molecular magnetism is a multidisciplinary field involving coordination chemistry, synthetic chemistry, theoretical chemistry, solid state physics, condensed matter physics, quantum physics, and functionalized material science. It is a rather new emerging field in which chemists and physicists pay huge attention to studying the local structure and magnetic properties of molecular magnetic systems. The specificities of molecular magnets make them good candidate for information storage and the elaboration of spintronics devices.[8] Importantly, the discovery of single molecule magnets (SMMs) by Dante Gatteschi *et al*[9-11] contributed to making the field of molecular magnetism more attractive thanks to the existence of superparamagnetic behavior above a blocking temperature (T_B) and quantum spin relaxation below T_B. In general, the magnetic centers of SMMs are transition metal ions, sometimes lanthanide ions, in coordination with organic ligands. The main feature of SMMs is the existence of a dynamical opening of the magnetic hysteresis loops, the origin of which stems from a local magnetic anisotropy. These openings by contrast to traditional magnetic systems are mostly

dynamical and highly temperature dependent. The origin of magnetism is mostly governed by the intramolecular coupling and intermolecular dipolar interactions between molecules.

1.1.2.2 Single Molecular Magnets (SMMs)

SMMs are one example of magnetic NPs presenting outstanding magnetic properties. SMMs are systems that behave as macroscale magnets with the addition of quantum properties because of their nanoscale nature. SMMs are synthesized as organometallic compounds where transition metal ions or lanthanide ions are coordinated to organic ligands. These SMMs behave as molecules with a giant spin, S, in the ground state and because of a large magnetic anisotropy the 2S+1 levels of the giant spin are split.[12-17] At low enough temperature, it has been found that when a SMM is prepared in one state, for instance the |S,M=-S> state, then a very slow relaxation of magnetization is observed when the external magnetic is reversed so that an hysteresis loops is observed.[17-21] Since the relaxation rate strongly depends on the intensity of the external magnetic field, the magnetization curve present a series of plateau characteristic for SMMs. At the difference of conventional magnets, the hysteresis loops also depend on the rate at which the external magnetic induction is swept, hence its dynamical nature.

In general, SMMs are studied as molecules present in molecular crystals, bulk crystals and in the recent decade, individual SMMs grafted on surfaces have also been studied. For instance, Mannini *et al.* chemically grafted SMMs on a gold Au(111) surface,[22-24] with the idea that isolated, grafted molecules on a surface have no large intermolecular interactions at the difference of what happens when they are embedded inside a crystal. The objective was to check that the characteristics of SMMs grafted on surfaces were preserved when isolated.

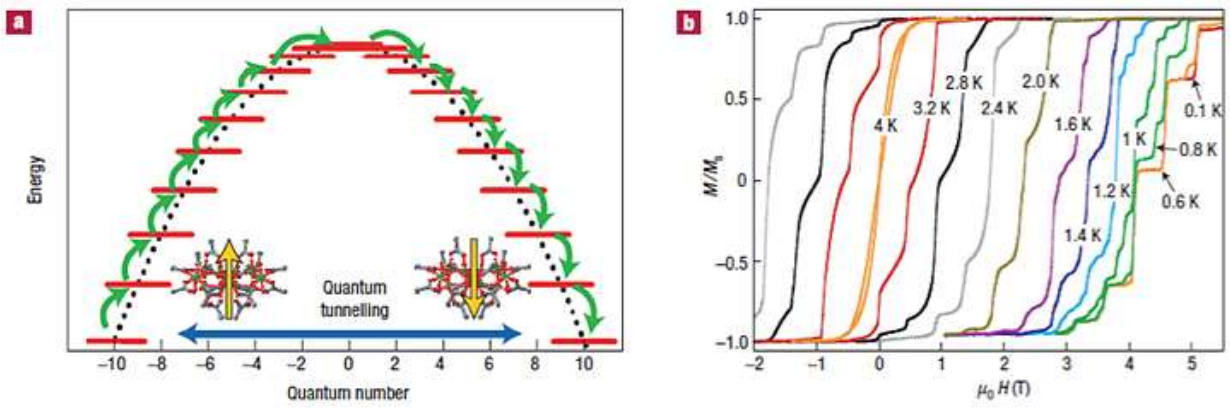

Figure 1-4. *(a) Schematic representation of the energy landscape of a SMM with a spin ground state S = 10. The magnetization reversal can occur via quantum tunnelling between energy levels (blue arrow) when the energy levels in the two wells are in resonance. Phonon absorption (green arrows) can also excite the spin up to the top of the potential energy barrier with the quantum number M = 0, and phonon emission descends the spin to the second well. (b) Hysteresis loops of single crystals of* $[Mn_{12}O_{12}(O_2CCH_2C(CH_3)_3)_{16}(CH_3OH)_4]$ *SMM at different temperatures. The loops exhibit a series of steps, which are due to resonant quantum tunnelling between energy levels.*[17]

Intriguingly, SMMs are ingredients to link spintronics and molecular electronics, in order to create the novel discipline of molecular spintronics.[17, 25] Dynamics of SMMs is schemed in ***Figure 1-4***, which illustrates the relationship between quantum tunneling effect and the magnetization reversal mechanism.[17]

1.1.3 Bistability of Magnetism

In functionalized materials, bistability results from the presence of two stable or metastable states which coexist at a given temperature and pressure. Due to external stimuli (such as light, thermal history, pressure history), one observes a reversible transition from one of the metastable state (shown as **2**) to the other (shown as **1** and **3**) illustrated as ***Figure 1-5***. Molecular magnetism is one of the fields where bistability has been widely investigated. Magnetic bistability is considered as a promising property for molecular materials that could be applied for spintronic devices, data storage, and photo-responsive devices.[8]

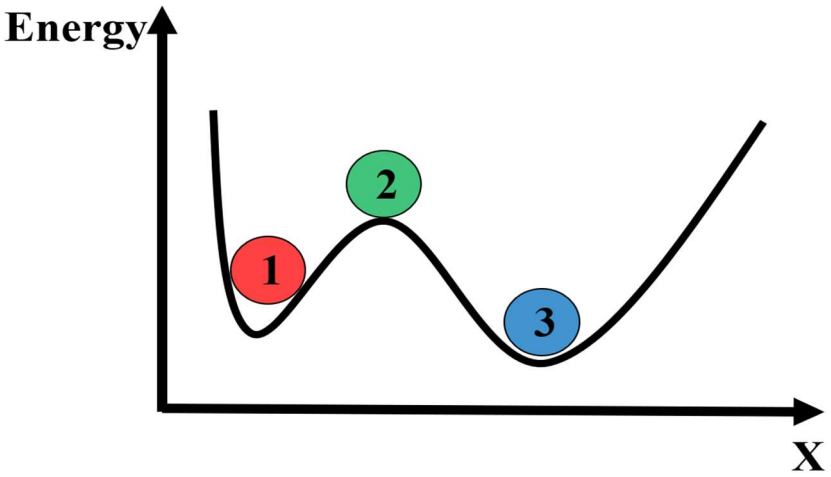

Figure 1-5. *The potential energy of a bistable system. Balls signed as "**1**" and "**3**" are in two stable positions while "**2**" ball is in the unstable equilibrium between "**1**" and "**3**".*

The TTTA organic molecule is an example of such bistable molecular complex. TTTA was first synthesized by Wolmershauser and Johann in 1989[28] and well characterized by Barcaly et al. (in 1998)[29], MaManus et al. (in 2001)[30], W Fujita (in 1999)[31] as a bistable molecule-based magnetic material. TTTA presents bistable magnetic interactions (a diamagnetic-to-paramagnetic transition) at room temperature (305 K). The appealing phenomenon is discovered by Gatteschi et al (in 1993)[32], that metallic clusters of Mn_{12} exhibit magnetic hysteresis different from the one of an ordered magnetic material below T_B and a superparamagnetic behavior exist at a low temperature with a slow relaxation ascribed to the single-ion anisotropy. Another interesting work is to study the multiferroic crossover by the electrical control for Co^{3+}: PTO.[33] Co^{3+} are doped into the nonmagnetic ferroelectric host $PbTiO_3$ (PTO). It is found Co^{3+} ions are bistable magnetism, and the electric field contributes to have the spin crossover phenomenon due to a strong spin-lattice coupling. And Mannini *et al*,[24, 34] in the recent 10 years, studied the Fe_4 compounds on gold surface, which pave a fundamental way to

explore SMMs as monolayer different from the bulk systems. Lastly, one important case for magnetic bistability is the case belonging to Fe^{II}-SCO systems, in which SCO behaviors are induced by changing temperature and light, in some cases, researchers pay attention to synthesize and characterize new Fe(II)-SCO molecules due to the bistability of metastable state.[27] The presence of bistability in molecular materials may bring a strong signal for hysteresis loops by varying external stimuli, which is quite useful and meaningful for devices applied for information storage and spintronic devices.

1.1.4 Applications

Magnetic materials are widely applied in the industry and in our daily life. They are obviously used on our fridges to hold shopping lists, in most of the electric motors, in captors, in sensors, in our smart-phones. They can also be used in the automotive industry where for instance car dampers of Audi cars rely mainly on the magnetic properties of nanoparticles. In art, one also finds artists creating pieces of art with magnetic liquids (ferrofluids). Another wide and obvious field of application is the communication industry and the computer industry where magnetic materials are ubiquitous in data storage. In order to store information, materials must have open hysteresis loops with a large enough coercive field ($\boldsymbol{H_C}$) and high remnant magnetization ($\boldsymbol{M_{rem}}$). $\boldsymbol{H_C}$ and $\boldsymbol{M_{rem}}$ are both important to characterize memory storage capacity. Currently, people are using molecules to create molecular magnets. This new research direction has potential applications to create spintronic devices, data storage devices, quantum gates and qubits, but they obviously not replace classical magnets with which they cannot compete. New original applications where molecular materials may bring an added-value are sought.

1.2 Prussian Blue Analogues

1.2.1 General History

For the sake of understanding the Prussian Blue analogues (PBAs) compounds, it is interesting to have information on its history[35-36] because Prussian Blue is an oldest coordination compound. Prussian blue, first synthesized by Diesbach, a paint maker, in Berlin around 1706, was used as a blue pigment in painting.[35, 37] It is made of iron cations (Fe^{II} and Fe^{III}), cyanide anions (CN^-) and water molecules. Its structure was determined by X-ray diffraction (XRD), Infrared-red (IR) spectroscopy and neutron crystallography, which finally found that PB has a 3D cubic lattice structures (***Figure 1-6***).[38-40] By means of structural analysis from the stoichiometric viewpoint, its composition is $Fe^{III}_4[Fe^{II}(CN)_6]_3 \cdot xH_2O$ (or $Fe_7(CN)_{18}$), where x is ranging from 14 to 16. This cubic 3D network is built by the unit of Fe^{II}-CN-Fe^{III}, so that Prussian blue is also called iron(III) hexacyanoferrate(II).

In ideal PB crystals, the bond distances of Fe(II)-C and Fe(III)-N are 1.92 Å and 2.03 Å, respectively. The Fe^{II} ions are low spin (LS) ions and Fe^{III} ions are high spin (HS). For both ions the 6-fold sites are almost octahedral. PB are used for medical applications.[41-42]

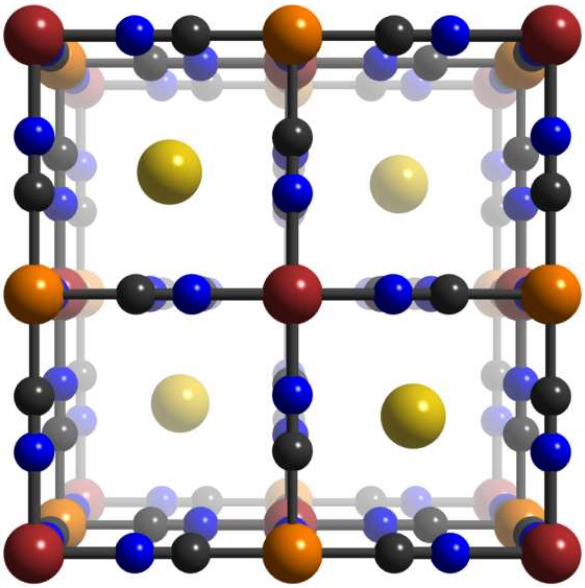

***Figure 1-6**. The chemical schematic of Prussian blue in 3D. The cubic pores are filled with water molecules and these water molecules are omitted for the clarity. Fe(II) ion is shown in the color orange, Fe(III) ion is in color of red, and potassium (K) is in yellow. Carbon and nitrogen are in black and blue, respectively. This structure of PB is cited from the following link: https://chemicalstructure.net/portfolio/prussian-blue/.*

1.2.2 General Formula for PBAs

Coordination networks based on bimetallic cyanide-bridged Prussian Blue Analogues (PBAs) have been extensively investigated because of their highly symmetric structure where the electronic and magnetic interactions can be varied by playing with the nature of the *3d* transitions metal elements.[42-43] These coordination networks are believed to receive applications in the fields of data storage, biology, catalysis and optics by predominately tailoring the magnetic and photomagnetic properties.[44-54] Bulk PBAs crystalize in a face-centered cubic (*fcc*) structure, (***Figure 1-7***), with space group *F-43m*, and with a general formula $A^{I}M^{II}[M'^{III}(CN)_6]$[43], where A^{I} is an alkaline ion (K, Rb, and Cs), M^{II} is a *3d* divalent metallic ion (Cr, Mn, Ni, Co, Fe, or Cu), and M'^{III} is a trivalent metallic ion (Cr or Fe). [44-46, 55-68]

The trivalent ion (M'^{III}) is surrounded by six cyanido bridges in octahedral coordination, i.e. the ion is connected to the carbon atoms of the cyanido bridges. This geometry is highly stable and departure from pure octahedral symmetry for the first neighbors has not been often observed. On the other hand, the divalent ion (M^{II}) is connected to the nitrogen atom of the cyanido bridge and its environment is much less rigid than for the trivalent ion.

Depending on the alkaline content, the ratio between the divalent and the trivalent transition ion can be varied to insure charge equilibrium. When there is one monovalent alkaline ion per unit formula,

the ratio between the divalent and the trivalent ions is 1:1. When the amount of alkaline ion is lowered, the amount of divalent ion has to be increased up to the ratio 3:2. The *fcc* (F-43m) network imposes a 1:1 ratio so that departure from the 1:1 ratio must be accompanied by vacancies on the sites that should have been occupied by trivalent ions. These $M'^{III}(CN)_6$ vacancies are occupied by water molecules. Then the 2:3 stoichiometry induces some disorder in the whole structure and 6-fold coordinated divalent ions are coordinated to nitrogen atoms from the cyanido ligands or oxygen atoms from water molecules.[55-56]

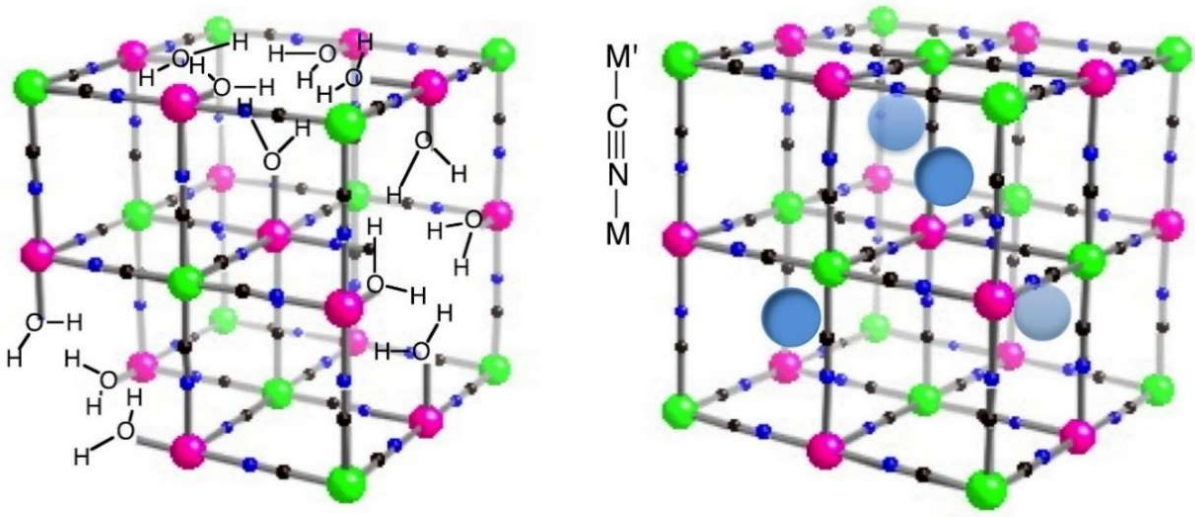

Figure 1-7. *Scheme of unit cell of a Prussian blue analog. Left: alkali free (x = 0). Right: with alkali in the tetrahedral sites (x = 1).*[57] *Trivalent metallic ions are drawn in green, divalent ions are in magenta, alkaline ions are in transparent bule, carbon in black and nitrogen in blue.*

Potential applications (***Figure 1-8***) range from information storage, medical imaging, data recording, or spintronics. They make use of charge-transfer phase transition, reversible photo-magnetism, second harmonic generation, ferroelectric ferromagnetism (in some special cases when a tetragonal phase transition is observed), humidity-sensitive magnetism, high ionic conductivity, and magnetic switching behaviors.[45-47, 50-51, 55-65]

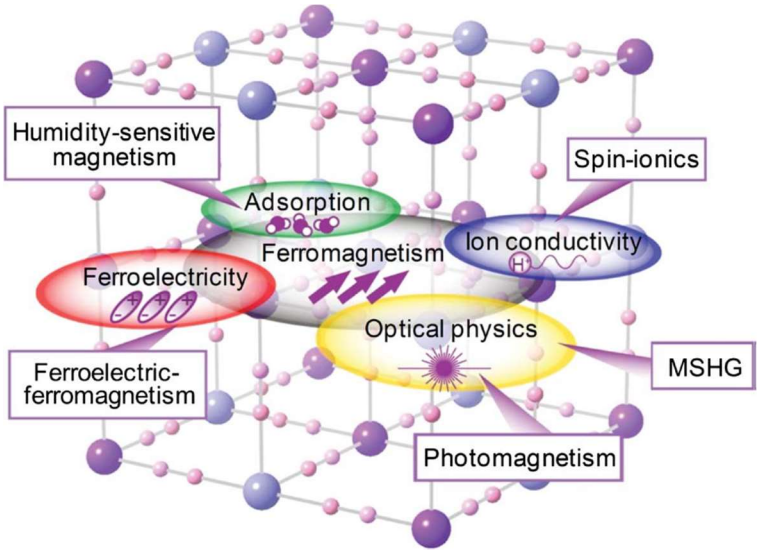

Figure 1-8*. Novel magnetic functionalities of Prussian blue analogs illustrating some potential applications.*[64]

1.2.3 Magnetic Properties in PB and PBAs

1.2.3.1 Magnetic Coupling in PB and PBAs

Prussian blue is a ferromagnet with Curie temperature T_C = 5.6 K[39] with ferromagnetic exchange coupling between Fe^{III}(HS, S=5/2) ions that are separated by around 10 Å. The presence of an inter-valence band located at 700 nm gives to PB its intense blue color. The inter-valence band is caused by an optically activated electron transfer from Fe^{II}(LS) to Fe^{III}(HS).[66-67] The intrinsically mixed valence of PB induces the ferromagnetic coupling as well the intense blue color.

On the other hand, the separation distance between two metal ions in a unit of PBAs is 5 Å since the metal ion that is 6-fold coordinated to cyanides is also paramagnetic. As a consequence, single electrons of metal ions can interact each other directly via the cyanide bridge yielding a much stronger exchange coupling. This magnetic coupling is dominated by the electrostatic interaction between the unpaired electrons. Depending on the relations of orthogonality between the orbital part of the unpaired electrons, one observes antiferromagnetic or ferromagnetic coupling. When the orbital part of the unpaired electrons are orthogonal, one generally observes ferromagnetic coupling. When they are not orthogonal, one generally observes antiferromagnetic coupling. The general magnetic coupling is shown as below ***Figure 1-9***.

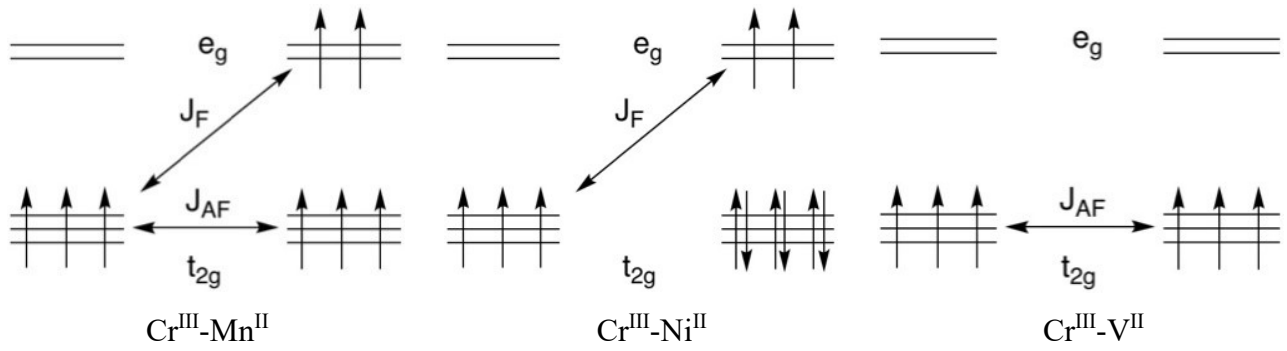

Figure 1-9. *Contribution of the different exchange pathways to the overall exchange interaction: t_{2g}/t_{2g}, J_{AF} and t_{2g}/e_g, J_F.*

In summary, PBAs, may have ferro- or ferrimagnetic ordering with Curie temperature (***Tc***) ranging between 66 and 315 K.[41] The magnetic nature (ferro- or ferri-) of the order depends on the nature of the divalent magnetic ions; V^{II}, Cr^{II} and Mn^{II} leads to a ferrimagnetic order while for Fe^{II} it depends on the trivalent ion (Fe^{III} or Cr^{III}).[41, 59-60, 68-69]

1.2.3.2 Prussian Blue Analogues at the Nanoscale

The first research focusing on PBA NPs was reported by Yamada *et al.* (1997 solid)[70] and Moulik *et al.*(1999 languir).[71] We will here, briefly focus on two types of PBA NPs.

PBA $CsNi^{II}Cr^{III}$ nanoparticles. Previous work by Catala *et al.* have reported the synthesis and the magnetic behavior of nanoparticles of the $CsNi^{II}Cr^{III}$ network.[55, 72-81] This network was already studied by Gadet *et al.* and found to behave as a ferromagnet with T_C = 90 K.[68] The nanocrystals are obtained by the reaction of $[Ni(H_2O)]^{2+}$ with freshly prepared $Cs_2K[Cs(CN)_6]$ in concentrated aqueous solution with the molar ratio of 1/1. The nucleation and growth processes of the particles are affected dramatically by the molar ratio between the two precursors.[55, 72-73] NPs with different sizes can be obtained by different molar ratio : 1) when Cr^{III}/Ni^{II} = 2/3 in water, large particles can form within several minutes and finally precipitate; 2) when Cr^{III}/Ni^{II} = 1/1, the NPs have smaller sizes, lower than 15 nm. The 6-nm particles are obtained by including Cs in the tetrahedral sites of the cubic network.

The 6nm-sized $CsNi^{II}Cr^{III}$ NPs have been initially studied as powders diluted in PVP (Polyvinyl Pyrrolidone) or coated with CTA cations (Cetyltrimethyllammonium),[72-74,76] The NPs present superparamagnetic properties with blocking temperature T_B = 9 K. Studies of $CsNi^{II}Cr^{III}$ NPs reported size effects of NPs[78], core-shell NPs[77-81], different effects of surfactants[55, 73], dipolar interactions[82]. In the core-shell NPs of $CsNi^{II}Cr^{III}$, the anisotropies in magnetism and structure are given in a detailed study by Prado *et al.* who investigated the dipolar interaction and surface effects.[77-81]

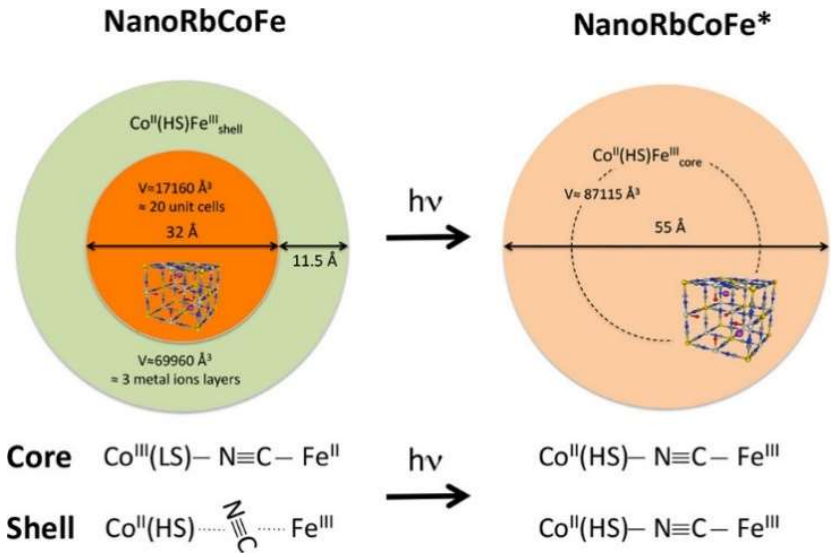

***Figure 1-10**. Structure of NanoRbCoFe before and after irradiation. Typical irradiation conditions are as follows: 10 K, λ = 635 nm, PW = 50 mW·cm^{-2}, 30 min.*[83]

PBA Co^{II}-Fe^{III} Nanoparticles. CoFe PBA are fascinating because their mixed valence behavior. Two stable states can be present at low temperature namely $Co^{II}Fe^{III}$ and $Co^{III}Fe^{II}$. Because Fe is in carbon cavity, it is always in the low spin state. Co is known to be low spin in the oxidation degree III, so that the $Co^{III}Fe^{II}$ phase is diamagnetic, while the $Co^{II}Fe^{III}$ is paramagnetic at high temperature and ferrimagnetic below 21 K.[45-46, 61] Because the magnetic behavior and the electron transfer may be affected by structural distortion, it is important to have information on the structural nature of the surface when nanoparticles are studied. Bleuzen *et al.* studied a series of nanoparticles of CoFe PBA

compounds in different states[45-46,61,69,84-86] and demonstrated thanks to X-ray Absorption Spectroscopy that the surface and the core of the objects possess different structures forming a kind of core-shell heterostructure as depicted in ***Figure 1-10***.[86]

1.3 Spin Crossover Compounds

The spin crossover (SCO) phenomenon may occur in molecular complexes, where high spin (HS) and low spin (LS) states are allowed from the electronic configuration of the complex, which correspond to the d^4, d^5, d^6 and d^7 configurations of the metal ion.[87-93] Experimentally, Fe^{II} (d^6) metal ions in octahedral geometry are dominating so that the discussion will focus on this type of complexes.[87, 91, 94-96]

1.3.1 Ligand Field Considerations

Considering a simple ligand field approach, Fe^{II} containing octahedral complexes may have two electronic configurations namely $t_{2g}^6e_g^0$ and $t_{2g}^4e_g^2$ that correspond to the LS and HS states respectively. Depending on the relative magnitude of the spin pairing energy (P) that depends on the electronic repulsion ($1/r_{ij}$) and the ligand field parameter $10Dq$ (Δ), such complexes may be in the high or the low states (***Figure 1-11***).[27, 97] When the two energies are close, some complexes may undergo a spin crossover between the LS to the HS state thermally upon heating up or by light illumination providing the temperature is below a given value (Light-induced Spin State Trapping; LIESST see ***Figure 1-12***).[87, 94, 98-100] Related Tanabe-Sugano diagrams are shown in **Figure I-1** in **Appendix I.**[101]

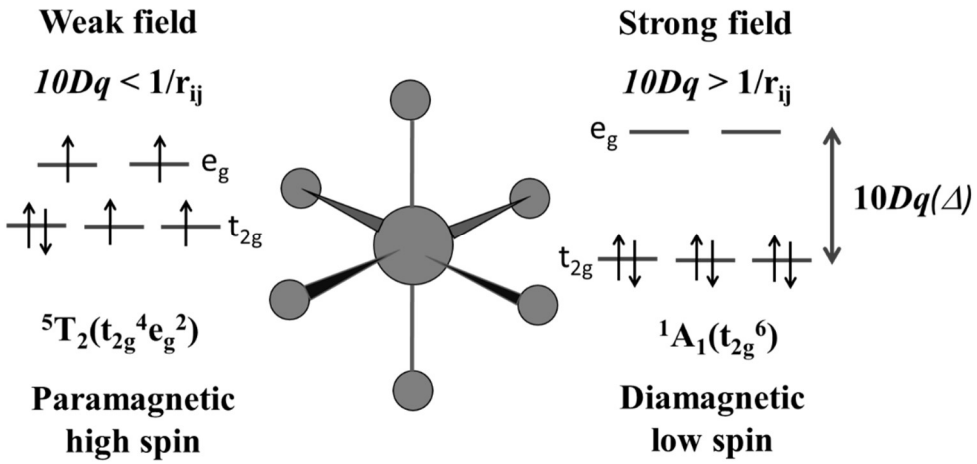

Figure 1-11. *The electronic configuration of two possible ground states for Fe(II) in an octahedral compound. Copyright from@2004 Springer-Verlag Berlin Heidelberg.*[97]

More generally, spin crossover systems may be addressed by different external stimuli such as temperature, light irradiation, pressure, magnetic field and electric field).[27, 84, 102-106]

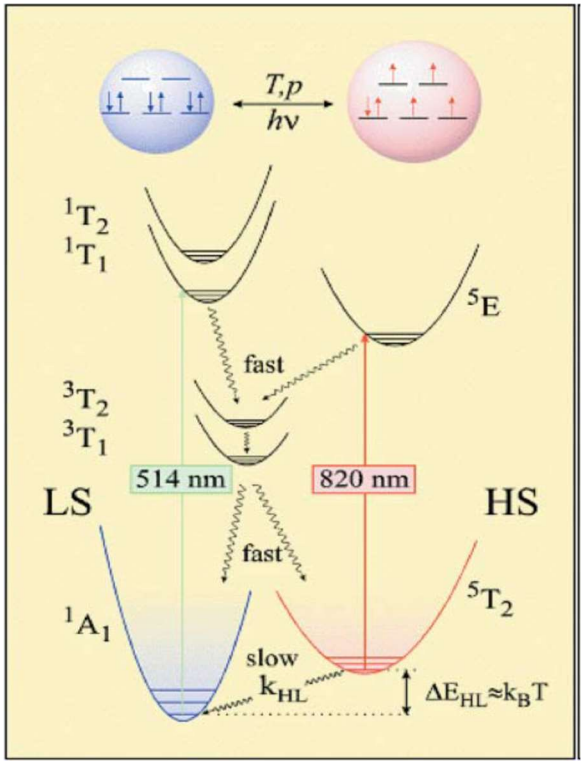

Figure 1-12. *Schematic potential surfaces of low-lying ligand field states for a d^6 spin-crossover complex. The arrows indicate the mechanism for LIESST (LS → HS) and reverse LIESST (LS ← HS). It described when introducing green light(λ=514.5nm) induces the LS states converting into the metastable HS states; while as the introduction of red light (λ=820nm) the stable HS states are converted into metastable LS states.*[102]

1.3.2 Thermal Driven SCO Mechanism

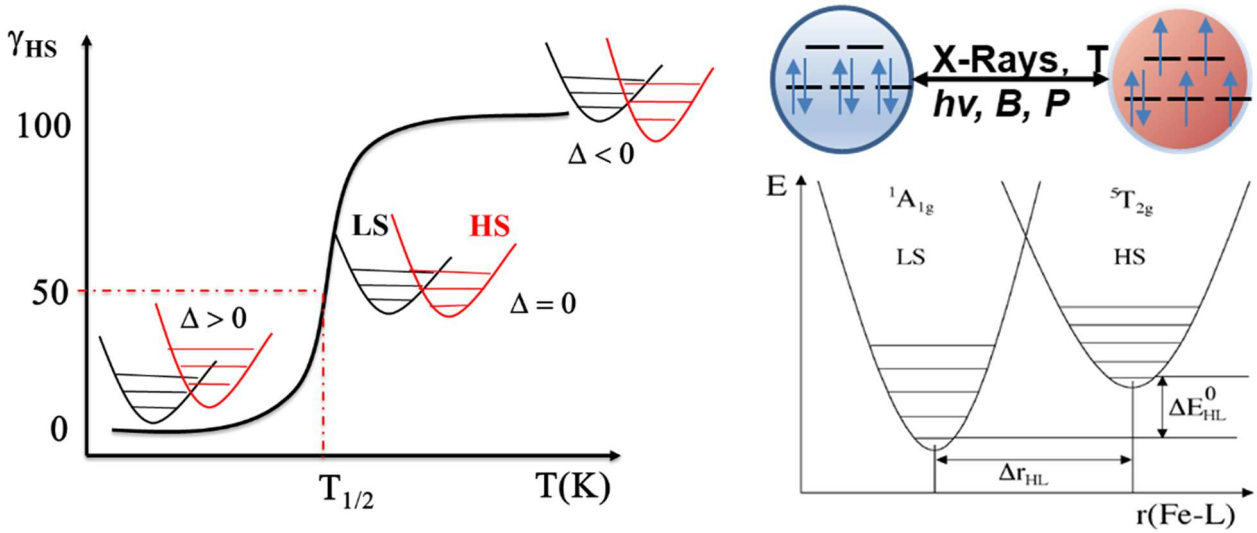

Figure 1-13. *(a)The thermal spin transition curve of the fraction of high spin (γ_{HS}) state vs temperature (T/K). (b)Adiabatic potentials for the high-spin and the low-spin state along the most important reaction coordinate for spin crossover, namely the totally symmetric metal-ligand stretch vibration denoted r(Fe-L).* [97] ***Note****: in the figure of* ***1-13(a)*** *the insets are corresponding to the three complete cases of potential surfaces for HS state and LS state. Thermal energy difference between HS state and LS state is denoted as Δ(HL), the Gibbs free energy between two states. When Δ(HL)>0, it is LS dominate and at the low LT it is mainly LS; Δ(HL)=0 means the fraction of HS state and the one of LS state both are 50% by varying temperatures; Δ(HL)<0, HS state predominates along with heating and up to 100% as the temperature is heat to a relatively high. And the fraction of HS (γ_{HS}) and the fraction of LS(γ_{LS}) are conformed to a linear combination, that is, $\gamma_{HS}+\gamma_{LS}=100\%$.*

The spin crossover is governed by the difference of the Gibbs free energy (G) between the two electronic states.

$$G(T,P) = H - TS \quad (1-3)$$

$$G(T,P)_{HS} = H_{HS} - TS_{HS} \quad (1-4)$$

$$G(T,P)_{LS} = H_{LS} - TS_{LS} \quad (1-5)$$

$$\Delta G^{\theta}(T) = G(T,P)_{HS} - G(T,P)_{LS} = \Delta H^{\theta} - T\Delta S^{\theta} \quad (1-6)$$

At equilibrium, $\Delta G^{\theta}(T) = 0$, and the transition temperature is defined as $T_{1/2} = \frac{\Delta H}{\Delta S}$. In such a case, because of the larger entropy energy of the HS state (electronic state $^5T_{2g}$) compared to the LS state ($^1A_{1g}$) and the larger enthalpy energy of the LS state, the HS state has lower energy at high temperature, while the reverse occurs at low temperature as depicted in ***Figure 1-13****.*

1.3.3 Cooperativity

The spin crossover for a single molecule or for an assembly of non-interacting molecules correspond to a smooth conversion form one state to another. For such a case, no genuine bistability is present. This is observed in solution or in the solid state when the SCO complexes are well isolated. However, when molecules are interacting (H-bonds, $\pi - \pi$ stacking, electrostatically, etc…)[27], the crossover may become abrupt and may in some cases lead the presence of a thermal hysteresis loop as depicted in ***Figure 1-14***.[94, 104] Taking into account this phenomenon, it is possible to introduce a new term (Γ) in the expression of the Gibbs free energy which involves the interaction among the molecules. As ***Figure 1-13*** shown, this SCO behavior is interpreted by the thermal force and expressed as follows:

$$\Delta G_{mix} = (1-\gamma_{HS})G_{LS} + r\gamma_{HS}G_{HS} + \Gamma - \mathrm{T}\Delta S_{mix}\,, \quad (1-7)$$

with

$$\Gamma = \Lambda\gamma_{HS}(\gamma_{LS}) = \Lambda\gamma_{HS}(1-\gamma_{HS})\,, \quad (1-8)$$

and

$$\Delta S_{mix} = -R[\gamma_{HS}\ln(\gamma_{HS}) + (1-\gamma_{HS})\ln(1-\gamma_{HS})]\,. \quad (1-9)$$

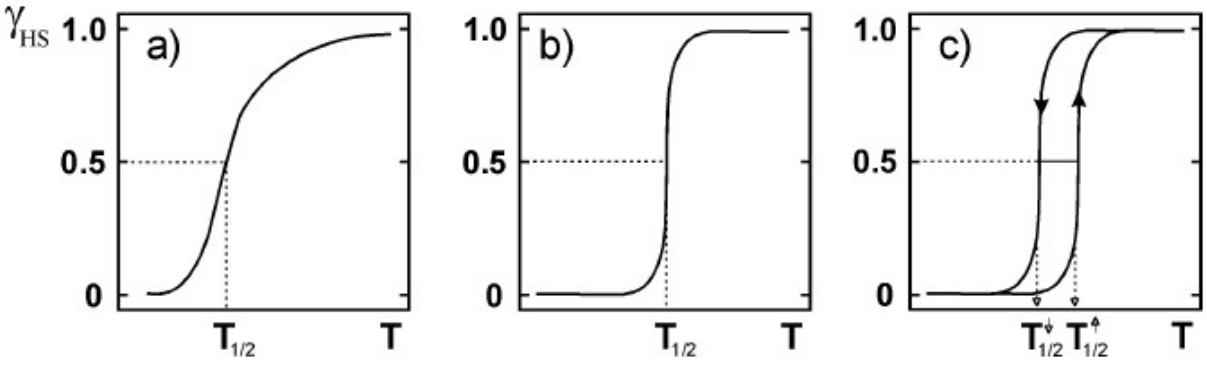

Figure 1-14*. Principal types of spin transition curves in terms of the molar fraction of HS state (γ_{HS}: y axis) vs temperature (T: x axis): a) gradual; b) abrupt; c) with hysteresis. (Reproduced with permission from reference of Philippe Gutlich et.al.* [94, 104] *(Copyright 2003 Wiley-VCH Verlag GmbH & Co. KGaA).*

In e.q.(1-8), the parameter Λ is used to describe the degree of the interplay interaction between LS and HS state.[26] If Λ is negative (< 0), LS-HS pair is more stable than the average of LS-LS and HS-HS pairs, ΔH_{mix} is also negative (since $-T\Delta S_{mix}$ is always negative), thus it is always possible to have a mixture of LS and HS state. If Λ is zero, it means that the state of one molecule in a crystal is independent upon the state of the neighbouring molecues. If Λ is positive (> 0), LS-HS pair is less stable than the average of LS-LS and HS-HS pairs, then there exists a competition between the entropy and enthalpy terms. In e.q.(1-9), ΔS_{mix} expresses an additional entropy due to entropy difference between molecules that have the spin state, on one hand, and molecules that have different spin states when they are close in the mixture. This allows deriving an expression of the transition temperature that depends on the interaction parameter Λ.[26] Such relationship between $\boldsymbol{T_C}$ and Λ is depicted as e.q.(1-10):

$$T_C = \frac{\Delta H + \Lambda(1 - 2\gamma_{HS})}{R ln\left(\frac{1-\gamma_{HS}}{\gamma_{HS}}\right) + \Delta S} . \qquad (1-10)$$

It is possible to show that when $\Lambda < 2R\boldsymbol{T_C}$ (no cooperativity), the inter-molecular interaction is very weak and the transition curve is smooth without hysteresis; when $\Lambda = 2R\boldsymbol{T_C}$, the cooperativity is strong and the spin transition is abrupt, but no hysteresis loop is observed and when $\Lambda > 2R\boldsymbol{T_C}$, a hysteresis loop is present as illustrated in ***Figure 1-15***.

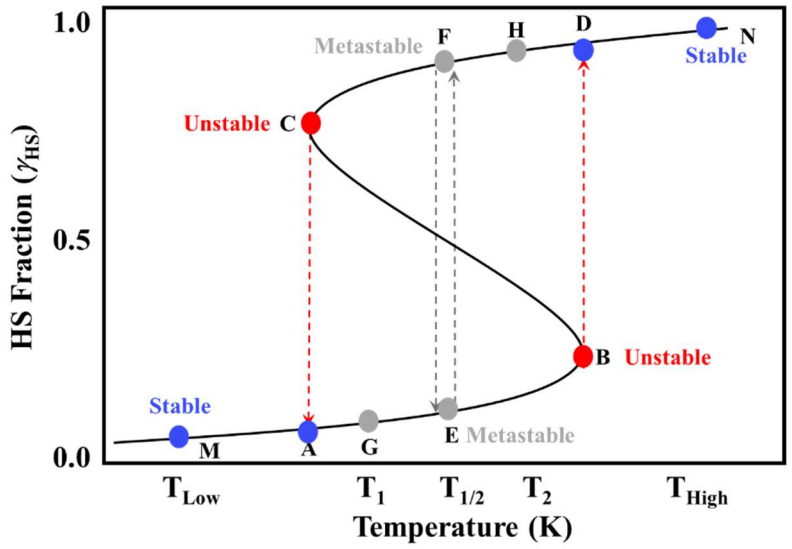

Figure 1-15. *The fraction of high spin (HS) as a function of temperature for a strongly cooperation system ($G > 2\ RT \approx 5000$ cm). From low temperature (T_{Low}) to $T_{1/2}$ the lower branch of LS is more stable, while from $T_{1/2}$ to high temperature (T_{High}) the upper branch of HS is more stable. Red dotted arrows: route without demixing; grey dotted arrows: route with demixing. At $T_{1/2}$, it means that the gibbs energy of system ΔG^{θ} is equavilent to zero ($\Delta G^{\theta} = 0$), and system can stay at two different spin states with the same energy (seeing the section of 1.3.2).*

One of the challenges in this area is to investigate the behavior of a small assembly of molecules in order to build devices for information processing using their bistability or their ability to switch from one to state to another by an electric field or/and by light. The group of Wolfang Kuch in Berlin has

made a series of pronounced investigations of SCO complexes assembled on HOPG using X-ray Absorption Spectroscopy (XAS).[107-112] It is worth noting XAS is among the rare techniques that allows investigating a submonolayer of molecules, particularly, as we will see below, the $L_{2,3}$ of Fe is very sensitive to change of the spin state. In 2012, the XAS studies demonstrated that a submonolayer of the $Fe(phen)_2(NCS)_2$ complex (where phen is o-phenantroline) displayed a thermally reversible SCO behavior when assembled on HOPG directly (***Figure 1-16***).[107] In 2013, W. Kuch and his colleagues studied the different SCO behaviors as a function of the number of layers, one single layer and multilayers of the iron (II) compounds $[Fe(bpz)_2(phen)]$ on Au(111) by a combinational study using STM and NEXAFS (Near-Edge X-rays Absorption Fine Structure).[108] In 2015 they discovered a highly thermal and light induced SCO phenomena of $[Fe(bpz)_2phen]$ on HOPG, which was investigated by a comparative study with the effect of light, temperature and X-rays (***Figure 1-17***).[109]

B. Warner *et al.*[113-114] studied $[Fe(H_2B(pz)_2)_2(2,2'\text{-bipy})]$ molecules on Au(111) using two different systems: (i) $[Fe(H_2B(pz)_2)_2(2,2'\text{-bipy})]$ molecules evaporated as submonolayer and (ii) $[Fe(H_2B(pz)_2)_2(2,2'\text{-bipy})]$ molecules deposited as submonolayer and bilayers. These two studies reveals clearly that the thickness of $Fe[(H_2B(pz)_2)_2(2,2'\text{-bipy})]$ molecules influenced the surface sensitivity towards the substrate. The general SCO behaviors of $[Fe(H_2B(pz)_2)_2(2,2'\text{-bipy})]$ molecules assembled as submonolayer is illustrated as ***Figure 1-18(a)***. Besides, Bairagi *et al.*[115-116] studied another Fe(II) SCO complex ($Fe[HB(3,5\text{-}(Me_2)(pz)_3)_2]$) assembled as monolayers on gold and demonstrated the presence of a complete thermal spin crossover and efficient LIESST effect shown in ***Figure 1-18(b)*.** Light effect induced an incomplete spin transition between HS and LS state.

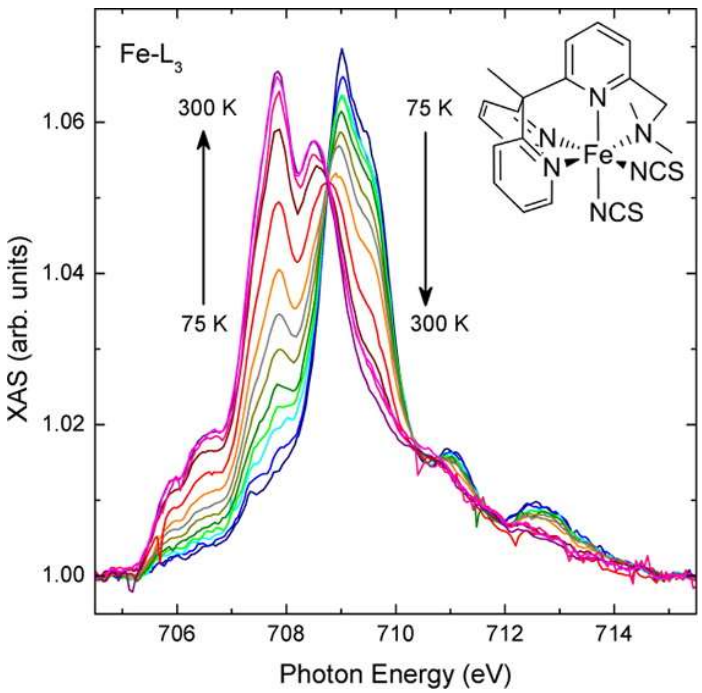

Figure 1-16. *XAS spectra at L_3 edge of Fe(II) sites for submonolayer $Fe[(phen)_2(NCS)_2]$ deposited on HOPG varying temperatures.*[108]

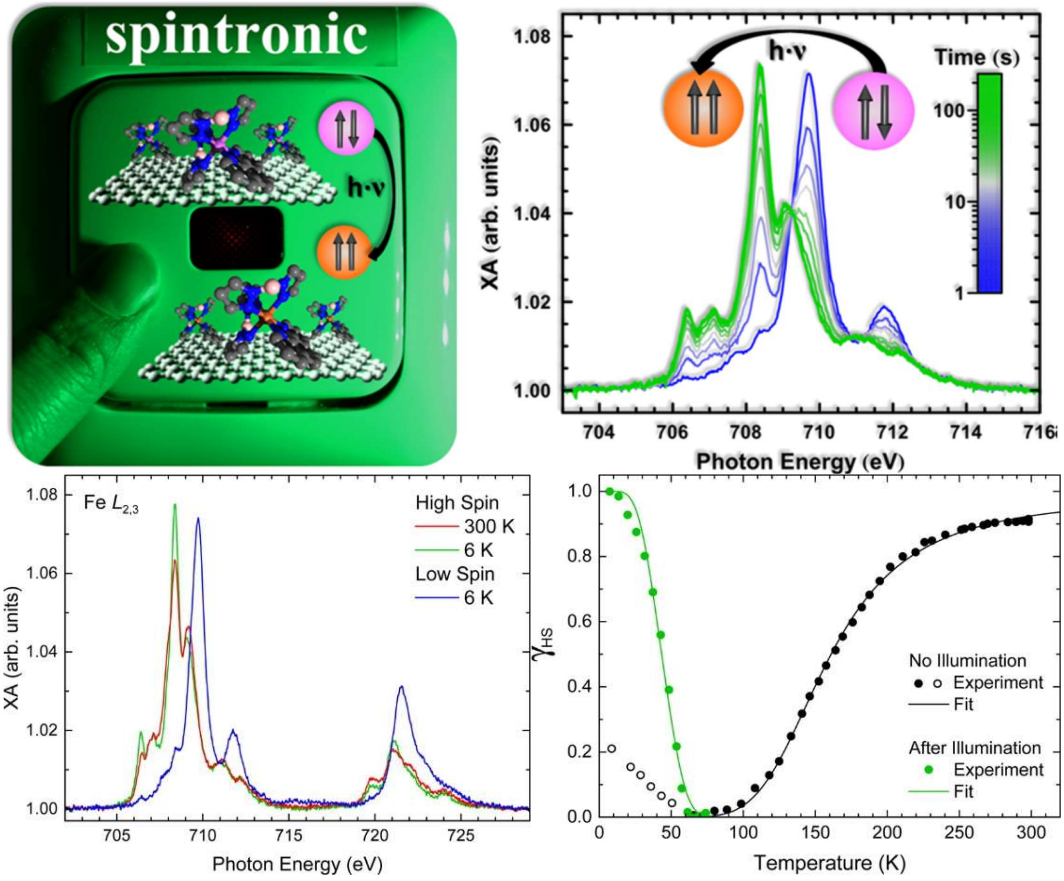

***Figure 1-17**. (**a**) Temperature-dependent Fe $L_{2,3}$ X-ray absorption spectra of 0.4 ML of [Fe(bpz)$_2$phen] on HOPG. Spectra before and after illuminating the sample with green light at T = 6 K are shown in blue and green, respectively and (**b**) Fraction of HS molecules as a function of temperature during cooling the sample without illuminations (black solid symbols) and after saturation of the light-induced HS state during heating the sample (green solid symbols), reproduced with permission from ref 117.*[117]

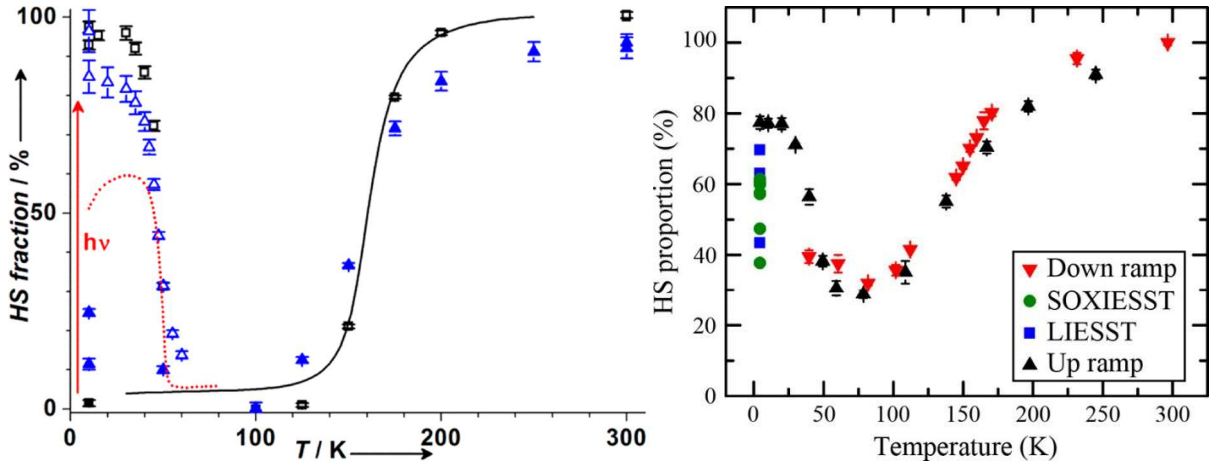

***Figure 1-18**. (**a**)HS fraction vs temperature for [Fe(H$_2$B(pz)$_2$)$_2$(2,2'-bipy)] evaporated as submonolayer on Au(111).*[113] *All values of HS fraction are derived from the linear interpolation of the XAS spectra for the bulk compound before (filled black squares) and after illumination (empty black squares) and the 300 nm thick film before (filled blue triangles) and after illumination (empty blue triangles) compared to the magnetometric results on the bulk compound before (full line) and after illumination (red dotted line). (**b**) HS fraction vs temperature for Fe[HB(3,5-(Me$_2$)(pz)$_3$)$_2$] assembled as monolayer on Au(111).*[115] *HS fraction as a function of temperature as cooling down the sample from 300 to 4.4 K(red down triangles), exposing it with the illumination of soft X-ray (eight green points) and blue light(three blue square), and warming it up to 250 K (labled as black up triangles).*[109]

1.4 Objectives of the Present Work

The objective of this thesis is to investigate the electronic and magnetic properties of molecular materials assembled on metallic surfaces. Two main challenges are addressed.

The first one is the study of the relationship between magnetic and electronic anisotropy of coordination nanoparticles based on the Prussian blue analogs and establish the role played by surface of the particles on the local magnetic anisotropy and on anisotropy of a single monolayer. Indeed, the surface of 6 nm nanoparticle contribute to 40% to its overall volume and any structural anisotropy may induce an electronic anisotropy and, hence, also magnetic in the presence of a magnetic field.

The second challenge is the investigation of the switching behavior of spin crossover complexes at the nanoscale and, in particular, when assembled as organized islands on metallic surfaces. SCO molecular materials have been studied for decades in the solid state and the mechanism of the switching phenomena established as being mainly due to elastic interaction among the molecules. The magnitude of this long-range interaction may lead to large cooperativity resulting in bistability behavior. When the size of the grain is decreased and obviously when dealing with an island of a single layer, the elastic interaction is confined which may lead to a disappearance of bistability. The present work aims at (partially) addressing this question. SCO materials, also, display a LIESST effect at low temperature that transforms LS to HS. We, therefore, also investigate the effect of light on a submonolayer of SCO molecules. And finally, because we are dealing with a submonolayer, the nature of the substrate and the substrate/molecules interface may play a major role in the switching behavior either when the stimulus is light or a change of temperature.

Because we are dealing with submonolayer s of molecular materials assembled on surfaces, we use X-rays Absorption Spectroscopy (XAS) at the $L_{2,3}$ edges of metal ions that is extremely sensitive to small amount of matter. XAS at the $L_{2,3}$ edges using total electron yield detection technique is extremely sensitive to the change in the electronic structure and is, therefore, perfectly adapted to SCO systems. X-ray Magnetic Circular Dichroism (XMCD) allows qualitatively measuring the magnetic moment of a submonolayer of magnetic objects, while X-ray Natural Linear Dichroism (XNLD) may give information of the anisotropy of the electronic distribution in the coordination sphere of a metal ion. It, therefore, allows us 1) to determine the orientation of the objects on a substrate and 2) have information on nature of the local distortion of the coordination sphere that together with XMCD give information on the magnetic anisotropy. Since XAS gives qualitative information, the analysis of the data quantitatively cannot be conducted without the help of calculations. We use Ligand Field Mutiplet (LFM) calculations to calibrate the experimental data for XAS, XMCD and XNLD. This allows us to determine the high to low spin ratio of the SCO molecules and the magnetization of the magnetic nanoparticles. For the last case, the sum rule must also be used.

References

1. Getzlaff, M., *Fundamentals of magnetism*. Springer Science & Business Media: 2007.
2. Fowler, M., Historical beginnings of theories of electricity and magnetism. *Recuperado el* **1997,** *23* (5), 2012.
3. Dill, J. G., Lodestone and needle: the rise of the magnetic compass. *Ocean Navigator* **2003,** *1*.
4. Bullard, E. C., The magnetic field within the Earth. *Proceedings of the Royal Society of London. Series A. Mathematical and Physical Sciences* **1949,** *197* (1051), 433-453.
5. Ronan, C. A.; Needham, J., *The Shorter'Science and Civilisation in China'*. Cambridge University Press Cambridge: 1978; Vol. 1.
6. Papaefthymiou, G. C., Nanoparticle magnetism. *Nano Today* **2009,** *4* (5), 438-447.
7. Kahn, O., Molecular magnetism. *VCH Publishers, Inc.(USA), 1993* **1993**, 393.
8. Kahn, O.; Martinez, C. J., Spin-transition polymers: From molecular materials toward memory devices. *Science* **1998,** *279* (5347), 44-48.
9. Caneschi, A.; Gatteschi, D.; Sessoli, R.; Barra, A. L.; Brunel, L. C.; Guillot, M., Alternating current susceptibility, high field magnetization, and millimeter band EPR evidence for a ground S= 10 state in [Mn12O12 (Ch3COO) 16 (H2O) 4]. 2CH3COOH. 4H2O. *Journal of the American Chemical Society* **1991,** *113* (15), 5873-5874.
10. Sessoli, R.; Tsai, H. L.; Schake, A. R.; Wang, S.; Vincent, J. B.; Folting, K.; Gatteschi, D.; Christou, G.; Hendrickson, D. N., High-spin molecules:[Mn12O12 (O2CR) 16 (H2O) 4]. *Journal of the American Chemical Society* **1993,** *115* (5), 1804-1816.
11. Sessoli, R.; Gatteschi, D.; Caneschi, A.; Novak, M., Magnetic bistability in a metal-ion cluster. *Nature* **1993,** *365* (6442), 141.
12. Heinze, S.; Bode, M.; Kubetzka, A.; Pietzsch, O.; Nie, X.; Blügel, S.; Wiesendanger, R., Real-space imaging of two-dimensional antiferromagnetism on the atomic scale. *Science* **2000,** *288* (5472), 1805-1808.
13. Leuenberger, M. N.; Loss, D., Quantum computing in molecular magnets. *Nature* **2001,** *410* (6830), 789.
14. Zhao, A.; Li, Q.; Chen, L.; Xiang, H.; Wang, W.; Pan, S.; Wang, B.; Xiao, X.; Yang, J.; Hou, J., Controlling the Kondo effect of an adsorbed magnetic ion through its chemical bonding. *Science* **2005,** *309* (5740), 1542-1544.
15. Gatteschi, D.; Sessoli, R.; Villain, J., *Molecular nanomagnets*. Oxford University Press on Demand: 2006; Vol. 5.
16. Hirjibehedin, C. F.; Lutz, C. P.; Heinrich, A. J., Spin coupling in engineered atomic structures. *Science* **2006,** *312* (5776), 1021-1024.
17. Bogani, L.; Wernsdorfer, W., Molecular spintronics using single-molecule magnets. *Nature Materials* **2008,** *7* (3), 179-186.
18. Friedman, J. R.; Sarachik, M.; Tejada, J.; Ziolo, R., Macroscopic measurement of resonant magnetization tunneling in high-spin molecules. *Physical review letters* **1996,** *76* (20), 3830.
19. Thomas, L.; Lionti, F.; Ballou, R.; Gatteschi, D.; Sessoli, R.; Barbara, B., Macroscopic quantum tunnelling of magnetization in a single crystal of nanomagnets. *Nature* **1996,** *383* (6596), 145.
20. Kim, G.-H.; Kim, T.-S., Electronic transport in single-molecule magnets on metallic surfaces. *Physical review letters* **2004,** *92* (13), 137203.
21. Rocha, A. R.; Garcia-Suarez, V. M.; Bailey, S. W.; Lambert, C. J.; Ferrer, J.; Sanvito, S., Towards molecular spintronics. *Nat Mater* **2005,** *4* (4), 335-9.
22. Mannini, M.; Pineider, F.; Sainctavit, P.; Joly, L.; Fraile‐Rodríguez, A.; Arrio, M. A.; Cartier dit Moulin, C.; Wernsdorfer, W.; Cornia, A.; Gatteschi, D., X‐ray magnetic circular dichroism picks out single‐molecule magnets suitable for nanodevices. *Advanced Materials* **2009,** *21* (2), 167-171.
23. Mannini, M.; Pineider, F.; Danieli, C.; Totti, F.; Sorace, L.; Sainctavit, P.; Arrio, M.-A.; Otero, E.; Joly, L.; Cezar, J. C., Quantum tunnelling of the magnetization in a monolayer of oriented single-molecule magnets.

Nature **2010,** *468* (7322), 417.

24. Mannini, M.; Pineider, F.; Sainctavit, P.; Danieli, C.; Otero, E.; Sciancalepore, C.; Talarico, A. M.; Arrio, M.-A.; Cornia, A.; Gatteschi, D., Magnetic memory of a single-molecule quantum magnet wired to a gold surface. *Nature materials* **2009,** *8* (3), 194.

25. Sanvito, S., Molecular spintronics. *Chemical Society Reviews* **2011,** *40* (6), 3336-3355.

26. Kahn, O.; Launay, J., Molecular bistability: An overview. *Chemtronics* **1988,** *3*, 140-151.

27. Gütlich, P.; Goodwin, H. A., Spin Crossover—An Overall Perspective. In *Spin Crossover in Transition Metal Compounds I*, Gütlich, P.; Goodwin, H. A., Eds. Springer Berlin Heidelberg: Berlin, Heidelberg, 2004; pp 1-47.

28. Wolmershauser, G.; Johann, R., 1,3,5-TRITHIA-2,4,6-TRIAZAPENTALENYL - A STABLE SULFUR-NITROGEN RADICAL. *Angewandte Chemie-International Edition in English* **1989,** *28* (7), 920-921.

29. Barclay, T. M.; Cordes, A. W.; George, N. A.; Haddon, R. C.; Itkis, M. E.; Mashuta, M. S.; Oakley, R. T.; Patenaude, G. W.; Reed, R. W.; Richardson, J. F.; Zhang, H., Redox, Magnetic, and Structural Properties of 1,3,2-Dithiazolyl Radicals. A Case Study on the Ternary Heterocycle S3N5C4. *Journal of the American Chemical Society* **1998,** *120* (2), 352-360.

30. McManus, G. D.; Rawson, J. M.; Feeder, N.; van Duijn, J.; McInnes, E. J. L.; Novoa, J. J.; Burriel, R.; Palacio, F.; Oliete, P., Synthesis, crystal structures, electronic structure and magnetic behaviour of the trithiatriazapentalenyl radical, CSN. *Journal of Materials Chemistry* **2001,** *11* (8), 1992-2003.

31. Fujita, W.; Awaga; Kunio, Room-Temperature Magnetic Bistability in Organic Radical Crystals. *Science* **1999,** *286* (5438), 261-262.

32. Sessoli, R.; Gatteschi, D.; Caneschi, A.; Novak, M. A., Magnetic bistability in a metal-ion cluster. *Nature* **1993,** *365* (6442), 141-143.

33. Weston, L.; Cui, X. Y.; Ringer, S. P.; Stampfl, C., Bistable Magnetism and Potential for Voltage-Induced Spin Crossover in Dilute Magnetic Ferroelectrics. *Physical Review Letters* **2015,** *114* (24), 247601.

34. Mannini, M.; Pineider, F.; Danieli, C.; Totti, F.; Sorace, L.; Sainctavit, P.; Arrio, M. A.; Otero, E.; Joly, L.; Cezar, J. C.; Cornia, A.; Sessoli, R., Quantum tunnelling of the magnetization in a monolayer of oriented single-molecule magnets. *Nature* **2010,** *468* (7322), 417-21.

35. Coleby, L. J. M., A history of Prussian blue. *Annals of Science* **1939,** *4* (2), 206-211.

36. Kraft, A., What a chemistry student should know about the history of Prussian blue. *ChemTexts* **2018,** *4* (4), 16.

37. Bartoll, J. In *The early use of Prussian blue in paintings*, Proceedings of the 9th International Conference on NDT of Art, 2008.

38. Robin, M. B., THE COLOR AND ELECTRONIC CONFIGURATIONS OF PRUSSIAN BLUE. *Spectrochimica Acta* **1961,** *17* (9-10), 1095-1095.

39. Buser, H. J.; Ludi, A.; Fischer, P.; Studach, T.; Dale, B. W., NEUTRON-DIFFRACTION STUDY OF PRUSSIAN BLUE, FE4 FE(CN)6 3.14D2O. *Zeitschrift Fur Physikalische Chemie-Frankfurt* **1974,** *92* (4-6), 354-357.

40. Buser, H.; Schwarzenbach, D.; Petter, W.; Ludi, A., The crystal structure of Prussian blue: Fe4 [Fe (CN) 6] 3. xH2O. *Inorganic Chemistry* **1977,** *16* (11), 2704-2710.

41. Ferlay, S.; Mallah, T.; Ouahes, R.; Veillet, P.; Verdaguer, M., A room-temperature organometallic magnet based on Prussian blue. *Nature* **1995,** *378* (6558), 701.

42. Dunbar, K. R.; Heintz, R. A., Chemistry of transition metal cyanide compounds: Modern perspectives. *Progress in Inorganic Chemistry* **1997,** *45*, 283-392.

43. Verdaguer, M.; Girolami, G. S.; Miller, J.; Drillon, M., Magnetic Prussian blue analogs. *Magnetism: molecules to materials V* **2005,** *5*, 283-346.

44. Sato, O.; Iyoda, T.; Fujishima, A.; Hashimoto, K., Photoinduced magnetization of a cobalt-iron cyanide. *Science* **1996,** *272* (5262), 704-705.

45. Bleuzen, A.; Lomenech, C.; Dolbecq, A.; Villain, F.; Goujon, A.; Roubeau, O.; Nogues, M.; Varret, F.; Baudelet, F.; Dartyge, E.; Giorgetti, C.; Gallet, J.-J.; Moulin, C. C. D.; Verdaguer, M., Photo-Induced Electron Transfer and Magnetic Switching in CoFe Cyanides: Study of the Metastable State. *Molecular Crystals and*

Liquid Crystals Science and Technology. Section A. Molecular Crystals and Liquid Crystals **1999,** *335* (1), 253-262.

46. Bleuzen, A.; Lomenech, C.; Escax, V.; Villain, F.; Varret, F.; Cartier dit Moulin, C.; Verdaguer, M., Photoinduced ferrimagnetic systems in Prussian blue analogues CI x Co4 [Fe (CN) 6] y (CI= alkali cation). 1. Conditions to observe the phenomenon. *Journal of the American Chemical Society* **2000,** *122* (28), 6648-6652.

47. Coronado, E.; Galan-Mascaros, J. R.; Gomez-Garcia, C. J.; Laukhin, V., Coexistence of ferromagnetism and metallic conductivity in a molecule-based layered compound. *Nature* **2000,** *408* (6811), 447.

48. Coronado, E.; Galán-Mascarós, J. R.; Gómez-García, C. J.; Martínez-Agudo, J. M., Tuning the magnetic properties in the layered molecular based magnets A [FeIIRuxIIIM1− xIII (ox) 3](MIII= Cr or Fe; ox= oxalate; A= organic or organometallic cation). *Synthetic metals* **2001,** *122* (3), 501-507.

49. de Tacconi, N. R.; Rajeshwar, K.; Lezna, R. O., Metal hexacyanoferrates: electrosynthesis, in situ characterization, and applications. *Chemistry of Materials* **2003,** *15* (16), 3046-3062.

50. Coronado, E.; Day, P., Magnetic molecular conductors. *Chemical reviews* **2004,** *104* (11), 5419-5448.

51. Ohkoshi, S.-i.; Arai, K.-i.; Sato, Y.; Hashimoto, K., Humidity-induced magnetization and magnetic pole inversion in a cyano-bridged metal assembly. *Nature materials* **2004,** *3* (12), 857.

52. Coronado, E.; Giménez-López, M. C.; Levchenko, G.; Romero, F. M.; García-Baonza, V.; Milner, A.; Paz-Pasternak, M., Pressure-tuning of magnetism and linkage isomerism in iron (II) hexacyanochromate. *Journal of the American Chemical Society* **2005,** *127* (13), 4580-4581.

53. Ohkoshi, S.-i.; Tokoro, H.; Hozumi, T.; Zhang, Y.; Hashimoto, K.; Mathonière, C.; Bord, I.; Rombaut, G.; Verelst, M.; Cartier dit Moulin, C., Photoinduced magnetization in copper octacyanomolybdate. *Journal of the American Chemical Society* **2006,** *128* (1), 270-277.

54. Sato, O.; Tao, J.; Zhang, Y. Z., Control of magnetic properties through external stimuli. *Angewandte Chemie International Edition* **2007,** *46* (13), 2152-2187.

55. Catala, L.; Volatron, F.; Brinzei, D.; Mallah, T., Functional coordination nanoparticles. *Inorganic chemistry* **2009,** *48* (8), 3360-3370.

56. Zakaria, M. B.; Chikyow, T., Recent advances in Prussian blue and Prussian blue analogues: synthesis and thermal treatments. *Coordination Chemistry Reviews* **2017,** *352*, 328-345.

57. Catala, L.; Mallah, T., Nanoparticles of Prussian blue analogs and related coordination polymers: From information storage to biomedical applications. *Coordination Chemistry Reviews* **2017,** *346*, 32-61.

58. Mallah, T.; Ferlay, S.; Auberger, C.; Helary, C.; L'Hermite, F.; Ouahes, R.; Vaissemann, J.; Verdaguer, M.; Veillet, P., Hexacyanometalates: Molecular Precursors for High-Spin Molecules and High-TC Molecule-Based Magnets. *Molecular Crystals and Liquid Crystals Science and Technology. Section A. Molecular Crystals and Liquid Crystals* **1995,** *273* (1), 141-151.

59. Mallah, T.; Ferlay, S.; Sculler, A.; Verdaguer, M., A Rationale Molecular Approach to High-Spin Molecules and Molecular Magnets. In *Magnetism: A Supramolecular Function*, Kahn, O., Ed. Springer Netherlands: Dordrecht, 1996; pp 597-614.

60. Verdaguer, M.; Bleuzen, A.; Marvaud, V.; Vaissermann, J.; Seuleiman, M.; Desplanches, C.; Scuiller, A.; Train, C.; Garde, R.; Gelly, G.; Lomenech, C.; Rosenman, I.; Veillet, P.; Cartier, C.; Villain, F., Molecules to build solids: high TC molecule-based magnets by design and recent revival of cyano complexes chemistry. *Coordination Chemistry Reviews* **1999,** *190-192*, 1023-1047.

61. Champion, G.; Escax, V.; Cartier dit Moulin, C.; Bleuzen, A.; Villain, F.; Baudelet, F.; Dartyge, E.; Verdaguer, M., Photoinduced Ferrimagnetic Systems in Prussian Blue Analogues CI x Co4 [Fe (CN) 6] y (CI= Alkali Cation). 4. Characterization of the Ferrimagnetism of the Photoinduced Metastable State in Rb1. 8Co4 [Fe (CN) 6] 3.3☉ 13H2O by K Edges X-ray Magnetic Circular Dichroism. *Journal of the American Chemical Society* **2001,** *123* (50), 12544-12546.

62. Frey, N. A.; Peng, S.; Cheng, K.; Sun, S., Magnetic nanoparticles: synthesis, functionalization, and applications in bioimaging and magnetic energy storage. *Chemical Society Reviews* **2009,** *38* (9), 2532-2542.

63. Altavilla, C.; Ciliberto, E., Inorganic nanoparticles: synthesis, applications, and perspectives. An overview. *Inorganic Nanoparticles: Synthesis, Applications, and Perspectives. ed by Altavilla C and Ciliberto E,*

CRC Press, New York **2011**, 1-17.

64. Tokoro, H.; Ohkoshi, S.-i., Novel magnetic functionalities of Prussian blue analogs. *Dalton Transactions* **2011,** *40* (26), 6825-6833.

65. Einaga, Y., Photo-switching magnetic materials. *Journal of Photochemistry and Photobiology C: Photochemistry Reviews* **2006,** *7* (2-3), 69-88.

66. Mayoh, B.; Day, P., Charge transfer in mixed-valence solids. Part VIII. Contribution of valence delocalisation to the ferromagnetism of Prussian Blue. *Journal of the Chemical Society, Dalton Transactions* **1976,** (15), 1483-1486.

67. Rogez, G.; Marvilliers, A.; Rivière, E.; Audière, J.-P.; Lloret, F.; Varret, F.; Goujon, A.; Mendenez, N.; Girerd, J.-J.; Mallah, T., A Mixed-Valence Mixed-Spin Prussian-Blue-Like Heptanuclear Complex. *Angewandte Chemie International Edition* **2000,** *39* (16), 2885-2887.

68. Gadet, V.; Mallah, T.; Castro, I.; Verdaguer, M.; Veillet, P., High-TC molecular-based magnets: a ferromagnetic bimetallic chromium (III)-nickel (II) cyanide with TC= 90 K. *Journal of the American Chemical Society* **1992,** *114* (23), 9213-9214.

69. Aouadi, M.; Fornasieri, G.; Briois, V.; Durand, P.; Bleuzen, A., Chemistry of Cobalt(II) Confined in the Pores of Ordered Silica Monoliths: From the Formation of the Monolith to the CoFe Prussian Blue Analogue Nanocomposite. *Chemistry – A European Journal* **2012,** *18* (9), 2617-2623.

70. Yamada, S.; Kuwabara, K.; Koumoto, K., Characterization of Prussian Blue analogue: nanocrystalline nickel-iron cyanide. *Materials Science and Engineering: B* **1997,** *49* (2), 89-94.

71. Moulik, S.; De, G.; Panda, A.; Bhowmik, B.; Das, A., Dispersed molecular aggregates. 1. Synthesis and characterization of nanoparticles of Cu2 [Fe (CN) 6] in H2O/AOT/n-heptane water-in-oil microemulsion media. *Langmuir* **1999,** *15* (24), 8361-8367.

72. Catala, L.; Gacoin, T.; Boilot, J. P.; Rivière, É.; Paulsen, C.; Lhotel, E.; Mallah, T., Cyanide‐Bridged CrIII–NiII Superparamagnetic Nanoparticles. *Advanced Materials* **2003,** *15* (10), 826-829.

73. Brinzei, D.; Catala, L.; Louvain, N.; Rogez, G.; Stéphan, O.; Gloter, A.; Mallah, T., Spontaneous stabilization and isolation of dispersible bimetallic coordination nanoparticles of Cs x Ni [Cr (CN) 6] y. *Journal of Materials Chemistry* **2006,** *16* (26), 2593-2599.

74. Catala, L.; Gloter, A.; Stephan, O.; Rogez, G.; Mallah, T., Superparamagnetic bimetallic cyanide-bridged coordination nanoparticles with TB= 9 K. *Chemical Communications* **2006,** (9), 1018-1020.

75. Clemente-León, M.; Coronado, E.; López-Muñoz, A. n.; Repetto, D.; Mingotaud, C.; Brinzei, D.; Catala, L.; Mallah, T., Magnetic Langmuir− Blodgett Films of Bimetallic Coordination Nanoparticles of Cs0. 4Ni [Cr (CN) 6] 0.9. *Chemistry of Materials* **2008,** *20* (14), 4642-4652.

76. Fleury, B.; Volatron, F.; Catala, L.; Brinzei, D.; Rivière, E.; Huc, V.; David, C.; Miserque, F.; Rogez, G.; Baraton, L., Grafting a monolayer of superparamagnetic cyanide-bridged coordination nanoparticles on Si (100). *Inorganic chemistry* **2008,** *47* (6), 1898-1900.

77. Catala, L.; Brinzei, D.; Prado, Y.; Gloter, A.; Stéphan, O.; Rogez, G.; Mallah, T., Core–multishell magnetic coordination nanoparticles: toward multifunctionality on the nanoscale. *Angewandte Chemie International Edition* **2009,** *48* (1), 183-187.

78. Prado, Y.; Lisnard, L.; Heurtaux, D.; Rogez, G.; Gloter, A.; Stéphan, O.; Dia, N.; Rivière, E.; Catala, L.; Mallah, T., Tailored coordination nanoparticles: assessing the magnetic single-domain critical size. *Chemical Communications* **2011,** *47* (3), 1051-1053.

79. Prado, Y.; Dia, N.; Lisnard, L.; Rogez, G.; Brisset, F.; Catala, L.; Mallah, T., Tuning the magnetic anisotropy in coordination nanoparticles: random distribution versus core–shell architecture. *Chemical Communications* **2012,** *48* (93), 11455-11457.

80. Prado, Y.; Arrio, M. A.; Volatron, F.; Otero, E.; Cartier dit Moulin, C.; Sainctavit, P.; Catala, L.; Mallah, T., Magnetic Anisotropy of Cyanide‐Bridged Core and Core–Shell Coordination Nanoparticles Probed by X‐ray Magnetic Circular Dichroism. *Chemistry–A European Journal* **2013,** *19* (21), 6685-6694.

81. Prado, Y.; Mazerat, S.; Rivière, E.; Rogez, G.; Gloter, A.; Stéphan, O.; Catala, L.; Mallah, T., Magnetization reversal in CsNiIICrIII (CN) 6 coordination nanoparticles: unravelling surface anisotropy and

dipolar interaction effects. *Advanced Functional Materials* **2014,** *24* (34), 5402-5411.

82. Prado, Y.; Mazerat, S.; Rivière, E.; Rogez, G.; Gloter, A.; Stéphan, O.; Catala, L.; Mallah, T., Magnetization Reversal in CsNiIICrIII(CN)6Coordination Nanoparticles: Unravelling Surface Anisotropy and Dipolar Interaction Effects. *Advanced Functional Materials* **2014,** *24* (34), 5402-5411.

83. Bordage, A.; Moulin, R.; Fonda, E.; Fornasieri, G.; Riviere, E.; Bleuzen, A., Evidence of the Core-Shell Structure of (Photo)magnetic CoFe Prussian Blue Analogue Nanoparticles and Peculiar Behavior of the Surface Species. *J Am Chem Soc* **2018,** *140* (32), 10332-10343.

84. Varret, F.; Bleuzen, A.; Boukheddaden, K.; Bousseksou, A.; Codjovi, E.; Enachescu, C.; Goujon, A.; Linares, J.; Menendez, N.; Verdaguer, M., Examples of molecular switching in inorganic solids, due to temperature, light, pressure, and magnetic field. *Pure and applied chemistry* **2002,** *74* (11), 2159-2168.

85. Fornasieri, G.; Aouadi, M.; Durand, P.; Beaunier, P.; Rivière, E.; Bleuzen, A., Fully controlled precipitation of photomagnetic CoFe Prussian blue analogue nanoparticles within the ordered mesoporosity of silica monoliths. *Chemical Communications* **2010,** *46* (42), 8061-8063.

86. Bordage, A.; Moulin, R.; Fonda, E.; Fornasieri, G.; Rivière, E.; Bleuzen, A., Evidence of the Core–Shell Structure of (Photo)magnetic CoFe Prussian Blue Analogue Nanoparticles and Peculiar Behavior of the Surface Species. *Journal of the American Chemical Society* **2018,** *140* (32), 10332-10343.

87. Gutlich, P., SPIN CROSSOVER IN IRON(II)-COMPLEXES. *Structure and Bonding* **1981,** *44*, 83-195.

88. Sim, P. G.; Sinn, E., First manganese (III) spin crossover, first d4 crossover. Comment on cytochrome oxidase. *Journal of the American Chemical Society* **1981,** *103* (1), 241-243.

89. Garcia, Y.; Gütlich, P., Thermal Spin Crossover in Mn(II), Mn(III), Cr(II) and Co(III) Coordination Compounds. In *Spin Crossover in Transition Metal Compounds II*, Springer Berlin Heidelberg: Berlin, Heidelberg, 2004; pp 49-62.

90. Gütlich, P., Goodwin, Harold A., *Spin crossover in transition metal compounds II*. 1 ed.; Springer-Verlag Berlin Heidelberg: Berlin Heidelberg, 2004; p XIV, 295.

91. Gütlich, P., Goodwin, Harold A., *Spin Crossover in Transition Metal Compounds I*. 1 ed.; Springer-Verlag Berlin Heidelberg: Berlin Heidelberg, 2004; p XIII, 342.

92. Tissot, A., Photoswitchable spin crossover nanoparticles. *New Journal of Chemistry* **2014,** *38* (5), 1840.

93. Takahashi, K., Spin-Crossover Complexes. *Inorganics* **2018,** *6* (1), 32.

94. Gütlich, P.; Hauser, A., Thermal and light-induced spin crossover in iron (II) complexes. *Coordination chemistry reviews* **1990,** *97*, 1-22.

95. Hauser, A., Intersystem crossing in the [Fe (ptz) 6](BF4) 2 spin crossover system (ptz= 1‐propyltetrazole). *The Journal of chemical physics* **1991,** *94* (4), 2741-2748.

96. Guionneau, P.; Marchivie, M.; Bravic, G.; Létard, J.-F.; Chasseau, D., Structural Aspects of Spin Crossover. Example of the [FeIILn(NCS)2] Complexes. In *Spin Crossover in Transition Metal Compounds II*, Springer Berlin Heidelberg: Berlin, Heidelberg, 2004; pp 97-128.

97. Hauser, A., Ligand field theoretical considerations. In *Spin Crossover in Transition Metal Compounds I*, Springer: 2004; pp 49-58.

98. Decurtins, S.; Gutlich, P.; Hasselbach, K. M.; Hauser, A.; Spiering, H., LIGHT-INDUCED EXCITED-SPIN-STATE TRAPPING IN IRON(II) SPIN-CROSSOVER SYSTEMS - OPTICAL SPECTROSCOPIC AND MAGNETIC-SUSCEPTIBILITY STUDY. *Inorganic Chemistry* **1985,** *24* (14), 2174-2178.

99. Hauser, A., REVERSIBILITY OF LIGHT-INDUCED EXCITED SPIN STATE TRAPPING IN THE FE(PTZ)6(BF4)2 AND THE ZN1-XFEX(PTZ)6(BF4)2 SPIN-CROSSOVER SYSTEMS. *Chemical Physics Letters* **1986,** *124* (6), 543-548.

100. Romstedt, H.; Hauser, A.; Spiering, H., High-spin → low-spin relaxation in the two-step spincrossover compound [Fe(pic)3]Cl2EtOH (pic = 2-picolylamine). *Journal of Physics and Chemistry of Solids* **1998,** *59* (2), 265-275.

101. Sugano, S., *Multiplets of transition-metal ions in crystals*. Elsevier: 2012.

102. Real, J. A.; Gaspar, A. B.; Munoz, M. C., Thermal, pressure and light switchable spin-crossover materials. *Dalton Transactions* **2005,** (12), 2062-2079.

103. Meded, V.; Bagrets, A.; Fink, K.; Chandrasekar, R.; Ruben, M.; Evers, F.; Bernand-Mantel, A.;

Seldenthuis, J. S.; Beukman, A.; van der Zant, H. S. J., Electrical control over the Fe(II) spin crossover in a single molecule: Theory and experiment. *Physical Review B* **2011,** *83* (24), 245415.

104. Gütlich, P.; Hauser, A.; Spiering, H., Thermal and optical switching of iron (II) complexes. *Angewandte Chemie International Edition in English* **1994,** *33* (20), 2024-2054.

105. Bousseksou, A.; Varret, F.; Goiran, M.; Boukheddaden, K.; Tuchagues, J. P., The Spin Crossover Phenomenon Under High Magnetic Field. In *Spin Crossover in Transition Metal Compounds III*, Springer Berlin Heidelberg: Berlin, Heidelberg, 2004; pp 65-84.

106. Ksenofontov, V.; Gaspar, A. B.; Gütlich, P., Pressure Effect Studies on Spin Crossover and Valence Tautomeric Systems. In *Spin Crossover in Transition Metal Compounds III*, Springer Berlin Heidelberg: Berlin, Heidelberg, 2004; pp 23-64.

107. Bernien, M.; Wiedemann, D.; Hermanns, C. F.; Krüger, A.; Rolf, D.; Kroener, W.; Müller, P.; Grohmann, A.; Kuch, W., Spin Crossover in a Vacuum-Deposited Submonolayer of a Molecular Iron(II) Complex. *The Journal of Physical Chemistry Letters* **2012,** *3* (23), 3431-3434.

108. Gopakumar, T. G.; Bernien, M.; Naggert, H.; Matino, F.; Hermanns, C. F.; Bannwarth, A.; Muhlenberend, S.; Kruger, A.; Kruger, D.; Nickel, F.; Walter, W.; Berndt, R.; Kuch, W.; Tuczek, F., Spin-Crossover Complex on Au(111): Structural and Electronic Differences Between Mono- and Multilayers. *Chemistry-a European Journal* **2013,** *19* (46), 15702-15709.

109. Bernien, M.; Naggert, H.; Arruda, L. M.; Kipgen, L.; Nickel, F.; Miguel, J.; Hermanns, C. F.; Krüger, A.; Krüger, D.; Schierle, E., Highly efficient thermal and light-induced spin-state switching of an Fe (II) complex in direct contact with a solid surface. *ACS nano* **2015,** *9* (9), 8960-8966.

110. Kipgen, L.; Bernien, M.; Nickel, F.; Naggert, H.; Britton, A. J.; Arruda, L. M.; Schierle, E.; Weschke, E.; Tuczek, F.; Kuch, W., Soft-x-ray-induced spin-state switching of an adsorbed Fe (II) spin-crossover complex. *Journal of Physics: Condensed Matter* **2017,** *29* (39), 394003.

111. Ossinger, S.; Naggert, H.; Kipgen, L.; Jasper-Toennies, T.; Rai, A.; Rudnik, J.; Nickel, F.; Arruda, L. M.; Bernien, M.; Kuch, W., Vacuum-evaporable spin-crossover complexes in direct contact with a solid surface: Bismuth versus gold. *The Journal of Physical Chemistry C* **2017,** *121* (2), 1210-1219.

112. Kipgen, L.; Bernien, M.; Ossinger, S.; Nickel, F.; Britton, A. J.; Arruda, L. M.; Naggert, H.; Luo, C.; Lotze, C.; Ryll, H., Evolution of cooperativity in the spin transition of an iron (II) complex on a graphite surface. *Nature communications* **2018,** *9* (1), 2984.

113. Warner, B.; Oberg, J. C.; Gill, T. G.; El Hallak, F.; Hirjibehedin, C. F.; Serri, M.; Heutz, S.; Arrio, M.-A.; Sainctavit, P.; Mannini, M., Temperature-and light-induced spin crossover observed by x-ray spectroscopy on isolated Fe (II) complexes on gold. *The journal of physical chemistry letters* **2013,** *4* (9), 1546-1552.

114. Beniwal, S.; Zhang, X.; Mu, S.; Naim, A.; Rosa, P.; Chastanet, G.; Letard, J. F.; Liu, J.; Sterbinsky, G. E.; Arena, D. A.; Dowben, P. A.; Enders, A., Surface-induced spin state locking of the [Fe(H2B(pz)2)2(bipy)] spin crossover complex. *J Phys Condens Matter* **2016,** *28* (20), 206002.

115. Bairagi, K.; Bellec, A.; Fourmental, C.; Iasco, O.; Lagoute, J.; Chacon, C.; Girard, Y.; Rousset, S.; Choueikani, F.; Otero, E.; Ohresser, P.; Sainctavit, P.; Boillot, M.-L.; Mallah, T.; Repain, V., Temperature-, Light-, and Soft X-ray-Induced Spin Crossover in a Single Layer of FeII-Pyrazolylborate Molecules in Direct Contact with Gold. *The Journal of Physical Chemistry C* **2018,** *122* (1), 727-731.

116. Bairagi, K.; Iasco, O.; Bellec, A.; Kartsev, A.; Li, D.; Lagoute, J.; Chacon, C.; Girard, Y.; Rousset, S.; Miserque, F.; Dappe, Y. J.; Smogunov, A.; Barreteau, C.; Boillot, M.-L.; Mallah, T.; Repain, V., Molecular-scale dynamics of light-induced spin cross-over in a two-dimensional layer. *Nature Communications* **2016,** *7* (1), 12212.

Chapter 2 - Methodologies

This chapter aims at giving a general and brief introduction of the experimental techniques and theoretical calculations, which have been carried out in a combinational study of the electronic and crystallographic properties of $Cs^{I}Ni^{II}Cr^{III}$ NPs deposited on HOPG and the monolayer or submonolayer of Fe(II)-SCO compounds deposited on Cu(111), Ag(111) and Au(111). Since the common chemical techniques (SQUID, STM, TEM, XRD, DLS……) could answers to the questions we wanted to raise, we resorted to X-ray absorption spectroscopy that is the appropriate technique for measuring ultra-thin films due to its chemical and site selectivity.[1] In combination with ligand field multiplet (LFM) calculations, we can obtain detailed structural information on the electronic structures of metal ions present in nano-objects. When playing with polarization, one can also record X-ray Natural Linear Dichroism (XNLD) and X-Ray Magnetic Linear Dichroism (XMCD) so that information of the spin and orbit magnetic moments can be given. All the LFM calculations have been carried out with the chain of codes labeled TT-Multiplet (where TT stands for Theo Thole).[2-4]

2.1 X-ray Absorption Spectroscopy (XAS) Technique

X-ray absorption spectroscopy (XAS) has been witnessed as an ancillary tool and technique in the field of biochemistry, coordination chemistry, inorganic chemistry, physics and material science to explore the oxidation states, spin states and local structure in metallic compounds.[1,5] By means of adjusting the X-ray energy to the binding energy of core electrons of a specific atom, XAS is chemically sensitive.

2.1.1 General Introduction for XAS

X-ray absorption spectroscopy is the measurement of the absorption of X-rays when they are travelling through an absorbing medium. It is performed by first shining a sample with X-rays and collecting the photons that are transmitted through the sample. In general, the photon energy of X-rays is in the range from few hundreds of eV to tens of keV, and in some special cases this energy could be up to few hundreds of keV. Depending upon the energy range, X-rays are classified into two types: hard X-rays and soft X-rays. Hard X-rays range from 1 keV to10 keV and have a strong penetration ability to sample but it could damage samples; by comparison, soft X-rays (300 eV to 3000 eV) owns a relatively lower energy and a weaker damage to samples, which plays an important role in studies of electronic structure and local structure in materials. The reason why soft X-rays are called “soft” is that these soft X-rays do not penetrate through air and they are safe to work with relatively. By comparison, in the case of soft X-rays, the photoelectric effect predominates in the

absorption process compared to other processes such as inelastic Compton and elastic Rayleigh scattering.[6] For the photo-electric effect, the Beer-Lambert law states that the infinitesimal absorption of flux dI scales linearly with the incoming flux and the probing depth dx for an infinitely thin absorbing slab. One then has

$$dI = -I.\mu.dx \qquad (2-1)$$

that solved as

$$I = I_0.e^{-\mu.x} \qquad (2-2)$$

where I_0 is the incoming photon flux before penetrating the sample, I is the photon flux after the sample absorption, x is the probing depth of sample and μ is the linear photo-absorption coefficient of the sample. One does not extract the coefficient μ directly when taking XAS measurement because of the unclarity of sample, but one can measure a signal that is roughly proportional to μ. By definition, the total electron yield (TEY) mode is one records the electric current which is necessary to compensate the flow of all primary photoelectrons, Auger and secondary electrons emerging from the sample surface during the absorption process.

2.1.1.1 Fermi Golden rule

The x-ray absorption is expressed as a cross-section that is homogeneous to a surface and corresponds to the ratio between the energy absorbed and the photon flux. Since the photon flux is homogeneous to an energy per surface unit, the cross-section is indeed a surface. The cross-section between a collection of initial states $|i\rangle$ and a collection of final states $|f\rangle$ is given by

$$\sigma(\omega) = 4\pi^2\alpha\hbar\omega \sum_{i,f} \frac{1}{d_i}\langle f|\vec{\varepsilon}.\vec{r}|i\rangle\ \delta\left(E_f - E_i - \hbar\omega\right) \qquad (2-3)$$

where $\vec{\varepsilon}$ is the polarization vector of the X-rays, $\hbar\omega$ is the energy of the x-rays, E_f and E_i are the energies of eigenvectors $|f\rangle$ and $|i\rangle$, d_i is the degeneracy of the initial state $|i\rangle$ and $\vec{r}$ is the integration variable. In writing Eq.(2-3), we have supposed that the interaction between the electromagnetic wave and the sample can be well written in the electric dipole approximation. For $L_{2,3}$ edges, as it is the case of the present piece of work, $|i\rangle$ is a *2p* spin-orbital and because of the electric dipole approximation $|f\rangle$ is a *3d* spin-orbital so that the $L_{2,3}$ edges are probing the magnetic levels of the absorbing atoms. Incidentally, *2p* to *4s* transitions are also allowed in the electric dipole approximation but they can be safely neglected as can be shown from LFM calculations. The nomenclature of the various types of X-ray absorption edges depends on the principal, n, and angular, ℓ, quantum numbers (***Figure 2-1***).

When playing with the nature of the polarization vector, one can get specific information either X-ray Natural Linear Dichroism (XNLD) with linear polarization or X-ray Magnetic Circular Dichroism (XMCD) with circular polarization.

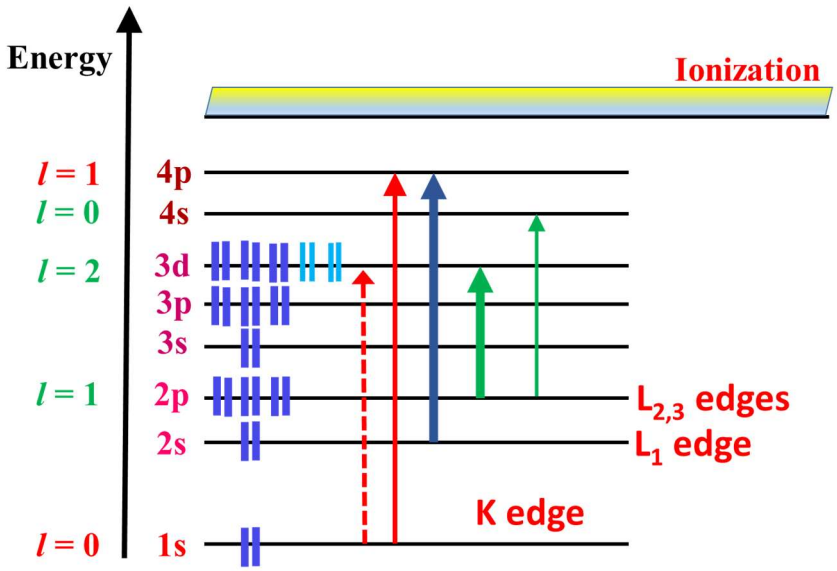

***Figure 2-1**. Nomenclature of the X-rays absorption transitions.*

2.1.1.2 DEIMOS Beamline

All XAS measurements in this thesis have been recorded on DEIMOS beamline at synchrotron SOLEIL.[7] Undulator with different functions, were implemented as the photon sources. A flux of circularly and linearly polarized X-rays is delivered by an Apple-II helical undulator with 52 mm period, ranging from 350 to 2500 eV (labeled HU52) and an Electromagnetic Mixed Permanent Helical Undulator) with 65 mm period (EMPHU65). Both undulators are used for XAS, XNLD, and XMCD measurements. EMPHU65 allows a fast switching of the X-ray polarization rate at 5 Hz. For technical implementations concerning the ring stability, the actual frequency is closer to 0.5 Hz.

2.1.1.3 Electric Polarizations

For *3d* transition metal elements, the electric dipole approximation is a good approximation[8]:

$$\boldsymbol{H}_{int} = \hat{\boldsymbol{\epsilon}} \cdot \hat{\boldsymbol{r}}. \qquad (2-4)$$

In Eq.(2-4), the term of $(\hat{\boldsymbol{\epsilon}} \cdot \hat{\boldsymbol{r}})$ is dependent on the polarization $\hat{\boldsymbol{\epsilon}} \cdot$ of incident photons. The polarization vector is always perpendicular to $\hat{\boldsymbol{k}}$, the X-ray propagation vector and it can be defined a linear combination of three different independant polarizations: linear polarization $\hat{\boldsymbol{\epsilon}}_{\parallel}$ along the quantification axis $\hat{\boldsymbol{z}}$, left $\hat{\boldsymbol{\epsilon}}_{+} = -\frac{1}{\sqrt{2}}(\vec{e}_x + i\vec{e}_y)$ and right $\hat{\boldsymbol{\epsilon}}_{-} = -\frac{1}{\sqrt{2}}(\vec{e}_x - i\vec{e}_y)$ circular polarizations in the plane perpendicular to the $\hat{\boldsymbol{z}}$ axis. $\sigma^{\parallel}$, σ^{-} and σ^{+} are the cross-sections associated to the three polarization vectors, with obvious correspondence.

The isotropic X-ray absorption in the electric dipole transition is defined as:

$$\sigma_{Iso} = \frac{1}{3}(\sigma^{\parallel} + \sigma^{-} + \sigma^{+}). \qquad (2-5)$$

The isotropic cross-section is the one that would be measured with any type of polarization for a sample that would be prepared as a fully disordered powder.

2.1.1.4 Chemical and Orbital Selectivity

By recording $L_{2,3}$ edges in the case of CsNiCr PBA, we measure *2p* to *3d* transitions. The energy range for the Cr^{III} $L_{2,3}$ edges is 567.5~597.5 eV and for Ni^{II} it is 845-875 eV so that there is no difficulty in recording well defined edges where we have no mixture between signals coming from Cr or Ni, seeing ***Figure 2-2***.

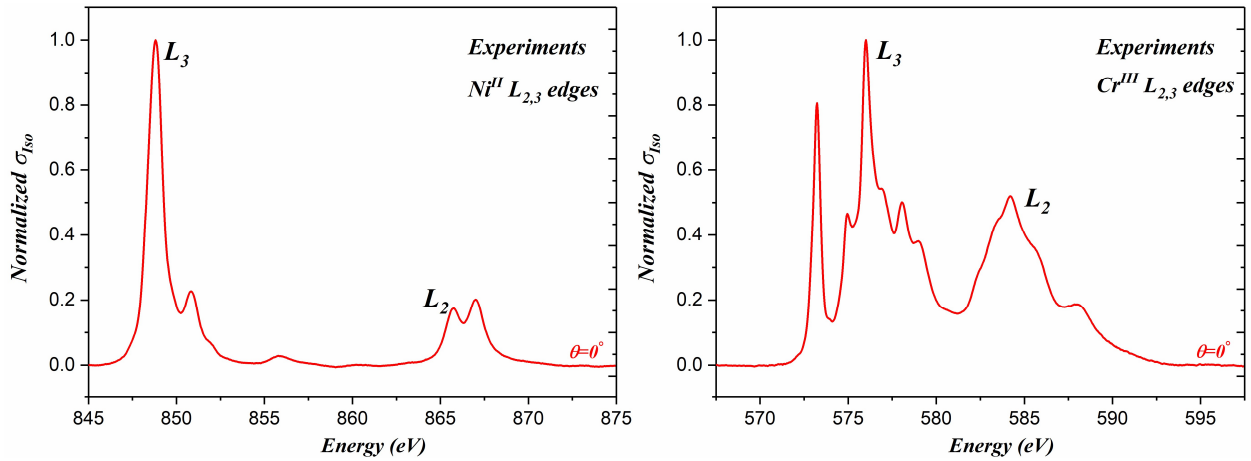

Figure 2-2. *Normalized Experimental XAS spectra of $L_{2,3}$ edges at Ni^{II} and Cr^{III} sites at θ = 0° recorded at 2 K, respectively. All experimental spectra are normalized as "1" for convenience.*

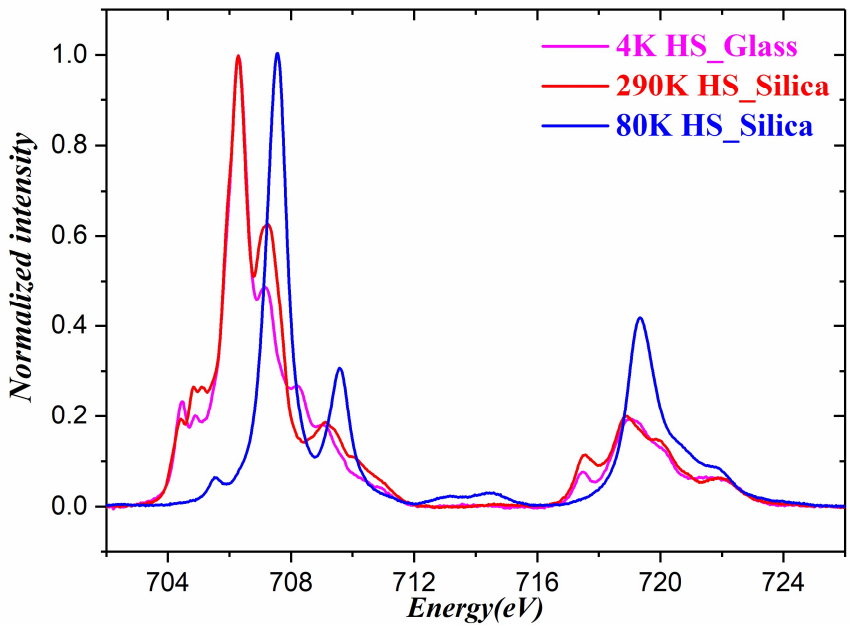

Figure 2-3. *The experimental XAS spectra of $L_{2,3}$ edges at Fe^{II} sites in $Fe^{II}[BH(3,5\text{-}Me_2)Pz_3]_2$ compounds. The magenta curve is HS at 4 K deposited on glass, the red line is the pure HS at 290 K deposited on silica, while the blue one is the curve of pure LS at 80 K deposited on silica. All experimental spectra are normalized as "1". XAS spectrum for pure HS at 4 K (290 K, respectively) is depicted in magenta color(red, respectively), while the XAS spectrum for pure LS at 80 K is shown in blue color.*

In the case of Fe^{II} SCO, the situation is not as satisfactory. Indeed, the Fe $L_{2,3}$ edges spreads between 702-725 eV, shown in ***Figure 2-3***. In SCO, one observes a change of total spin for the absorbing iron depending on temperature or laser irradiation so that the two types of ions at stake for the study of Fe

SCO is low spin Fe(II) and high spin Fe(II). Unfortunately, the average energy separation between the type of Fe is a couple of electron-Volts whereas the energy separation between L_3 and L_2 edges is a bit less than 10 eV and the intrinsic width of the L_3 edge is more than 4 eV. Then the two spin configurations cannot be separated from each other.

2.1.2 X-ray Natural Linear Dichroism

For XNLD, one generally uses a set polarized X-rays with two different linear polarization. In this thesis, I have been using both linear vertical polarized X-rays and linear horizontal polarized X-rays. If the frame is oriented in such a way that the propagation vector is along the z axis and the vertical is along x then $\vec{\varepsilon}_{\mathrm{Ver}} = (1,0,0)$ and $\vec{\varepsilon}_{\mathrm{Hor}} = (0,1,0)$. In the following of the text, I shall define the XNLD cross section as

$$\sigma_{XNLD} = \sigma_{Ver} - \sigma_{Hor} . \qquad (2-6)$$

This cross section depends on the orientation of the propagation vector with sample normal. In ***Figure 2-4***, I have reported the top view of the experimental geometry is reported where $\boldsymbol{k}$ is the X-ray propagation vector, ε_{Ver} and ε_{Hor} are the vertical and horizontal linear polarization vectors, $\boldsymbol{n}$ is the vector normal to the sample surface and $\theta = \pi - (\widehat{\boldsymbol{k},\boldsymbol{n}})$.

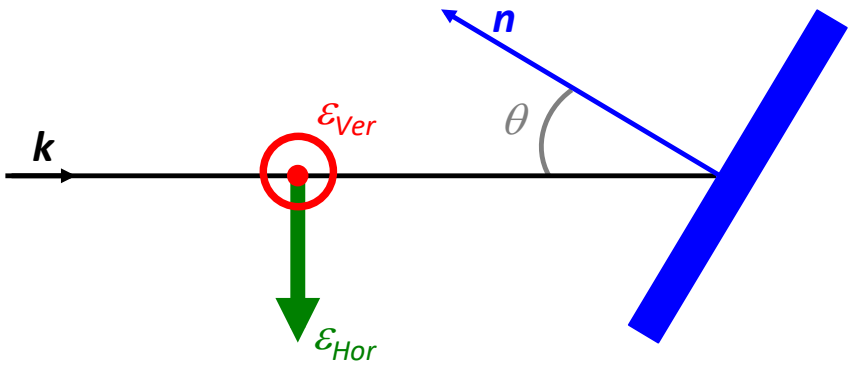

Figure 2-4. *Sketch of the experimental set-up for angular dependence of XAS.*

With the definition that $\sigma_{XNLD}(\theta) = \sigma_{Ver}(\theta) - \sigma_{Hor}(\theta)$, the angular dependence of $\sigma_{XNLD}(\theta)$ is a pure geometrical factor. If σ_{para} is the cross section measured when the polarization vector $\boldsymbol{\varepsilon}$ is parallel to the normal of the sample and σ_{perp} is the cross section measured when $\boldsymbol{\varepsilon}$ is perpendicular to the normal of the sample, then it can be shown that in the electric dipole approximation:

$$\sigma_{Ver}(\theta) = \sigma_{perp} , \qquad (2-7)$$

$$\sigma_{Hor}(\theta) = cos^2(\theta)\sigma_{perp} + sin^2(\theta)\sigma_{para} , \qquad (2-8)$$

so that

$$\sigma_{Iso} = \frac{1}{3}\cdot\frac{1}{sin^2(\theta)}\cdot[\sigma_{Hor}(\theta) + (3sin^2(\theta) - 1)\cdot\sigma_{Ver}(\theta)] = (\sigma_{para} + 2\sigma_{perp})/3 , \qquad (2-9)$$

$$\sigma_{XNLD}(\theta) = \sigma_{Ver}(\theta) - \sigma_{Hor}(\theta) = sin^2(\theta)\cdot(\sigma_{per} - \sigma_{para}), \qquad (2-10)$$

where θ is the angle between the normal of the sample surface and the X-ray propagation vector. To consider other formulas found in the literature, one should notice that in the present situation, the rotation is along the z vertical axis, so that the angle between the sample surface and the horizontal linear polarization is $(\pi/2 - \theta)$. It can be noticed that σ_{Iso} does not depend on θ but since both $\sigma_{Ver}(\theta)$ and $\sigma_{Hor}(\theta)$ do, the relation between σ_{Iso} and $\sigma_{Ver}(\theta)$, $\sigma_{Hor}(\theta)$ involves a complicated expression with θ.

2.1.3 X-ray Magnetic Circular Dichroism

For XMCD measurements, the geometry of the experimental set-up is essentially identical to the one of ***Figure 2-4***, but for the polarization of light that has either a left or right helicity as follows:

$$\vec{\varepsilon}_{\text{Left}} = \frac{1}{\sqrt{2}}\begin{pmatrix}1\\ i\\ 0\end{pmatrix} \quad \text{and} \quad \vec{\varepsilon}_{\text{Right}} = \frac{1}{\sqrt{2}}\begin{pmatrix}1\\ -i\\ 0\end{pmatrix}, \qquad (2-11)$$

and

$$\sigma_{XMCD} = \sigma_{Right} - \sigma_{Left} \qquad (2-12)$$

where the cross sections are measured with the external magnetic field parallel to the X-ray propagation vector. Because we are in the electric dipole approximation, then reversing the magnetic field is equivalent to reversing the photon helicity. This property of symmetry is fully used when measuring actual XMCD signals:

$$\sigma^{+} = \frac{1}{2}\left(\sigma_{CL}(H^{+}) + \sigma_{CR}(H^{-})\right) = \sigma_{CR}(H^{-}) = \sigma_{CL}(H^{+}) \qquad (2-13)$$

$$\sigma^{-} = \frac{1}{2}\left(\sigma_{CL}(H^{-}) + \sigma_{CR}(H^{+})\right) = \sigma_{CR}(H^{+}) = \sigma_{CL}(H^{-}). \qquad (2-14)$$

When linear dichroism is small or neglected, the isotropic cross-section is often approximated by $\sigma_{Iso} = (\sigma^{-} + \sigma^{+})/2$.

At $L_{2,3}$ edges of 3d transition elements, one generally observes large XMCD signals, close to 100 % of the isotropic cross-section.[9] XMCD is an excellent local probe to understand the electronic and magnetic structures in coordination chemistry compounds.[10-14]

When the energy of the monochromator is set at a specific energy where XMCD is present, it is possible by sweeping the intensity of the magnetic field to record chemically selective magnetization curves.

2.2 Ligand Field Multiplet Calculations

Structural and magnetic properties of transition atoms are commonly investigated by XAS so that an appropriate theoretical framework is needed. For the case of $L_{2,3}$ edges of *3d* elements, the appropriate framework is the Ligand Field Multiplet method that was first developed by Theo Thole.[15-16]

2.2.1 Ligand Field Multiplet Theory

The five *d* monoelectronic orbitals are degenerate in spherical symmetry. In a real basis of wave-functions, they can be represented following the scheme in ***Figure 2-5***. Due to various types of interactions, such as spin-orbit coupling, Coulomb repulsion, crystal or ligand field, exchange or external magnetic field, one observes various splittings of the multielectronic wave-functions.[2, 8, 15, 17-18]

The basic idea of LFM theory as developed by Thole is to calculate the cross section defined in Eq.(2-3). The two unknowns are the initial $|i\rangle$ and final $|f\rangle$ states that are both calculated by finding the eigenvectors of the following Hamiltonian:

$$\boldsymbol{H} = \boldsymbol{H}_{kin} + \boldsymbol{H}_{en} + \boldsymbol{H}_{ee} + \boldsymbol{H}_{SOC} + \boldsymbol{H}_{zeeman} + \boldsymbol{H}_{CF}\,. \qquad (2-15)$$

In Eq.(2-15), $\boldsymbol{H}$ is an atomic Hamiltonian where

$\boldsymbol{H}_{\text{kin}}$ is the kinetic energy of the electrons,

$\boldsymbol{H}_{en}$ is the electron-nucleus attraction, defined as $\boldsymbol{H}_{en} = \sum_{i=1}^{N} -\frac{Ze^2}{4\pi\varepsilon_0 r_i}$,

$\boldsymbol{H}_{ee}$ is the Coulomb electron-electron repulsion, defined as $\boldsymbol{H}_{ee} = \sum_{i<j=1}^{N} -\frac{e^2}{4\pi\varepsilon_0 r_{ij}}$,

$\boldsymbol{H}_{SOC}$ is the spin-orbit coupling term, defined as $\boldsymbol{H}_{SOC} = \sum_{i=1}^{N} \xi_i(r_i) \cdot l_i \cdot s_i$. It is a purely relativistic term where both spin and orbit angular momenta contribute,

$\boldsymbol{H}_{zeeman}$ is the Zeeman term that needs to be considered in the presence of an external magnetic field, $\boldsymbol{H}_{zeeman} = \mu_B(g_L\boldsymbol{L} + g_S\boldsymbol{S})H$.

$\boldsymbol{H}_{CF}$ is the crystal field term. It is an electrostatic potential created by the atoms neighboring atom of the Hamiltonian.

The initial state $|i\rangle$ correspond to the ground state configuration for the absorbing atom. For instance for Ni(II), the ground state configuration is $1s^2 2s^2 2p^6 3s^2 3p^6 3d^8 4s^0 4p^0$. The space spanned by the multi-electronic wave functions associated to this configuration (i.e. all the occupation number for each atomic level is fixed) are simply $\binom{10}{8} = 45$, the number of different ways to order 8 electrons in 10 monoelectronic wavefunctions. The configuration of the final state is $1s^2 2s^2 2p^5 3s^2 3p^6 3d^9 4s^0 4p^0$, so that there are $\binom{10}{9}.\binom{6}{5} = 60$ different multi-electronic wavefunctions. Electronic configuration and symmetries for 3d TM systems are shown in Appendix I. The calculation of the cross-section in Eq.(2-3) follows the various steps:

i) solve equation $\boldsymbol{H}\,|i_n\rangle = E_{i,n}|i_n\rangle$, to yield the 45 different $|i_n\rangle$,

ii) populate the 45 levels with a Boltzmann law,

iii) solve equation $\boldsymbol{H}\,|f_n\rangle = E_{f,n}|f_n\rangle$, to yield the 60 different $|f_n\rangle$,

iv) compute the 45x60 possible transitions between all the ground state and the final state configurations.

For sake of simplicity, the computation is usually limited to the first populated multi-electronic, wavefunctions of the ground state population.

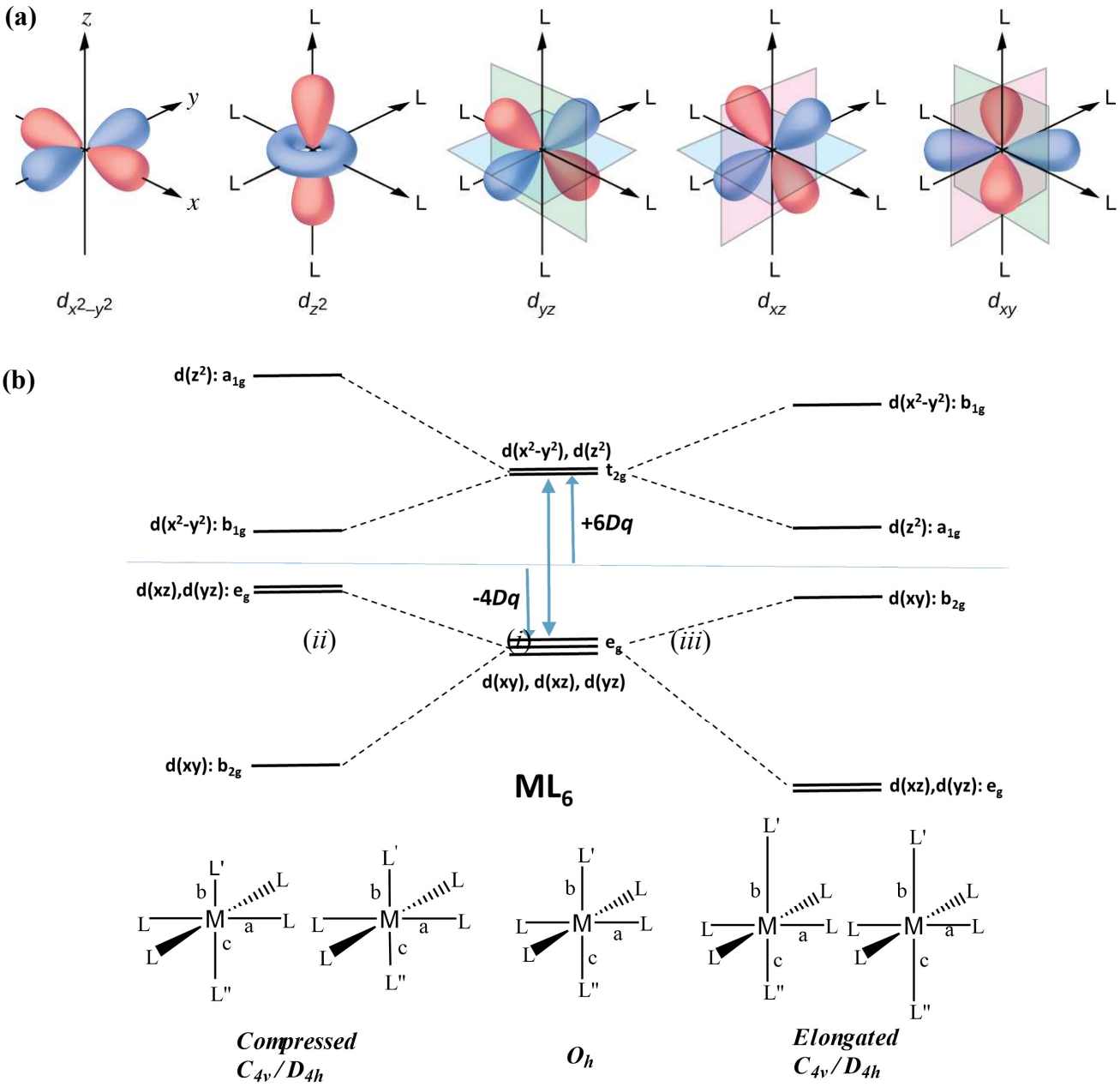

Figure 2-5. (a) Symmetry of the five 3d, real, monoelectronic orbitals. The shaded portions indicate the phase of the orbitals. The ligands (L) coordinate along the x, y, and z axes. (b) Partial energy level diagram showing the energy splitting of 3d orbitals in (i) an octahedral complex, (ii) a tetragonal complex with a strong axial interaction, and (iii) a tetragonal complex with a weak axial interaction.

2.2.2 Suit of TT-Multiplet Programs

The Ligand Field Multiplet calculations for the computation of the XAS cross-sections were first developed by B.T Thole, using a combination of atomic theory in spherical symmetry developed by

Cowan and theory of subduction for point groups developed by Bulter.[8, 18-20] The suite of programs is labeled TT-Multiplet.

RCN program was written by Cowan based on atomic theory in the Hartree Fock mode.[18] This program is used to calculate the radial integrals for a given atomic configuration in a spherical Hamiltonian including the kinetic energy of the electrons, the electron-nucleus Coulomb attraction, the electron-electron Coulomb repulsion, and the spin-orbit coupling. Then in the output files, one obtains the following information:

1. average energy of electronic configurations,
2. radial slater integrals of the multi-electronic repulsions:
   $F^k(3d, 2p)$, $F^k(3d, 3p)$ and $G^k(3d, 2p)$,
3. spin-orbit coupling constants of the open, atomic shells : ζ_{2p} and ζ_{3d}.
   For *3d* elements, 0.02 eV $\leqslant$ ζ_{2p} $\leqslant$ 0.1 eV, 2.5 eV $\leqslant$ ζ_{3d} $\leqslant$ 15 eV,
4. the radial matrix element of the transition between the initial and final states configurations, calculated in the electric dipole approximation.

TTRCG Program calculates the matrix elements for the initial states configuration in the presence of the atomic Hamiltonian defined in RCN plus all the other Hamiltonian terms of Eq.(2-15). It does the same for the final states configuration. The calculation is performed in the *jj* coupling, i.e. in the atomic, multielectronic basis defined by $|J,L,S,J_z>$. Because of the presence of the Hamiltonians for the external magnetic field and the crystal field, the basic functions $|J,L,S,J_z>$ cannot be eigenvectors of the total Hamiltonian. TTRCG also computes in the *jj* coupling, the transition elements between the initial and the final configurations.

TTRAC Program finds the eigenvectors of ***H*** as defined in Eq.(2-15) for the initial configuration and the final configuration. It finally computes all the transition matrix elements between the multi-electronic eigenvectors of the initial configuration and the multi-electronic eigenvectors of the final configuration.

PLOTTER Program calculates Eq.(2-3) by squaring the matrix elements for all the pairs of $|i_n>$ and $|f_m>$ eigenvectors, multiplying by a Dirac distribution and convolving by a Lorentzian function to account for the *2p* core-hole life-time and a Gaussian function to account for the instrumental resolution.

References

1. Van der Laan, G. In *Applications of soft x-ray magnetic dichroism*, Journal of Physics: Conference Series, IOP Publishing: 2013; p 012127.
2. De Groot, F.; Fuggle, J.; Thole, B.; Sawatzky, G., 2p x-ray absorption of 3d transition-metal compounds: An atomic multiplet description including the crystal field. *Physical Review B* **1990,** *42* (9), 5459.
3. De Groot, F., Multiplet effects in X-ray spectroscopy. *Coordination Chemistry Reviews* **2005,** *249* (1-2), 31-63.
4. De Groot, F.; Fuggle, J.; Thole, B.; Sawatzky, G., L 2, 3 x-ray-absorption edges of d 0 compounds: K+, Ca 2+, Sc 3+, and Ti 4+ in O h (octahedral) symmetry. *Physical Review B* **1990,** *41* (2), 928.
5. Wende, H., Recent advances in x-ray absorption spectroscopy. *Reports on Progress in Physics* **2004,** *67* (12), 2105-2181.
6. Beaurepaire, E.; Scheurer, F.; Krill, G.; Kappler, J.-P., *Magnetism and synchrotron radiation*. Springer: 2001; Vol. 34.
7. Ohresser, P.; Otero, E.; Choueikani, F.; Chen, K.; Stanescu, S.; Deschamps, F.; Moreno, T.; Polack, F.; Lagarde, B.; Daguerre, J. P.; Marteau, F.; Scheurer, F.; Joly, L.; Kappler, J. P.; Muller, B.; Bunau, O.; Sainctavit, P., DEIMOS: a beamline dedicated to dichroism measurements in the 350-2500 eV energy range. *Rev Sci Instrum* **2014,** *85* (1), 013106.
8. De Groot, F.; Kotani, A., *Core level spectroscopy of solids*. CRC press: 2008.
9. van der Laan, G.; Thole, B. T., Strong magnetic x-ray dichroism in 2pabsorption spectra of 3dtransition-metal ions. *Physical Review B* **1991,** *43* (16), 13401-13411.
10. Dujardin, E.; Ferlay, S.; Phan, X.; Desplanches, C.; Cartier dit Moulin, C.; Sainctavit, P.; Baudelet, F.; Dartyge, E.; Veillet, P.; Verdaguer, M., Synthesis and magnetization of new room-temperature molecule-based magnets: Effect of stoichiometry on local magnetic structure by X-ray magnetic circular dichroism. *Journal of the American Chemical Society* **1998,** *120* (44), 11347-11352.
11. Champion, G.; Escax, V.; Cartier dit Moulin, C.; Bleuzen, A.; Villain, F.; Baudelet, F.; Dartyge, E.; Verdaguer, M., Photoinduced Ferrimagnetic Systems in Prussian Blue Analogues CI x Co4 [Fe (CN) 6] y (CI= Alkali Cation). 4. Characterization of the Ferrimagnetism of the Photoinduced Metastable State in Rb1. 8Co4 [Fe (CN) 6] 3.3☉ 13H2O by K Edges X-ray Magnetic Circular Dichroism. *Journal of the American Chemical Society* **2001,** *123* (50), 12544-12546.
12. Kuepper, K.; Derks, C.; Taubitz, C.; Prinz, M.; Joly, L.; Kappler, J.-P.; Postnikov, A.; Yang, W.; Kuznetsova, T. V.; Wiedwald, U., Electronic structure and soft-X-ray-induced photoreduction studies of iron-based magnetic polyoxometalates of type {(M) M 5} 12 Fe III 30 (M= Mo VI, W VI). *Dalton Transactions* **2013,** *42* (22), 7924-7935.
13. Bunau, O.; Arrio, M.-A.; Sainctavit, P.; Paulatto, L.; Calandra, M.; Juhin, A.; Marvaud, V.; Cartier dit Moulin, C., Understanding the Photomagnetic behavior in copper octacyanomolybdates. *The Journal of Physical Chemistry A* **2012,** *116* (34), 8678-8683.
14. Cafun, J.-D.; Lejeune, J.; Itié, J.-P.; Baudelet, F. o.; Bleuzen, A., XMCD at the transition metal k-edges as a probe of small pressure-induced structural distortions in Prussian blue analogues. *The Journal of Physical Chemistry C* **2013,** *117* (38), 19645-19655.
15. Groot, F. d., Multiplet effects in X-ray spectroscopy. *Coordination Chemistry Reviews* **2005,** *249* (1-2), 31-63.
16. Ikeno, H.; de Groot, F. M.; Stavitski, E.; Tanaka, I., Multiplet calculations of L(2,3) x-ray absorption near-edge structures for 3d transition-metal compounds. *J Phys Condens Matter* **2009,** *21* (10), 104208.
17. Weissbluth, M., *Atoms and molecules*. Elsevier: 2012.
18. Cowan, R. D., *The theory of atomic structure and spectra*. Univ of California Press: 1981.
19. Butler, P. H., *Point group symmetry applications: methods and tables*. Springer Science & Business Media: 2012.
20. van der Laan, G., Hitchhiker's guide to multiplet calculations. *Magnetism: A Synchrotron Radiation Approach* **2006**, 143-199.

Chapter 3 - 6nm-sized CsNiCr PBA NCs Assembled Monolayer on HOPG

The present chapter is the subject of a submitted paper that collects all the work that I have done on 6nm sized nanocrystals (NCs) of $Cs^{I}Ni^{II}[Cr^{III}(CN)_6]\bullet nH_2O$. The chapter follows closely the ordering of the paper.

The structural, electronic and magnetic anisotropies of a monolayer of bimetallic $Cs^{I}Ni^{II}[Cr^{III}(CN)_6]\bullet nH_2O$ NCs deposited on a Highly Oriented Pyrolytic Graphite (HOPG) substrate have been investigated by angular dependent X-ray Natural Linear Dichroism (XNLD) and X-ray Magnetic Circular Dichroism (XMCD) at both Ni^{II} and Cr^{III} $L_{2,3}$ edges. The NCs belong to the family of Prussian Blue Analogues (PBA); they crystallize as cubes with 6 nm edges. Angular dependent XNLD and XMCD studies reveal the presence of an anisotropy of the electronic cloud around Ni^{II} and magnetic hysteresis loops at the Ni^{II} and Cr^{III} edges. The experimental data have been analyzed within the Ligand Field Multiplet (LFM) framework that nicely reproduce the experimental XNLD and XMCD signals and their angular dependence with the same set of parameters, giving a unified picture of the electronic and magnetic structures of the Ni^{II} and Cr^{III} ions. This combined experimental and theoretical approach allowed us to determine the presence of an elongated C_{4v} distortion of the electronic cloud around Ni^{II} ions present at the very surface of the NCs, which is consistent with an easy plane of magnetization parallel to the monolayer. The elongation of the Ni site is accompanied by a distortion of the Cr site. The nature of the Cr distortion has not been fully investigated. The whole set of the present experimental measurements allow showing how the electronic anisotropies of the individual NCs can generate the magnetic anisotropy of the NCs monolayer.

3.1 Introduction

Coordination networks based on bimetallic cyanide-bridged Prussian Blue Analogues (PBAs) have been extensively investigated because of the versatility of their magnetic and photomagnetic behavior.[1-4] In particular, they can be prepared as nanocrystals dispersible in water,[5-6] opening the route for applications in the fields of data storage, biology, catalysis and optics.[7] Bulk PBAs crystalize in a face-centered cubic (*fcc*) structure with the space group $F\bar{4}3m$.[8-9] In the absence of hexacyanometalate vacancies, the general formula is $A^{I}M^{II}[M^{III}(CN)_6]$,[10-11] where A^{I} is an alkali ion (Rb^{+}, Cs^{+}), M^{II} is a *3d* divalent metallic ion (Cr, Mn, Ni, Co, Ni, or Cu), and M^{III} is in most cases the trivalent Cr^{III} or Fe^{III} metallic ions.[2, 5, 9, 11-15]

The properties of the bulk $Cs^{I}Ni^{II}[Cr^{III}(CN)_6]\bullet nH_2O$ PBA and of the associated nanocrystals (NCs), mostly diluted in organic matrices such as polyvinyl pyrrolidone (PVP) or dimethyl dioctadecyl ammonium (DODA), have been extensively studied.[5, 11, 15-17] In all cases, the NCs have the same structure as the bulk. In its bulk form, the compound orders ferromagnetically below 90 K as a result of a ferromagnetic exchange coupling between the Cr^{III} (S = 3/2) and Ni^{II} (S = 1/2) magnetic ions through the cyanide bridge,[11] while the overall magnetic behavior of the nanocrystals depends on their size, their shape and their environment.[6, 15, 17-19] We have recently demonstrated by studying nanocrystals, on one hand, with different sizes and, on the other hand, embedded in a PVP matrix with different dilutions that the surface highly impacts their magnetic behavior and particularly their magnetic anisotropy.[15] This was attributed to water molecules that complete the coordination sphere of Ni^{II} ions belonging to the nanocrystals' surface. Indeed, X-ray Absorption Spectroscopy studies at the Ni $L_{2,3}$ edges of the nanocrystals surrounded by DODA reveal that the Ni^{II} ions belonging to the surface have a distorted geometry compatible with a *compressed* octahedral coordination sphere.[16] We speculated that as a result of the departure of the local environment of Ni^{II} ions from pure cubic to axial symmetry, the symmetry of the individual NCs would be reduced, creating thus an anisotropy of the electronic density responsible for their magnetic anisotropy.[5, 15-16] However, the experimental electronic density anisotropy of the individual objects and the related magnetic anisotropy could not be measured on objects randomly oriented in an organic matrix. We, thus, assembled the nanocrystals as single layers on a flat substrate allowing the investigation of the angular dependence of the electronic density and magnetic anisotropy by X-ray Natural Linear Dichroism (XNLD) and X-ray Magnetic Circular Dichroism (XMCD) respectively.

In the present chapter, we focus on 6 nm $Cs^{I}Ni^{II}[Cr^{III}(CN)_6]\bullet nH_2O$ cubic NCs, noted 6-CsNiCr, that have been assembled on a surface of Highly Oriented Pyrolytic Graphite (HOPG). When a monolayer of NCs is self-assembled on a HOPG surface with the [100] direction perpendicular to the substrate plane, one then expects two types of anisotropies: the ones coming from the individual NCs that will not average to zero if the NCs are properly oriented on the substrate and those coming from the interaction between NCs within the monolayer. It is then possible to probe separately intra-particle and inter-particle anisotropies and determine to which extent they contribute to the electronic and magnetic anisotropies of the whole system. At this point it should be stressed that conventional magnetometry (SQUID or VSM) is not appropriate to explore the magnetic anisotropy of a single layer of these very small NCs (6 nm size) because the amount of magnetic material is too small compared to the diamagnetic contribution of the substrate. More importantly, it is not possible to determine the anisotropy of the *electronic density* of the nanocrystals and the symmetry of the coordination sphere of the Ni^{II} and Cr^{III} ions present at their surface. One then needs to resort to chemically selective probes such as X-ray Absorption Spectroscopy (XAS), XNLD, or XMCD.[20-23] With these advanced core spectroscopies applied to an oriented monolayer of 6-CsNiCr assembled

on HOPG, we have determined the electronic and magnetic anisotropies around the 3d ions of the individual NCs and made connection with the magnetic anisotropy of the monolayer.

3.2 Experimental Section

3.2.1 Assembly on HOPG

6nm-CsNiCr NCs were prepared by spontaneous electrostatic stabilization in the absence of any stabilizing agent and fully characterized as already reported.[5] The NCs are negatively charged, have the general formula $Cs_{0.4}[Cs_{0.45}Ni(Cr(CN)_6)_{0.95}]\bullet xH_2O$ and possess a slightly elongated cubic shape with an aspect ratio around 1.2:1.[18, 24] The synthesis route is illustrated in **Figure II-I** in APPENDIX II. The structure of the assembled 6nm-CsNiCr NCs is the same as the bulk and has a cubic cell parameter of 10.5 Å; the distance between two layers of a nanocrystal is half of the unit cell value (i.e. 5.25 Å). For 6 nm objects, the surface atoms contribute to 40% of the overall number of atoms. Their surface are assumed to have water molecules that complete the coordination sphere of Ni^{II} and nitrogen atoms belonging to the $Cr(CN)_6$ species (***Figure 3-1***).

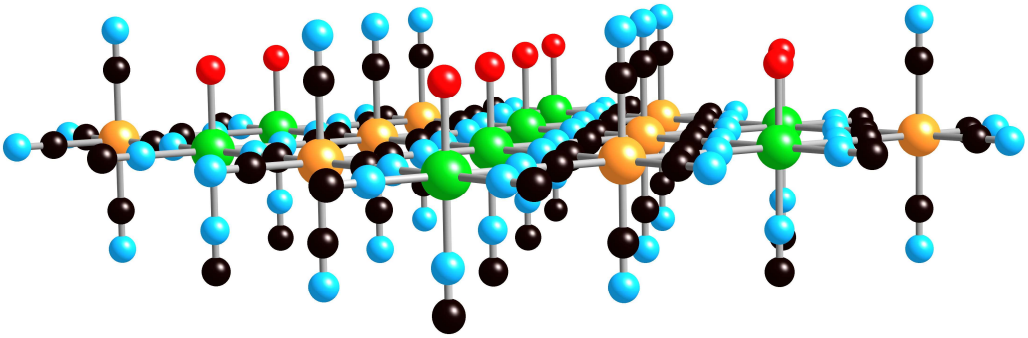

Figure 3-1. *Schematic view of a CsNiCr NC/air interface (Ni, green; Cr, yellow; oxygen, red; carbon, black; nitrogen, blue).*

The NCs are stable in aqueous solution for a long period of time, which allows their manipulation in solution and their assembly on different substrates.[25-29] HOPG is particularly adapted because, at ambient atmosphere, it has a hydrophilic surface due to the presence of a layer of water molecules on which it is possible to assemble the NCs via hydrogen bonds.[30-31] The assembly of the NCs is carried out by immerging a freshly cleaved HOPG substrate for three hours in an aqueous solution containing the NCs. The substrate is then thoroughly rinsed with water. Depending on the immersion time, nearly isolated or a compact layer of the NCs can be obtained, we used a compact layer of nanoparticles in the present study. Atomic Force Microscopy (AFM) imaging allows precisely measuring the height of the objects that was found consistent with 6 nm as expected (***Figures 3-2*** and ***3-3***). The assembly of the objects is due to the simultaneous interaction of the particles with the substrate via hydrogen bonds and among the particles mediated by the electrostatic interaction with the Cs^+ ions present in

solution. It is not possible to get insight into the orientation of the objects from AFM but, as we will see below, the XNLD results are consistent with the presence of non-randomly oriented nanocrystals on HOPG. Hydrogen bonding is assumed as the main interaction to explain why these 6nm-CsNiCr NPs can be deposited on HOPG, seeing **Figure II-3** in APPENDIX II.

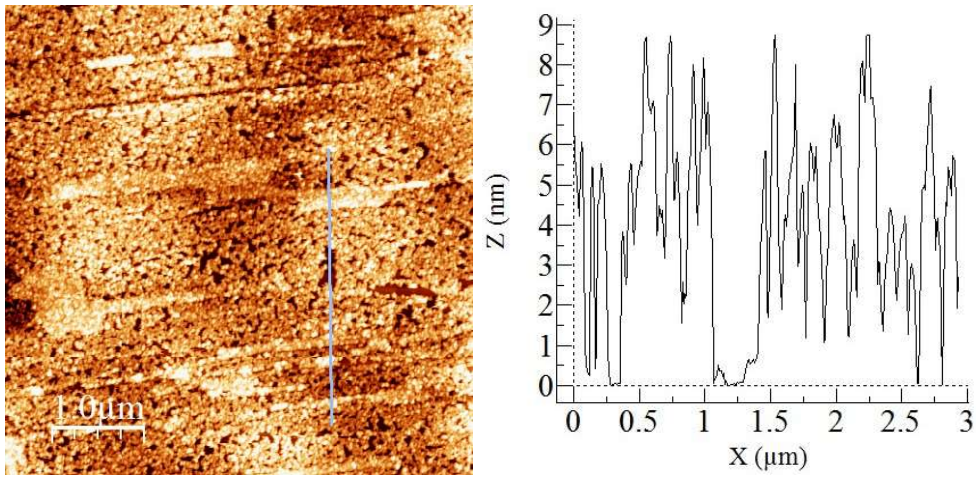

***Figure 3-2**. Atomic Force Microscopy topographic image of a single layer of 6-CsNiCr nanocrystals on HOPG; notice the presence of the underlying terraces of HOPG.*

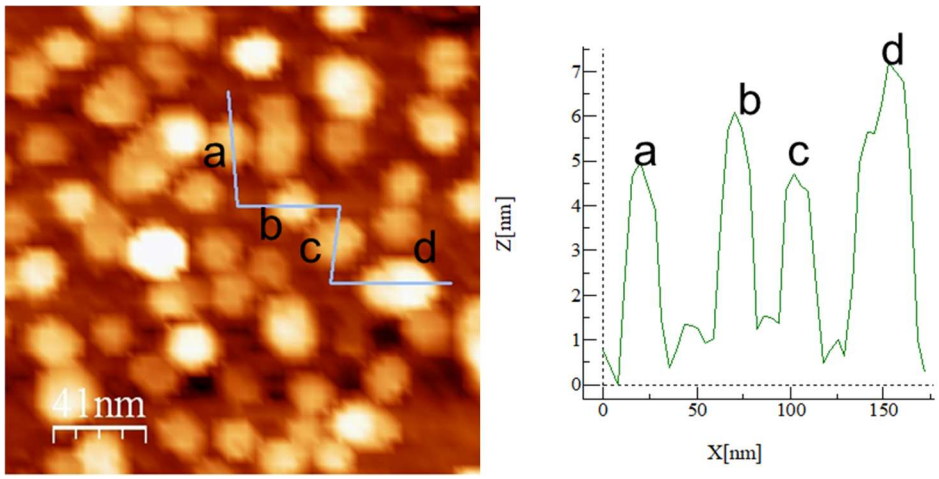

***Figure 3-3**. Atomic Force Microscopy topographic image (200 x 200 nm^2) of nearly isolated nanocrystals on HOPG.*

3.2.2 X-Ray Absorption Measurements

In order to investigate the surface anisotropy of the NCs, we have performed angular and polarization dependent XAS measurements at the $L_{2,3}$ edges of Cr^{III} and Ni^{II} ions. Metal $L_{2,3}$ edges mainly correspond to transitions from the *2p* to the *3d* orbitals, directly probing the magnetic levels of the *3d* metallic ions.[32-33] In addition, the chemical selectivity of XAS makes it only sensitive to the probed element so that when measuring specific ion $L_{2,3}$ edges from a monolayer, we have no contribution from the other magnetic neighbors, nor from the much more abundant substrate.[34-35]

XNLD is the angular and polarization dependence of XAS with linearly polarized X-rays.[36-37] It is usually performed by measuring XAS for a variety of angles between the X-ray polarization vector

and some symmetry axis of the sample. The theoretical basis for the understanding of XNLD has been fully detailed by Brouder.[36, 38] XNLD gives information on the deformation of the electronic cloud of the *3d* levels below the cubic symmetry.[37, 39-40] It is both sensitive to the ***structural orientation*** of anisotropic nano-objects and to the ***anisotropy of the electronic density*** around the absorbing atom.[37, 39] In the case of a single layer of molecules or nanocrystals, the presence of an XNLD signal is a direct proof of both the structural orientation of the objects and of the anisotropy of the electronic cloud of the layer. By measuring XAS with both vertical and horizontal linear polarized X-rays, it is possible to record the isotropic cross-section and the XNLD signals.

For instance, for a flat sample similar to a film completely isotropic in the plane of the film, σ_{Iso} and σ_{XNLD} are best obtained by setting the normal of the sample at 45° to the ***k*** vector of the X-rays and by recording cross-sections for horizontal and vertical linear polarized light. In this geometry (***Figure 2-4***, seeing **Chapter 2.1**), following Brouder's seminal paper[36]:

$$\sigma_{Iso} = [2 \cdot \sigma_{Hor}(45°) + \sigma_{Ver}(45°)]/3 \text{ and } \sigma_{XNLD}(45°) = [\sigma_{Ver}(45°) - \sigma_{Hor}(45°)] \qquad (3-1)$$

where σ_{Iso}, σ_{Ver}, and σ_{Hor} are the isotropic cross-section, the cross-section with vertical linear polarization, and the cross-section with horizontal linear polarization, respectively. The expressions of σ_{Iso} as a function of $\sigma_{Ver}(\theta)$ and $\sigma_{Hor}(\theta)$ and the angular dependence of $\sigma_{XNLD}(\theta)$ are given in the following for an arbitrary value of θ.

With the definition that $\sigma_{XNLD}(\theta) = \sigma_{Ver}(\theta) - \sigma_{Hor}(\theta)$, the angular dependence of $\sigma_{XNLD}(\theta)$ is a pure geometrical factor. If σ_{para} is the cross section measured when the polarization vector $\boldsymbol{\varepsilon}$ is parallel to the normal of the sample and σ_{perp} is the cross section measured when $\boldsymbol{\varepsilon}$ is perpendicular to the normal of the sample, then it can be shown that in the electric dipole approximation:

$$\sigma_{Ver}(\theta) = \sigma_{perp}\,, \qquad (3-2)$$

$$\sigma_{Hor}(\theta) = cos^2(\theta)\sigma_{perp} + sin^2(\theta)\sigma_{para}\,, \qquad (3-3)$$

so that

$$\sigma_{Iso} = \frac{1}{3} \cdot \frac{1}{sin^2(\theta)} \cdot [\sigma_{Hor}(\theta) + (3sin^2(\theta) - 1) \cdot \sigma_{Ver}(\theta)] = (\sigma_{para} + 2\sigma_{perp})/3 \qquad (3-4)$$

$$\sigma_{XNLD}(\theta) = \sigma_{Ver}(\theta) - \sigma_{Hor}(\theta) = sin^2(\theta) \cdot (\sigma_{perp} - \sigma_{para}) \qquad (3-5)$$

where the angle θ is the angle between the normal of the sample surface and the X-ray propagation vector (***Figure 2-4***). To make contact with other formulas found in the literature, one should notice that in the present situation, the rotation is along the *z* vertical axis, so that the angle between the sample surface and the horizontal linear polarization is $(\pi/2 - \theta)$. It can be noticed that σ_{Iso} does not depend on θ but since both $\sigma_{Ver}(\theta)$ and $\sigma_{Hor}(\theta)$ do, the relation between σ_{Iso} and $\sigma_{Ver}(\theta)$, $\sigma_{Hor}(\theta)$ involves a complicated expression with θ.

When using circularly instead of linearly polarized X-rays, it is possible to record XMCD signals and their angular dependence. XMCD is performed by recording XAS with left and right circularly polarized X-rays for which the propagation vector is parallel to the external magnetic field.[20, 22-23, 41] For XMCD measurements, the geometry of the experimental set-up is essentially identical to the one of ***Figure 2-4*** but for the polarization of light that has either a left or right helicity. XMCD at $L_{2,3}$ edges of 3d elements is also conveniently interpreted in the framework of the electric dipole approximation.[41-42] The interpretation of XMCD relies mostly on the application of the magneto-optical sum rules that were first derived by Thole.[41, 43] The angular dependence of XMCD is recorded by varying the angle between the X-ray propagation vector and some symmetry axis of the sample. For all measurements, the external magnetic field remains parallel to the X-ray propagation vector. By selecting a specific feature of the XMCD signal and varying the intensity of the external magnetic field, one can record element selective magnetization curves. Doing so and monitoring the angular dependence of XMCD, it is possible to record angular-dependent XMCD-detected magnetization curves that are expected to give direct information on the magnetic anisotropy of the system.[34, 43-44]

Spectra have been recorded on the DEIMOS beamline at SOLEIL synchrotron[45-46] using the CroMag experimental set-up in UHV conditions and detecting the signals in the Total Electron Yield (TEY) mode. For sake of comparison between spectra, one first calculates the isotropic spectrum by an appropriate linear combination of spectra recorded with left, right, and linear polarizations. Then one removes the $2p_{3/2}$ and $2p_{1/2}$ to continuum transitions by subtracting arctangent functions with inflection points at the energies of the maximum of the L_3 and L_2 edges respectively.[47-48] In a last step, the maximum of the isotropic spectra is normalized to "*1*" at the maximum of the L_3 edge.[48]

3.3 Ligand Field Multiplet Calculations

At $L_{2,3}$ edges of 3d elements, XAS, XNLD and XMCD can be efficiently interpreted in the Ligand Filed Multiplet (LFM) approach that has first been developed by Thole *et al*.[33, 49-51] By fitting the spectral features with electronic parameters, such as crystal field splitting, spin-orbit coupling, or magnetic exchange interaction, one can determine valuable electronic and magnetic information such as the electric quadrupole moment of the 3d electronic distribution, or the spin and orbit magnetic moments.[34, 42-43, 52-55]

We have applied LFM calculations to compute the XAS, XNLD and XMCD signals at Ni^{II} and Cr^{III} $L_{2,3}$ edges. The method is best described in many previous papers and textbooks.[32,38-40,49,56-58] Practical implementations have been carried out by Thole,[49] on the basis of an atomic theory developed by Cowan[50] and a ligand field interaction (i.e. symmetry) described by Butler.[51] Ni^{II} ions are bonded to the nitrogen side of the cyanide bridge and water molecules for ions belonging to the surface, so that

one expects a moderate Ni-ligand hybridization; the Ni^{II} ground state is correctly described by the $|2p^6 3d^8>$ configuration.[37, 39-40] In the electric dipole approximation where the *2p* to *4s* transitions are known to be negligible, the final state is described by the unique configuration $|2p^5 3d^9>$.[40] The Cr^{III} ions are connected to the carbon part of the cyanide bridge that induces a large crystal field and large hybridization due to a noticeable back-bonding character.[34, 39, 42, 49, 56, 59] For Cr^{III}, the ground state is best simulated by a linear combination of two configurations $|2p^6 3d^3>$ and $|2p^6 3d^2 L^1>$ where L^1 describes an extra electron sitting on the ligands; the excited state is then a linear configuration of $|2p^5 3d^4>$ and $|2p^5 3d^3 L^1>$.[38,56,59] The covalent σ bond responsible for the Ligand-to-Metal Charge Transfer (LMCT) is simply treated by reducing the nephelauxetic κ parameter to 60% (Slater integrals reduction). The LMCT character of the σ bond could also have been treated by adding an extra configuration with a hole on the ligand but this would have been at the expense of using more empirical parameters. The set of parameters necessary for the calculations at both Ni^{II} and Cr^{III} edges can be found in ***Table 3-1***.

Table 3-1. *Ligand Field Multiplet parameters used for the XAS, XNLD, and XMCD calculations at the Ni^{II} and Cr^{III} $L_{2,3}$ edges.*

Ion	Symmetry	κ(%)	*10Dq*	*Ds*	*Dt*	Δ_i	Δ_f	V_{e_g}	$V_{t_{2g}}$
Ni^{II}	O_h	77	1.38	-	-	-	-	-	-
Ni^{II}	C_{4v}	77	0.70	–0.010	+0.007	-	-	-	-
Cr^{III}	O_h	60	3.50	-	-	6.0	4.6	1.0	0.7

Note: All parameters are given in eV (except for κ in %). For all calculations, the external magnetic field acting on the orbit and spin angular momenta is 2 T ($\mu_B.\boldsymbol{B}_{external}$ = 0.12 meV for orbit and $g_0.\mu_B.\boldsymbol{B}_{external}$ = 0.24 meV for spin to account for the free electron Landé factor), and an additional exchange energy acting on spin only is $g_0.\mu_B.\boldsymbol{B}_{exchange}$ = 20 meV.

3.4 Results and Analysis

3.4.1 Structural and Electronic Anisotropy

3.4.1.1 XAS and XNLD at Ni $L_{2,3}$ edges

The XNLD signals at Ni^{II} $L_{2,3}$ edges have been recorded at 2 K with no external magnetic field. The angle θ between the normal of the sample and the ***k*** propagation vector is varied between 0° and 60° (***Figure 2-4***). As stated previously, the shape of all XNLD signals should be identical when θ varies, whereas the intensity of the XNLD signals should vary with θ following a $sin^2(\theta)$ dependence.[36] Although the XNLD signal at the Ni^{II} $L_{2,3}$ edges is rather small (10 to 15 % of the maximum of the isotropic cross-section), one observes that the larger the θ angle, the larger the XNLD signal

(***Figure 3-4***). This indicates that XNLD directly originates from the Ni environment and is a direct proof that the symmetry of the probed Ni^{II} sites is on average lower than cubic (***Figure 3-5***).

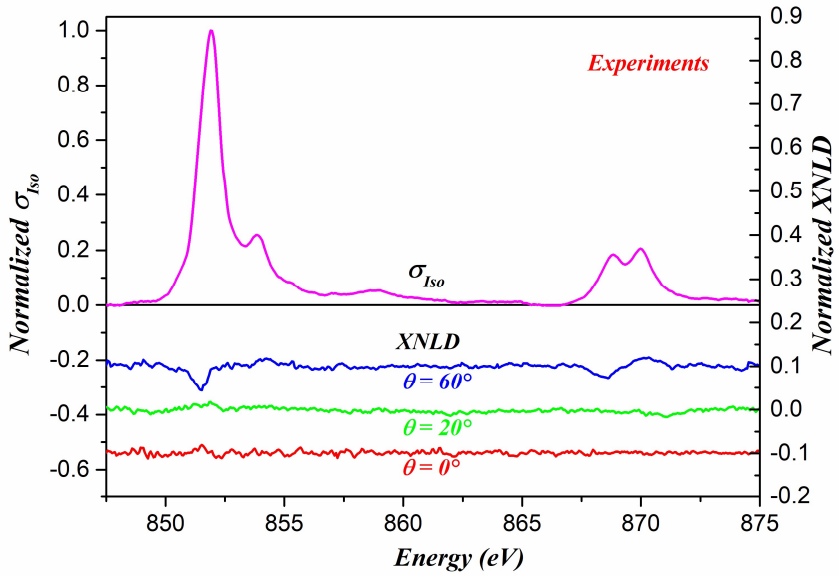

Figure 3-4. *Experimental spectra among XAS and XNLD recorded at the $L_{2,3}$ edges of Ni^{II} sites. All spectra are normalized so that the maximum of the L_3 edges is "1". Magenta solid line is the normalized isotropic spectrum, XNLD signals are reported for 0° (red), 20° (green) and 60° (blue) solid lines.*

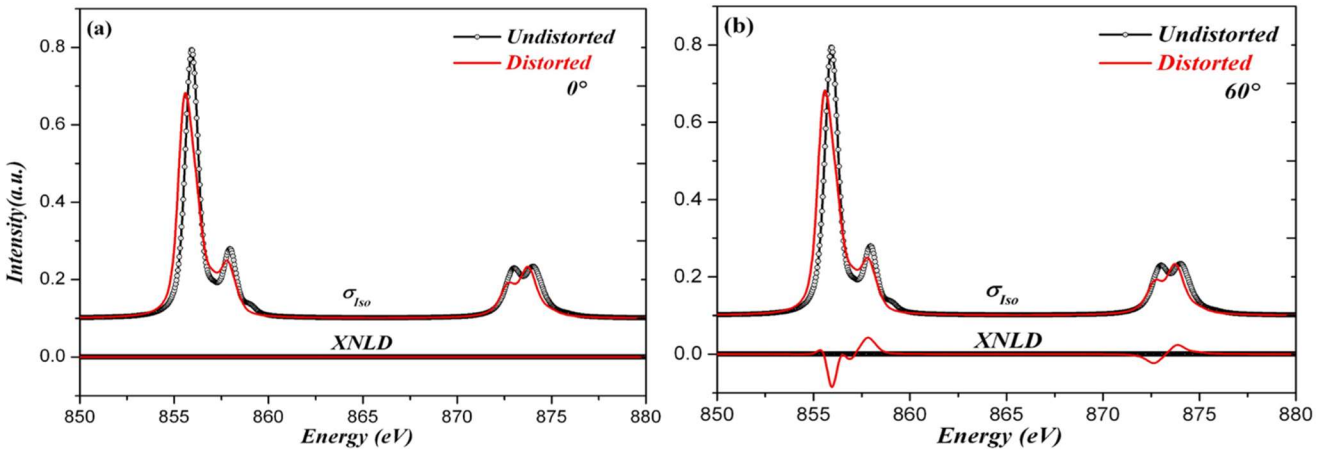

Figure 3-5. *Simulated X-ray absorption spectra at the $L_{2,3}$ edges of Ni^{II} obtained from different symmetries carried out by LFM calculations, including pure O_h (Undistorted) and C_{4v} (Distorted).* ***Figure 3-5(a)*** *is for the calculated XAS spectra at θ = 0°, while* ***Figure 3-5(b)*** *is for calculated spectra at θ = 60°. All CF parameters are listed in* ***Table 3-1***.

It is worth stressing that if the NCs were randomly orientated on the substrate there would not be any measurable XNLD signal. Then the existence of XNLD is the proof that i) some of the Ni^{II} ions are not sitting in a perfect octahedral environment and ii) these ions are not randomly distributed within the layer leading to the conclusion that the NCs forming the layer are not randomly distributed. Because the coordination sphere of the surface Ni^{II} ions is completed by water molecules, one can then assume that their local symmetry is axial and closer to C_{4v} than O_h. This axial distortion is known to be responsible for a zero-field splitting (ZFS) of the S = 1 Ni^{II} spin into two sub-levels M_S = ±1 and 0 and will thus be responsible for the local magnetic anisotropy.[60-62] However, the nature of the

axial magnetic anisotropy, easy axis or easy plane, depends on whether the $M_S = \pm 1$ sub-levels are ground or excited levels. This can be determined by complementary investigation of the angular dependence of XNLD and XMCD coupled to LFM calculations.

Angular dependence of the electronic density around Ni^{II} ions.

In order to perform the calculations of the XAS signals, it is necessary to estimate the contribution of the distorted species to the signal. All XAS measurements have been recorded in TEY mode for which the probing depth can be estimated to be 6 nm (i.e. 95% of TEY signal would come from the first 6 nm). One generally considers that the emission of the photoelectron and secondary electrons follows an exponential decay law such that the emitted photons from the slice dx at the distance $x = x_0$ below the sample surface are given by $e^{-\frac{x_0}{\lambda}dx}$ where λ is the escape depth of the electrons. If 95% of the TEY signal comes from the first 6 nm, then $\lambda = 2$ nm. One first needs to divide the NC into various slabs and calculate the contribution from each slab to the TEY. The NC is built from the top and bottom slabs, the four lateral slabs and the inner part of the NC. The details for the calculation of the various slab contributions to the TEY is a bit tedious and is given in the following.

We first divide the NCs into 4 different parts:

-the top part (labeled Top) that covers the whole surface of the NC and is 0.5 nm deep,

-the bottom part (labeled Bottom) that covers the whole surface of the NC and is 0.5 nm deep,

-the inner part (labeled Inner) that is a cube with 5 nm edges,

-the lateral slabs (labeled Lateral) that is the whole volume left by the 3 other parts.

The TEY contribution for the whole NC with e nm edges, is given $e^2 \cdot [1 - \exp(-e/\lambda)]/\lambda$. The contribution of a specific slab with surface S and with a depth varying between x_0 and x_1 is given by $S \cdot [\exp\left(\frac{-x_0}{\lambda}\right) - \exp\left(\frac{-x_1}{\lambda}\right)]/\lambda$. From these expressions and from λ=2 nm, one can deduce that the Top part contributes to 23%, the Bottom part to 1.5%, the Inner part to 52% and the Lateral part to 23%. One assumes that the site symmetry of Ni ions is C_{4v} in the Top, Bottom, and Lateral parts and O_h in the Inner part so that

$$\sigma_{Iso} = 0.52 \cdot \sigma_{Iso}\,(O_h) + 0.48 \cdot \sigma_{Iso}\,(C_{4v})\,. \qquad (3-6)$$

In Eq.(3-1), σ_{Iso} is the isotropic spectrum for a NPs (i.e. the XAS spectrum that would be measured for a completely non oriented powder of such NPs), $\sigma_{Iso}\,(O_h)$ and $\sigma_{Iso}\,(C_{4v})$ are the isotropic cross-sections for a pure O_h site, or a C_{4v} site, respectively.

For the XNLD calculation, one proceeds in the same way except for the fact that the Lateral sides give a XNLD contribution that is divided by two and with a different sign compared to the one of the Top and Bottom parts (this result directly stems from geometry). Hence,

$\sigma_{XNLD} = 0.52\ \sigma_{XNLD}(O_h) + 0.23\ \sigma_{XNLD}(C_{4v}) + 0.015\ \sigma_{XNLD}(C_{4v}) - (0.23/2)\ \sigma_{XNLD}(C_{4v})$ $(3-7)$

where

$\sigma_{XNLD}(C_{4v}) = \sigma_{Ver}(C_{4v}) - \sigma_{Hor}(C_{4v})$ for the Top layer. Since $\sigma_{XNLD}(O_h) = 0$

then

$$\sigma_{XNLD} = 0.13 \cdot \sigma_{XNLD}\ (C_{4v})\ . \qquad (3-8)$$

σ_{XNLD} is the Linear Dichroic signal as measured for the NPs monolayer, $\sigma_{XNLD}\ (C_{4v})$is the linear dichroic signal for a C_{4v} site. It can be noticed that if one assumes that 95% of the signal come from either 5 nm or from 7 nm instead of 6 nm, the contribution from the C_{4v} sites would change by less than ± 2% for σ_{Iso} and by less than ± 3% for σ_{XNLD}.

We then performed LFM calculations for two types of symmetries, O_h and C_{4v}, following common procedures detailed elsewhere.[39, 49, 57] In the framework of the crystal field theory, a C_{4v} symmetry can be modelled by three independent parameters (10*Dq*, *Ds* and *Dt*).[32] The various types of axially distorted octahedral geometries can be determined by the energy levels of the monoelectronic *3d* orbitals.[32] For C_{4v} symmetry, ligand field theory states that the metal ion site is compressed when the energy of the two degenerate orbitals $3d_{xz}$ and $3d_{yz}$ is lower than that of the $3d_{xy}$ orbital; while the metal ion site is elongated in the reverse situation.[32] We, therefore, performed LFM calculations for a set of *Ds* and *Dt* values and plotted the energy of the monoelectronic *3d* orbitals corresponding to the elongated and compressed C_{4v} distortions (***Figure 3-6*** and ***Table 3-2***). The relationship between CF parameters (10*Dq*, *Ds* and *Dt*), O_h and D_{4h} are listed in **Table I-9** of APPENDIX due to which we could estimate the energy of monoelectronic *3d* orbital.

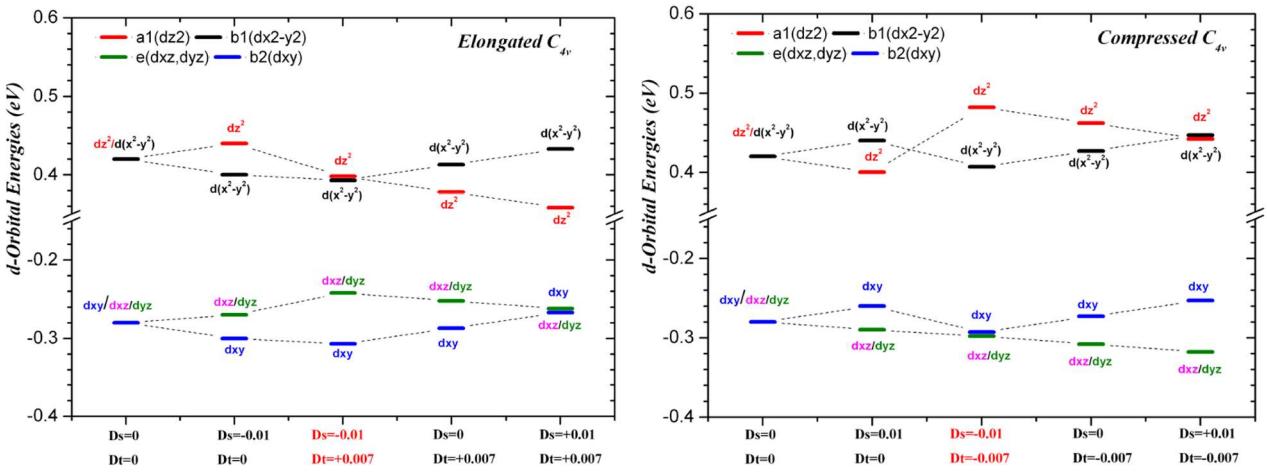

Figure 3-6. *Energy diagrams of 3d monoelectronic orbitals for Ni^{II} sites as a function of crystal field parameters Ds and Dt in elongated (top) and compressed (bottom) C_{4v} symmetry; 10Dq = 0.70 eV.*

It is important to stress that when the energy of the monoelectronic d_{xy} orbital is lower than that of the two degenerate orbitals (d_{xz}, d_{yz}), this defines an elongated distortion, while the reverse situation is obtained for a compressed distortion. This is important because the relative energy of the two lower-lying states of symmetry $B_2(C_{4v})$ and $E(C_{4v})$ obtained after considering the multiplet configurations

together with the spin-orbit coupling is directly correlated to the nature (elongated/compressed) of the distortion as shown in ***Table 3-2***. For elongated C_{4v}, the ground state is non-degenerate with symmetry B_2; while for compressed C_{4v}, the ground state is the two-fold degenerate E state.

Table 3-2. *Energy of states obtained from LFM calculations for different values of Ds and Dt with 10Dq=0.70 eV for Ni^{II} with octahedral geometries.*

Ds	**0**	**-0.01**	**-0.01**	**0**	**0.01**	**0.01**	**-0.01**	**0**	**0.01**
Dt	**0**	**0**	**0.007**	**0.007**	**0.007**	**0**	**-0.007**	**-0.007**	**-0.007**
E1 (eV)	-2.03365	-2.03368	-1.98629	-1.98626	-1.98624	-2.03367	-2.08189	-2.08189	-2.08190
E2 (eV)	-2.03365	-2.03364	-1.98553	-1.98555	-1.98557	-2.03367	-2.08189	-2.08189	-2.08190
E3 (eV)	-2.03365	-2.03364	-1.98553	-1.98555	-1.98557	-2.03363	-2.08131	-2.08128	-2.08126
E4 (eV)	-1.36977	-1.37210	-1.38224	-1.38457	-1.38744	-1.37224	-1.40594	-1.40443	-1.40309
E5 (eV)	-1.36977	-1.36787	-1.35973	-1.36311	-1.36696	-1.36771	-1.37993	-1.37878	-1.37777
E6 (eV)	-1.34791	-1.34967	-1.35223	-1.34930	-1.34675	-1.35135	-1.37993	-1.37878	-1.37777
E7 (eV)	-1.34791	-1.34967	-1.34320	-1.34201	-1.34138	-1.34647	-1.35402	-1.35546	-1.35749
E8 (eV)	-1.34791	-1.34498	-1.34320	-1.34201	-1.34138	-1.34647	-1.33064	-1.33310	-1.33610
E9 (eV)	-1.28938	-1.29247	-1.30043	-1.29788	-1.29591	-1.29091	-1.29441	-1.29454	-1.29515
E10 (eV)	-1.28938	-1.28813	-1.25882	-1.25998	-1.26117	-1.29091	-1.29441	-1.29454	-1.29515
E11 (eV)	-1.28938	-1.28813	-1.25882	-1.25998	-1.26117	-1.28690	-1.28475	-1.28112	-1.27811
E12 (eV)	-1.27110	-1.27127	-1.25401	-1.25502	-1.25623	-1.27128	-1.27545	-1.27388	-1.27278
(E)-E(B_2) (meV)	0	0.04210	0.75994	0.71343	0.67171	-0.03800	-0.57350	-0.61187	-0.64670
(E)-E(B_2) (cm^{-1})	0	0.33955	6.12893	5.75379	5.41732	0.30644	4.62528	4.93472	5.21560

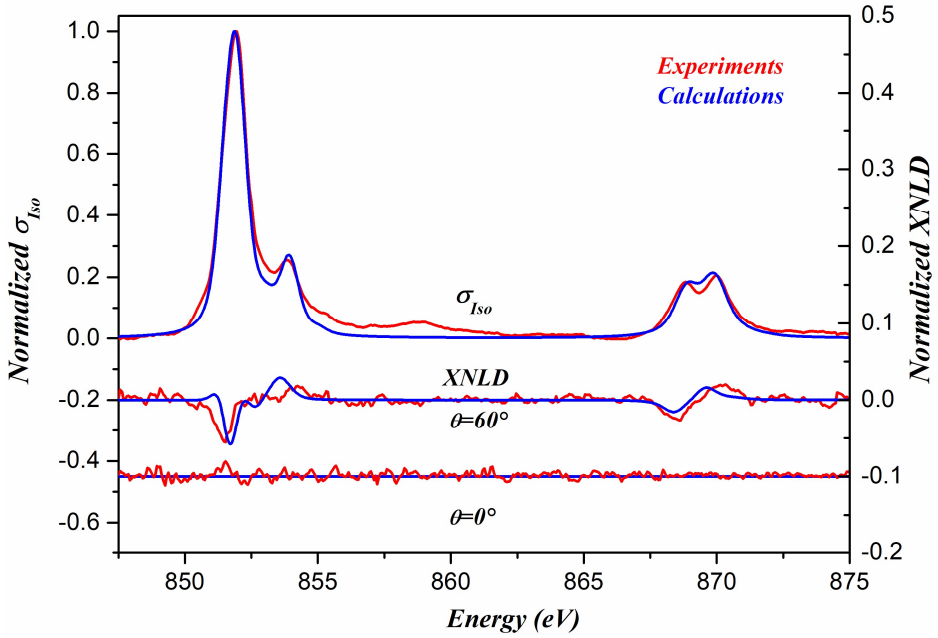

Figure 3-7. *Isotropic cross section and XNLD signals for $\theta = 0°$ and $\theta = 60°$ at the Ni^{II} $L_{2,3}$ edges at $T = 2$ K and $B = 2$ T.*

A direct correlation is found between the nature (elongated/compressed) of the C_{4v} distortion, the relative energies of the monoelectronic *3d* orbitals and the relative energy of the low-lying states, as

expected.[63] It is then possible for an arbitrary case to deduce the nature of the distortion from the relative energy of the two low-lying states. The LFM calculations were then carried out considering Eq.(3-1). The best parameters that reproduce the experimental spectrum at 60° correspond to elongated C_{4v} symmetry (***Figures 3-7*** and ***3-8***). In these LFM calculations, the crystal field parameter for pure O_h sites is $10Dq$ = 1.38 eV whereas for the elongated C_{4v} symmetry we found $10Dq$ = 0.70 eV, Ds = –0.010 eV, and Dt = +0.007 eV.

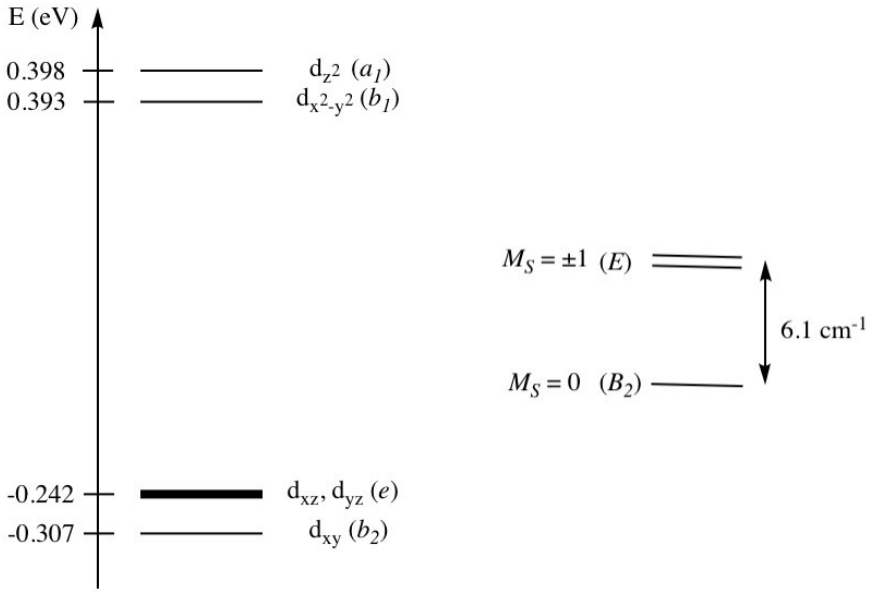

Figure 3-8*. Energy of the mono-electronic 3d orbitals and the two states of symmetries B_2 and E obtained from LFM calculations that reproduce best the XNLD experimental data with 10Dq = 0.7 eV, Ds = –0.010 eV and Dt = +0.007 eV.*

For cubic NCs sitting on the substrate, the Ni^{II} sites present on the NCs faces *perpendicular* to the substrate have their *electronic* anisotropy axis parallel to the surface, thus making an angle of 90° with the X-ray propagation vector ***k***; a XNLD signal should, thus, be observed for θ = 0° (seeing ***Figure 2-4***). The absence of such signal is due to the averaging of the anisotropy coming from the four perpendicular faces of the NCs. The same reasoning can be made for θ = 60°, so that the signal observed at this angle is mainly due to the nanocrystals' faces parallel to the substrate.

3.4.1.2 XAS and XNLD at Cr $L_{2,3}$ edges

Cr^{III} ions are bound to the carbon side of six cyanide ligands with relatively large π back bonding character and an almost regular octahedral geometry. Although we were not expecting any distortion of the coordination sphere of Cr^{III} ions, we did record a rather large XNLD signal at Cr $L_{2,3}$ edges as can be shown of ***Figure 3-9***.

The isotropic XAS signals are quite similar to the ones simulated using O_h symmetry including the strong π back bonding as described in the LFM calculations section.[38] We did not try to calculate the XNLD signal at Cr $L_{2,3}$ edges. Indeed, because of presence of the π back bonding, it is mandatory to

use Configuration Interaction in order to simulate the isotropic spectra. Then a rather large number of empirical parameters are entering the description of the ground state. Introducing new distortion parameters acting on the various configurations present in the ground state in order to simulate XNLD would have probably reach the limit of LFM method. Nevertheless, it can be said that the presence of a XNLD signal signs the fact that the Cr site is distorted. In the following we guess that it might be an elongated distortion similar to the one that was found for Ni sites.

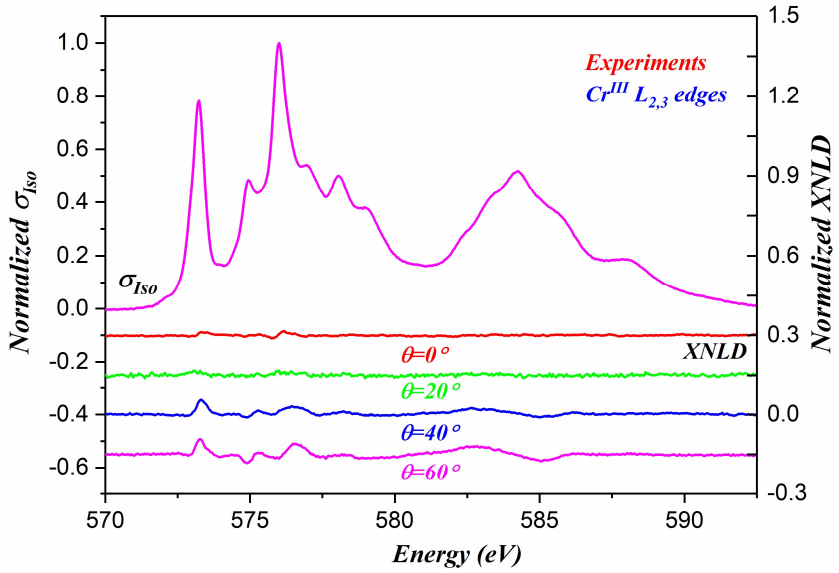

***Figure 3-9**. Experimental XAS and XNLD signals recorded at 2 K, at the $L_{2,3}$ edges of Cr^{III} for θ varying from 0° to 60°. All experimental XAS spectra have been normalized to "1".*

3.4.2 Magnetic Anisotropy

We have recorded both XMCD signals and XMCD-detected magnetization curves at both Ni^{II} and Cr^{III} $L_{2,3}$ edges and their angular dependence.

3.4.2.1 XMCD measurements at 2T

The XMCD spectra at the Ni^{II} and Cr^{III} $L_{2,3}$ edges have been recorded at 2 K and with an external magnetic field ***B*** of 2 T. The XMCD signals have been measured as a function of the angle θ between the ***k*** X-ray propagation vector and the substrate normal ***n*** (***Figure 2-4***). The spectra for $\theta = 0°$ and 60° for the Ni^{II} and Cr^{III} $L_{2,3}$ edges are reported in ***Figure 3-10***.

The isotropic signals have been properly normalized for each angle so that the comparison of the intensity of the XMCD signals is meaningful. One first notices the absence of angular dependence of the XMCD signals for both Cr^{III} and Ni^{II}. It is expected for Cr^{III} since the environment is highly symmetric. On the contrary the absence of angular dependence for XMCD at Ni^{II} $L_{2,3}$ edges indicates that despite the anisotropic electronic structure of Ni^{II} present at the very surface of the NCs, the distortion has no visible incidence on the magnetic anisotropy at low temperature (2 K) in a highly saturating external magnetic field (2 T). The XMCD signals are large, since the maximum of XMCD

amounts to 105 % of the Ni^{II} isotropic cross-section and to 76 % of the Cr^{III} isotropic one, indicating that both ions are close to be fully saturated in the present experimental conditions. Therefore, one must investigate the magnetic anisotropy at magnetic fields lower than 2 T (see below).

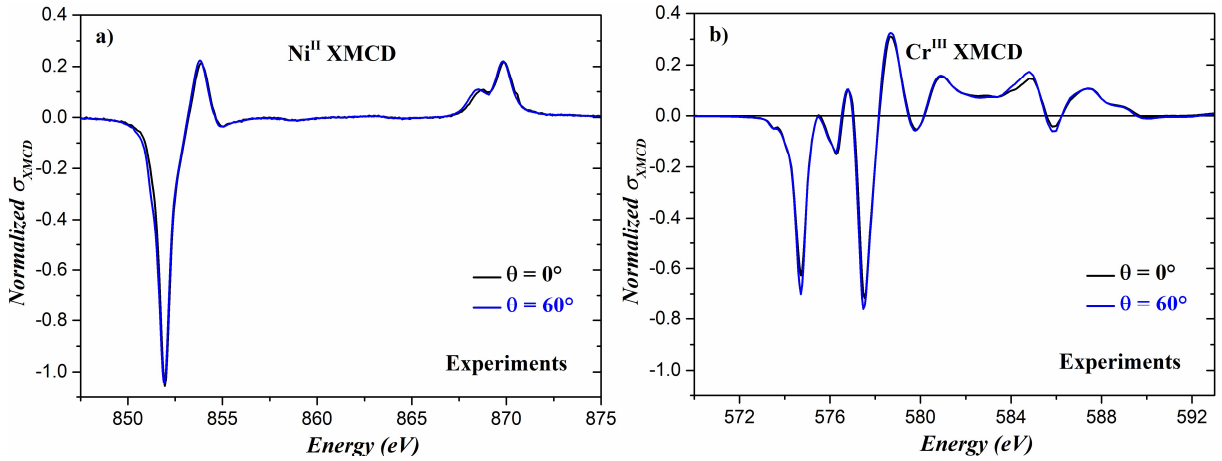

Figure 3-10. *Angular dependence of XMCD for $\theta = 0°$ and $\theta = 60°$: (a) at the Ni $L_{2,3}$ edges, (b) at the Cr $L_{2,3}$ edges. For both ions, the intensity of the isotropic spectra at the L_3 edge has been normalized to 1, T = 2 K and B = 2 T*

The isotropic and XMCD experimental and LFM calculated spectra ($\theta = 60°$) for Ni^{II} and Cr^{III} $L_{2,3}$ edges (***Figure 3-11***) are in excellent agreement. The crystal field parameters used for Ni^{II} are those determined for the fit of the XNLD signal. We can, therefore, reasonably conclude that the description of the electronic structure of the ground state for both ions is accurate, which allows computing their orbit and spin angular momenta, the number of holes on the *3d* levels and the magnetic dipole operator $< T_z >$.[41] Such tensors values can be calculated at 0 K and also at finite temperatures following a Boltzmann population of the lowest lying multi-electronic levels. The orbit and spin angular momenta $< L_z >$ and $< S_z >$ do not vary with temperature, at least between 0 and 2 K (***Table 3-1***). It can also be noticed that $< T_z >$ is quite small compared to $< S_z >$ so that the spin sum rule reads $< S_z > + < \frac{7}{2} T_z > \approx < S_z >$.

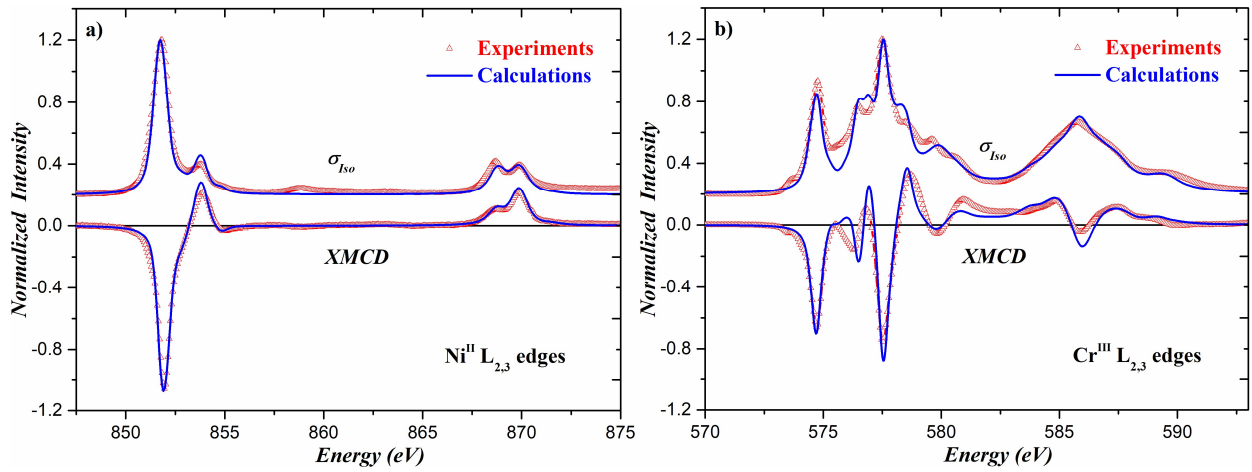

Figure 3-11. *Comparison between theoretical and experimental isotropic cross-sections and XMCD signals for $\theta = 60°$: (a) at the Ni^{II} $L_{2,3}$ edges, (b) at the Cr^{III} $L_{2,3}$ edges. The isotropic cross-sections have been artificially shifted upwards.*

From the LFM calculations and for Ni^{II}, one finds m_{orbit} = +0.346 μ_B, m_{spin} = +1.984 μ_B so that the total magnetic moment is m_{Ni} = +2.33 μ_B (g_{Ni} = 2.35). For Cr^{III}, m_{orbit} (-0.041 μ_B) and m_{spin} (+2.980 μ_B) lead to m_{Cr} = +2.94 μ_B and g_{Cr} = 1.97 very close to 2.0 as for most octahedral Cr^{III} complexes. Note that the number of electrons (respectively holes) on the *3d* shell of the Ni^{II} ions is 8 (2) and 2.98 (7.02) for the Cr^{III} ions.

The orbit and spin magnetic moments could also be obtained from the application of the magneto-optical sum rules.[42, 47, 53-54] Since the sum rule for the orbit magnetic moment is very robust, it can be applied to both Ni^{II} and Cr^{III} ions. But because of intermixing, the spin sum rule does not hold at all for Cr^{III} $L_{2,3}$ edges; it presents a ≈ 10 % error at the Ni^{II} $L_{2,3}$ edges (see ***Table 3-3***). One finds, from LFM, that the orbit magnetic moments compare well with those extracted from the sum rules (***Table 3-3***). Values obtained from LFM sum rules and experiments are estimated on spectra shown in Figure I-4 in Appendix I. The *g* values determined from the magnetic moments extracted from the experimental data and from calculations agree and lie within the range found experimentally for distorted octahedral Ni^{II} complexes

Table 3-3. *Values for m_{orbit}, m_{spin}, $<T_z>$, and Landé factor g obtained from the LFM calculations at T = 2 K and from the magneto-optical sum rules applied to the experimental spectra or to the LFM theoretical spectra.*

Magnetic	Ni^{II}			Cr^{III}		
Parameters	Exp. Sum rules	LFM Sum rules	LFM	Exp. Sum rules	LFM Sum rules	LFM
m_{spin}	+1.68	+1.80	+1.98	/	/	+2.98
m_{orbit}	+0.32	+0.35	+0.35	0.05	-0.04	-0.04
$<T_z>$	/	/	–0.003	/	/	0.000
g	2.37	/	2.35	/	/	1.97

3.4.2.2 Magnetization Curves and Remnant Magnetizations

By setting the energy of the monochromator at the energy of the maximum (in absolute value) of the XMCD signal (i.e. 852.0 eV for Ni^{II} and 877.5 eV for Cr^{III}) and by sweeping the external magnetic field, it is possible to record an element selective magnetization curve. The magnetization curves reported in ***Figure 3-12*** have been measured at 2 K and between –2.5 T and +2.5 T.

The magnetization curves for both ions are saturated in a 2 T external magnetic field (***Figure 3-13***). For ***B*** = 2 T, the value of the total magnetization has been determined by XMCD so that the magnetization curves can be plotted in absolute values with the *y* axis expressed in Bohr Magnetons. Contrary to the XMCD signals at 2 T for which one did not observe any angular dependence, the magnetization curves present a large angular dependence that is best observed for small magnetic

fields (***Figure 3-13***). One observes that when $\theta = 60°$, the magnetization loops have an enhanced square shape with larger coercive fields and larger remnant magnetizations than for $\theta = 0°$. Therefore, when the magnetic field is perpendicular to the substrate ($\theta = 0°$) it is difficult to magnetize the sample, which is consistent with an easy plane of magnetization parallel to the NCs monolayer.

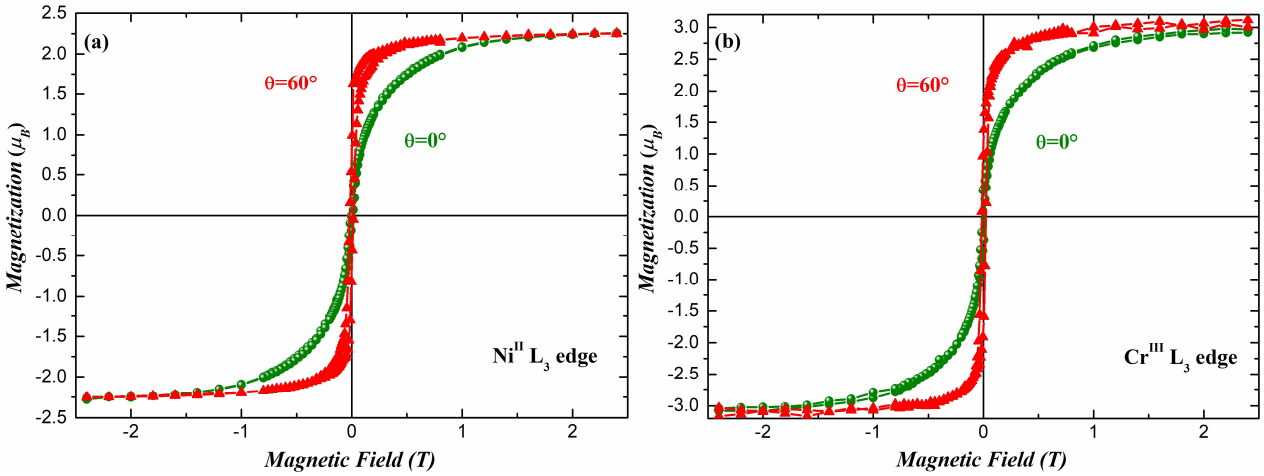

Figure 3-12. *XMCD-detected Magnetization curves between 2 T and -2 T for Ni^{II} and Cr^{III} by setting the energy of the monochromator at the energy of the maximum (in absolute value) of the XMCD signal (i.e. 852.0 eV for Ni^{II} and 877.5 eV for Cr^{III})*

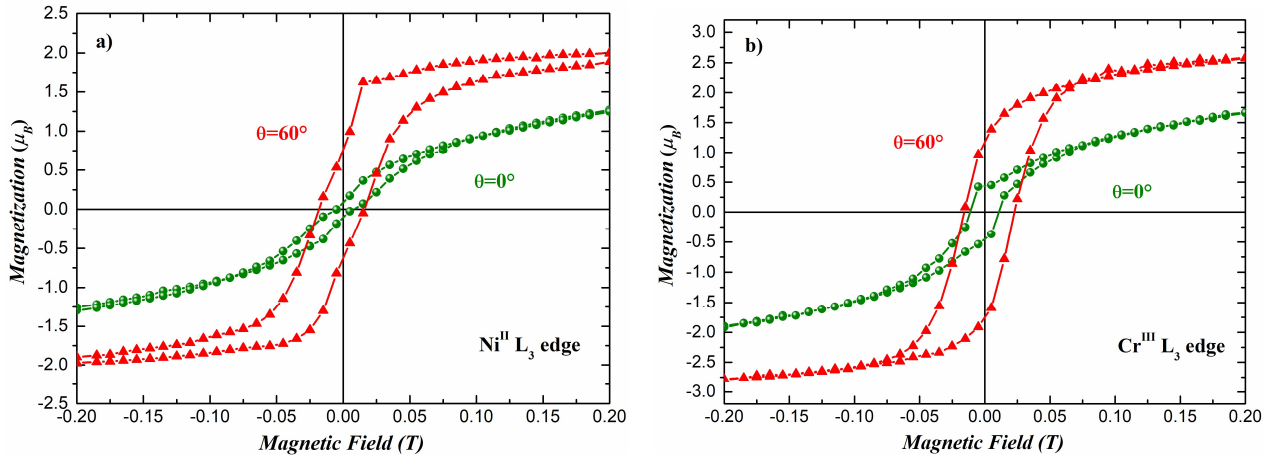

Figure 3-13. *XMCD detected magnetization curves for Ni^{II} (a) and Cr^{III} (b) ions at T = 2 K at the fixed energy of maximum L_3 energy (i.e. 852.0 eV for Ni^{II} and 877.5 eV for Cr^{III})*

From the magnetization curves, the remnant magnetization for Ni^{II} ions is ≈ 0.75 μ_B at 60° and between 0.10 and 0.20 μ_B at 0°. One can also measure the remnant magnetization more accurately by first applying a saturating magnetic field of 2 T (or -2 T) then switching it off and recording the XMCD signal. We expect a reversal of the remnant magnetization depending on the sign of the saturating field (***Figure 3-14***).

The remnant magnetization amounts to 0.80 μ_B for $\theta = 60°$ (i.e. 36 % of the isotropic L_3 edge) whereas it is only 0.18 μ_B for $\theta = 0°$ (i.e. 8 %), which confirms that the plane perpendicular to the monolayer normal is an easy plane of magnetization. The remnant magnetization at $\theta = 60°$ is more than 4 times

larger than the one at $\theta = 0°$, indicating that the NCs monolayer possesses an easy plane of magnetization perpendicular to the normal of the monolayer (***Figure 3-15***). The raw $(\sigma_{Right}+\sigma_{Left})/2$ cross sections spectra have been plotted and the variation of intensity simply follows the $\approx 1/\cos(\theta)$ function that is expected when rotating a sample and measuring the XAS signal in TEY.

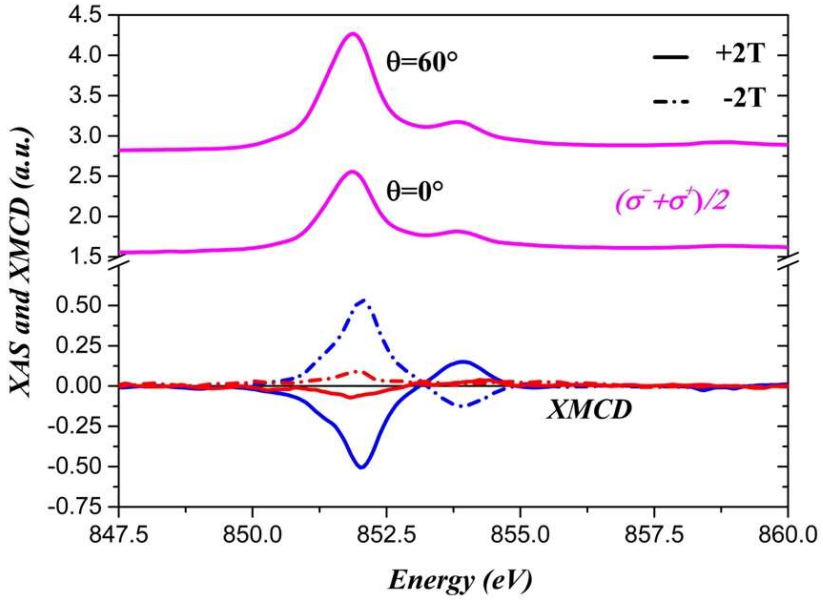

Figure 3-14. *Angular dependence of the remnant XMCD signals for $\theta = 0°$ and $\theta = 60°$ at $T = 2$ K; +2T (-2T) indicate the initial value of the external magnetic field. The $(\sigma_{Right} + \sigma_{Left})/2$ cross-sections are raw data and have not been normalized at the difference of* ***Figure 3-15***.

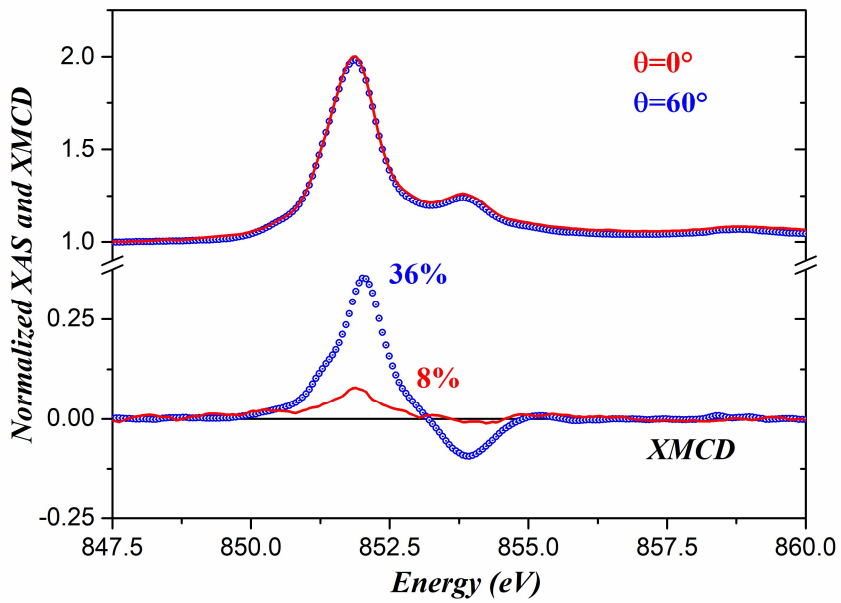

Figure 3-15. *XMCD signals for remnant magnetization of Ni^{II} ions recorded between 0° and 60° at 2 K.*

3.5 Discussion

It has been found, from XNLD, that the Ni^{II} ions at the very surface of the NCs are sitting in an elongated C_{4v} site because of the presence of a water molecule coordinated to Ni^{II} at the nanocrystal/air interface. In order to fairly reproduce the XNLD spectra at the Ni edges, we used a

crystal field parameter 10*Dq* equal to 0.7 eV for the Ni^{II} species belonging to the surface. This value is lower than that used for Ni^{II} belonging to the core of the particles (1.38 eV) and cannot be justified by the mere replacement of one nitrogen cyanide ligand by one water molecule in the coordination sphere of Ni^{II} without additional distortion. Recently, Bleuzen *et al.* demonstrated by XAS studies at the Co^{II} K-edge of 5.5 nm RbCoFe particles that the Co^{II} species belonging to the surface are in a distorted environment attributed to the presence a Co–NC angle lower than 180°.[64] Such distortion would reduce the strength of the crystal field of Co^{II} ions.[65] The same situation may occur in the case of the present CsNiCr NCs, where the Ni–NC angles at the NCs surface would not be linear, consistent with a reduction of the crystal field in addition to the presence of a water molecule at the apical position as depicted below. We, thus, attribute the lowering of 10*Dq* to a structural distortion on the Ni^{II} surface species (***Figure 3-16***).

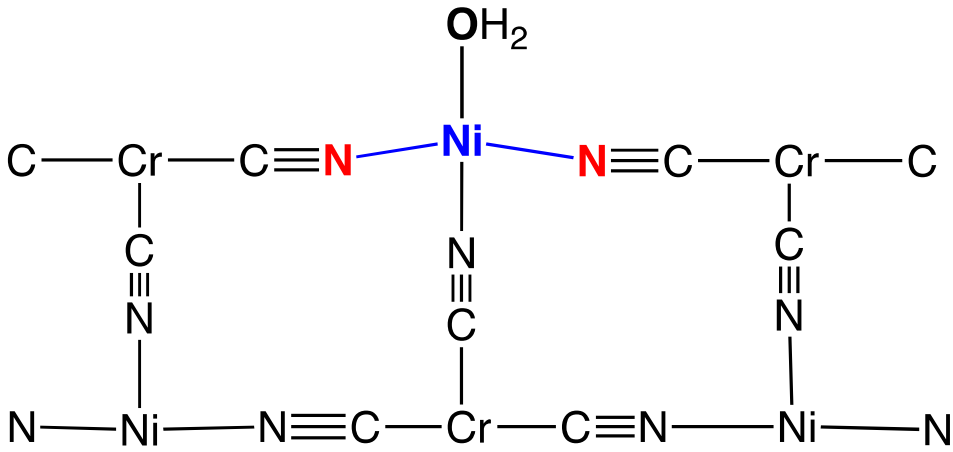

Figure 3-16. *Schematic view of a side face of a NC showing the C_{4v} elongation distortion of the Ni^{II} surface species coordination sphere highlighting the Ni-CN non-linear angle.*

In O_h symmetry and when the effect of spin-orbit coupling is neglected, the ground state for a high spin Ni^{II} species would be $^3A_{2g}(O_h)$ and further lowering of the site symmetry down to C_{4v} transforms it to $^3B_1(C_{4v})$. Considering the effect of spin-orbit coupling further splits the 3-fold degenerate ground state into a doublet with symmetry $E(C_{4v})$ and a singlet with symmetry $B_2(C_{4v})$. In the case of an elongated C_{4v} symmetry, group theory treatment shows that the lowest lying level is the singlet $B_2(C_{4v})$ level that is separated from the highest lying $E(C_{4v})$ doublet (***Figure 3-17***). The energy difference between the 1-fold lower lying state and the 2-fold higher lying states correspond to ZFS and from combined XNLD experiments and LFM calculations, we determined that it is equal to 0.76 meV (6.1 cm^{-1}) (***Figure 3-9***), with the ground state being the 1-fold degenerate $B_2(C_{4v}$ + SOC). Time reversal symmetry imposes that $< S_z > = < L_z > = 0$ for the 1-fold $B_2(C_{4v}$ + SOC) level so that the magnetization along *z* is zero, which correspond to a hard axis of magnetization. Therefore, the plane perpendicular to *z* is an easy plane of magnetization for the Ni^{II} ions at the very surface of the NCs.

In ***Figure 3-16***, it should be reminded that the notation for the $^3F^+$ representation in O_3 means that the irreducible representation for the spin is $1^+(O_3)$ and the irreducible representation for the orbit is

$3^{+}(O_3)$. The spin irreducible representations are usually not signed because they are always even. On the contrary, the orbit irreducible representations need to be properly signed in O_3, hence F^{+}. We write ^3X for the irreducible representations in O_h, D_{4h} with no spin-orbit coupling, or C_{4v} with no spin-orbit coupling, because the spin triplet remains degenerate in these three cases. For the sake of clarity, it is to be remembered that the irreducible representation for the spin triplet in O_3 transforms into $T_{1g}(O_h)$ for O_h, into $A_{2g}(D_{4h}) \oplus E_g(D_{4h})$ for D_{4h}, and into $A_2(C_{4v}) \oplus E(C_{4v})$ for C_{4v}.

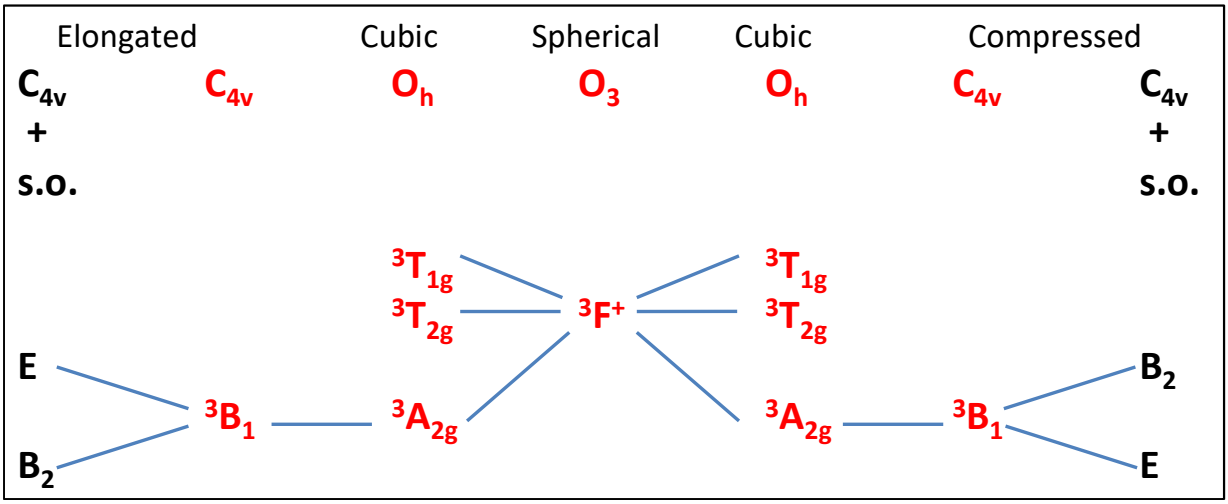

***Figure 3-17**. Energy diagrams of 3d multi-electronic levels for Ni^{II} as a function of crystal field symmetry and spin-orbit coupling; when spin-orbit coupling is not considered, the irreducible representations are drawn in red and when spin-orbit coupling is turned on, they are reported in black.*

The magnetization curves (***Figures 3-12*** and ***3-13***) allow observing that the percentage of remnant magnetizations and the coercive fields at the Ni and Cr edges are roughly the same. This is consistent with a coherent reversal of the magnetization of the nanocrystals as expected from single magnetic domain objects where surface ions are exchanged coupled with ions present in the volume.[15] Because of intra-particle exchange coupling, the magnetization of each Ni^{II} would tend to be lying in the plane of the monolayer. Then due to magnetic dipole interactions between NCs, the magnetic moments of the NCs would be coupled in the plane of the substrate so that the whole monolayer would present an easy plane of magnetization. These findings are supported by the present XNLD and angular-dependent, XMCD-detected magnetization curves and it also stems from simple group theory considerations. Nevertheless, we do not have at hand a micro-magnetic description of the exchange interactions inside individual NCs, nor a precise description of the intensity of the magnetic dipole interactions between NCs.

However, from previous studies on highly diluted 6 nm CsNiCr NCs we estimated that surface anisotropy is about 10 times larger than anisotropy due to the volume.[15] In addition, the exchange coupling parameter between Cr^{III} and Ni^{II} through the cyanide bridge was determined to be around 2 meV (16 cm^{-1}) on molecular complexes,[66] while dipolar interaction between two 6 nm NCs that are at 1 nm distance is about 1000 times larger.[15] Therefore, the behavior of a compact monolayer of

6nm-CsNiCr nanocrystals must be dominated by inter-particle dipolar interactions within the plane of the monolayer that is responsible for the easy plane of magnetization experimentally observed and this is indeed due to the local easy plane of the individual Ni^{II} ions present at the NCs surface.

In this study, we demonstrated that the XNLD and XMCD data are consistent with elongated Ni^{II} coordination sphere of the type $(CN)_5Ni(OH_2)$ for surface atoms that leads to a ZFS value of +0.76 meV (+6.1 cm^{-1}). Water molecules are known to induce a weaker crystal field than the nitrogen side of the cyanide.[67] But, we show here that XNLD data are consistent with a reduced crystal field for the Ni(II) surface species so that a structural distortion due to a non-linear Ni-N-C angle must also be considered. Nevertheless, in our previous study on the same nanocrystals that were embedded in DODA, the XAS and XMCD data were consistent with a slightly *compressed* C_{4v} geometry for the surface Ni^{II} ions (with ZFS value of -0.1 cm^{-1} where we adopt the convention that ZFS is negative when the two-fold level *E* is the ground level; ***Figure 3-7***), which corresponds to an easy axis of magnetization of the Ni^{II} species belonging to the NCs' surface. The origin of the different electronic structures (elongated *vs.* compressed) between embedded NCs and those assembled as monolayer can be ascribed to the ammonium groups of DODA surrounding the NCs (in the previous study), while for the monolayer the Ni^{II} surface ions are at the layer/air interface and do not experience the effect of the environment of an organic matrix. The effect of the environment of organic/inorganic matrices on the electronic behavior of coordination-based nanocrystals has been mainly evidenced in spin crossover nanoparticles,[68-71] where surface molecules are believed to highly impact their magnetic behavior because of an alteration of their crystal field as it is observed here for electronic and magnetic anisotropy.

3.6 Conclusion

The present combined experimental and theoretical approach allowed to determine the electronic and magnetic anisotropies around Ni^{II} and Cr^{III} ions in 6-CsNiCr NCs. From XNLD, angular-dependent XMCD, and angular-dependent, XMCD-detected, magnetization curves, it has been possible to determine two types of anisotropies: a) an intra-particle, electronic anisotropy associated to the NCs surface Ni^{II} sites, b) an inter-particle magnetic anisotropy inducing an easy plane of magnetization for the NCs monolayer.

The intra-particle electronic anisotropy concerns the Ni^{II} ions in the first 5 Å at the top of the NCs for which the site symmetry is an elongated C_{4v} site. The origin of the elongated C_{4v} symmetry is to be found in the replacement of an apical N ≡ C ligand by a water molecule together with a structural distortion of the NiN_5 coordination environment. Although only 8 % of the Ni^{II} ions are present in the first 5 Å of the upper face of the cubic NCs, the extreme surface sensitivity of the TEY mode

exalts the spectroscopic contribution of these Ni^{II} species so that a rather large XNLD signal could be detected.

The electronic anisotropy associated to the Ni^{II} species at the very surface of the NCs induces a "hard" axis of magnetization along the *z* axis so that all the NCs would tend to have their magnetic moments lying in the plane of the substrate. Magnetic dipole interactions, that are much larger than intra-particle exchange coupling, would then tend to build an easy plane of magnetization for the NCs monolayer.

Thanks to advanced experimental X-ray spectroscopy coupled to up-to-date LFM theory, it has been possible to determine the magnetic anisotropy in a NCs monolayer and to find that the microscopic origin of the magnetic anisotropy lies in the distortion of the electronic density of the Ni^{II} species at the very surface of the individual NCs.

References

1. Ferlay, S.; Mallah, T.; Ouahes, R.; Veillet, P.; Verdaguer, M., A Room-Temperature Organometallic Magnet Based on Prussian Blue. *Nature* **1995,** *378* (6558), 701-703.
2. Sato, O.; Iyoda, T.; Fujishima, A.; Hashimoto, K., Photoinduced magnetization of a cobalt-iron cyanide. *Science* **1996,** *272* (5262), 704-705.
3. Verdaguer, M.; Girolami, G. S.; Miller, J.; Drillon, M., Magnetic Prussian blue analogs. *Magnetism: molecules to materials V* **2005,** *5*, 283-346.
4. Tokoro, H.; Ohkoshi, S.-i., Novel magnetic functionalities of Prussian blue analogs. *Dalton Transactions* **2011,** *40* (26), 6825-6833.
5. Brinzei, D.; Catala, L.; Louvain, N.; Rogez, G.; Stéphan, O.; Gloter, A.; Mallah, T., Spontaneous stabilization and isolation of dispersible bimetallic coordination nanoparticles of Cs x Ni [Cr (CN) 6] y. *J. Mater. Chem.* **2006,** *16* (26), 2593-2599.
6. Catala, L.; Brinzei, D.; Prado, Y.; Gloter, A.; Stephan, O.; Rogez, G.; Mallah, T., Core-Multishell Magnetic Coordination Nanoparticles: Toward Multifunctionality on the Nanoscale. *Angew. Chem. Int. Ed.* **2009,** *48* (1), 183-187.
7. Catala, L.; Mallah, T., Nanoparticles of Prussian blue analogs and related coordination polymers: From information storage to biomedical applications. *Coord. Chem. Rev.* **2017,** *346*, 32-61.
8. Basset Brown, D.; Shriver, D. F., Structures and Solid-State Reactions of Prussian Blue Analogs Containing Chromium, Manganese, Iron, and Cobalt. *Inorg. Chem.* **1969,** *8* (1), 37-42.
9. Buser, H.; Schwarzenbach, D.; Petter, W.; Ludi, A., The crystal structure of Prussian blue: Fe4 [Fe (CN) 6] 3. xH2O. *Inorganic Chemistry* **1977,** *16* (11), 2704-2710.
10. Mallah, T.; Ferlay, S.; Auberger, C.; Helary, C.; L'Hermite, F.; Ouahes, R.; Vaissemann, J.; Verdaguer, M.; Veillet, P., Hexacyanometalates: Molecular Precursors for High-Spin Molecules and High-TC Molecule-Based Magnets. *Molecular Crystals and Liquid Crystals Science and Technology. Section A. Molecular Crystals and Liquid Crystals* **1995,** *273* (1), 141-151.
11. Gadet, V.; Mallah, T.; Castro, I.; Verdaguer, M.; Veillet, P., High-TC molecular-based magnets: a ferromagnetic bimetallic chromium (III)-nickel (II) cyanide with TC= 90 K. *J. Am. Chem. Soc.* **1992,** *114* (23), 9213-9214.
12. Bleuzen, A.; Lomenech, C.; Escax, V.; Villain, F.; Varret, F.; Cartier dit Moulin, C.; Verdaguer, M., Photoinduced ferrimagnetic systems in Prussian blue analogues CI x Co4 [Fe (CN) 6] y (CI= alkali cation). 1. Conditions to observe the phenomenon. *J. Am. Chem. Soc.* **2000,** *122* (28), 6648-6652.
13. Arai, M.; Miyake, M.; Yamada, M., Metal (II) Hexacyanochromate (III) MCr (M= Co, Cu, Fe) coordination nanoparticles stabilized by alkyl surface coordination ligand: downsizing effect on their crystal structure and magnetic properties. *The Journal of Physical Chemistry C* **2008,** *112* (6), 1953-1962.
14. Prado, Y.; Dia, N.; Lisnard, L.; Rogez, G.; Brisset, F.; Catala, L.; Mallah, T., Tuning the magnetic anisotropy in coordination nanoparticles: random distribution versus core–shell architecture. *Chem. Commun.* **2012,** *48* (93), 11455-11457.
15. Prado, Y.; Mazerat, S.; Rivière, E.; Rogez, G.; Gloter, A.; Stéphan, O.; Catala, L.; Mallah, T., Magnetization reversal in CsNiIICrIII (CN) 6 coordination nanoparticles: unravelling surface anisotropy and dipolar interaction effects. *Adv. Funct. Mater.* **2014,** *24* (34), 5402-5411.
16. Prado, Y.; Arrio, M. A.; Volatron, F.; Otero, E.; Cartier dit Moulin, C.; Sainctavit, P.; Catala, L.; Mallah, T., Magnetic Anisotropy of Cyanide‐Bridged Core and Core–Shell Coordination Nanoparticles Probed by X‐ray Magnetic Circular Dichroism. *Chem. Eur. J.* **2013,** *19* (21), 6685-6694.
17. Catala, L.; Gacoin, T.; Boilot, J. P.; Rivière, É.; Paulsen, C.; Lhotel, E.; Mallah, T., Cyanide‐Bridged CrIII–NiII Superparamagnetic Nanoparticles. *Adv. Mater.* **2003,** *15* (10), 826-829.
18. Prado, Y.; Lisnard, L.; Heurtaux, D.; Rogez, G.; Gloter, A.; Stephan, O.; Dia, N.; Riviere, E.; Catala, L.; Mallah, T., Tailored coordination nanoparticles: assessing the magnetic single-domain critical size. *Chem. Commun.* **2011,** *47* (3), 1051-1053.

19. Ridier, K.; Gillon, B.; Chaboussant, G.; Catala, L.; Mazerat, S.; Riviere, E.; Mallah, T., Individual-collective crossover driven by particle size in dense assemblies of superparamagnetic nanoparticles. *Eur. Phys. J. B* **2017,** *90* (4).

20. Funk, T.; Deb, A.; George, S. J.; Wang, H.; Cramer, S. P., X-ray magnetic circular dichroism—a high energy probe of magnetic properties. *Coord. Chem. Rev.* **2005,** *249* (1-2), 3-30.

21. Beaurepaire, E.; Scheurer, F.; Krill, G.; Kappler, J.-P., *Magnetism and synchrotron radiation*. Springer: 2001; Vol. 34.

22. van der Laan, G.; Figueroa, A. I., X-ray magnetic circular dichroism—a versatile tool to study magnetism. *Coord. Chem. Rev.* **2014,** *277*, 95-129.

23. Van der Laan, G. In *Applications of soft x-ray magnetic dichroism*, J. Phys. Conf. Ser., IOP Publishing: 2013; p 012127.

24. Catala, L.; Gloter, A.; Stephan, O.; Rogez, G.; Mallah, T., Superparamagnetic bimetallic cyanide-bridged coordination nanoparticles with T-B=9 K. *Chem. Commun.* **2006,** (9), 1018-1020.

25. Clemente-Leon, M.; Coronado, E.; Lopez-Munoz, A.; Repetto, D.; Mingotaud, C.; Brinzei, D.; Catala, L.; Mallah, T., Magnetic langmuir-blodgett films of bimetallic coordination nanoparticles of Cs0.4Ni[Cr(CN)(6)](0.9). *Chem. Mater.* **2008,** *20* (14), 4642-4652.

26. Fleury, B.; Volatron, F.; Catala, L.; Brinzei, D.; Rivire, E.; Huc, V.; David, C.; Miserque, F.; Rogez, G.; Baraton, L.; Palacin, S.; Mallah, T., Grafting a monolayer of superparamagnetic cyanide-bridged coordination nanoparticles on Si(100). *Inorg. Chem.* **2008,** *47* (6), 1898-1900.

27. Ghirri, A.; Candini, A.; Evangelisti, M.; Gazzadi, G. C.; Volatron, F.; Fleury, B.; Catala, L.; David, C.; Mallah, T.; Affronte, M., Magnetic Imaging of Cyanide-Bridged Co-ordination Nanoparticles Grafted on FIB-Patterned Si Substrates. *Small* **2008,** *4* (12), 2240-2246.

28. Clemente-Leon, M.; Coronado, E.; Lopez-Munoz, A.; Repetto, D.; Catala, L.; Mallah, T., Patterning of Magnetic Bimetallic Coordination Nanoparticles of Prussian Blue Derivatives by the Langmuir-Blodgett Technique. *Langmuir* **2012,** *28* (9), 4525-4533.

29. Pinilla-Cienfuegos, E.; Kumar, S.; Manas-Valero, S.; Canet-Ferrer, J.; Catala, L.; Mallah, T.; Forment-Aliaga, A.; Coronado, E., Imaging the Magnetic Reversal of Isolated and Organized Molecular-Based Nanoparticles using Magnetic Force Microscopy. *Part. Part. Syst. Charac.* **2015,** *32* (6), 693-700.

30. Argyris, D.; Tummala, N. R.; Striolo, A.; Cole, D. R., Molecular structure and dynamics in thin water films at the silica and graphite surfaces. *The Journal of Physical Chemistry C* **2008,** *112* (35), 13587-13599.

31. Yang, D.-S.; Zewail, A. H., Ordered water structure at hydrophobic graphite interfaces observed by 4D, ultrafast electron crystallography. *Proceedings of the National Academy of Sciences* **2009,** *106* (11), 4122-4126.

32. De Groot, F.; Kotani, A., *Core level spectroscopy of solids*. CRC press: 2008.

33. van der Laan, G.; Thole, B. T., Strong magnetic x-ray dichroism in 2p absorption spectra of 3d transition-metal ions. *Phys. Rev. B* **1991,** *43* (16), 13401.

34. Dhesi, S. S.; van der Laan, G.; Dudzik, E., Determining element-specific magnetocrystalline anisotropies using x-ray magnetic linear dichroism. *Applied Physics Letters* **2002,** *80* (9), 1613-1615.

35. van der Laan, G.; Hoyland, M. A.; Surman, M.; Flipse, C. F.; Thole, B. T., Surface orbital magnetic moment of ferromagnetic nickel studied by magnetic circular dichroism in Ni3p core level photoemission. *Phys Rev Lett* **1992,** *69* (26), 3827-3830.

36. Brouder, C., Angular dependence of X-ray absorption spectra. *Journal of Physics: Condensed Matter* **1990,** *2* (3), 701.

37. Arenholz, E.; van der Laan, G.; Chopdekar, R. V.; Suzuki, Y., Angle-dependent Ni 2+ X-ray magnetic linear dichroism: Interfacial coupling revisited. *Phys. Rev. Lett.* **2007,** *98* (19), 197201.

38. Juhin, A.; Brouder, C.; Arrio, M.-A.; Cabaret, D.; Sainctavit, P.; Balan, E.; Bordage, A.; Seitsonen, A. P.; Calas, G.; Eeckhout, S. G., X-ray linear dichroism in cubic compounds: The case of Cr 3+ in MgAl 2 O 4. *Phys. Rev. B* **2008,** *78* (19), 195103.

39. Van der Laan, G.; Kirkman, I., The 2p absorption spectra of 3d transition metal compounds in

tetrahedral and octahedral symmetry. *Journal of Physics: Condensed Matter* **1992,** *4* (16), 4189.

40. Van der Laan, G.; Thole, B.; Sawatzky, G.; Verdaguer, M., Multiplet structure in the L 2, 3 x-ray-absorption spectra: A fingerprint for high-and low-spin Ni 2+ compounds. *Physical Review B* **1988,** *37* (11), 6587.

41. Carra, P.; Thole, B.; Altarelli, M.; Wang, X., X-ray circular dichroism and local magnetic fields. *Physical Review Letters* **1993,** *70* (5), 694.

42. Crocombette, J.; Thole, B.; Jollet, F., The importance of the magnetic dipole term in magneto-circular x-ray absorption dichroism for 3d transition metal compounds. *J. Phys. Condens. Mat.* **1996,** *8* (22), 4095.

43. Thole, B.; Carra, P.; Sette, F.; van der Laan, G., X-ray circular dichroism as a probe of orbital magnetization. *Physical review letters* **1992,** *68* (12), 1943.

44. Laan, G. v. d., Applications of soft x-ray magnetic dichroism. *Journal of Physics: Conference Series* **2013,** *430*, 012127.

45. Ohresser, P.; Otero, E.; Choueikani, F.; Chen, K.; Stanescu, S.; Deschamps, F.; Moreno, T.; Polack, F.; Lagarde, B.; Daguerre, J.-P., DEIMOS: a beamline dedicated to dichroism measurements in the 350–2500 eV energy range. *Rev. Sci. Instrum.* **2014,** *85* (1), 013106.

46. Joly, L.; Otero, E.; Choueikani, F.; Marteau, F.; Chapuis, L.; Ohresser, P., Fast continuous energy scan with dynamic coupling of the monochromator and undulator at the DEIMOS beamline. *J. Synchr. Rad.* **2014,** *21*, 502-506.

47. Chen, C.; Idzerda, Y.; Lin, H.-J.; Smith, N.; Meigs, G.; Chaban, E.; Ho, G.; Pellegrin, E.; Sette, F., Experimental confirmation of the X-ray magnetic circular dichroism sum rules for iron and cobalt. *Phys. Rev. Lett.* **1995,** *75* (1), 152.

48. Jafri, S. F.; Koumousi, E. S.; Arrio, M.-A.; Juhin, A.; Mitcov, D.; Rouzieres, M.; Dechambenoit, P.; Li, D.; Otero, E.; Wilhelm, F., Atomic Scale Evidence of the Switching Mechanism in a Photomagnetic CoFe Dinuclear Prussian Blue Analogue. *J. Am. Chem. Soc.* **2019,** *141* (8), 3470–3479.

49. De Groot, F.; Fuggle, J.; Thole, B.; Sawatzky, G., 2p x-ray absorption of 3d transition-metal compounds: An atomic multiplet description including the crystal field. *Physical Review B* **1990,** *42* (9), 5459.

50. Cowan, R. D., *The theory of atomic structure and spectra*. Univ of California Press: 1981.

51. Butler, P. H., *Point group symmetry applications: methods and tables*. Springer Science & Business Media: 2012.

52. Chen, C. T.; Smith, N. V.; Sette, F., Exchange, spin-orbit, and correlation effects in the soft-x-ray magnetic-circular-dichroism spectrum of nickel. *Physical Review B* **1991,** *43* (8), 6785-6787.

53. Sainctavit, P.; Arrio, M.-A.; Brouder, C., Analytic calculation of the spin sum rule at the L 2, 3 edges of Cu 2+. *Phys. Rev. B* **1995,** *52* (17), 12766.

54. Wu, R.; Wang, D.; Freeman, A., Validity and the applicablity of magnetic ‐ circular ‐ dichroism sum rules for transition metals. *J. Appl. Phys.* **1994,** *75* (10), 5802-5806.

55. Peredkov, S.; Neeb, M.; Eberhardt, W.; Meyer, J.; Tombers, M.; Kampschulte, H.; Niedner-Schatteburg, G., Spin and orbital magnetic moments of free nanoparticles. *Phys. Rev. Lett.* **2011,** *107* (23), 233401.

56. Arrio, M.-A.; Sainctavit, P.; Cartier dit Moulin, C.; Mallah, T.; Verdaguer, M.; Pellegrin, E.; Chen, C., Characterization of chemical bonds in bimetallic cyanides using X-ray absorption spectroscopy at L2, 3 edges. *J. Am. Chem. Soc.* **1996,** *118* (27), 6422-6427.

57. Figgis, B. N.; Hitchman, M. A., *Ligand field theory and its applications*. Wiley-Vch: 2000.

58. van der Laan, G., Hitchhiker's guide to multiplet calculations. *Magnetism: A Synchrotron Radiation Approach* **2006**, 143-199.

59. Arrio, M.-A.; Scuiller, A.; Sainctavit, P.; Cartier dit Moulin, C.; Mallah, T.; Verdaguer, M., Soft X-ray Magnetic Circular Dichroism in Paramagnetic Systems: Element-Specific Magnetization of Two Heptanuclear CrIII MII6 High-Spin Molecules. *J. Am. Chem. Soc.* **1999,** *121* (27), 6414-6420.

60. Ruamps, R.; Maurice, R.; Batchelor, L.; Boggio-Pasqua, M.; Guillot, R.; Barra, A. L.; Liu, J. J.; Bendeif, E.; Pillet, S.; Hill, S.; Mallah, T.; Guihery, N., Giant Ising-Type Magnetic Anisotropy in Trigonal Bipyramidal Ni(II) Complexes: Experiment and Theory. *J. Am. Chem. Soc.* **2013,** *135* (8), 3017-3026.

61. Ruamps, R.; Batchelor, L. J.; Maurice, R.; Gogoi, N.; Jimenez-Lozano, P.; Guihery, N.; de Graaf, C.; Barra, A. L.; Sutter, J. P.; Mallah, T., Origin of the Magnetic Anisotropy in Heptacoordinate Ni-II and Co-II Complexes. *Chem. Eur. J.* **2013,** *19* (3), 950-956.

62. Charron, G.; Malkin, E.; Rogez, G.; Batchelor, L. J.; Mazerat, S.; Guillot, R.; Guihery, N.; Barra, A. L.; Mallah, T.; Bolvin, H., Unraveling sigma and pi Effects on Magnetic Anisotropy in cis-NiA(4)B(2) Complexes: Magnetization, HF-HFEPR Studies, First-Principles Calculations, and Orbital Modeling. *Chem. Eur. J.* **2016,** *22* (47), 16848-16860.

63. Rogez, G. Modulation des propriétés électroniques et de l'anisotropie magnétique de complexes mono et polynucléaires: influence des ligands pontant et périphériques. Université Paris Sud 11, 2002.

64. Bordage, A.; Moulin, R.; Fonda, E.; Fornasieri, G.; Riviere, E.; Bleuzen, A., Evidence of the Core-Shell Structure of (Photo)magnetic CoFe Prussian Blue Analogue Nanoparticles and Peculiar Behavior of the Surface Species. *J. Am. Chem. Soc.* **2018,** *140* (32), 10332-10343.

65. Escax, V.; Champion, G.; Arrio, M. A.; Zacchigna, M.; Moulin, C. C. D.; Bleuzen, A., The Co ligand field: A key parameter in photomagnetic CoFe Prussian blue derivatives. *Angew. Chem. Int. Ed.* **2005,** *44* (30), 4798-4801.

66. Mallah, T.; Auberger, C.; Verdaguer, M.; Veillet, P., A Heptanuclear Criiiniii(6) Complex with a Low-Lying S=15/2 Ground-State. *J. Chem. Soc. Chem. Commun.* **1995,** (1), 61-62.

67. Shriver, D. F.; Shriver, S. A.; Anderson, S. E., Ligand Field Strength of the Nitrogen End of Cyanide and Structures of Cubic Cyanide Polymers. *Inorg. Chem.* **1965,** *4* (5), 725-730.

68. Volatron, F.; Catala, L.; Riviere, E.; Gloter, A.; Stephan, O.; Mallah, T., Spin-crossover coordination nanoparticles. *Inorg. Chem.* **2008,** *47* (15), 6584-6586.

69. Raza, Y.; Volatron, F.; Moldovan, S.; Ersen, O.; Huc, V.; Martini, C.; Brisset, F.; Gloter, A.; Stephan, O.; Bousseksou, A.; Catala, L.; Mallah, T., Matrix-dependent cooperativity in spin crossover Fe(pyrazine)Pt(CN)(4) nanoparticles. *Chem. Commun.* **2011,** *47* (41), 11501-11503.

70. Tissot, A.; Enachescu, C.; Boillot, M. L., Control of the thermal hysteresis of the prototypal spin-transition Fe-II(phen)(2)(NCS)(2) compound via the microcrystallites environment: experiments and mechanoelastic model. *J. Mater. Chem.* **2012,** *22* (38), 20451-20457.

71. Tanasa, R.; Laisney, J.; Stancu, A.; Boillot, M. L.; Enachescu, C., Hysteretic behavior of Fe(phen)(2)(NCS)(2) spin-transition microparticles vs. the environment: A huge reversible component resolved by first order reversal curves. *Appl. Phys. Lett.* **2014,** *104* (3).

Chapter 4 - Fe(II)-SCO Compounds Assembled on Metallic Substrates

This chapter is organized in five sections. Section 4.1 is a general introduction. Section 4.2 presents the magnetometry study of the SCO complex **1** deposited as a thick film. Section 4.3 deals with the analysis method that allows to determine the HS/LS ratio of the XAS data of the submonolayers considering the XAS data of thick films of the SCO complexes **1** and a high spin complex **2** together with Ligand Field Multiplet calculations. Section 4.4 is focused on the analysis of the data of the submonolayer s of **1** deposited on Cu(111) and Au(111) metallic substrates. Section 4.5 discusses the mechanism the light induced switching observed at low temperature. And section 4.6 is a general conclusion.

4.1 General Introduction

Spin-crossover (SCO) compounds are bistable molecular systems that can be addressed by external stimuli such as temperature, light, pressure, magnetic or electric field;[1-5] they can be used for the design of molecular memory devices.[6-14] For Fe(II) containing complexes ($3d^6$ electronic configuration) in octahedral geometry, when the ligand field and the spin pairing energies are of the same order of magnitude, the two spin states have close energy. The LS state is the ground state because its lower free Gibbs energy. Therefore, a variation of the temperature from 300 to 2 K leads to a crossover from the high spin (HS; $t_{2g}^4e_g^2$) to the low spin (LS; $t_{2g}e_g^0$) state. Furthermore, it is possible at low temperature (when the molecule is in the LS state) to induce a trapping of the metastable HS state upon visible light irradiation; this is called the Light induced Spin State Trapping (LIESST).[15, 16] This phenomenon occurs also with X-rays photons (Soft X-ray Induced Excited Spin State Trapping (SOXIESST)) and must be considered when analyzing the X-ray Absorption Spectroscopy (XAS) data.[17, 18] A reverse LIESST (r-LIESST, i.e. switching from HS to LS) that can only be promoted by near infrared excitation has also been observed,[16, 19] giving rise to applications in light driven memory devices.[10]

The spin crossover phenomenon is accompanied by changes in optical properties and also in the coordination sphere of the metal ion, mainly a contraction upon HS to LS change. The structural change at the molecular level may or may not induce an effect in the solid. Two cases can be considered: 1) absence of interaction among the molecules leading to a smooth crossover reminiscent of a Boltzmann distribution between two levels and 2) presence of interaction among the molecules leading to a first order transition that can be accompanied by a hysteresis loop (bistability). The

interaction between the molecules have elastic origin and is due to the local change of size due to the spin change.[2, 4, 20, 21] One of the challenges of the last decade consisted, therefore, in investigating the size effect on the critical temperature and more importantly on the width of the hysteresis loop.[5, 12, 22] Research effort has, thus, focused on the investigation of the behavior of spin crossover materials at the nanoscale, e.g. in nanoparticles,[23-26] in thin films grown on surfaces,[5, 20, 21, 27-32] and also on single molecules or objects trapped in junctions.[32-38] While the switching by electrical signals seems promising but yet challenging,[35, 38, 39] visible and near-infrared lights are still considered as the main switching stimuli considering their intrinsic properties (e.g. wavelength, power, polarization, temporal dynamics, and easy manipulation).[3, 11, 15, 16, 19, 31, 40, 41] To develop efficient nanoscale devices, it is necessary to investigate the light-induced processes at the level of few molecules and ultimately at the level of a single layer of molecules assembled on a substrate.[27, 28, 30, 42] In such a case, one may expect a large effect of the molecules/substrate interface on the thermal and light-induced SCO behavior.[4, 21, 31, 40, 41, 43, 44]

In order to investigate the SCO behavior of a single layer or a submonolayer of SCO molecules two powerful techniques can be used: Scanning Tunnel Microscopy (STM) that allows the observation of single molecules and X-ray absorption spectroscopy (XAS) that gives information on the assembly of the molecules.[38] In particular, the XAS spectra at the $L_{2,3}$ edge of Fe are very sensitive to the change of the spin state and may give qualitative and quantitative information on the nature of the spin state and on the HS to LS ratio as a function of temperature and when light irradiation is applied. It has already been shown that SCO Fe^{II} complexes assembled as submonolayer s on graphite, bismuth and on other surfaces can undergo a complete LS to HS transition at low temperature through the LIESST effect with green light.[40, 45]

The objective of this part is the investigation of the thermal and light-induced spin change in SCO molecules assembled on Cu(111) and Au(111) as submonolayer s with the perspective of building memory devices that can be addressed by light.

When the properties of a submonolayer are investigated, the molecules are assembled on the substrate by sublimation in ultra-high vacuum. One of the problems encountered concerns the stability of the molecules during the sublimation process and more importantly on the metallic substrate where the coordination of the ligands on Fe(II) may compete with their coordination on the metallic substrate. Such competition led in some cases to the decomposition of the molecules where some organic ligands where found to better interact with the substrate.[28, 33, 34] When the SCO complex possesses a bidentate ligands such as phenantroline, bipyridine or similar, decomposition was evidenced.[20, 45-50]

In order to preclude such decomposition, we chose a neutral SCO Fe(II) complex bearing two *tridentate* ligands in order to enhance its thermodynamic stability towards its interaction with the

substrate i.e. [Fe^{II} (3,5-$(CH_3)_2Pz)_3BH_2$] where Pz = pyrazolyl, noted **1** in the following (***Figure 4-1***). It has been proved that the tris pyrazolyl ligands ensure good stability without dissociation when the molecules are assembled on Au(111); as a result, it turns out that this molecule interplays a weakly interaction with substrate and presents an incomplete spin transition.[51] As a reference for the high spin state, we used a similar complex with a slightly different ligand i.e. [Fe^{II}(3-$(C_6H_5)Pz)_3BH_2$] noted **2** (***Figure 4-1***) that remains high spin in the whole temperature range.

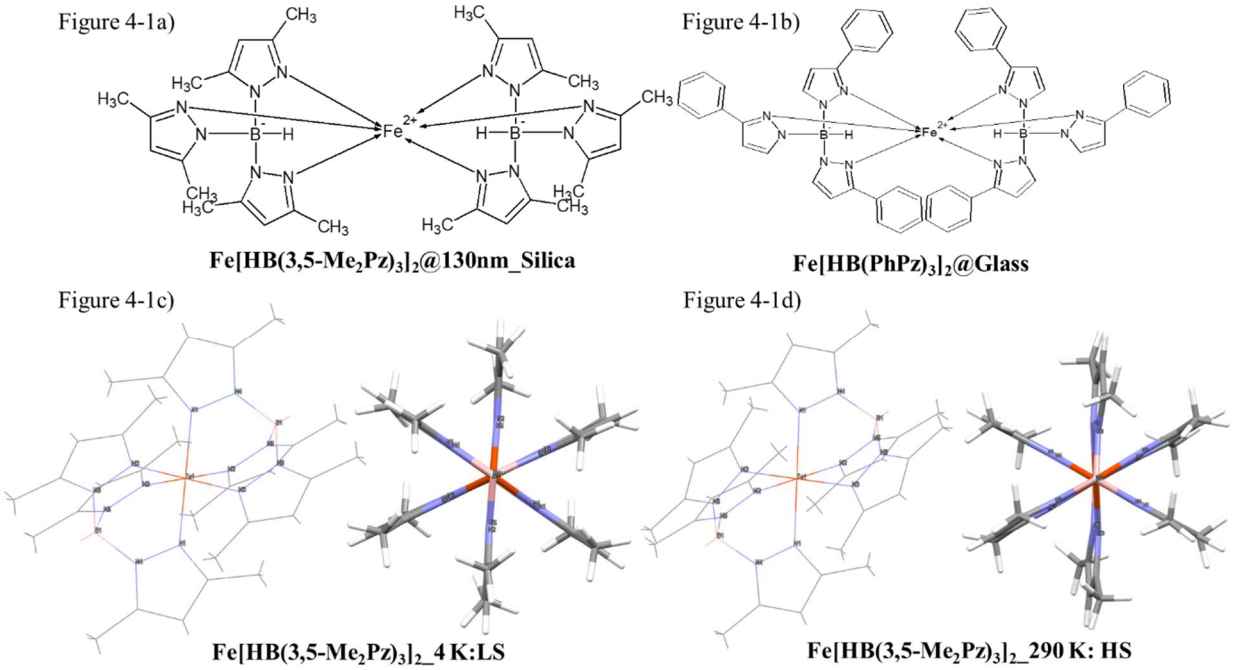

Figure 4-1*. Schematic structure for $Fe^{II}[(3,5\text{-}(CH_3)_2Pz)_3BH]_2$ and $Fe^{II}[HB(PhPz)_3]_2$, respectively. Figure 4-1a) and Figure 4-1b) is the planar structure for (1) and (2); while Figure 4-1c) and Figure 4-1d) are the chemical Structures of (1) at LS (4 K) and HS (290 K) state, respectively.*

4.2 Magnetic Behavior of a Thick Film

Synthesis and Assembled Processes: The investigated Fe^{II} containing complexes were already reported and their magnetic properties studied.[5, 21, 22, 52-54] These samples used in the following experiments were prepared by O. Iasco and studied by Dr. M.-L. Boillot at ICMMO. They investigated the behavior of thick films (few microns) of the two compounds that were deposited on glass and silica.[5] The SCO sample was studied by magnetometry first and the two samples were subsequently studied by XAS.

The magnetic study of an as-sublimed layer of 7 microns thickness shows an incomplete spin crossover with around 50% residual HS fraction. Annealing the sample at 400 K leads to an almost complete transition with a thermal hysteresis loop (***Figure 4-2***).[5] The annealed sample was subsequently investigated by XAS (see below).

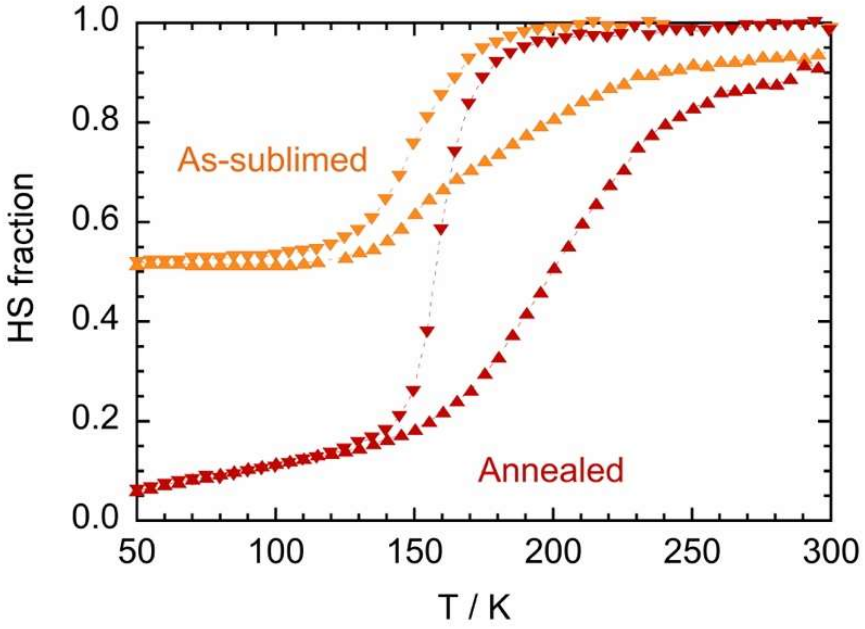

***Figure 4-2**. The thermal hysteresis of HS Fraction vs measured temperature (T) from magnetic measurements of compound $Fe^{II}[HB(3,5\text{-}Me_2Pz)_3]_2$ in the as-sublimed and the annealed form with a 7 microns thickness.*[5]

4.3 Analysis Methods

As we will observe below, the XAS spectra of the HS and LS species are sufficiently different in order to be able to qualitatively analyze the spectra. However, a quantitative analysis is not possible when incomplete transition occurs as in the present work. Furthermore, the shape and the intensity of the high spin species at high and low temperatures are different. Finally, the presence of SOXIESST at low temperature adds a high spin contribution that precludes a quantitative analysis of the LIESST effect. It is, therefore, compulsory to set a methodology that allows to determine the absolute intensity of the XAS spectrum of the LS and HS species at high and low temperatures. This methodology will be introduced following four steps:

------Experimental XAS spectra for pure HS and LS states

------Calculated XAS spectra by LFM methods for pure HS and LS states

------Normalized reference spectra combining calculations and experiments

------Analysis method for reference spectra and real-time experimental spectra

4.3.1 Experimental XAS Spectra for Pure HS and LS states

On the basis of previous studies on **1**,[41, 51] it reported that a monolayer of **1** deposited on Au(111) has a SCO behavior under the illumination with blue light. The temperature dependent XAS spectra of the monolayer has contributions from the two spin states.[41, 43, 44] Accordingly, we investigated samples containing the pure high spin state at room temperature (298 K) and low temperature (4 K) in order to determine the evolution of the spectrum of the pure HS with temperature. To do so, we studied the following two thick samples:

(i) $Fe^{II}[HB(3,5\text{-}Me_2Pz)_3]_2$ molecules **1** deposited on silica: HS at 298 K and LS at 80 K with a thickness of few micrometers;

(ii) $Fe^{II}[HB(PhPz)_3]_2$ high spin molecules **2**[52] deposited on glass that were investigated at 4 K.

The XAS spectra (L_3 edge) normalized to "1" are illustrated in ***Figure 4-3***. Sample **1** shows different spectra at 298 and 80 K illustrating qualitatively the change from the HS to the LS state. The energy shift (ΔE) of the main peak between the HS and the LS spectra is 1.28 eV. The spectrum of the HS spin sample **2** at 4 K is slightly different from that of sample **1** at 298 K showing that the HS species have different spectroscopic responses at high and low temperature. This difference can be qualitatively explained by the thermal population of the low-lying states upon heating up (ground electronic state $^5T_{2g}$ that has a degeneracy of 15) and was confirmed by LFM calculations. The LS species have the same spectra at low and high temperatures because the absence of degeneracy (ground electronic state $^1A_{1g}$). LFM calculations of the LS spectrum at 80 and 4 K confirm that they are temperature independent. The spectra of ***Figure 4-3*** can be used as reference spectra for the three cases high temperature HS species, low temperature HS species and LS species. It is worth noting that the spectrum of the LS species was recorded at 80 K and not 4 K in order to avoid the SOXIESST effect that transforms LS to HS during the measurement. Indeed, at 80 K the relaxation from HS to LS is very fast so the SOXIESST effect can be neglected at this temperature, while it affects the spectrum at 4 K.

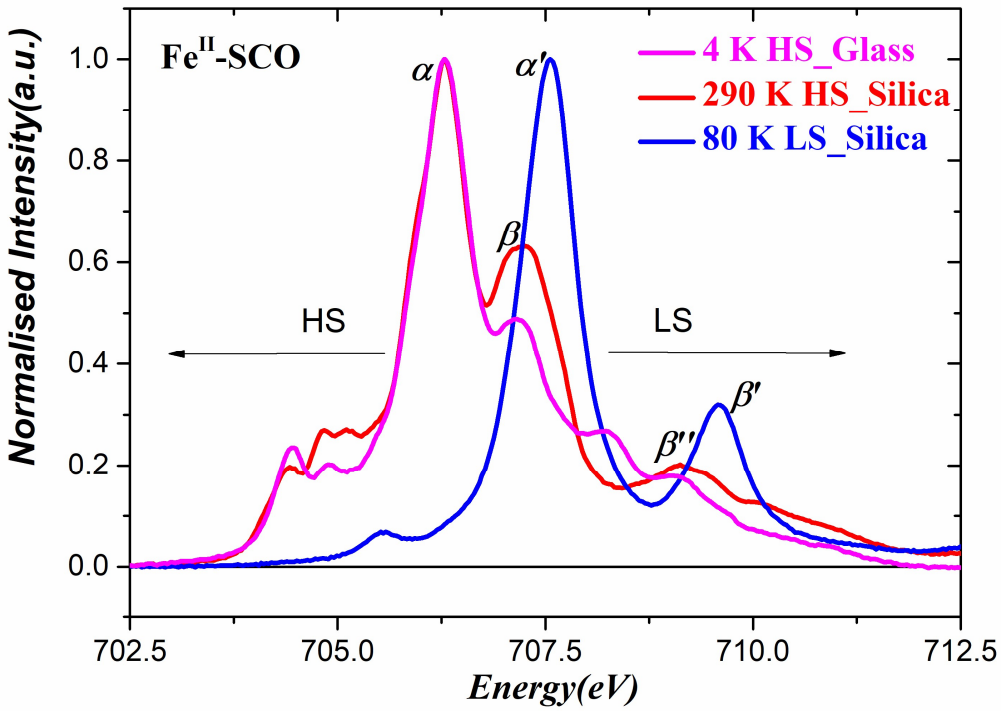

Figure 4-3. *Normalized XAS spectra for pure HS at 4 K (in magenta color), HS at 290 K (in red color) and LS at 80 K (in blue color), experimentally. Note pure HS state at 4 K is obtained from* $Fe^{II}[BH(PhPz)_3]_2$ *molecules deposited on glass substrate as powder while pure HS at 290 K and pure LS at 80 K both are obtained from* $Fe^{II}[HB(3,5\text{-}Me_2Pz)_3]_2$ *deposited on silica (130 nm) annealed in the range of 400 K and 80 K. In the range of 290 K-400 K, molecules (**1**) are in high spin states purely.*

In order to determine the proportion of high spin and low spin species in the samples made of single or submonolayer of SCO molecules, we have fitted the experimental spectra with a linear combination of the experimental spectra of pure HS and LS phases of ***Figure 4-3*** using the methodology developed below.

4.3.2 Calculated Pure HS and LS Spectra

As stated above, experimental pure XAS spectra of HS and LS species were both normalized as "1". However, the absolute intensities of the spectra of the two species are different and it is necessary to have a correct intensity ratio between the HS and LS references that will subsequently be used to fit the proportion of the two species of the spectra of the submonolayer s samples. Due to measurements on different samples in different conditions (temperature, charging effects...), we have decided to calibrate those intensities by using Ligand Field Multiplet (LFM) calculations.[55-59] In order to determine the relative intensities of the HS to LS species that will be used to analyze the experimental spectra, the intensity (integral of the spectrum) of the LS species is set to 1 and that of the HS species at different temperature calculated from LFM calculations.

In general, calculated spectra in the O_h group are carried out by using $10Dq$ = 2.2 eV for the LS spectrum and $10Dq$ = 1 eV for the HS one.[59-61] The pure HS (LS, respectively) XAS spectra simulated varying at different temperatures are shown in **Figure III-1** and **Figure III-2** of the Appendix III.

Thermal dependence of HS states. The spectroscopic term of the ground state of the Fe^{II} ion is ^5D ($2p^6 3d^6$).[62] Accordingly, the spectroscopic terms of the initial HS state in O_h symmetry are $^5T_{2g}$, and ^5E_g corresponding to the following electronic configurations $(t_{2g})^4(e_g)^2$ and $(t_{2g})^3(e_g)^3$ respectively. We assume here that the excited triplet and singlet states are much higher in energy. For the LS state, the ground electronic configuration $(t_{2g})^6(e_g)^0$ leads to the spectroscopic term $^1A_{1g}$; the other excited states are assumed to be high in energy to affect the spectra and are neglected. Spectroscopic data of the HS state in the UV-visible range shows that the ^5E_g excited state is located at energies higher than 1 eV and cannot, thus, be populated at room temperature (300 K or 25 meV). So, only the ground states $^5T_{2g}$ and $^1A_{1g}$ corresponding to the HS and LS species respectively are populated at room temperature. The electronic $^5T_{2g}$ term is degenerate 15 times, while the $^1A_{1g}$ term has a degeneracy of 1. This explains that upon the promotion of an electron form the p to the d orbitals the calculated XAS spectra at the $L_{2,3}$ edges of the LS species have no temperature dependence (**Figure III-1** in Appendix III), while the HS ones depend on temperature (**Figure III-2** in Appendix III).

The integration of the calculated spectra for the different species allows comparing them on one plot as shown in ***Figure 4-4*** and **Figure III-3** of the Appendix III.

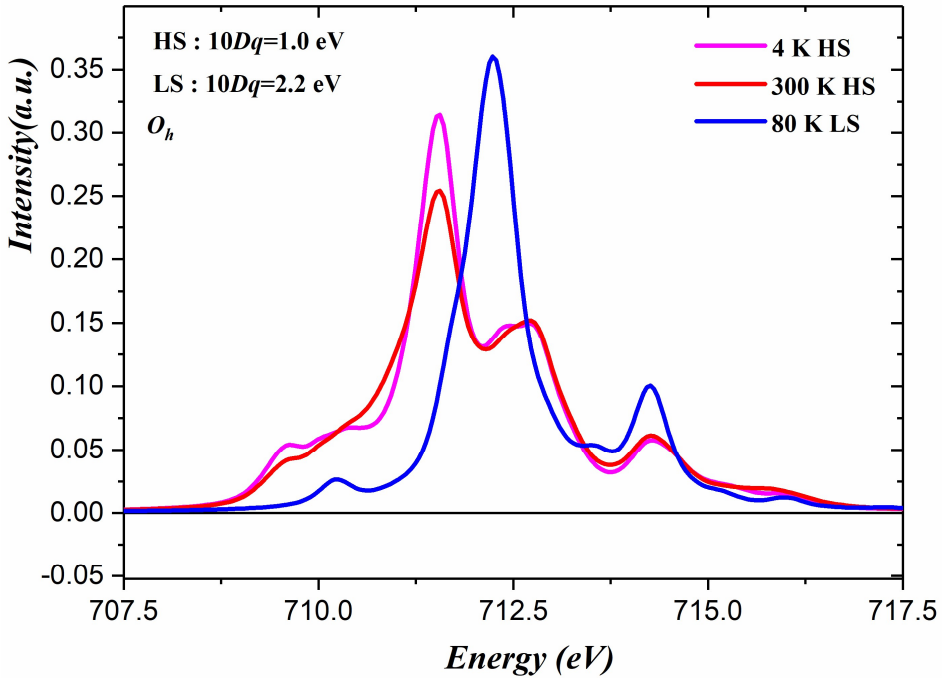

***Figure 4-4**. Normalized X-ray absorption spectra for pure HS at 4 K, HS at 290 K and LS at 80 K as references using LFM calculations. The magenta curve is for HS at 4 K, the red curve is for HS at 300 K, and the blue curve is for LS at 80 K. All calculations are carried out in O_h.*

4.3.3 Normalized Reference Spectra Combined Calculations and Experiments

In order to find the relationship between the ratio of σ_{th}^{HS} to σ_{th}^{LS} for the theoretical and experimental spectra, we introduce a correction factor λ seeing Eq. (4-1).

$$\frac{\int \sigma_{th}^{HS}}{\int \sigma_{th}^{LS}} = \frac{\lambda \cdot \int \sigma_{exp}^{HS}}{\int \sigma_{exp}^{LS}}, \text{ namely, } \frac{A}{B} = \frac{\lambda \cdot C}{D}, \qquad (4-1)$$

with

$$\int \sigma_{th}^{HS} = A \quad \int \sigma_{th}^{LS} = B$$
$$\int \sigma_{exp}^{HS} = C \quad \int \sigma_{exp}^{HS} = D$$

The value of λ is used to calibrate the pure HS spectrum which is initially normalized to "1". The estimation of λ is listed in ***Table 4-1*** (for low temperature: LT) and ***Table 4-2*** (for high temperature: HT). Due to the introduction of λ values, experimental pure HS state spectrum for low and high temperature are calibrated and illustrated in ***Figure 4-5.*** This figure is used to confirm the match between experiments and calculations.

All spectra are in good agreement with the ones of ***Figure 4-4***. We, therefore, use the ratio of the integrals of the HS to LS spectra at low temperature (high temperature, respectively), calculated to be 1.193 (1.167 respectively), to normalize the intensities of the experimental spectra, fixing the ratio of their integrals to the calculated ones. The ratio of integrals $\frac{\sigma^{HS}}{\sigma^{LS}}$ is listed in ***Table 4-3***. The final normalized experimental spectra for Fe^{II} HS and LS at low temperature are shown in ***Figure 4-5.***

Table 4-1. *The comparison of pure HS at low temperature and LS spectra between experiments and LFM calculations.*

	Pure HS	Pure LS
Theoretical Spectra	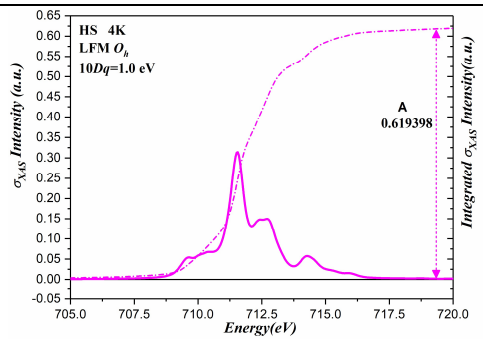	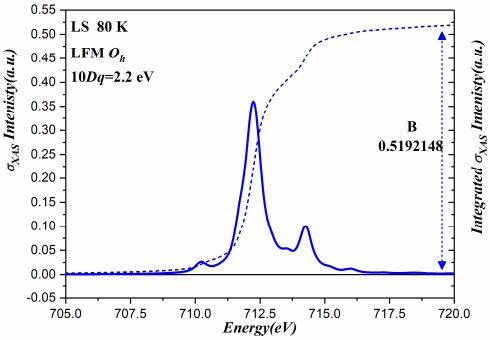
Experimental Spectra	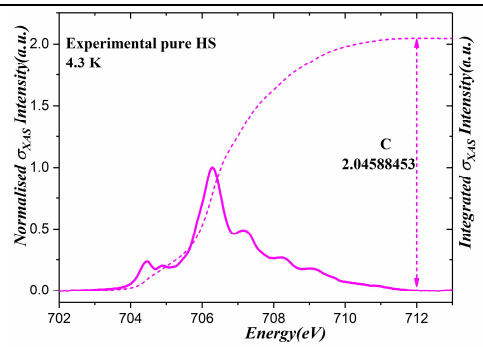	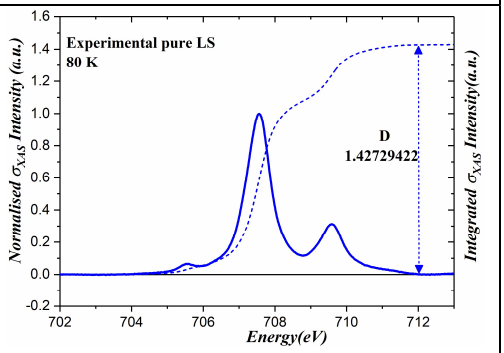
Correction factor	**λ = D · A/(BC) = 0.8318485**	

Table 4-2. *The comparison of pure HS at high temperature and LS spectra between experiments and LFM calculations.*

	Pure HS	Pure LS
Theoretical Spectra	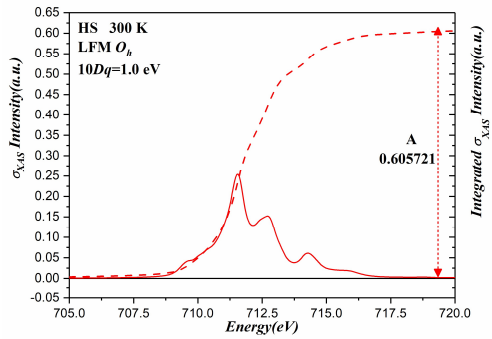	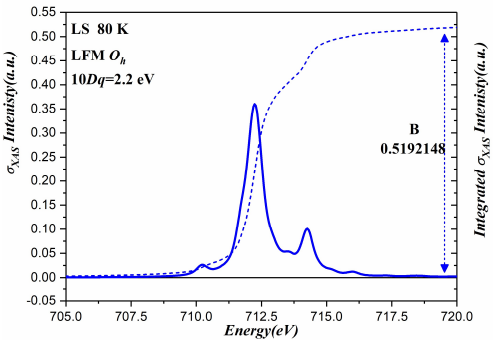
Experimental Spectra	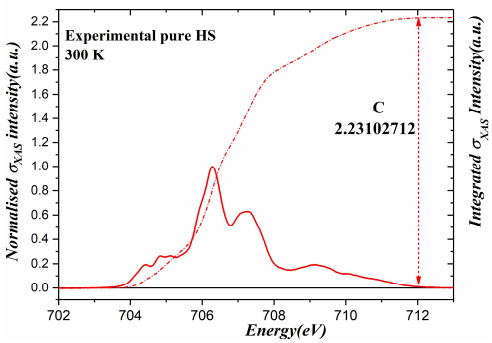	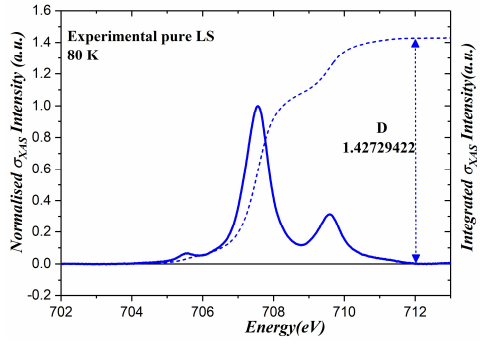
Corrected factor	**λ = D · A/(BC) = 0.7468436**	

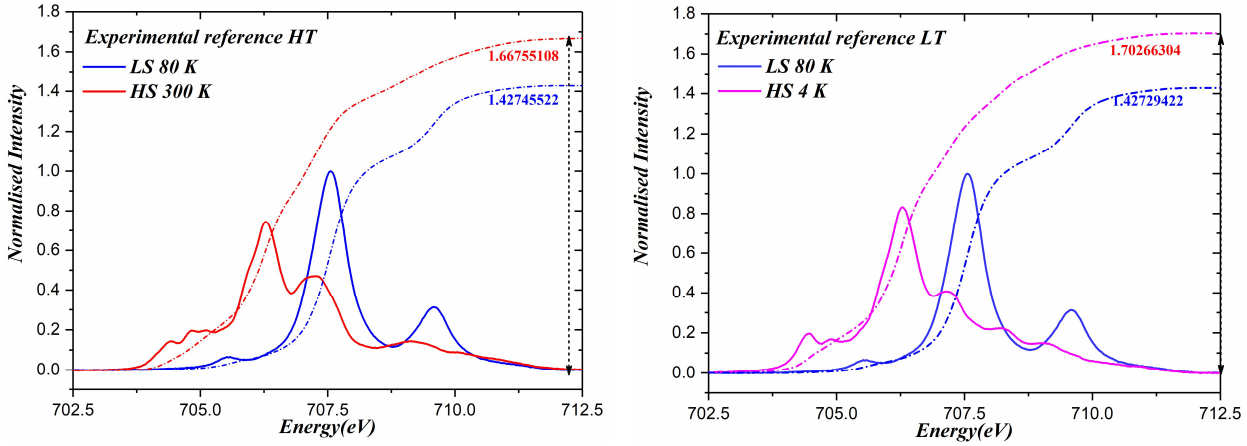

Figure 4-4. *Comparisons between corrected HS spectrum and LS spectrum due to the correction factors.* ***Figure 4-4(left)*** *is for high temperature and* ***Figure 4-4(right)*** *is for low temperature.*

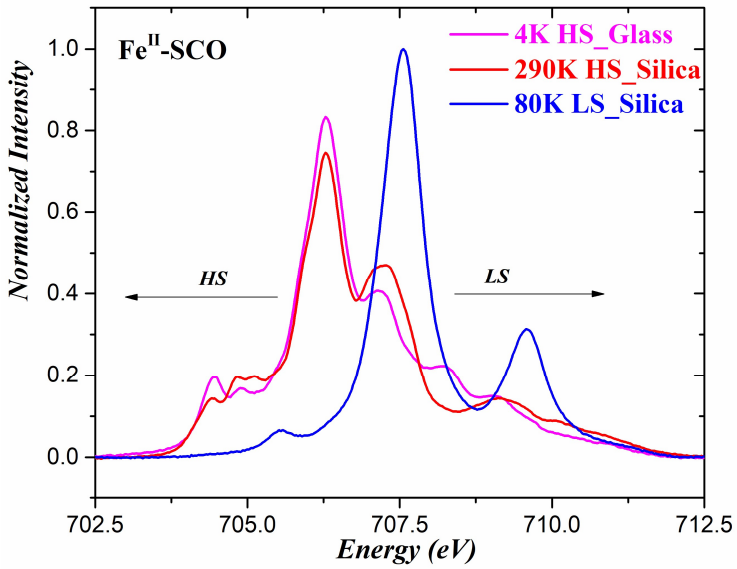

Figure 4-5. *Reference spectra for HS and LS state after using correction factors based on pure XAS spectra obtained from LFM calculations. The relative intensity of the spectra has been determined by LFM calculations of the Fe^{II} HS and LS XAS signal at the L_3 edge.*

Table 4-3*. Ratio values among spectral integrals of HS to LS.*

Parameters	$(\sigma^{HS}/\sigma^{LS})_{theo}$	$(\sigma^{HS}/\sigma^{LS}{}_{exp,corrected}$
HS at 4 K	***1.193***	***1.193***
HS at 300 K	***1.167***	***1.168***

4.3.4 Analysis Method between Reference and Real-time Spectra

The normalized, experimental XAS spectra recorded between 4 K and 290 K can be fitted as linear combinations of reference spectra for HS state and LS state Eq.(4-2). For temperatures between 4 K and 80 K, the HS reference spectrum is the one recorded at 4 K. For temperatures between 80 K and 300 K, it is the one recorded at 290 K. From Eq. (4-3), it is possible to extract the HS vs LS contributions, i.e. the coefficients α^{HS} and β^{LS}. Eq. (4-4) is a simple, direct equation derived from the definitions Eq.(4-3).

$$\sigma^{T}_{norm=1} = \sigma^{HS}_{norm=N} \cdot a^{HS} + \sigma^{LS}_{norm=1} \cdot b^{LS} \qquad (4-2)$$

$$\alpha^{HS} = \frac{a^{HS}}{a^{HS}+b^{LS}}; \quad \beta^{LS} = \frac{b^{LS}}{a^{HS}+b^{LS}} \qquad (4-3)$$

$$\alpha^{HS} + \beta^{LS} = 1 \qquad (4-4)$$

Note that it is somewhat complicated to obtain α^{HS} and β^{LS}, since backgrounds and baselines for all raw spectra can be quite different with temperature. In ***Figure 4-5***, the final calibrated reference spectra for HS (4 K and 298 K) and LS (80 K) are shown. The LS spectrum has been arbitrarily normalized to "1" and the HS spectra have been normalized so that the sum rule for the number of holes is fully satisfied for the three spectra and where the radial integrals extracted from LFM calculations have also been considered. From spectra of ***Figure 4-5***, the theoretical spectra for various HS/LS ratio are reported in ***Figure 4-6***.

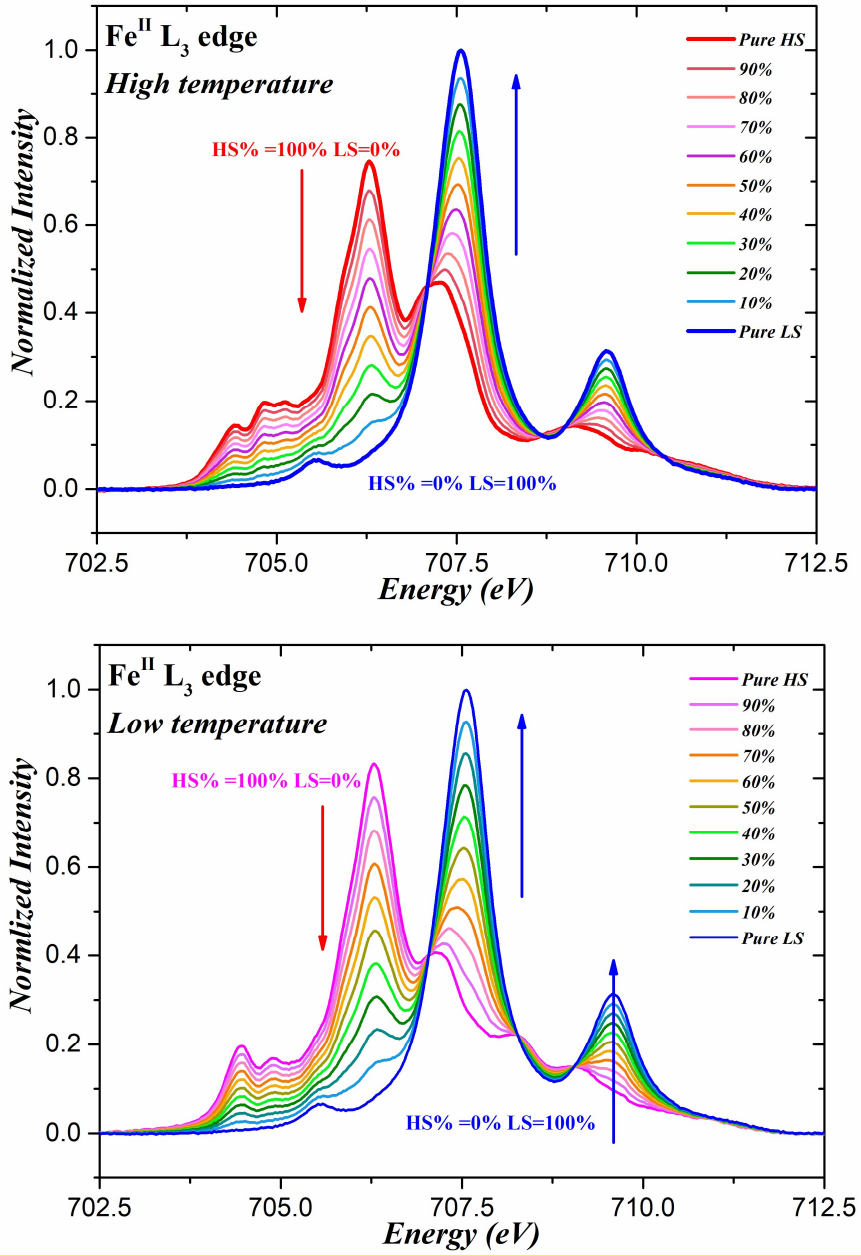

Figure 4-6. *Theoretical XAS spectra simulated as linear combination HS and LS reference spectra for low temperature (T < 80 K, lower panel) and high temperature (T > 80 K, upper panel). Inset values are for HS fraction.*

4.4 Definition of the Thickness of Different Samples

For samples Fe^{II}-SCO@Cu and Fe^{II}-SCO@Au, the molecular coverage of **1** have both been directly measured with scanning tunneling microscopy (STM) and by the comparison with the jump at the edge of a sample of Fe^{II}SCO@Ag. STM images for Fe^{II}-SCO@Cu and Fe^{II}-SCO@Au are shown in ***Figure 4-7***, while the related spectra of these three samples are displayed in ***Figure 4-8***.

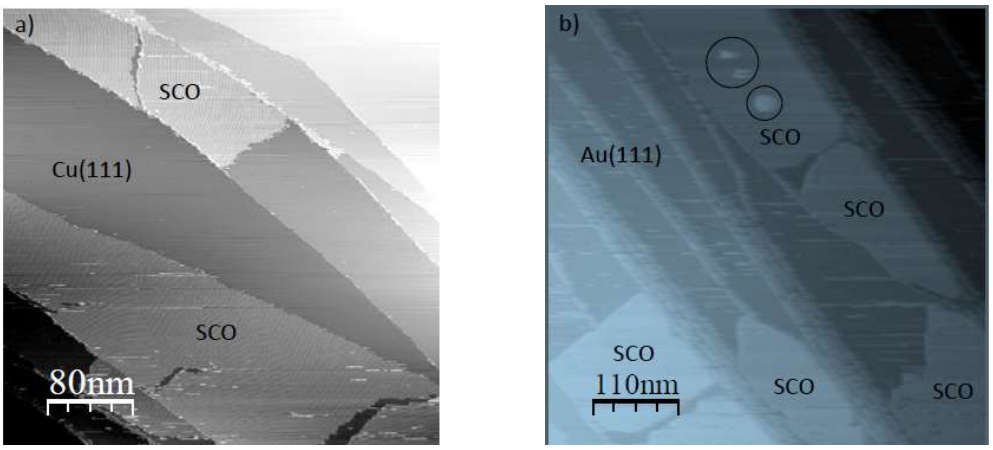

Figure 4-7*. STM images of the samples measured in the main text.* ***a)*** *0.4±0.1 ML of* ***(1)*** *on Cu(111): 400×400 nm², T=200 K, I=100 pA, V=-1.5 V.* ***b)*** *0.5±0.1 ML of* ***(1)*** *on Au(111): 530×530 nm², T=4.7 K, I=50 pA, V=-2 V. Black circles underline small islands of a second molecular layer.*

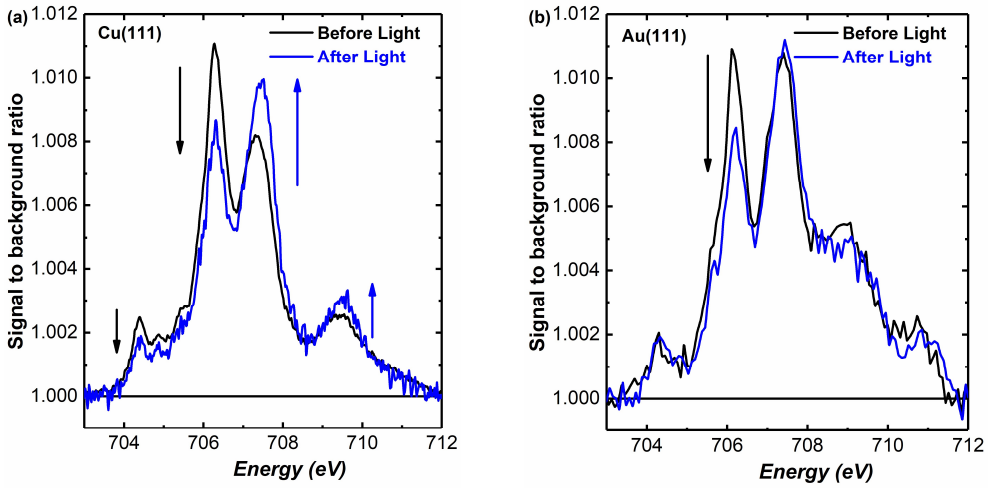

Figure 4-8*. X-ray absorption spectra of the Fe^{II} L_3 edge before and after illumination of the sample with a blue light at 405 nm for around 20 minutes for 0.4 ±0.1 ML of (1) on Cu(111: average over 11 spectra before light and 10 spectra after light in steady state conditions (**Figure 4-8a**) and 0.5 ±0.1 ML of (1) on Au(111): average over 6 spectra before light and 13 spectra after light in steady state conditions (**Figure 4-8b**). All the spectra have been recorded at a temperature around 4 K. A linear background has been removed and the spectra have been normalized to the background value at 706.4 eV. The jump at the L_3 edge can therefore be read as a percentage of the background signal.*

Figure 4-7a) corresponds to ***Figure 4-8a)***, and ***Figure 4-7b)*** to ***Figure 4-8b)***. Islands of a densely packed single molecular layer are clearly visible in both STM images. On Au(111), a small regions with two layers can be observed (black circles). The coverage of (**1**) has been determined from a statistical analysis of 8 images on Cu(111) and 8 images on Au(111) recorded at different places, the

error bar giving the standard deviation of the average value.

The estimation of the coverage of **(1)** on Cu(111) and Au(111) is done by the analysis of several large scale (typically 1 mm) STM images. The uncertainty reflects the coverage fluctuations from image to image. The corresponding XAS is measured at room temperature after the sample is transferred from STM chambers to the beamline. For all the samples, the XAS spectroscopy is performed with circularly polarized X-ray with an energy resolution of 150 meV. The total incoming photon flux on the different samples is typically 108 photons.s^{-1}.mm^{-2}. The samples are placed with the X-ray incident direction at 45° to the surface normal for purpose of light exposure through a window perpendicular to the incoming X-rays. A total electron yield mode (drain current measurement) is used to detect the Fe^{II} L_2 and L_3 edges. The calibration of the energy scale has been done by measuring the L_3 edge of a freshly prepared Co film. The STM measurements are performed on commercial Omicron STM setups, either at 4.3 K or at variable temperatures. Illuminations of blue and red lights are produced by laser diodes with wavelengths of 405 nm and 635 nm, respectively. An *ex-situ* measurement of the fluences gives an estimate of 0.5 mW.cm^{-2} for both wavelengths. The anomalous light transition from HS to LS under blue light illumination (see below) has been reproduced on four samples on different Au(111) substrates and on two samples on different Cu(111) substrates, all in the submonolayer range. Interestingly, we have found that the light effect of submonolayer **(1)** on Au(111) is different from the effect arising from thicker layers **(1)** on same metallic substrates.

For Cu(111), we have found a jump at the edge of 7.7% for the unknown coverage, whereas we have measured a jump of 5.2% for the sample measured with STM to be 0.4±0.1 ML. We can, therefore, deduce that the coverage is 0.6±0.15 ML. We have calculated, using the X-ray database of the Center for X-ray optics of the Lawrence Berkeley Laboratory, the absorption of 10 nm thick Cu and Au at 706.4 eV, in order to have an estimation of the relative total electron yield backgrounds. We find respectively 2.8% and 15.8%. The jumps at the edge on different samples have, therefore, to be normalized by those absorption values for a proper calibration. We can test this procedure on the previously STM calibrated Cu(111) and Au(111) samples. On Cu(111), 5.2% of jump corresponds to 0.4±0.1 ML (***Figure 4-8a***). On Au(111), we measure a jump of 1.1%, that leads to $1.1 \bullet \frac{0.158}{0.028} = 6.2\%$ when normalized to the Cu background, giving finally a coverage 0.5±0.1 ML, in perfect agreement with the STM determination (***Figure 4-8b***).

4.5 Results

Here we investigate two samples that have been prepared and measured by STM and XAS:

-- $Fe^{II}[(3,5\text{-}(CH_3)_2Pz)_3BH]_2$ molecules on Cu(111), noted Fe^{II}-SCO@Cu

-- $Fe^{II}[(3,5\text{-}(CH_3)_2Pz)_3BH]_2$ molecules on Au(111), noted Fe^{II}-SCO@Au

4.5.1 Fe^{II}-SCO@Cu

First of all, XAS spectra have been measured at 4 K, 80 K and 300 K (***Figure 4-9***).

In order to check whether the sample has evolved upon X-ray irradiation during a series of measurements, one measurement on a virgin spot was systematically carried out at the end of a given series. This methodology showed that no detectable evolution (decomposition) of the samples occurs. Another important point is the effect of X-rays on the low spin to high spin transformation called SOXIESST.[17, 18, 63] This is similar to LIESST and corresponds to the transformation of low spin species to high spin ones. We checked that SOXIESST is active only at low temperature, decreases upon heating up and disappears above 80 K.

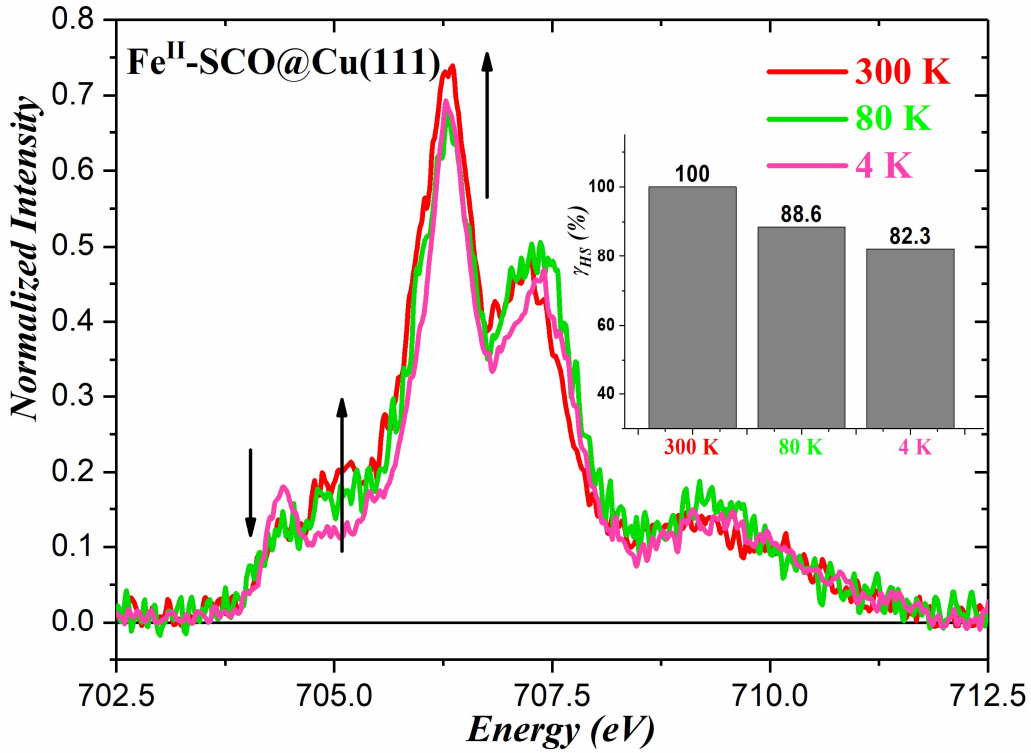

Figure 4-9. *Normalized experimental XAS spectra at virgin spots for $Fe^{II}[(3,5\text{-}(CH_3)_2Pz)_3BH]_2$ molecules on Cu(111) at 4 K, 80 K and 300 K.*

4.5.1.1 Thermal Dependence of the Fe^{II}-SCO Molecules on Cu(111)

We first studied the effect of temperature on the spin crossover phenomenon by performing spectra in the 280 - 4 K range, first in the cooling and then in the heating mode as shown in ***Figure 4-10***. In the cooling mode, one observes an increase of the intensity of the band around 707 eV accompanied by slight shift towards high energy and a decrease of the band at 706 eV (***Figure 4-10a***). The opposite behavior is observed in the heating mode from 4 to 293 K (***Figure 4-10b***).

The analysis of these spectra using the methodology presented in the previous section allowed the determination of the HS fraction at each temperature. The variation of the HS fraction is plotted as a function of temperature for the two series of experiments (***Figure 4-11***).

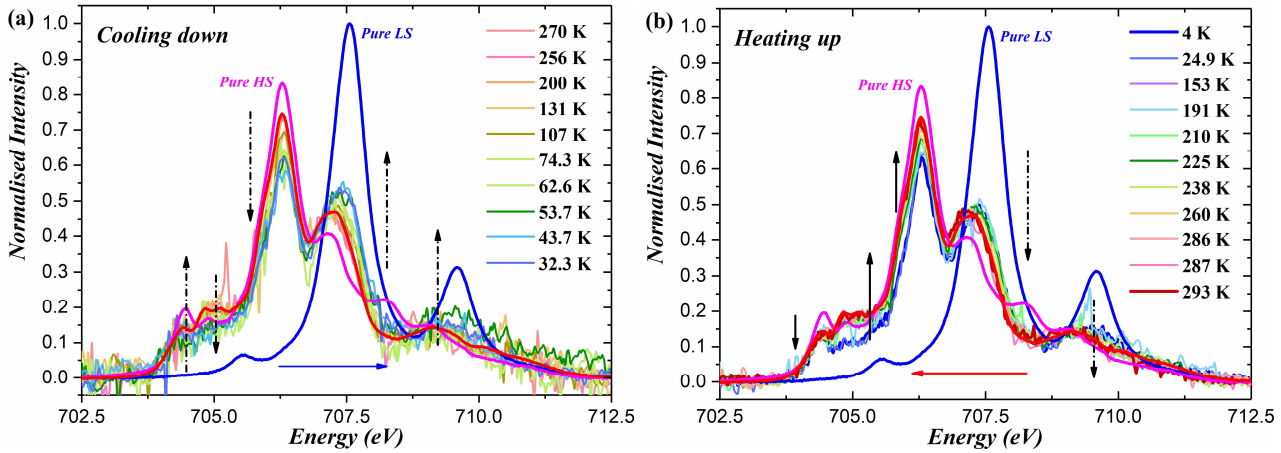

Figure 4-10. *Evolutions of the XAS spectra in the cooling (**a**) and heating (**b**) modes in the 293 – 4 K temperature range; the spectra in blue corresponds to the pure low spin species taken as a reference.*

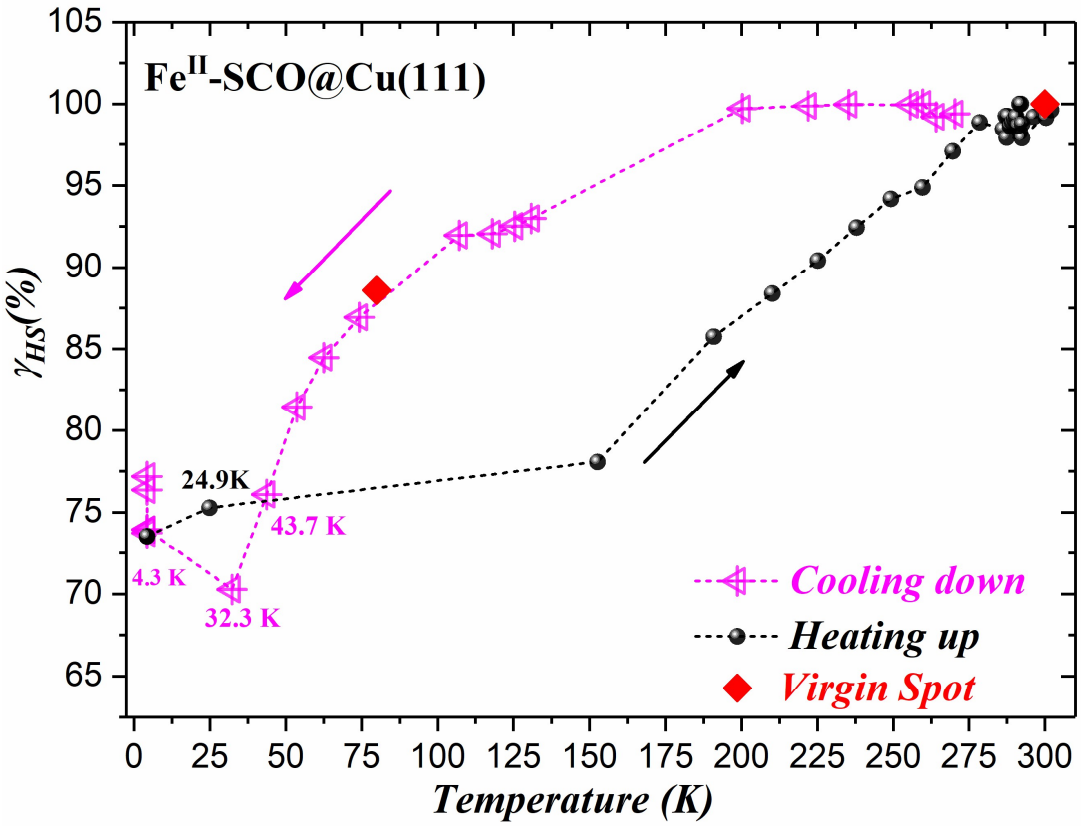

Figure 4-11. *Thermal variation of the HS fraction upon a cooling-heating process; the full rhombus red dots correspond to a spectrum measured at a different location of the sample.*

At high temperature, molecules forming the submonolayer are all in the HS state. Upon cooling, a spin crossover occurs; the fraction of HS species reaches a value of 70 % at T = 32.3 K. In order to check whether the sample suffered from exposition to X-ray when acquiring the spectra between 300 and 80 K, a spectrum was recorded on another region of the sample (red diamond at T = 80 K in F***igure 4-11***) that gives the same HS fraction which demonstrates the integrity of the molecules. Cooling from T = 32.3 to 4 K leads to a slight increase of the HS spin fraction, while one would expect a decrease upon additional crossover from HS to LS. This increase of the HS spin fraction is due to SOXIESST that leads to an increase of the HS fraction.

4.5.1.2 Thermal Dependence in the Presence of Blue Light for Fe^{II}-SCO@Cu

In order to investigate the effect of blue light on the spin crossover of the submonolayer, we performed a series of experiments consisting in shining the sample by blue light (λ = 405 nm) and measuring while heating from 4 to 300 K (***Figure 4-12***).

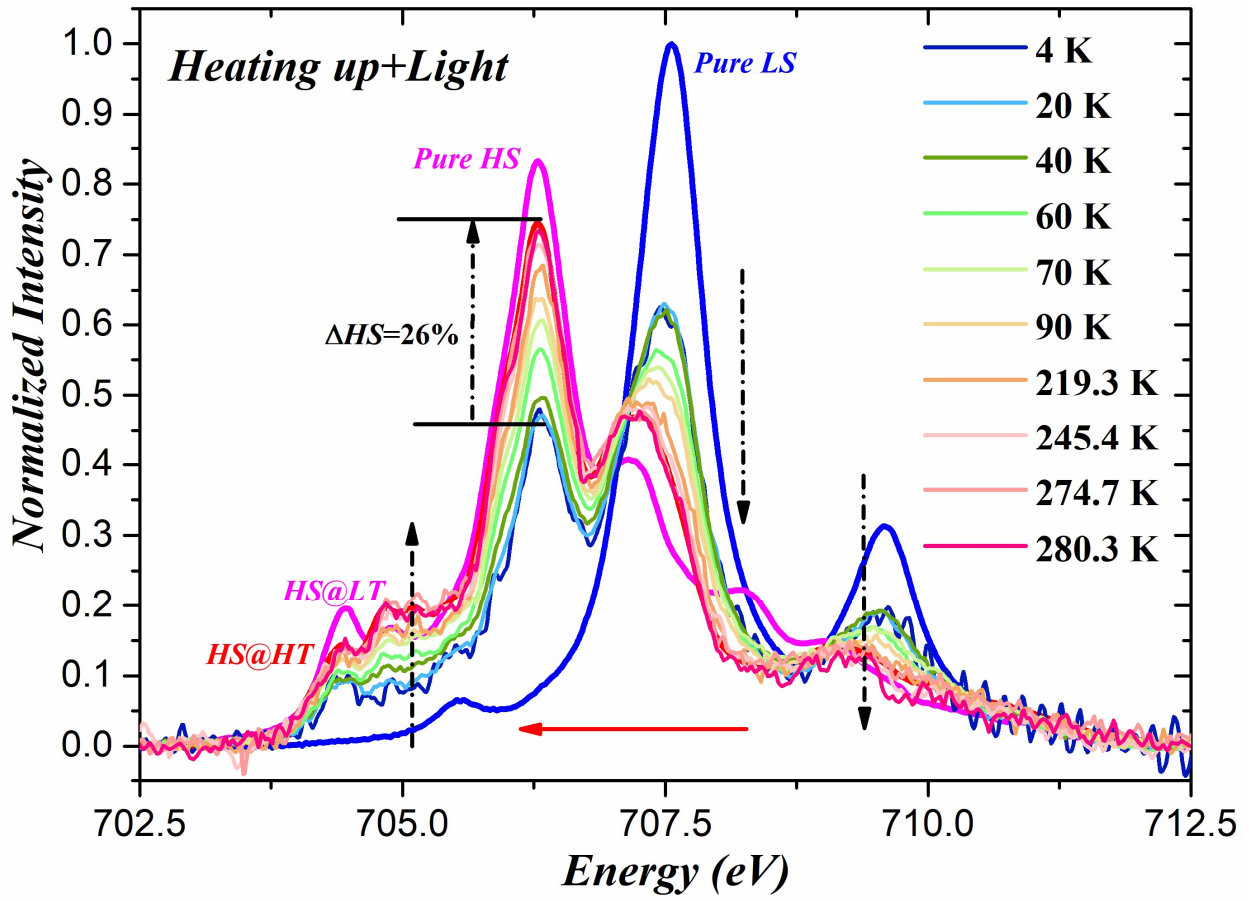

Figure 4-12. *XAS spectra from 4 to 280 K under irradiation by blue light; the blue and the magenta traces correspond to the reference LS and HS species for comparison.*

The sample is at 4 K after having been cooled down from room temperature and the fraction at HS species is 73 %. We recorded several spectra at 4 K and observed a slight increase in the HS fraction to 78 % corresponding to SOXIESST. It, therefore, worth noting that even though SOXIESST is present at T = 4 K, its effect is not too large since the HS fraction increases from 73 to 78%. Then the sample was illuminated by blue light for few minutes and a measurement was carried out that shows a decrease of the HS fraction from 78 to around 50 % (***Figures 4-12*** and ***4-13***).

This corresponds to a transformation of about 33 % of the HS species to low spin. This is a reverse LIESST (r-LIESST) effect because it transforms HS species to LS ones. Reverse-LIESST is well known and documented,[16, 19] but it usually occurs when shinning in the far infra-red region because the energy separation between the electronic states of the HS species are lower than those of the LS ones. More importantly, in order to observe any effect due to light illumination, the species must absorb within the specific wavelength region of the light applied. In the present case, the high spin

species have no absorption at all in the whole visible region or any region close to blue light. One may, therefore, tentatively conclude that this effect is not the classical r-LIESST and may be due to the substrate (see the discussion section below). After applying the blue light at T = 4.3 K, the sample was heated-up under continuous blue light irradiation until T = 90 K. The HS fraction increases from 50 to around 80 %. Further heating-up to room temperature restores the 100 % HS species. This perfectly reversible process is a strong indication of the perfect integrity of the molecules upon exposure to X-rays and light during the heating process.

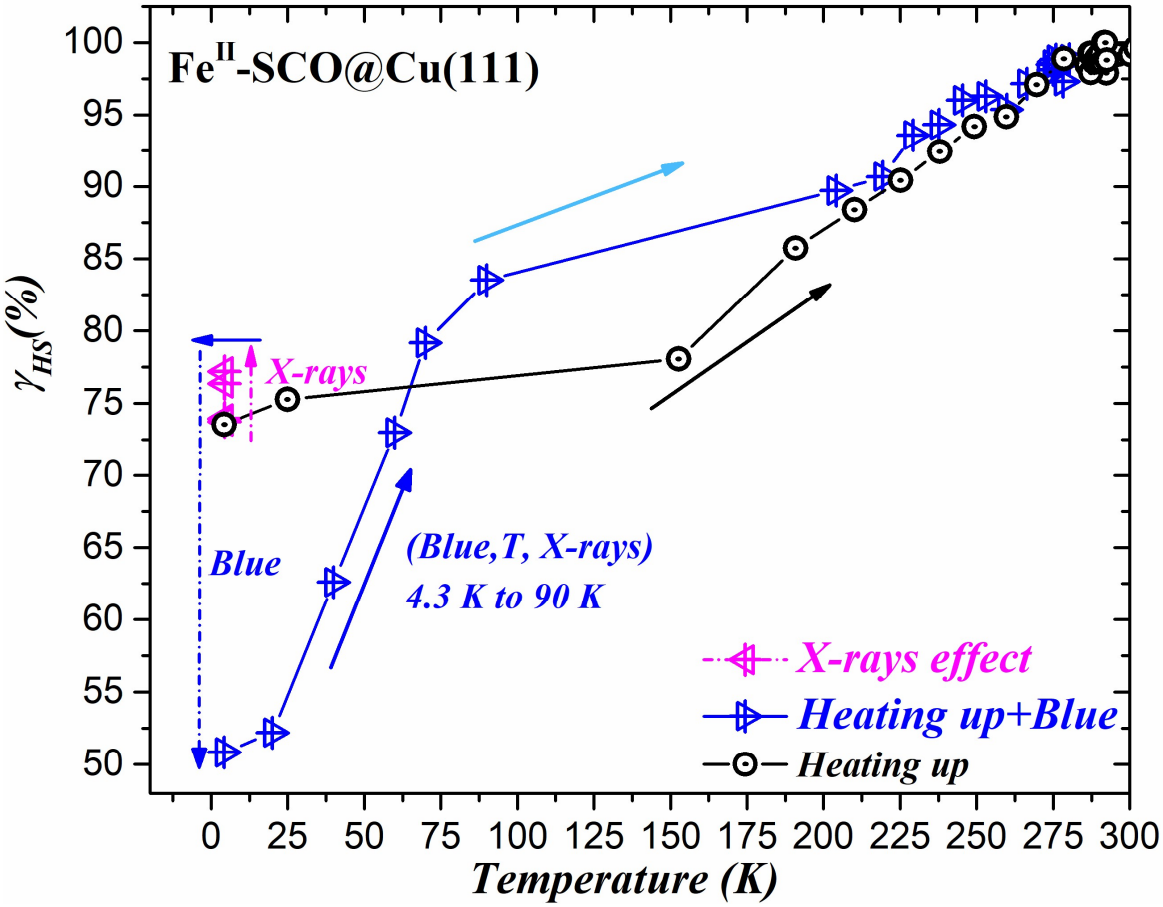

Figure 4-13. *Thermal variation of the HS fraction upon heating while illuminating the sample by blue light (blue triangles) and without light (black dots); the magenta triangles correspond to XAS spectra measured before illumination by blue light and are due to SOXIESST.*

The comparison of the blue and black curves (***Figure 4-13***) both measured in the heating mode with and without the presence of blue light shows a larger fraction of HS species above 70 K when the sample is illuminated. While, since blue light seems to favor the LS species, one may expect a better stabilization of the LS spin species. STM observation of the submonolayer shows that light affects the organization of the molecules in the islands of the submonolayer s (not shown here). The decrease of the organization of the molecules may highly affect the long-range interaction that is usually responsible of a "delay" of the transition temperature (hysteresis cycle) and favors the HS state at lower temperatures than if elastic interactions still operate.

4.5.1.3 Time Dependence of Blue Light and X-ray Effect on Fe^{II}-SCO@Cu at 4 K

In order to investigate the time dependence of X-rays that were shown to induce SOXIESST (LS to HS) at low temperature and blue light that has the reverse effect, we performed a series of 5 sequences of XAS measurements at T = 4 K. The sequences are the following: 1) a first scan is carried then blue light is applied, then 2) blue light is switched off, then 3) blue light is switched on again and a series of XAS spectra recorded at given time intervals, then 4) blue light is switched off and finally 5) red light is switched on. A series of XAS spectra recorded at given time intervals after the beginning of each sequence. It worth noting that when light is switched off as in sequence 2), the XAS spectra will measure the effect of X-rays. ***Figure 4-14***, top depicts the XAS spectra of sequences 1), 3) and 5). The three spectra present at the bottom of the Figure correspond to sequence 1); the red trace being the spectrum at t = 0, the green after 74 s (that corresponds to a single scan) and the blue at the end of sequence. The other two sets of three spectra follow the same order. ***Figure 4-14***, bottom corresponds to the HS spin fraction extracted from the XAS spectra during the time evolution from sequence 1 to 5.

•At t = 0 (beginning of sequence 1), the HS fraction is equal to 78% and after shining blue light for 74 s it is reduced to 65 %. At t = 13.4 minutes, the fraction of HS species reaches about 55%; shining for another 20.4 minutes and recording several spectra do not lead to additional decrease of the HS fraction. One observes from ***Figure 4-14***, bottom that shining blue light for around 10 minutes without recording a XAS spectrum leads to HS fraction of 50%. The 55% value obtained here is probably the result of the opposite effects of blue light and X-rays. One notices, though, that blue light is more efficient than X-rays at T = 4 K.

•At t = 30.8 min (beginning of sequence 2), blue light is switched off and XAS spectra are recorded; they show an increase of the HS fraction, as expected, that saturates at t = 100 min with a value of 73 % lower than the starting value before the beginning of sequence 1. The process is, therefore, not strictly reversible, about 5 % of the HS species remain in the LS state. Because of the moderate quality of the spectra that correspond to a single scan (and not to an accumulation of 16 scans) in order to minimize the effect of X-rays, the apparent lack of reversibility may be due to errors in determining the HS fraction.

•At t = 138.1 min (beginning of sequence 3), the blue light is switched on again leading to the expected HS to LS transformation. The HS fraction reaches to a saturation around 58% after 6-minute illumination of blue light.

•At t = 171.6 min (beginning of sequence 4), blue light is switched off and X-rays restore the HS spin fraction of 73% obtained at the end of sequence 2).

•At t = 278.5 min (beginning of sequence 5), red light (625 nm) is switched on and spectra are recorded every 74 s. One observes (***Figure 4-14***, **bottom**) a slight decrease of the HS fraction from 73 to 69% after 100 minutes of irradiation indicating the presence of a reverse LIESST effect albeit with weaker intensity than that of the blue light. The effective change in the HS spin fraction is larger than 4% because the opposite effect SOXIESST.

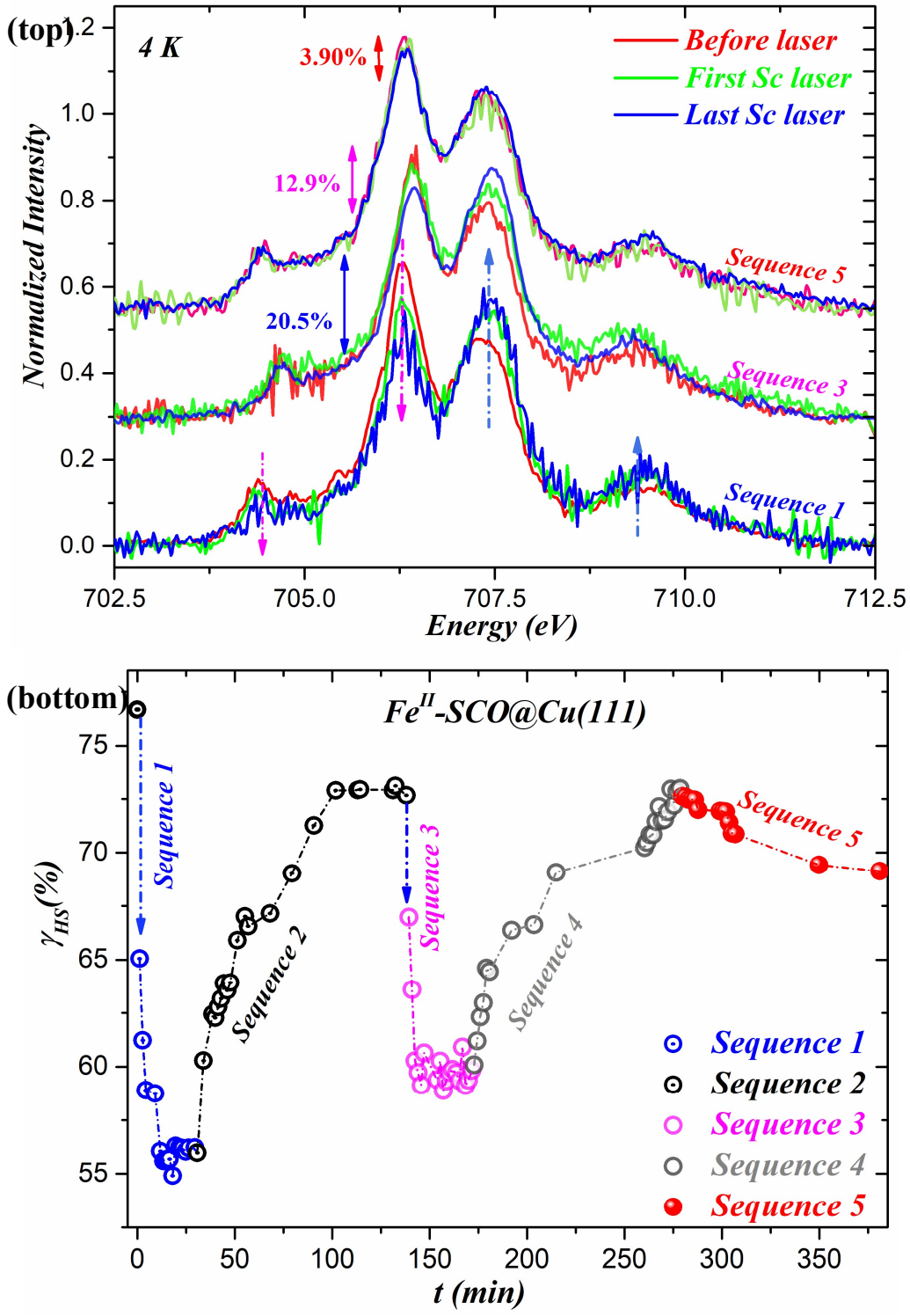

Figure 4-14. *(**top**) XAS spectra corresponding to the irradiation with blue (sequences 1 and 3) and red (sequence 5) light; the set of three spectra correspond to the beginning of the sequence (red traces), the first scan (green traces) and the end of the sequence (blue traces), and (**bottom**) fraction of HS species as a function of time during the 5 sequences (see text for the detail of each sequence).*

4.5.1.4 Scanning Tunneling Microscopy (STM) Observation of Light Effect

A small portion of the submonolayer (30 x 30 nm^2) containing an island of molecules in the HS state surrounded by LS molecules was illuminated with blue light and observed by STM as shown in ***Figure 4-15***, **top**. The STM image confirms the reverse LIESST observation made by XAS study. The same experiment was also performed on another sample using red light and the same effect is observed (***Figure 4-15***, **bottom**).

The STM study shows that red light effect is as efficient as blue light while XAS study suggested that red light has less effect. This may be due to SOXIESST that is not quantitatively the same in the two experiments corresponding to sequences 3) and 5) shown in ***Figure 4-14***, **bottom**.

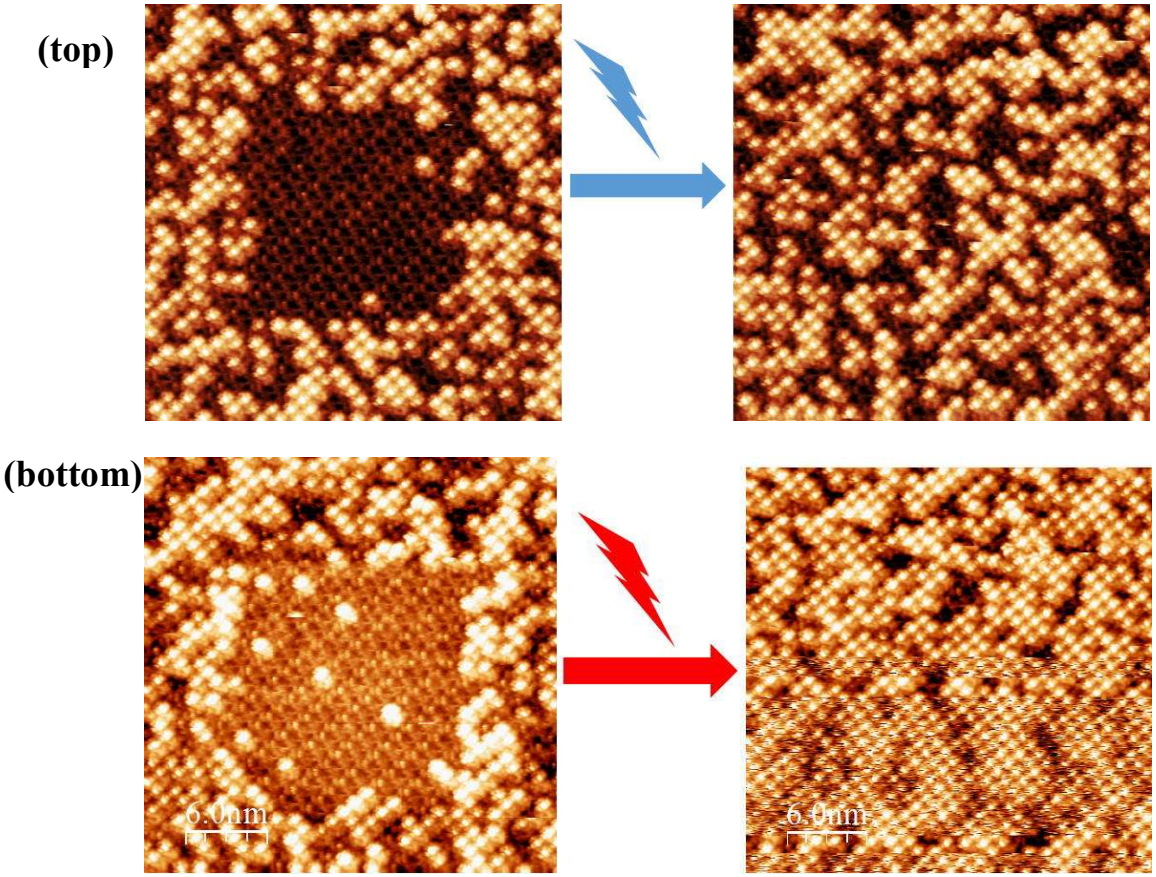

Figure 4-15*. STM images for Fe^{II}-SCO@Cu measured at 4 K under the continuous illumination of blue (**top**) and red (**bottom**) laser. The size of each image is 30.00 x 30.00 nm^2, tunneling voltage is 0.30 V and the tunneling current is 20.00 pA. STM measurements without the tip effect observed with blue light is shown in **Figure III-4** in Appendix III.*

We can conclude that upon cooling from room temperature, where all the molecules are in the HS spin state, 33% are converted to LS at T = 32 K leading to a residual HS fraction of 70%. Then, further cooling down to 4 K increases the HS fraction to around 78% due the SOXIESST effect. Illuminating the sample by blue light at T = 4 K, induces a crossover from HS to LS leading to a residual HS fraction of 50%, and, therefore, 50% of LS species which is the maximum LS fraction that can be obtained at T = 4 K. Part of the LS spin species can be converted to HS by X-rays at

T = 4 K and the reverse transformation can be carried out by blue (or red) light. We, therefore, have a system where it is possible to go between two states using blue (or red) light and X-rays as depicted in ***Figure 4-16***.

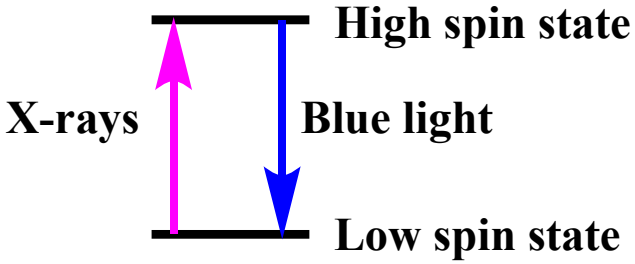

Figure 4-16. *Scheme of the spin crossover with blue and X-rays photons at T = 4 K.*

4.5.2 Fe^{II}-SCO@Au(111)

4.5.2.1 Thermal and Blue Light effect on Fe^{II}-SCO@Au(111)

The submonolayer of SCO molecules on Au(111) was determined to be 0.5±0.1 ML. the general behavior of the SCO on gold is similar to that observed on copper. The XAS spectra carried out at 300 and 80 K are depicted in ***Figure 4-17***.

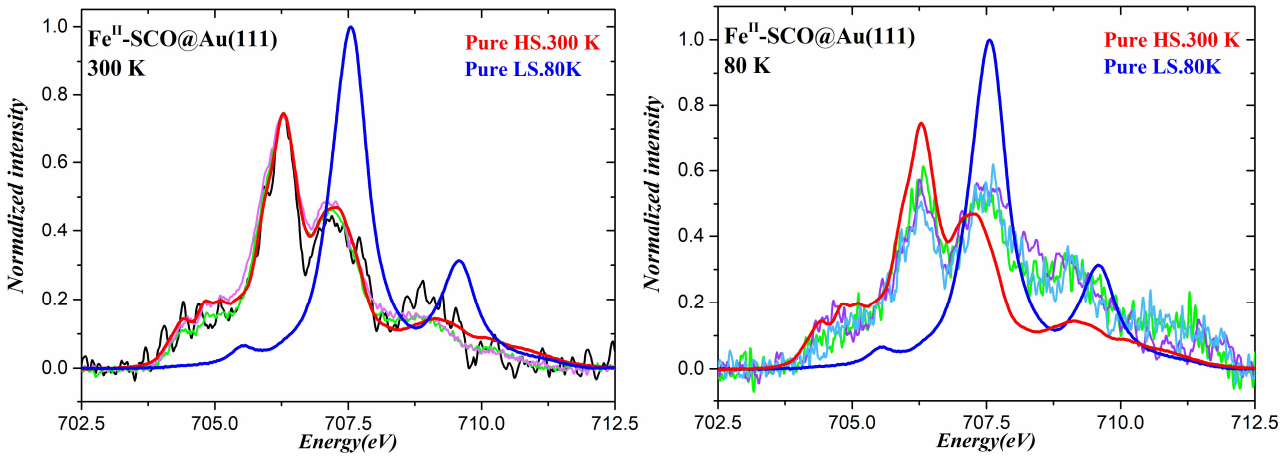

Figure 4-17. ***(left)*** *experimental XAS spectra of Fe^{II}-SCO@Au at T = 300 K and the simulated high temperature HS spectrum (red trace) showing that the experimental spectra are due to pure HS state, and* ***(right)*** *experimental XAS spectra of Fe^{II}-SCO@Au at T = 80 K, the simulated high temperature HS spectrum (red trace) and the simulated LS spectrum (blue trace) showing that the experimental spectra are due to a mixture of the two spin states.*

The analysis of the data shows that a 100% HS fraction at T = 300 K converted to around 80% at T = 80 K is similar to the case of the copper substrate. In order to check the integrity of the molecules, three series of spectra were performed at T = 300 K that give 100% HS fraction within 2% variation (***Figure 4-18***). At T = 80 K, a series of XAS spectra was carried out at a different region of the sample (in order to exclude any degradation coming from X-rays), it shows a residual 81% of HS species (***Figure 4-18***). Then, two other series of measurements were carried out at the same temperature (80 K) but on another region of the sample where 79.2 and 80.7% residual HS fraction were obtained

(***Figure 4-18***). These studies confirm that 20% of the HS species were converted upon cooling down from 300 to 80 K.

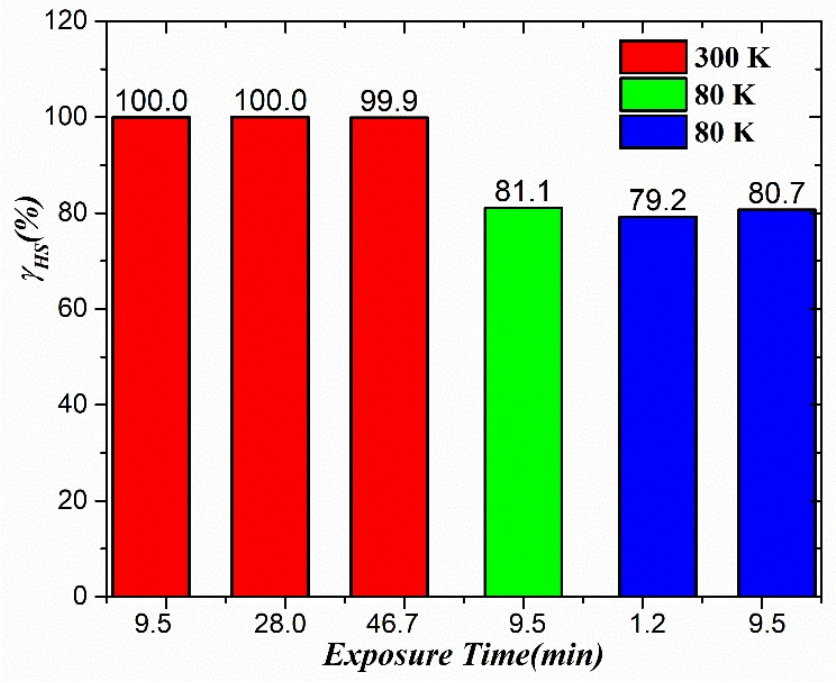

Figure 4-18. *HS spin fraction at T = 300 and 80 K; the green and blue traces correspond to spectra recorded on two different regions of the sample on Au(111).*

The sample was, then, cooled down to 4 K; the XAS data show a residual HS fraction of 58% (***Figure 4-19***). The data presented in ***Figure 4-19*** are not the experimental ones because they are too noisy; they correspond to a fit of the experimental ones with given fraction of HS and LS species.

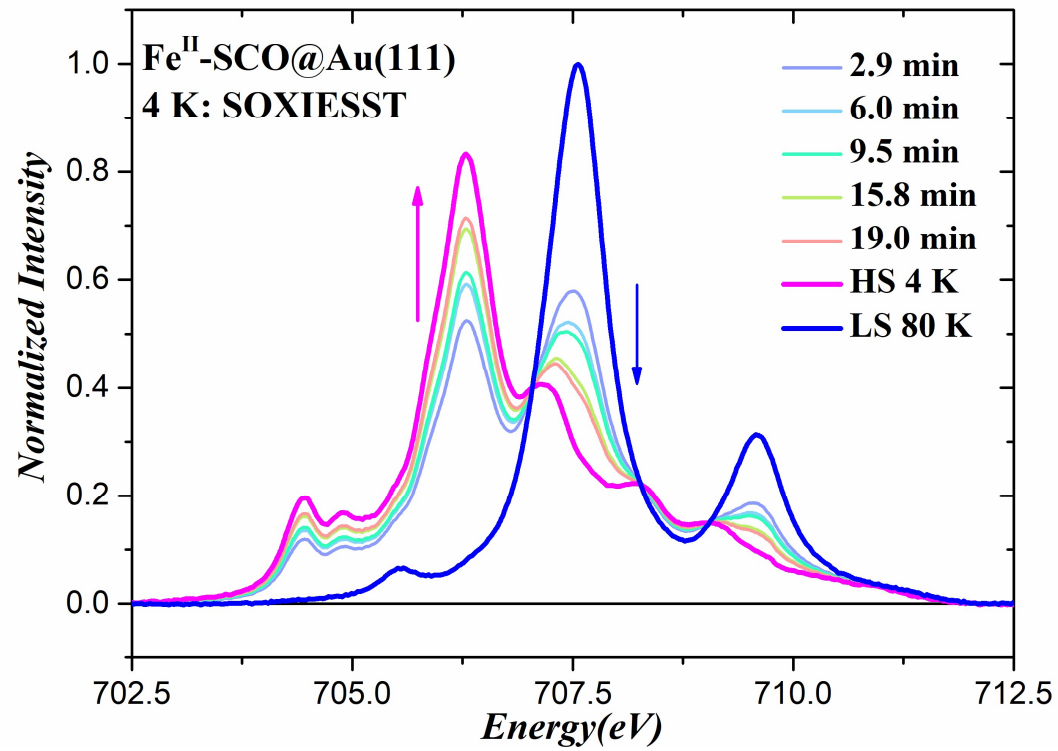

Figure 4-19. *Fits of the experimental XAS spectra recorded at T = 4 K at different time intervals, the blue and magenta traces correspond to the pure LS spectrum at 80 K and the pure HS one at 4K, respectively.*

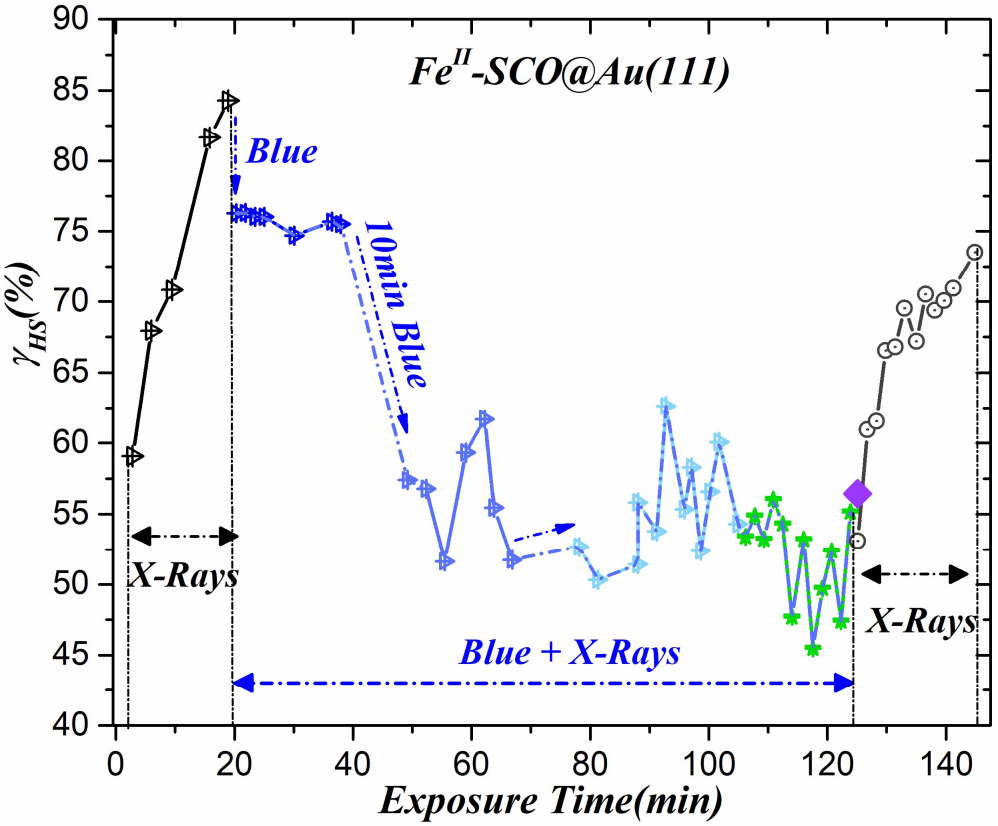

***Figure 4-20**. HS fraction as a function of exposure time when X-rays is on without blue light (black trace), when blue is on (blue trace) and then when blue light is switched off (grey trace). The whole dynamic process under the illumination of X-ray and blue light and the XAS evolution spectra are shown in **Figure III-5**, **6** and **7** in Appendix III.*

At 4 K, the SOXIESST effect was measured with 20 minutes X-rays resulting in an increase of the HS fraction from 58 to 85% (***Figures 4-19*** and ***4-20***). It is worth noting that SOXIESST seems to have a larger effect here than on Cu(111). The effect of blue light was also measured in a similar manner as for the Cu(111) sample and shows a similar behavior as summarized in ***Figure 4-20***. After 125 minutes of blue light irradiation, the light was switched off and a series of XAS spectra recorded. One observes the expected conversion from LS to HS; the HS fraction reaching around 75% less that the starting value (85%) before blue light irradiation. One can conclude that, on Au(111), blue light has the same effect as on copper but with weaker effective. Since the effect of SOXIESST seems to be larger. One may conclude that the real magnitude of the effect of blue light on Au(111) may not be weaker than that on Cu(111). The comparison of kinetic dynamics of blue light and red light both are illustrated in **Figure III-8** of Appendix III, in which it reveals the exponential fit for the HS fraction *vs* exposure time based on the real values (α^{HS} and β^{LS}) obtained from the linear fits.

4.5.2.2 Time Dependence of Blue Light on Fe^{II}-SCO@Au at 20 K

The time dependence of blue light and SOXIESST was also examined at T = 20 K. the results are similar to the behavior at T = 4 K but with different values for the HS fractions that can be due to a less efficient SOXIESST effect at this temperature (***Figure 4-21***).

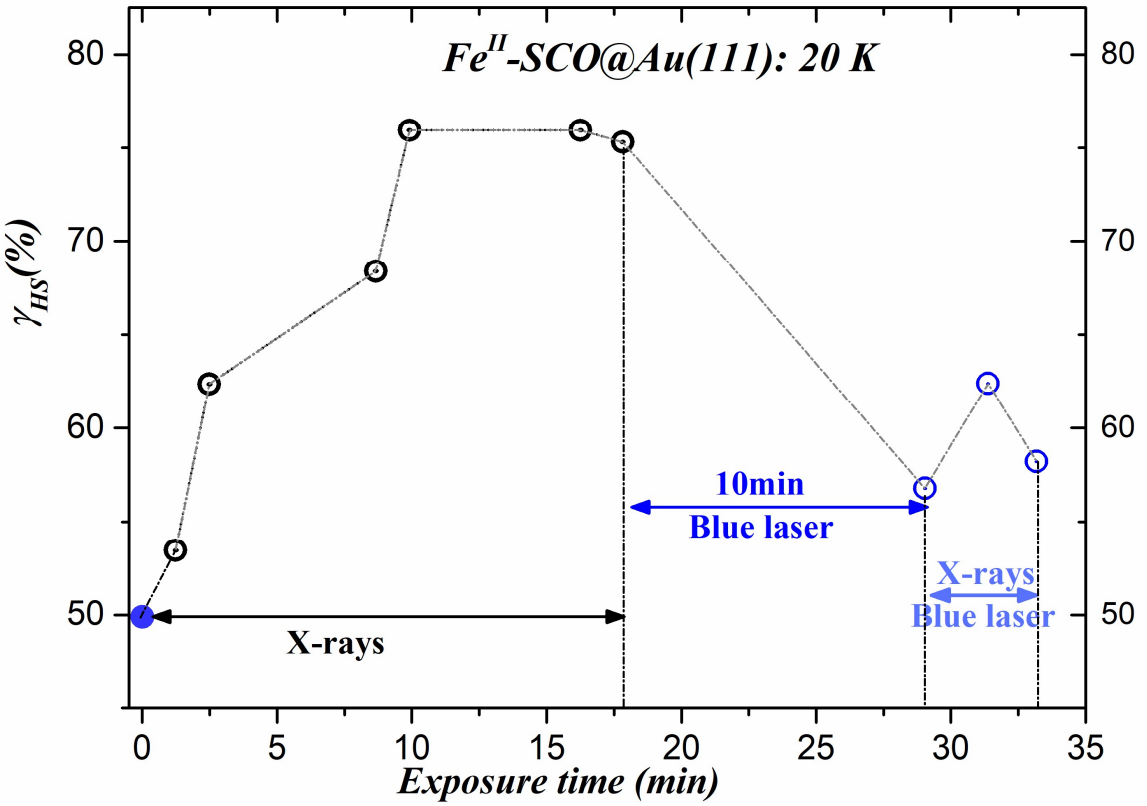

Figure 4-21. *HS fraction as a function of exposure time of X-rays for 18 minutes; then blue light is switched on for 10 minutes without recording spectra and then three spectra recorded keeping blue light.*

4.5.2.3 Time Dependence of Red Light on Fe^{II}-SCO@Au at 4 K

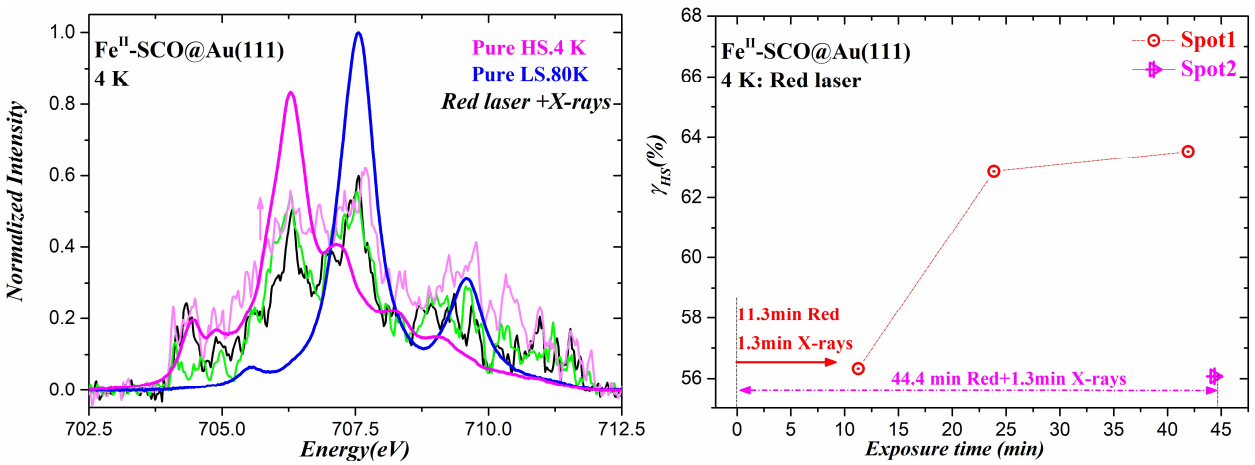

Figure 4-22. *XAS spectra of Fe^{II}-SCO@Au at T = 4 K at different red light exposure; the blue and magenta traces correspond to LS and low temperature high spin reference species, respectively* ***(left)****, and HS fraction as a function of time exposure of red light and X-rays* ***(right)****. A new series of XAS spectra are measured after and the related evolution of XAS spectra at 4 K on the same sample is depicted in* ***Figure III-9*** *in Appendix III.*

The XAS spectra recorded upon red light illumination at T = 4 K are depicted in ***Figure 4-22***, ***left***. The sample was first cooled to low temperature where the HS fraction was measured by a single scan and found to be equal to 56%. Red light was applied for 14 minutes and a single scan (74 s) was recorded (***Figure 4-22***, **left**); it shows an *increase* of the HS fraction from 56 to 63% (***Figure 4-22***, **right**). It is worth noting that the similar experiment on Cu(111) led to a *decrease* of

the HS fraction highlighting the reverse LIESST effect that is absent here. The sample was irradiated by red light for additional 20 minutes; the XAS spectrum shows no evolution in the HS fraction (***Figure 4-22***, **left**). In order to unravel the effect of red light from SOXIESST, we performed a XAS spectrum at another region of the sample (Spot 2 in ***Figure 4-22***, **right**) that have been irradiated by red light for 34 minutes and by X-rays for 74 s; we obtain the same HS fraction as for the first scan. In summary, under continuous red light irradiation, when a region of the sample have been subject to X-rays for 74 s, no change in the HS fraction is observed indicating that red light has no effect when the molecules are on Au(111). The change in the HS fraction after 2x74 s of X-rays is due to SOXIESST.

4.6 Discussion about Mechanism of LIESST Effect

On the basis of the results presented and discussed in the previous section, the maximum proportion of HS molecules that switches for those molecular layers in direct interaction with metallic surfaces is no more than 35%. This has been already observed for similar systems[38] or in devices[17] and has been ascribed to structural changes or degraded molecules, presumably modified by the X-ray beam. Although this latter explanation is likely and depends on both the molecular moieties and the X-rays fluence, we believe that this phenomenon is also intrinsic to the molecule-substrate interactions. Mechano-elastic simulations considering a substrate and dynamical effects of light could confirm indeed how the elastic energy stored in the molecular layer can strongly modify the proportion of switched molecules.

Concerning the observation of the anomalous light induced SST from HS to LS, we can rule out the direct photon absorption by the molecules in the HS state as thin films of **1** show no clear absorption resonance in the blue light range.[21] Thus, the usual mechanism for r-LIESST involving the transition through excited states seems very unlikely. Moreover, it would not explain why the effect is more pronounced on Cu(111) and Au(111) than on Ag(111) (the case of Ag(111) is not discussed in this thesis). Therefore, we propose an alternative mechanism involving the absorption of light by the substrate and the SST driven by low-energy photo-electrons. Indeed, in usual LIESST, r-LIESST and SOXIESST phenomena, it has been proposed and demonstrated that the SST occurred through transitions, driven either by direct light or secondary photoelectrons (***Figure 4-23***), from the ground states ($^1A_{1g}$ for LS and $^5T_{2g}$ for HS) to excited states (Metal to Ligand Charge-Transfer levels for LS and ^5E_g for HS), eventually decaying through intermediate states ($^3T_{2g}$ and ^3T_g).[64, 65]

Once again, in these cases, the direct photon absorption can be ruled out, or has a very small efficiency, as the SST is observed out of the absorption band. The absorption cross sections by the metallic substrates are well-known.[66] In the case of Ag (not discussed in this thesis), it is due to conduction

electrons and can be well interpreted by a simple Drude model, giving rise to a very small absorption in the whole visible range (resulting to an almost perfect optical mirror surface).

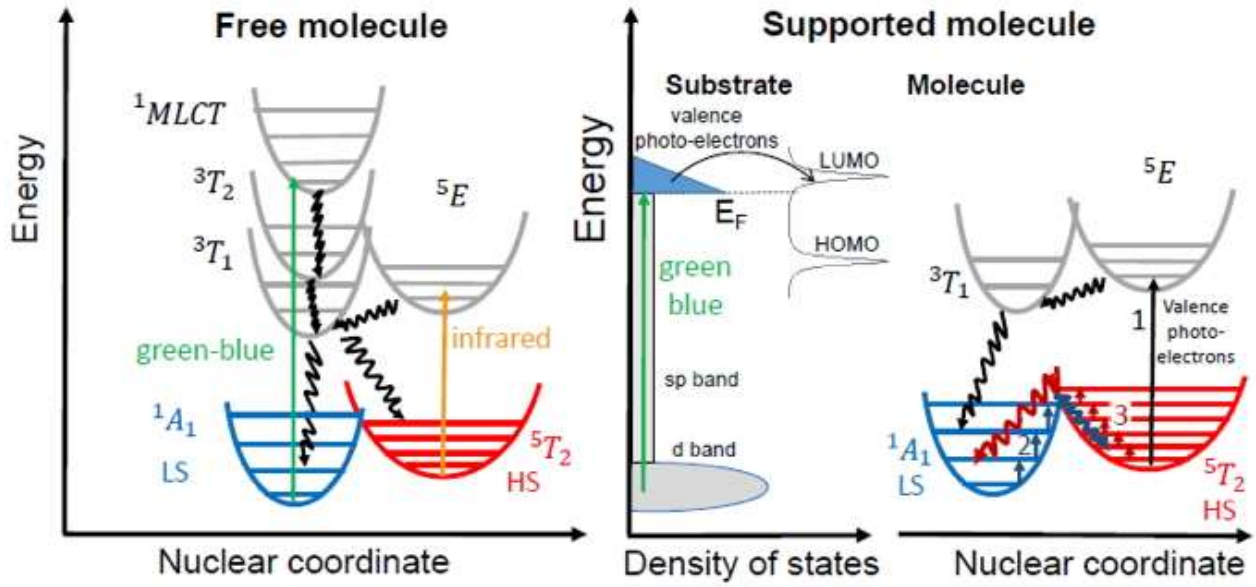

Figure 4-23. ***(left)*** *Schematic drawing of the usual LIESST (green arrow) and r-LIESST (orange arrow) mechanisms through excited state, and* ***(right)*** *schematic drawing of the interband light absorption by the substrate and the induced low-energy valence photo-electrons HS to LS switching through the transition by excited molecular states (path labeled 1) or through vibrational heating (path labeled 2 from LS to HS and labeled 3 from HS to LS). For simplicity, we have skipped the parity index for all the irreducible representations since they are all even.*

For Cu and Au, it is due to *d-sp* interband optical transitions that occur typically for green and blue lights that is at the origin of their reddish and yellowish colors, respectively. Using data from reflectance measurements, the absorption coefficients ($\alpha = \frac{2nk}{\lambda}$) can be estimated for Cu to 14 and 3 μm^{-1}, for Au to 14 and 2 μm^{-1}.[66] As a consequence of this rather strong interband absorption in the blue for Cu and Au, transient low energy valence photo-electrons, typically between 0 and 1 eV with a typical lifetime of 100 fs[67, 68] are excited at the interface between the substrate and the molecular layer. We propose that those electrons, by a hopping, tunneling or energy transfer process, can either populate directly the ^5E_g excited state (path labeled 1 in ***Figure 4-23***), for the most energetic of them or, most probably, the vibrational modes of the Fe^{II} complex for lower energy electrons (paths labeled 2 and 3 in ***Figure 4-23***, ***right***), allowing finally the switching from HS to LS.[33] In this second mechanism, both HS and LS molecules are, *a priori*, excited by the photo-electrons but it is known that the vibrational energy spacing of LS molecules is higher than for HS molecules, in a ratio close to 1.8 (the spacing between energy levels being typically 30 meV for HS and 50 meV for LS).[69] The larger density of vibrational states for HS therefore induces a more efficient vibrational heating of HS molecules as compared to LS ones. Moreover, considering that the HS state is higher in energy than the LS one, the energy barrier to switch from HS to LS is smaller than the one to switch from LS to HS. Accordingly, the rate of switching from HS to LS by this mechanism is expected to be larger

than the rate of switching from LS to HS, leading to an anomalous spin state switching. It is worth noting that this mechanism is in competition with the direct photon absorption by the LS molecules, which leads to the usual LIESST effect, switching from LS to HS. This can explain why for the case of red light, where a very small density of inter-band photo-electrons are excited on Au, we observe a very slight increase of the HS proportion under illumination. In contrast, for blue light, the density of valence photo-electrons is much larger and their contribution to the switching, from HS to LS, dominates over the usual LIESST mechanism. Finally, it seems that the influence of substrate induced low-energy valence photo-electrons on the switching is inherently limited to the first molecular layer in direct contact with the metallic substrate, as a dominant LIESST effect is already measured for the second molecular layer.[44] It is worth noting that this whole mechanism is very close to what has been proposed recently for the photo-induced tautomerization of porphycene molecules on Cu(111).[37]

4.7 Conclusion

We investigated by X-ray Absorption Spectroscopy (XAS) the switching behavior of a submonolayer of Fe^{II} containing molecular species (spin crossover complexes) adsorbed on two noble metal surfaces, namely Cu(111) and Au(111). We found that, at room temperature, the molecules are in the high spin state as in the condensed solid state. Upon cooling down to 4 K, only a fraction (less than 35%) of molecules switches to the LS state. X-rays that are used to perform the XAS study were found to induce a switch from LS to HS at low temperature precluding reaching the most stable phase. However, this effect was quantified not to affect more than 10% of the LS fraction and vanishes at T = 80 K. More surprisingly, we found that illumination with blue light induces a switching from HS to LS at low temperature, in contrast with the bulk behavior where the opposite occurs. By comparing the efficiency of this anomalous light induced spin state trapping from HS to LS on the different substrates and at different wavelengths, we propose that the underlying mechanism is rather different to the ones previously described. In particular, we propose that this transition does not need to populate electronic excited states that would require more than one electron-volt of excitation but more probably involves the excitation of vibrational states by low-energy electrons produced by a photo excitation of the substrate. We believe that this specific interfacial effect between metals and spin-crossover molecules is rather general and could be observed in other systems, with strong implications for electronic devices where the interface is known to play a crucial role.

References

1. Kahn, O.; Launay, J., Molecular bistability: An overview. *Chemtronics* **1988,** *3*, 140-151.
2. Hinek, R.; Hauser, A.; Gutlich, P., *Cooperative effects and bistability in the Fe(etz)(6) (BF4)(2) spincrossover system; Spin transition in two lattice sites*. 1996; Vol. 50, p 3-6.
3. Hauser, A.; Jeftić, J.; Romstedt, H.; Hinek, R.; Spiering, H., Cooperative phenomena and light-induced bistability in iron(II) spin-crossover compounds. *Coord. Chem. Rev.* **1999,** *190-192*, 471-491.
4. Sciortino, N. F.; Neville, S. M.; Letard, J. F.; Moubaraki, B.; Murray, K. S.; Kepert, C. J., Thermal- and light-induced spin-crossover bistability in a disrupted Hofmann-type 3D framework. *Inorg Chem* **2014,** *53* (15), 7886-93.
5. Iasco, O.; Boillot, M. L.; Bellec, A.; Guillot, R.; Rivière, E.; Mazerat, S.; Nowak, S.; Morineau, D.; Brosseau, A.; Miserque, F.; Repain, V.; Mallah, T., The disentangling of hysteretic spin transition, polymorphism and metastability in bistable thin films formed by sublimation of bis(scorpionate) Fe(ii) molecules. *J. Mater. Chem. C* **2017,** *5* (42), 11067-11075.
6. Kahn, O.; Codjovi, E.; Garcia, Y.; van Koningsbruggen, P. J.; Lapouyade, R.; Sommier, L., Spin transition molecular materials for display and data processing. **1996**.
7. Kahn, O.; Martinez, C. J., Spin-transition polymers: From molecular materials toward memory devices. *Science* **1998,** *279* (5347), 44-48.
8. Murray, K. S.; Kepert, C. J., Cooperativity in spin crossover systems: Memory, magnetism and microporosity. In *Spin Crossover in Transition Metal Compounds I*, Springer: 2004; pp 195-228.
9. Boillot, M.-L., *Spin Crossover in Transition Metal Compounds II*. Springer Science & Business Media: 2004; Vol. 2.
10. Létard, J.-F.; Guionneau, P.; Goux-Capes, L., Towards spin crossover applications. In *Spin Crossover in Transition Metal Compounds III*, Springer: 2004; pp 221-249.
11. Real, J. A.; Gaspar, A. B.; Munoz, M. C., Thermal, pressure and light switchable spin-crossover materials. *Dalton Trans.* **2005,** (12), 2062-2079.
12. Bousseksou, A.; Molnar, G.; Salmon, L.; Nicolazzi, W., Molecular spin crossover phenomenon: recent achievements and prospects. *Chem Soc Rev* **2011,** *40* (6), 3313-35.
13. Hauser, A., Spin-Crossover Materials Properties and Applications. *Angew. Chem. Int. Ed.* **2013,** *52* (40), 10419-10419.
14. Kumar, K. S.; Ruben, M., Emerging trends in spin crossover (SCO) based functional materials and devices. *Coordination Chemistry Reviews* **2017,** *346*, 176-205.
15. Decurtins, S.; Gütlich, P.; Köhler, C.; Spiering, H.; Hauser, A., Light-induced excited spin state trapping in a transition-metal complex: The hexa-1-propyltetrazole-iron (II) tetrafluoroborate spin-crossover system. *Chem. Phys. Lett.* **1984,** *105* (1), 1-4.
16. Gütlich, P.; Hauser, A., Thermal and light-induced spin crossover in iron (II) complexes. *Coord. Chem. Rev.* **1990,** *97*, 1-22.
17. Collison, D.; Garner, C. D.; McGrath, C. M.; Mosselmans, J. F. W.; Roper, M. D.; Seddon, J. M.; Sinn, E.; Young, N. A., Soft x-ray induced excited spin state trapping and soft X-ray photochemistry at the iron L 2, 3 edge in [Fe (phen) 2 (NCS) 2] and [Fe (phen) 2 (NCSe) 2](phen= 1, 10-phenanthroline). *J. Chem. Soc. Dalton Trans.* **1997,** (22), 4371-4376.
18. Davesne, V.; Gruber, M.; Miyamachi, T.; Da Costa, V.; Boukari, S.; Scheurer, F.; Joly, L.; Ohresser, P.; Otero, E.; Choueikani, F.; Gaspar, A. B.; Real, J. A.; Wulfhekel, W.; Bowen, M.; Beaurepaire, E., First glimpse of the soft x-ray induced excited spin-state trapping effect dynamics on spin cross-over molecules. *J Chem Phys* **2013,** *139* (7), 074708.
19. Hauser, A., Reversibility of light-induced excited spin state trapping in the Fe (ptz) 6 (BF4) 2, and the Zn1− xFex (ptz) 6 (BF4) 2 spin-crossover systems. *Chem. Phys. Lett.* **1986,** *124* (6), 543-548.
20. Ellingsworth, E. C.; Turner, B.; Szulczewski, G., Thermal conversion of [Fe(phen)3](SCN)2 thin films into the spin crossover complex Fe(phen)2(NCS)2. *RSC Advances* **2013,** *3* (11), 3745-3754.

21. Davesne, V.; Gruber, M.; Studniarek, M.; Doh, W.; Zafeiratos, S.; Joly, L.; Sirotti, F.; Silly, M.; Gaspar, A.; Real, J., Hysteresis and change of transition temperature in thin films of Fe {[Me2Pyrz] 3BH} 2, a new sublimable spin-crossover molecule. *J. Chem. Phys.* **2015,** *142* (19), 194702.

22. Laisney, J.; Tissot, A.; Molnár, G.; Rechignat, L.; Rivière, E.; Brisset, F.; Bousseksou, A.; Boillot, M. L., Nanocrystals of Fe(phen)2(NCS)2 and the size-dependent spin-crossover characteristics. *Dalton Trans.* **2015,** *44* (39), 17302-17311.

23. Coronado, E.; Galán-Mascarós, J. R.; Monrabal-Capilla, M.; García-Martínez, J.; Pardo-Ibáñez, P., Bistable Spin-Crossover Nanoparticles Showing Magnetic Thermal Hysteresis near Room Temperature. *Adv. Mater.* **2007,** *19* (10), 1359-1361.

24. Forestier, T.; Mornet, S.; Daro, N.; Nishihara, T.; Mouri, S.-i.; Tanaka, K.; Fouché, O.; Freysz, E.; Létard, J.-F., Nanoparticles of iron (II) spin-crossover. *Chem. Commun.* **2008,** (36), 4327-4329.

25. Volatron, F.; Catala, L.; Rivière, E.; Gloter, A.; Stéphan, O.; Mallah, T., Spin-Crossover Coordination Nanoparticles. *Inorg. Chem.* **2008,** *47* (15), 6584-6586.

26. Raza, Y.; Volatron, F.; Moldovan, S.; Ersen, O.; Huc, V.; Martini, C.; Brisset, F.; Gloter, A.; Stephan, O.; Bousseksou, A.; Catala, L.; Mallah, T., Matrix-dependent cooperativity in spin crossover Fe(pyrazine)Pt(CN)4 nanoparticles. *Chem Commun (Camb)* **2011,** *47* (41), 11501-3.

27. Mallah, T.; Cavallini, M., Surfaces, thin films and patterning of spin crossover compounds. *Cr. Chim.* **2018,** *21* (12), 1270-1286.

28. Shi, S.; Schmerber, G.; Arabski, J.; Beaufrand, J.-B.; Kim, D. J.; Boukari, S.; Bowen, M.; Kemp, N. T.; Viart, N.; Rogez, G.; Beaurepaire, E.; Aubriet, H.; Petersen, J.; Becker, C.; Ruch, D., Study of molecular spin-crossover complex Fe(phen)2(NCS)2 thin films. *Appl. Phys. Lett.* **2009,** *95* (4), 043303.

29. Naggert, H.; Bannwarth, A.; Chemnitz, S.; von Hofe, T.; Quandt, E.; Tuczek, F., First observation of light-induced spin change in vacuum deposited thin films of iron spin crossover complexes. *Dalton Trans* **2011,** *40* (24), 6364-6.

30. Cavallini, M., Status and perspectives in thin films and patterning of spin crossover compounds. *PCCP* **2012,** *14* (34), 11867-11876.

31. Ludwig, E.; Naggert, H.; Kalläne, M.; Rohlf, S.; Kröger, E.; Bannwarth, A.; Quer, A.; Rossnagel, K.; Kipp, L.; Tuczek, F., Iron (II) Spin‐Crossover Complexes in Ultrathin Films: Electronic Structure and Spin‐State Switching by Visible and Vacuum‐UV Light. *Angew. Chem. Int. Ed.* **2014,** *53* (11), 3019-3023.

32. Gruber, M.; Davesne, V.; Bowen, M.; Boukari, S.; Beaurepaire, E.; Wulfhekel, W.; Miyamachi, T., Spin state of spin-crossover complexes: From single molecules to ultrathin films. *Phys. Rev. B* **2014,** *89* (19), 195415.

33. Miyamachi, T.; Gruber, M.; Davesne, V.; Bowen, M.; Boukari, S.; Joly, L.; Scheurer, F.; Rogez, G.; Yamada, T. K.; Ohresser, P., Robust spin crossover and memristance across a single molecule. *Nat. Comm.* **2012,** *3*, 938.

34. Gopakumar, T. G.; Matino, F.; Naggert, H.; Bannwarth, A.; Tuczek, F.; Berndt, R., Electron‐Induced Spin Crossover of Single Molecules in a Bilayer on Gold. *Angew. Chem. Int. Ed.* **2012,** *51* (25), 6262-6266.

35. Harzmann, G. D.; Frisenda, R.; van der Zant, H. S.; Mayor, M., Single‐Molecule Spin Switch Based on Voltage‐Triggered Distortion of the Coordination Sphere. *Angew. Chem. Int. Ed.* **2015,** *54* (45), 13425-13430.

36. Gueddida, S.; Alouani, M., Spin crossover in a single Fe(phen${)}_{2}$(NCS${)}_{2}$ molecule adsorbed onto metallic substrates: An ab initio calculation. *Phys. Rev. B* **2013,** *87* (14), 144413.

37. Böckmann, H.; Liu, S.; Mielke, J.; Gawinkowski, S.; Waluk, J.; Grill, L.; Wolf, M.; Kumagai, T., Direct observation of photoinduced tautomerization in single molecules at a metal surface. *Nano Lett.* **2016,** *16* (2), 1034-1041.

38. Bellec, A.; Lagoute, J.; Repain, V., Molecular electronics: Scanning tunneling microscopy and single-molecule devices. *Cr. Chim.* **2018,** *21* (12), 1287-1299.

39. Lefter, C.; Rat, S.; Costa, J. S.; Manrique‐Juárez, M. D.; Quintero, C. M.; Salmon, L.; Séguy, I.; Leichle, T.; Nicu, L.; Demont, P., Current Switching Coupled to Molecular Spin‐States in Large‐Area

Junctions. *Adv. Mater.* **2016,** *28* (34), 7508-7514.

40. Bernien, M.; Naggert, H.; Arruda, L. M.; Kipgen, L.; Nickel, F.; Miguel, J.; Hermanns, C. F.; Krüger, A.; Krüger, D.; Schierle, E., Highly efficient thermal and light-induced spin-state switching of an Fe (II) complex in direct contact with a solid surface. *ACS nano* **2015,** *9* (9), 8960-8966.

41. Bairagi, K.; Iasco, O.; Bellec, A.; Kartsev, A.; Li, D.; Lagoute, J.; Chacon, C.; Girard, Y.; Rousset, S.; Miserque, F.; Dappe, Y. J.; Smogunov, A.; Barreteau, C.; Boillot, M.-L.; Mallah, T.; Repain, V., Molecular-scale dynamics of light-induced spin cross-over in a two-dimensional layer. *Nat. Comm.* **2016,** *7*, 12212.

42. Kipgen, L.; Bernien, M.; Ossinger, S.; Nickel, F.; Britton, A. J.; Arruda, L. M.; Naggert, H.; Luo, C.; Lotze, C.; Ryll, H., Evolution of cooperativity in the spin transition of an iron (II) complex on a graphite surface. *Nat. Comm.* **2018,** *9* (1), 2984.

43. Bairagi, K.; Bellec, A.; Fourmental, C.; Iasco, O.; Lagoute, J.; Chacon, C.; Girard, Y.; Rousset, S.; Choueikani, F.; Otero, E.; Ohresser, P.; Sainctavit, P.; Boillot, M.-L.; Mallah, T.; Repain, V., Temperature-, Light-, and Soft X-ray-Induced Spin Crossover in a Single Layer of FeII-Pyrazolylborate Molecules in Direct Contact with Gold. *J. Phys. Chem. C* **2018,** *122* (1), 727-731.

44. Bairagi, K.; Bellec, A.; Fourmental, C.; Tong, Y.; Iasco, O.; Lagoute, J. r. m.; Chacon, C.; Girard, Y.; Rousset, S.; Choueikani, F., Correction to Temperature-, Light-, and Soft X-ray-Induced Spin Crossover in a Single Layer of FeII-Pyrazolylborate Molecules in Direct Contact with Gold. *J. Phys. Chem. C* **2018,** *122* (50), 29080-29080.

45. Ossinger, S.; Naggert, H.; Kipgen, L.; Jasper-Toennies, T.; Rai, A.; Rudnik, J.; Nickel, F.; Arruda, L. M.; Bernien, M.; Kuch, W., Vacuum-evaporable spin-crossover complexes in direct contact with a solid surface: Bismuth versus gold. *J. Phys. Chem. C* **2017,** *121* (2), 1210-1219.

46. Gopakumar, T. G.; Bernien, M.; Naggert, H.; Matino, F.; Hermanns, C. F.; Bannwarth, A.; Muhlenberend, S.; Kruger, A.; Kruger, D.; Nickel, F.; Walter, W.; Berndt, R.; Kuch, W.; Tuczek, F., Spin-crossover complex on Au(111): structural and electronic differences between mono- and multilayers. *Chem. Eur. J.* **2013,** *19* (46), 15702-9.

47. Beniwal, S.; Zhang, X.; Mu, S.; Naim, A.; Rosa, P.; Chastanet, G.; Letard, J. F.; Liu, J.; Sterbinsky, G. E.; Arena, D. A.; Dowben, P. A.; Enders, A., Surface-induced spin state locking of the [Fe(H2B(pz)2)2(bipy)] spin crossover complex. *J Phys Condens Matter* **2016,** *28* (20), 206002.

48. Gruber, M.; Miyamachi, T.; Davesne, V.; Bowen, M.; Boukari, S.; Wulfhekel, W.; Alouani, M.; Beaurepaire, E., Spin crossover in Fe(phen)2(NCS)2 complexes on metallic surfaces. *J. Chem. Phys.* **2017,** *146* (9), 092312.

49. Rohlf, S.; Gruber, M.; Floser, B. M.; Grunwald, J.; Jarausch, S.; Diekmann, F.; Kallane, M.; Jasper-Toennies, T.; Buchholz, A.; Plass, W.; Berndt, R.; Tuczek, F.; Rossnagel, K., Light-Induced Spin Crossover in an Fe(II) Low-Spin Complex Enabled by Surface Adsorption. *J Phys Chem Lett* **2018,** *9* (7), 1491-1496.

50. Rohlf, S.; Grunwald, J.; Jasper-Toennies, T.; Johannsen, S.; Diekmann, F.; Studniarek, M.; Berndt, R.; Tuczek, F.; Rossnagel, K.; Gruber, M., Influence of Substrate Electronic Properties on the Integrity and Functionality of an Adsorbed Fe (II) Spin-Crossover Compound. *J. Phys. Chem. C* **2019,** *123* (29), 17774-17780.

51. Fourmental, C.; Mondal, S.; Banerjee, R.; Bellec, A.; Garreau, Y.; Coati, A.; Chacon, C.; Girard, Y.; Lagoute, J.; Rousset, S., Importance of Epitaxial Strain at a Spin-Crossover Molecule–Metal Interface. *J. Phys. Chem. Lett.* **2019,** *10* (14), 4103-4109.

52. Jesson, J. P.; Trofimenko, S.; Eaton, D. R., Spin equilibria in octahedral iron(II) poly((1-pyrazolyl)-borates. *J. Am. Chem. Soc.* **1967,** *89* (13), 3158-3164.

53. Grandjean, F.; Long, G. J.; Hutchinson, B. B.; Ohlhausen, L.; Neill, P.; Holcomb, J. D., STUDY OF THE HIGH-TEMPERATURE SPIN-STATE CROSSOVER IN THE IRON(II) PYRAZOLYLBORATE COMPLEX FE HB(PZ)3 2. *Inorg. Chem.* **1989,** *28* (24), 4406-4414.

54. Iasco, O.; Rivière, E.; Guillot, R.; Buron-Le Cointe, M.; Meunier, J.-F.; Bousseksou, A.; Boillot, M.-L., FeII(pap-5NO2)2 and FeII(qsal-5NO2)2 Schiff-Base Spin-Crossover Complexes: A Rare Example with Photomagnetism and Room-Temperature Bistability. *Inorg. Chem.* **2015,** *54* (4), 1791-1799.

55. De Groot, F.; Fuggle, J.; Thole, B.; Sawatzky, G., 2p x-ray absorption of 3d transition-metal compounds:

An atomic multiplet description including the crystal field. *Phys. Rev. B* **1990,** *42* (9), 5459.

56. De Groot, F., Multiplet effects in X-ray spectroscopy. *Coord. Chem. Rev.* **2005,** *249* (1), 31-63.

57. van der Laan, G., Hitchhiker's guide to multiplet calculations. *Magnetism: A Synchrotron Radiation Approach* **2006**, 143-199.

58. Butler, P. H., *Point group symmetry applications: methods and tables*. Springer Science & Business Media: 2012.

59. Briois, V.; dit Moulin, C. C.; Sainctavit, P.; Brouder, C.; Flank, A.-M., Full multiple scattering and crystal field multiplet calculations performed on the spin transition FeII (phen) 2 (NCS) 2 complex at the iron K and L2, 3 X-ray absorption edges. *J. Am. Chem. Soc.* **1995,** *117* (3), 1019-1026.

60. Sugano, S., *Multiplets of transition-metal ions in crystals*. Elsevier: 2012.

61. Warner, B.; Oberg, J. C.; Gill, T. G.; El Hallak, F.; Hirjibehedin, C. F.; Serri, M.; Heutz, S.; Arrio, M. A.; Sainctavit, P.; Mannini, M.; Poneti, G.; Sessoli, R.; Rosa, P., Temperature- and Light-Induced Spin Crossover Observed by X-ray Spectroscopy on Isolated Fe(II) Complexes on Gold. *J Phys Chem Lett* **2013,** *4* (9), 1546-52.

62. De Groot, F.; Kotani, A., *Core level spectroscopy of solids*. CRC press: 2008.

63. Kipgen, L.; Bernien, M.; Nickel, F.; Naggert, H.; Britton, A. J.; Arruda, L. M.; Schierle, E.; Weschke, E.; Tuczek, F.; Kuch, W., Soft-x-ray-induced spin-state switching of an adsorbed Fe (II) spin-crossover complex. *J. Phys. Condens. Mat.* **2017,** *29* (39), 394003.

64. Gutlich, P., Spin crossover in transition metal compounds. **2004**.

65. Marino, A.; Chakraborty, P.; Servol, M.; Lorenc, M.; Collet, E.; Hauser, A., The Role of Ligand ‐ Field States in the Ultrafast Photophysical Cycle of the Prototypical Iron (II) Spin ‐ Crossover Compound [Fe (ptz) 6](BF4) 2. *Angew. Chem. Int. Ed.* **2014,** *53* (15), 3863-3867.

66. Johnson, P. B.; Christy, R.-W., Optical constants of the noble metals. *Phys. Rev. B* **1972,** *6* (12), 4370.

67. Petek, H.; Ogawa, S., Femtosecond time-resolved two-photon photoemission studies of electron dynamics in metals. *Progress in surface science* **1997,** *56* (4), 239-310.

68. Pawlik, S.; Bauer, M.; Aeschlimann, M., Lifetime difference of photoexcited electrons between intraband and interband transitions. *Surface science* **1997,** *377*, 206-209.

69. Tuchagues, J. P.; Bousseksou, A.; Molnar, G.; McGarvey, J. J.; Varret, F., *The Role of Molecular Vibrations in the Spin Crossover Phenomenon. In Spin Crossover in Transition Metal Compounds III*. Springer Berlin Heidelberg: Berlin, Heidelberg: 2004.

Chapter 5 - General Conclusions and Future Work

5.1 General Conclusions

The objective of this dissertation was to study the electronic and geometrical structures between nano-objects (nanocrystals, nanoparticles and molecules et al) and solid surfaces. These nano-objects can be integrated into the devices where a hysteresis or a pronounced spin transition leading to cooperativity may occur.

In the first part (**Chapter 3**), 6nm-sized PBA $Cs^{I}Ni^{II}Cr^{III}$ nanocrystals were chosen as a promising candidate to be assembled on the solid surface of highly oriented pyrolytic graphite (HOPG). These NCs are ferromagnetic in powder below 90 K assembled on HOPG,[1] however, rare studies were carried out on the anisotropic properties for these NCs on solid surface. For the sake of understanding the electronic and geometrical anisotropies, XAS as the cutting-edge technique is used combined with LFM calculations. Comparing experimental XAS with simulated spectra obtained from LFM calculations provides information on the geometrical structures on the surface of NCs based on the combinational investigation of Ni and Cr sites. Due to a comprehensive study of XNLD spectra at $L_{2,3}$ edges at Ni^{II} and Cr^{III} sites, experimentally and theoretically, it demonstrates that there is C_{4v} elongation on the surface. Besides, the distortion of C_{4v} are reproduced by the mono-electronic approach of *d* orbital energies diagrams.

Moreover, it is well-known that structure determines properties so that the NCs on HOPG have different properties from bulk and in diluted cases. The magnetic anisotropies of $Cs^{I}Ni^{II}Cr^{III}$[6] on HOPG has an easy-plane of magnetization shown by the magnetization curves recorded by XMCD measurement at 2 T. The angular-XMCD study shows that the occurrence of a larger open hysteresis loop observed at 60º reveals NCs assembled on HOPG possess an easy plane of magnetization. This magnetic anisotropy is consistent with the structural anisotropies analyzed by the angular-dependent XAS, XNLD and XMCD. In conclusion, the electronic anisotropy associated to the Ni^{II} species at the very surface of the NCs induces a "hard" axis of magnetization so that all the NCs would tend to have their magnetic moments lying in the plane of the substrate. Magnetic dipole interactions, that are much larger than intra-particle exchange coupling, would then tend to build an easy plane of magnetization for the NCs monolayer.

The second part (**Chapter 4**) was devoted to a very new study the SCO behaviors of $Fe^{II}[HB(3,5\text{-}Me_2Pz)_3]_2$ molecules deposited as submonolayer on oriented metallic substrates (Au(111) and Cu(111)). In the recent 10 years, the study of ultra-thin film of SCO compounds in

contact with solid surface is an emerging and challenging field in molecular spintronics and molecular switching devices. In the previous studies of Bairagi *et al.*[2-5] *and* Bowen *et al.*[6] observed that the cooperativity of Fe^{II}-SCO molecules is reduced along with the reduction of the dimensionality of systems. In the case of a monolayer of $Fe^{II}[HB(3,5\text{-}Me_2Pz)_3]_2$ molecules on Au(111), there occur a mixed spin state of HS and LS state, which could have a spin conversion led by temperature and irradiation.[2-4]

A versatile exploration of a submonolayer SCO compound contacting on solid substrates is i) to carry out STM measurements to understand the current or voltage control of spin transition and to probe the kondo effect in the interface between molecules and substrates surface, ii) to adopt XAS measurements to detect the thickness of the assembled molecular layer, iii) to simulate XAS spectra based on LFM calculations. All the above techniques are favorable to estimate the relatively ratio of spin transition. XAS is a state-of the-art method to detect and record signals from nano-objects due to its surface sensitivity and chemical selectivity, which not only enables us to distinguish different spin states but also to explore the dynamic kinetics of SCO behaviors caused by several light, temperature, and pressure.[7]

As there is a co-external stimuli of X-ray irradiation and temperatures, varying temperature is the dominate effect to induce the spin transition while when temperature is fixed X-rays can play the principal role in the range of LT (0 - 80 K). Especially, we found that SOXIESST effect took place at 4 K and 20 K in the samples of $Fe^{II}[HB(3,5\text{-}Me_2Pz)_3]_2$ molecules on Cu(111) and Au(111).

When XAS measurements recorded at 4 K under the co-illumination of blue laser and X-rays, an abnormal light effect caused by blue laser was observed----blue light induces a HS-to-LS conversion in all samples unlike the previous light effect (LIESST: a LS-to-HS) on the sample of monolayer on Au(111)[2] and the sample of 1.57±0.25ML on Au both are reported by Bairagi *et al.*[3-4] Comparisons are listed in the ***Figure 5-1***. The effect caused by blue laser on one submonolayer of Fe^{II}-SCO molecules on Au(111) is completely reverse to the case of monolayer on Au(111). Besides, we also found that light effect is different depending upon the thickness of the coverage of SCO molecular layers:1.5±0.1 ML and 0.5±0.1ML. The quantity of ST switched by blue light in the case of 0.5±0.1ML is 4% less than the one in the case of 1.5±0.1 ML.

Finally, to study the interfacial interaction between molecules and substrates is full of interests and challenges. The underlying mechanism we proposed in this part can be introduced to interpret similar systems. The interfacial properties is becoming more and more crucial in today's research.

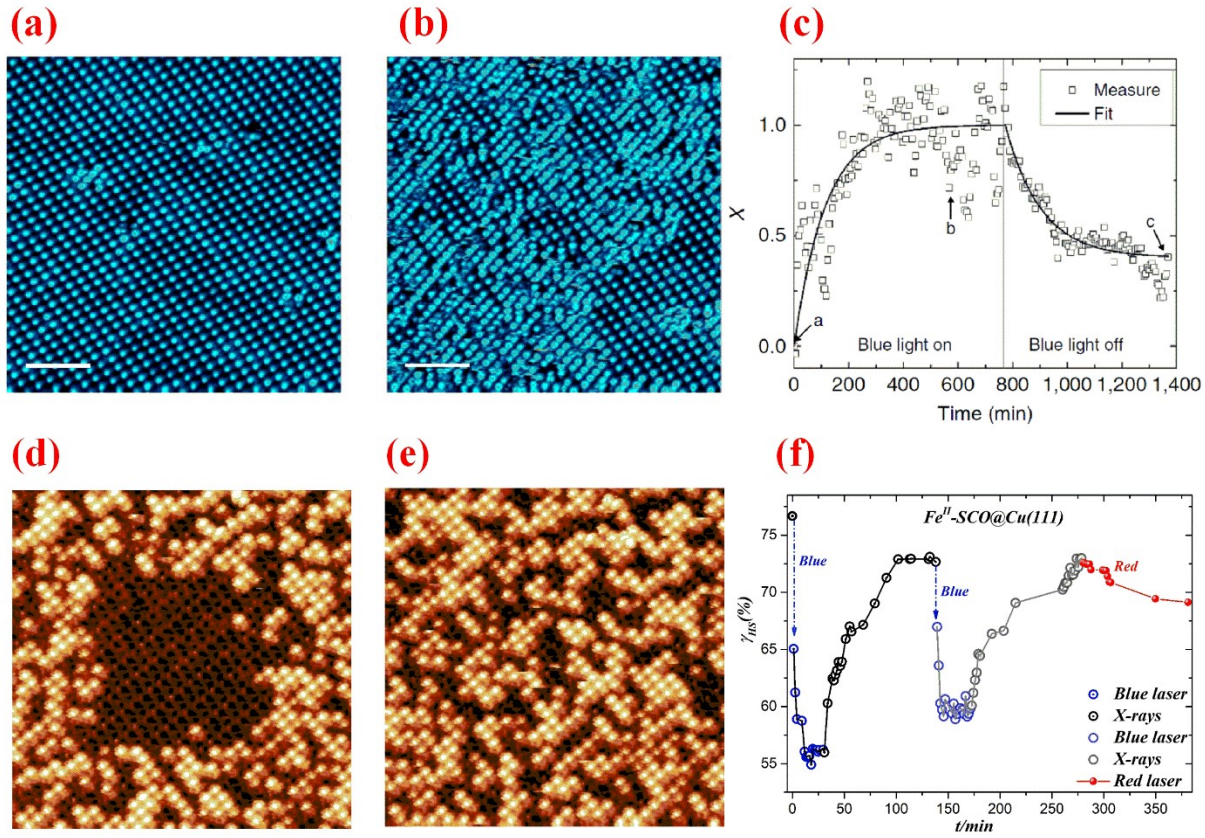

Figure 5-1. *Light-induced SCO at molecular scale. Up-panel: $Fe^{II}[HB(3,5\text{-}Me_2Pz)_3]_2$ molecules assembled monolayer on Au(111); down-panel: $Fe^{II}[HB(3,5\text{-}Me_2Pz)_3]_2$ molecules assembled submonolayer on Au(111).* ***Fig.5-1(a)*** *and* ***(b)*** *is the STM measurement (at 4.6 K) measured before and after the illumination of 9h45min blue light,* ***Fig.5-1(c)*** *is the corresponding spin transition curve defined as the function of HS fraction vs exposure time (min).* ***Fig.5-1(d)*** *and* ***(e)*** *is the STM images measured at 4.5K before and after blue light illumination, and* ***Fig. 5-1(f)*** *is the ST curved simulated based on XAS spectra measured at 4.3 K. So as to explain the mechanism of the abnormal blue light effect, one alternative route for ST contains the absorption of light on substrate and the SST driven by low-energy photo-electrons. This underlying assumption is a very new mechanism for nano-objects deposited as submonolayer, which is an effective and critical idea to solve difficulties to the abnormal light effect (HS-to-LS transition).*

5.2 Future Work

The most interesting and important future work is based on the above two stated parts in this thesis.

First and most, it is to have a better and deeper insight into the interfacial interactions between molecules and surface of substrates and intra-molecule interactions. Since interfacial interactions play an essential role in the properties of nano-objects which can be applied into the field of molecular spintronic devices and information storage.

Second, DFT calculations based on ab initio theory is an effective method to study the electronic properties and structures between molecules and substrates, theoretically. Hence, in the future I would like to take DFT calculations to study objects from bulk to molecular or nano scale.

Lastly, by virtue of the development of computational chemistry, molecular design and simulations of properties pave a better way for me to study magnetic properties and structural anisotropies for new designed molecules which would be accounted for better promising candidates for memory devices and spintronic devices. Such theoretical study can provide rational and reasonable shortcuts for chemists to synthesize related molecules.

References

1. Gadet, V.; Mallah, T.; Castro, I.; Verdaguer, M.; Veillet, P., High-TC molecular-based magnets: a ferromagnetic bimetallic chromium (III)-nickel (II) cyanide with TC= 90 K. *Journal of the American Chemical Society* **1992,** *114* (23), 9213-9214.

2. Bairagi, K.; Iasco, O.; Bellec, A.; Kartsev, A.; Li, D.; Lagoute, J.; Chacon, C.; Girard, Y.; Rousset, S.; Miserque, F., Molecular-scale dynamics of light-induced spin cross-over in a two-dimensional layer. *Nature communications* **2016,** *7*, 12212.

3. Bairagi, K.; Bellec, A.; Fourmental, C.; Iasco, O.; Lagoute, J.; Chacon, C.; Girard, Y.; Rousset, S.; Choueikani, F.; Otero, E.; Ohresser, P.; Sainctavit, P.; Boillot, M.-L.; Mallah, T.; Repain, V., Temperature-, Light-, and Soft X-ray-Induced Spin Crossover in a Single Layer of FeII-Pyrazolylborate Molecules in Direct Contact with Gold. *The Journal of Physical Chemistry C* **2018,** *122* (1), 727-731.

4. Bairagi, K.; Bellec, A.; Fourmental, C.; Tong, Y.; Iasco, O.; Lagoute, J. r. m.; Chacon, C.; Girard, Y.; Rousset, S.; Choueikani, F., Correction to Temperature-, Light-, and Soft X-ray-Induced Spin Crossover in a Single Layer of FeII-Pyrazolylborate Molecules in Direct Contact with Gold. *The Journal of Physical Chemistry C* **2018,** *122* (50), 29080-29080.

5. Iasco, O.; Boillot, M. L.; Bellec, A.; Guillot, R.; Rivière, E.; Mazerat, S.; Nowak, S.; Morineau, D.; Brosseau, A.; Miserque, F.; Repain, V.; Mallah, T., The disentangling of hysteretic spin transition, polymorphism and metastability in bistable thin films formed by sublimation of bis(scorpionate) Fe(ii) molecules. *Journal of Materials Chemistry C* **2017,** *5* (42), 11067-11075.

6. Davesne, V.; Gruber, M.; Studniarek, M.; Doh, W. H.; Zafeiratos, S.; Joly, L.; Sirotti, F.; Silly, M. G.; Gaspar, A. B.; Real, J. A.; Schmerber, G.; Bowen, M.; Weber, W.; Boukari, S.; Costa, V. D.; Arabski, J.; Wulfhekel, W.; Beaurepaire, E., Hysteresis and change of transition temperature in thin films of Fe{[Me2Pyrz]3BH}2, a new sublimable spin-crossover molecule. *The Journal of Chemical Physics* **2015,** *142* (19), 194702.

7. Davesne, V.; Gruber, M.; Miyamachi, T.; Costa, V. D.; Boukari, S.; Scheurer, F.; Joly, L.; Ohresser, P.; Otero, E.; Choueikani, F.; Gaspar, A. B.; Real, J. A.; Wulfhekel, W.; Bowen, M.; Beaurepaire, E., First glimpse of the soft x-ray induced excited spin-state trapping effect dynamics on spin cross-over molecules. *The Journal of Chemical Physics* **2013,** *139* (7), 074708.

APPENDIX - I

In the first appendix, the background for x-ray absorprtion spectroscopy, core level spectroscopy, crystal field theory are given in brief.[1] Electronic configurations of initial state ($2p^6 3d^n$) and final state ($2p^5 3d^{n+1}$) are listed for 3d TM ions, which is of great importance to study the XAS spectra. And associated symmetries for each electronic configurations also are appended, which is favorable to understanding the electron properties of each 3d metal ions.

Tanabe-sugano diagrams provide supportative information for classical metal compounds owning octahedral symmetries. Since the objects in my work are nano-objects containing Ni(II), Cr(III) and Fe(II) ions, Tanabe-sugano diagrams are just cited for these three above metal ions. As for 3d TM ions, it is necessary to study the relationship between ligand (crystal) field theory to interactions generating from *jj* coupling, spin-orbit coupling and/or zeeman effect. Symmetries for classical 3d compounds are subducted from SO_3-O_h-D_{4h}/C_{4v}.

In my work, all these three metal ions are satisfied with the dipole electric approximation, sothat all possible electronic configurations are considered on the basis of selection rules. Temperature imposes an significant effect upon the distribution of states due to the Boltzmann Law. Each state are expressed using spectroscopy term, hence, this appendix is quite important for me to understand and to analyze the experimental XAS spectra and LFM calculations.

Table I-1. Relevant X-ray absorption edges for magnetic 3d, 4d and 5d transition metals, and for lanthanides, and their corresponding energy region.

Absorption edge	Transition state	Energy / keV				
		3d TM	4d TM	5d TM	Ln	U
K	$1s \rightarrow p$	5-11	17-27	65-82	39-60	115.6
$L_{2,3}$	$2p \rightarrow d$	0.45-0.95	2-4	9-14	5.5-10	17-21
$M_{2,3}$	$3p \rightarrow d$	0.03-0.125	150-650	1.7-3	1.2-2.2	4.3-5.2
$M_{4,5}$	$3d \rightarrow f$	-	-	-	0.8-1.5	3.5-3.7
$N_{2,3}$	$4p \rightarrow d$	-	-	380-610	-	-
$N_{4,5}$	$4d \rightarrow f$	-	-	-	0.1-0.175	0.736-0.774
$O_{4,5}$	$5d \rightarrow f$	-	-	-	-	0.1-0.12

Table I-2. Configurations of *s* and *p* electrons

Configurations	J	Term Symbols	Degeneracy	∑(2J + 1)
$1s^0$	0	$^1S_0$	1	1
$1s^1$	1/2	$^2S_{1/2}$	1	2
$1s^1 2s^1$	0	$^1S_0$	1	4
	1	$^3S_0$	1	
$2p^1 = 2p^5$	1/2	$^2P_{1/2}$	1	6
	3/2	$^2P_{3/2}$	1	
$2p^2 = 2p^4$	0	$^1S_0$ $^3P_0$	2	15
	1	$^3P_1$	1	
	2	$^1D_2$ $^3P_2$	2	
$2p^3$	1/2	$^2P_{1/2}$	1	20
	3/2	$^4S_{3/2}$ $^2P_{3/2}$ $^2D_{3/2}$	3	
	5/2	$^2D_{5/2}$	1	
$2p^1 3p^1$	0	$^1S_0$ $^3P_0$	2	36
	1	$^1P_1$ $^3S_1$ $^3P_1$ $^3D_1$	4	
	2	$^1D_2$ $^3P_2$ $^3D_2$	3	
	3	$^3D_3$	1	

Note: ALL the terms are sorted for their J values. The third column gives the number of term symbols per J values. The last column gives the overall degeneracy of the configuration.

Table I-3. Symmetries of $3d^n$ electrons.

Configurations	J	Term Symbols	Degeneracy
$3d^0$	0	^1S	1
$\sum = 1$			$\sum = 1$
$3d^2$	0	$^1S\ ^3P$	2
$3d^8$	1	^3P	1
	2	$^1D\ ^3P\ ^3F$	3
	3	^3F	1
	4	$^1G\ ^3F$	2
$\sum = 45$			$\sum = 9$
$3d^4$	0	$^1S\ ^1S\ ^3P\ ^3P\ ^5D$	5
$3d^6$	1	$^3P\ ^3P\ ^3D\ ^5D$	4
	2	$^1D\ ^1D\ ^3P\ ^3P\ ^3D\ ^3F\ ^3F\ ^5D$	8
	3	$^1F\ ^3D\ ^3F\ ^3F\ ^3G\ ^5D$	6
	4	$^1G\ ^1G\ ^3F\ ^3F\ ^3G\ ^3H\ ^5D$	7
	5	$^3G\ ^3H$	2
	6	$^1I\ ^3H$	2
$\sum = 210$			$\sum = 34$
$3d^1$	3/2	^2D	1
$3d^9$	5/2	^2D	1
$\sum = 10$			$\sum = 2$
$3d^3$	1/2	$^2P\ ^4P$	2
$3d^7$	3/2	$^2P\ ^2D\ ^2D\ ^4P\ ^4F$	5
	5/2	$^2D\ ^2D\ ^2F\ ^4P\ ^4F$	5
	7/2	$^2F\ ^2G\ ^4F$	3
	9/2	$^2G\ ^2H\ ^4F$	3
	1/2	^2H	1
$\sum = 120$			$\sum = 19$
$3d^5$	1/2	$^2S\ ^2P\ ^4P\ ^4D$	4
	3/2	$^2P\ ^2D\ ^2D\ ^2D\ ^4P\ ^4D\ ^4F$	7
	5/2	$^2D\ ^2D\ ^2D\ ^2F\ ^2F\ ^4P\ ^4D\ ^4F\ ^4G\ ^6S$	10
	7/2	$^2F\ ^2F\ ^2G\ ^2G\ ^4D\ ^4F\ ^4G$	7
	9/2	$^2G\ ^2G\ ^2H\ ^4F\ ^4G$	5
	11/2	$^2H\ ^2I\ ^4G$	3
	13/2	^2I	1
$\sum = 252$			$\sum = 37$

Note: For each number of electrons, all term symbols are given, selected by their *J* value. The number of representations per *J* value is given, with the total number of representations in the bottom line. The total number of states is given in the first column.

The total degeneracy of p^n electrons can be determined by the formula as C_6^n:

$$C_6^n = \binom{6}{n} = \frac{6!}{(6-n)!\,n!}\,. \qquad (\mathrm{I}-1)$$

The total degeneracy of d^n electrons can be determined by the formula as C_{10}^n:

$$C_{10}^n = \binom{10}{n} = \frac{10!}{(10-n)!n!}\,. \qquad (\mathrm{I}-2)$$

The configurations of the $2p^5 3d^n$ final states are important for the $2p$ X-ray absorption edge. The term symbols of the $2p^5 3d^n$ states are found by multiplying the configurations of $3d^n$ with a 2P term symbol. For example, 2P $\otimes$ 3P yields ^{2}S + ^{2}P + ^{2}D + ^{4}S + ^{4}P + ^{4}D. Referring to Tables I-3 and I-4, the last two columns give the number of term symbols for each J value and the degeneracy. Tables I-3 and I-4 with J-value degeneracies are also important for crystal field effects. The total degeneracy $\boldsymbol{d}$ of a $2p^5 3d^n$ state is given in Equation (I-3).

$$\boldsymbol{d} = 6 \times \binom{10}{n} = 6 \times \frac{10!}{(10-n)!n!} \qquad (\mathrm{I}-3)$$

Table I-4. Symmetries of the $2p^5 3d^n$ systems

Configurations	J	Term Symbols	Degeneracy
$3p^5 3d^{10}$	1/2	^{2}P	1
	3/2	^{2}P	1
∑ = 6			∑ = 2
$3p^5 3d^2$	1/2	^{2}S ^{2}P3 ^{4}P ^{4}D2*	7
($3p^5 3d^8$)	3/2	^{2}P3 ^{2}D3 ^{4}S ^{4}P ^{4}D2 ^{4}F	11
	5/2	^{2}D3 ^{2}F3 ^{4}P ^{4}D2 ^{4}F ^{4}G	11
	7/2	^{2}F3 ^{2}G2 ^{4}D2 ^{4}F ^{4}G	9
	9/2	^{2}G2 ^{2}H ^{4}F ^{4}G	5
	11/2	^{2}H ^{4}G	2
∑ = 45			∑ = 45
$3p^5 3d^4$	1/2	^{1}S2 ^{2}P7 ^{4}P4 ^{4}D6 ^{6}D ^{6}F	21
($3p^5 3d^6$)	3/2	^{2}P7 ^{2}D8 ^{4}S2 ^{4}P4 ^{4}D6 ^{4}F5 ^{6}P ^{6}D ^{6}F	35
	5/2	^{2}D8 ^{2}F9 ^{4}P4 ^{4}D6 ^{4}F5 ^{4}G4 ^{6}P ^{6}D ^{6}F	39
	7/2	^{2}F9 ^{2}G7 ^{4}D6 ^{4}F5 ^{4}G4 ^{4}H2 ^{6}P ^{6}D ^{6}F	36
	9/2	^{2}G7 ^{2}H5 ^{4}F5 ^{4}G4 ^{4}H2 ^{4}I ^{6}D ^{6}F	26
	11/2	^{2}H5 ^{2}I2 ^{4}G4 ^{4}H2 ^{4}I ^{6}F	15
	13/2	^{2}I2 ^{2}K ^{4}H2 ^{4}I	6
	15/2	^{2}K ^{4}I	2
∑ = 1260			∑ = 180
$3p^5 3d^1$	0	^{3}P	1
($3p^5 3d^9$)	1	^{1}P ^{3}P ^{3}D	3
	2	^{1}D ^{3}P ^{3}D ^{3}F	4
	3	^{1}F ^{3}D ^{3}F	3
	4	^{3}F	1
∑ = 60			∑ = 12
$3p^5 3d^3$	0	^{1}S ^{3}P4 ^{5}D2	7
($3p^5 3d^7$)	1	^{1}P3 ^{3}S2 ^{3}P4 ^{3}D6 ^{5}P ^{5}D2 ^{5}F	19
	2	^{1}D4 ^{3}P4 ^{3}D6 ^{3}F5 ^{5}S ^{5}P ^{5}D2 ^{5}F ^{5}G	25
	3	^{1}F4 ^{3}D6 ^{3}F5 ^{3}G4 ^{5}P ^{5}D2 ^{5}F ^{5}G	24
	4	^{1}G3 ^{3}F5 ^{3}G4 ^{3}H2 ^{5}D2 ^{5}F ^{5}G	18
	5	^{1}H2 ^{3}G4 ^{3}H2 ^{3}I ^{5}F ^{5}G	11
	6	^{1}I ^{3}H2 ^{3}I ^{5}G	5
	7	^{3}I	1
∑ = 270			∑ = 110
$3p^5 3d^5$	0	^{1}S ^{3}P7 ^{5}D3	11
	1	^{1}P5 ^{3}S2 ^{3}P7 ^{3}D9 ^{5}P3 ^{5}D3 ^{5}F3	32
	2	^{1}D6 ^{3}P7 ^{3}D9 ^{3}F10 ^{5}S ^{5}P3 ^{5}D3 ^{5}F3 ^{5}G2 ^{7}P	45
	3	^{1}F7 ^{3}D9 ^{3}F10 ^{3}G7 ^{5}P3 ^{5}D3 ^{5}F3 ^{5}G2 ^{5}H ^{7}P	46
	4	^{1}G5 ^{3}F10 ^{3}G7 ^{3}H5 ^{5}D3 ^{5}F3 ^{5}G2 ^{5}H ^{7}P	37
	5	^{1}H4 ^{3}G7 ^{3}H5 ^{3}I2 ^{5}F3 ^{5}G2 ^{5}H	24
	6	^{1}I2 ^{3}H5 ^{3}I2 ^{3}K ^{5}G2 ^{5}H	13
	7	^{1}K ^{3}I2 ^{3}K ^{5}H	5
	8	^{3}K	1
∑ = 1512			∑ = 205

Note: For each number of electrons, all term symbols are given, selected by their *J* value. The last column gives the number of representations per *J* value and the total number of representations and the total number of states. * Notations such as $4D^2$ should be read as two 4D configurations.

Figure I-1 Tanabe-Sugano diagrams for Cr, Ni and Fe ions.[2]

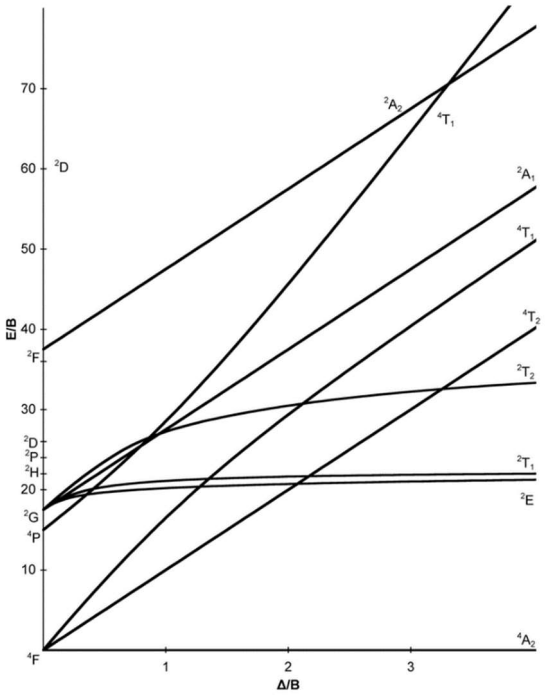

$Cr^{III}(d^3)$

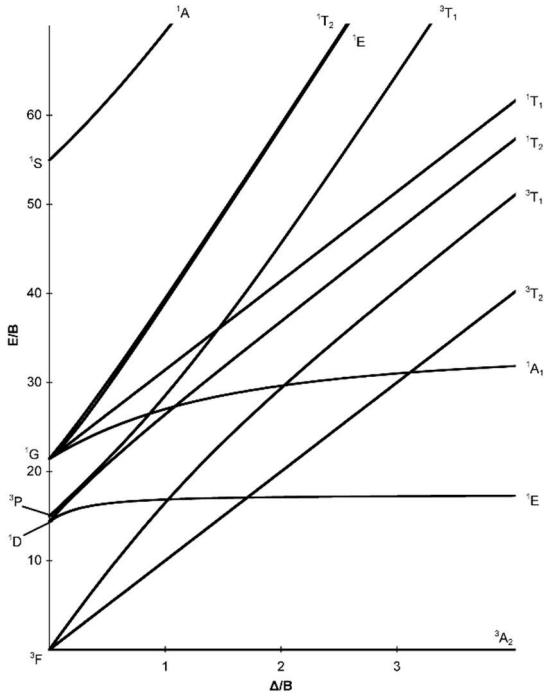

$Ni^{II}(d^8)$

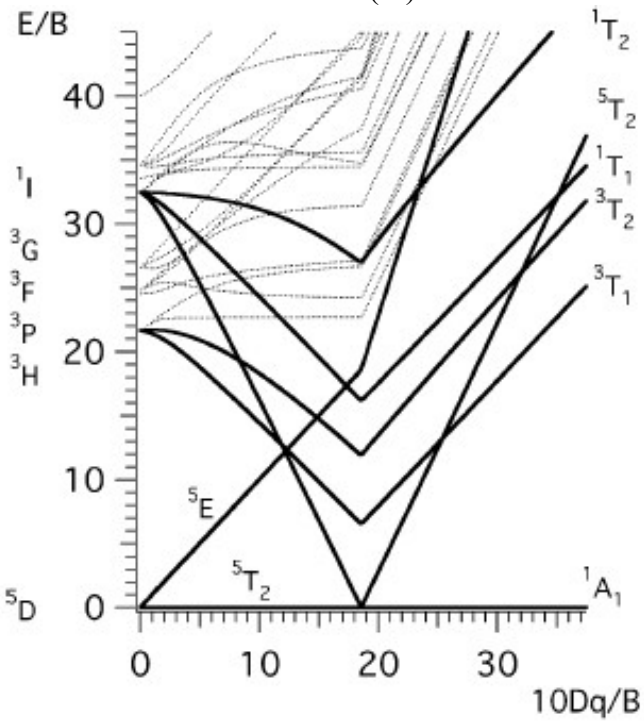

$Fe^{II}(d^6)$

Table I-5. Configurations for all possible HS and LS states in 3d electrons in O_h symmetry.

Configurations	Ground State in SO_3	HS Ground Sate in O_h	HS Ground Sate in Single Particle Models	LS Ground State in Single Particle Models	LS Ground State in O_h
$3d^0$	$^1S_0$	$^1A_1$	-	-	-
$3d^1$	$^2D_{3/2}$	$^2T_2$	t_{2g+}^1	-	-
$3d^2$	$^3F_2$	$^3T_1$	t_{2g+}^2	-	-
$3d^3$	$^4F_{3/2}$	$^4A_2$	t_{2g+}^3	-	-
$3d^4$	$^5D_0$	^5E	$t_{2g+}^3\ e_{g+}^1$	$t_{2g+}^3\ t_{2g-}^1$	$^3T_1$
$3d^5$	$^6S_{5/2}$	$^6A_1$	$t_{2g+}^3\ e_{g+}^2$	$t_{2g+}^3\ t_{2g-}^2$	$^2T_2$
$3d^6$	$^5D_2$	$^5T_2$	$t_{2g+}^3\ e_{g+}^2\ t_{2g-}^1$	$t_{2g+}^3\ t_{2g-}^3$	$^1A_1$
$3d^7$	$^4F_{9/2}$	$^4T_1$	$t_{2g+}^3\ e_{g+}^2\ t_{2g-}^2$	$t_{2g+}^3\ t_{2g-}^3\ e_{g+}^1$	^2E
$3d^8$	$^3F_4$	$^3A_2$	$t_{2g+}^3\ e_{g+}^2\ t_{2g-}^3$	-	-
$3d^9$	$^2D_{5/2}$	^2E	$t_{2g+}^3\ e_{g+}^2\ t_{2g-}^3\ e_{g-}^1$	-	-

Note: The third column gives the (high spin) HS term symbols and the last column the (low spin) LS term symbols. The fourth and fifth columns give the respective occupations of the t_{2g} and e_g orbitals.

Table I-6. Branching of the spin symmetry states and its consequences on states found after the spin orbit coupling SOC inclusion.

Configurations	Ground State in SO_3	HS Ground Sate in O_h	Spin in O_h	Degeneracy	Overall Symmetry in O_h
$3d^0$	$^1S_0$	$^1A_1$	A_1	1	A_1
$3d^1$	$^2D_{3/2}$	$^2T_2$	U_1	2	$U_2 + G$
$3d^2$	$^3F_2$	$^3T_1$	T_1	4	$E + T_1 + T_2 + A_1$
$3d^3$	$^4F_{3/2}$	$^4A_2$	G	1	G
$3d^4$	$^5D_0$	^5E	$E + T_2$	5	$A_1 + A_2 + E + T_1 + T_2$
		$3T_1$	T_1	4	$E + T_1 + T_2 + A_1$
$3d^5$	$^6S_{5/2}$	$^6A_1$	$G + U_2$	2	$G + U_2$
		$2T_2$	U_1	2	$G + U_2$
$3d^6$	$^5D_2$	$^5T_2$	$E + T_2$	6	$A_1 + E + T_1 + T_1 + T_2 + T_2$
		$1A_1$	A_1	1	A_1
$3d^7$	$^4F_{9/2}$	$^4T_1$	G	4	$U_1 + U_2 + G + G$
		2E	U_1	1	G
$3d^8$	$^3F_4$	$^3A_2$	T_1	1	T_2
$3d^9$	$^2D_{5/2}$	^2E	U_1	1	G

Note: The fourth column gives the spin-projection and the fi fth column its degeneracy. The last column lists all the symmetry states after inclusion of spin–orbit coupling.

Subductions for 3d TM ions.

Table I-7. Branching rules for the symmetry elements by going from SO_3 symmetry to O_h symmetry.

SO_3	O_h (Butler)	O_h (Mulliken)
S 0	0	A_1
P 1	1	T_1
D 2	$2 + \hat{1}$	$E + T_2$
F 3	$\hat{0} + 1 + \hat{1}$	$A_2 + T_1 + T_2$
G 4	$0 + 1 + 2 + \hat{1}$	$A_2 + E + T_1 + T_2$

Table I-8. Branching rules for the symmetry elements by going fron O_h syymetry to D_{4h} symmetry.

O_h (Butler)	O_h (Mulliken)	D_{4h} (Mulliken)	D_{4h} (Mulliken)
0	A_1	0	A_1
$\hat{0}$	A_2	2	B_1
1	T_1	$1 + \hat{0}$	$E + A_2$
$\hat{1}$	T_2	$1 + \hat{2}$	$E + B_2$
2	E	$0 + 2$	$A_1 + B_1$

Table I-9. Energy of the 3d orbitals 1s expressed in X_{400}, X_{420}, and X_{220} in the second column and in *Dq*, *Ds* and *Dt* in the third column.

Γ	Energy Expressed in X-Terms	In D-terms	d Orbitals
b_1	$30^{-\frac{1}{2}} \cdot X_{400} - 42^{-\frac{1}{2}} \cdot X_{420} - 2 \cdot 70^{-\frac{1}{2}} \cdot X_{220}$	$6Dq + 2Ds - 1Dt$	x^2-y^2
a_1	$30^{-\frac{1}{2}} \cdot X_{400} + 42^{-\frac{1}{2}} \cdot X_{420} + 2 \cdot 70^{-\frac{1}{2}} \cdot X_{220}$	$6Dq - 2Ds - 6Dt$	z^2
b_2	$-\frac{2}{3} \cdot 30^{-\frac{1}{2}} \cdot X_{400} + \frac{4}{3} \cdot 42^{-\frac{1}{2}} \cdot X_{420} - 2 \cdot 70^{-\frac{1}{2}} \cdot X_{220}$	$-4Dq + 2Ds - 1Dt$	xy
e	$-\frac{2}{3} \cdot 30^{-\frac{1}{2}} \cdot X_{400} - \frac{2}{3} \cdot 42^{-\frac{1}{2}} \cdot X_{420} + 70^{-\frac{1}{2}} \cdot X_{220}$	$-4Dq - 1Ds + 4Dt$	xz, yz

This table gives the action of the X_{400}, X_{420}, and X_{220} on the 3d orbitals and relates to the respective symmetries to a linear combinations of parameters *X*, a linear combination of *Dq*, *Ds* and *Dt*, and also the specific d orbitals with particular symmetries. The series of *X* and general CF parameters (*Dq*, *Ds* and *Dt*) are adopted to define the local symmetries of metal ions. The most direct and straightforward approach to specify the strength of CF parameters is to calculate the energy differences among 3d orbitals due to the above definitions, which helps us to study the structural geometries and electronic properties at the metal ions' sites.

Indeed, the CF operators X_{400}, X_{420}, and X_{220} are described as a function of *Dq*, *Ds* and *Dt*, as below shown:

$$i) \quad X_{400} = 6 \cdot 30^{-\frac{1}{2}} \cdot Dq - \frac{7}{2} \cdot 30^{-\frac{1}{2}} \cdot Dt \qquad (\mathrm{I}-4)$$

$$ii) \quad X_{420} = -\frac{5}{2} \cdot 42^{-\frac{1}{2}} \cdot Dt \qquad (\mathrm{I}-5)$$

$$iii) \quad X_{400} = -70^{-\frac{1}{2}} \cdot Ds \qquad (\mathrm{I}-6)$$

Inversely, *Dq*, *Ds* and *Dt* are expressed as

$$Dq = \frac{1}{6} \cdot 30^{-\frac{1}{2}} \cdot X_{400} - \frac{7}{30} \cdot 42^{-\frac{1}{2}} \cdot X_{420} \qquad (\mathrm{I}-7)$$

$$Ds = -70^{-\frac{1}{2}} \cdot X_{220} \qquad (\mathrm{I}-8)$$

$$Dt = -\frac{2}{5} \cdot 42^{-\frac{1}{2}} \cdot X_{420} \qquad (\mathrm{I}-9)$$

In brief, there exist only one crystal field parameter X_{40} in octahedral symmetry (O_h), while in tetragonal geometry (D_{4h}) and square pyramidal symmetry (C_{4v}) both are determined by *Dq*, *Ds* and *Dt* linked to X_{400}, X_{420}, and X_{220}.

The above relationships allow to define the local symmetries by ligand field calculations with known *Dq*, *Ds*, and *Dt* compared to the X-ray absorption spectroscopy which providing the *X*-values. Crystal field effect, spin orbital coupling and Zeeman effect can be realized by specifying X-parameters in the TT-Multiplet Program.

NOTE: In AAPPNDIX-I, tables (from Table I-1 to Table I-9) are cited from ref.1 while Figure I-1 is cited from ref.2.

References

1. De Groot, F.; Kotani, A., Core level spectroscopy of solids. CRC press: 2008.
2. Sugano, S., *Multiplets of transition-metal ions in crystals*. Elsevier: 2012.

APPENDIX- II

Figure II-1. Synthesis route of Prussian Blue analogues: $CsNi[Cr(CN)_6]\cdot yH_2O$ nanocrystals.

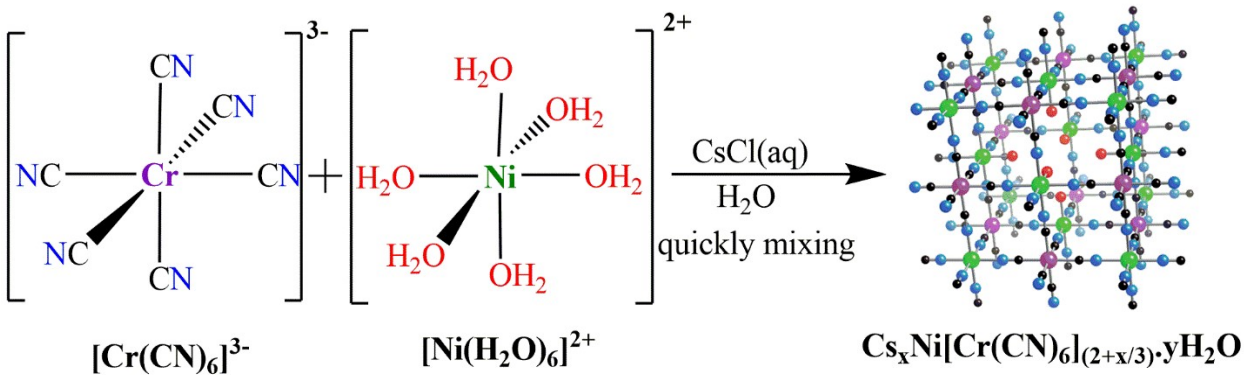

Figure II-2. SQUID measurements for $Cs^{I}Ni^{II}Cr^{III}[6]$ NCs in powder at 2K

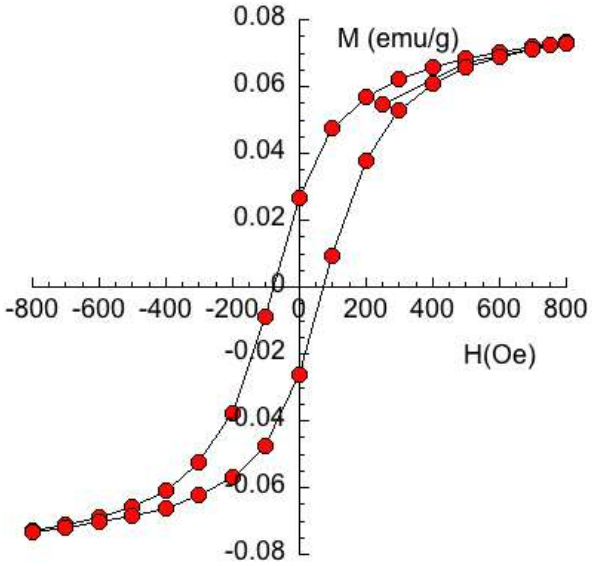

Figure II-3. Calculated Spectra applied magneto-optical sum rules for Ni^{II} and Cr^{III} site located in $Cs^{I}Ni^{II}Cr^{III}$@HOPG. All the applied CF parameters in atomic multiplet calculations are listed in Table 3-1. For Ni^{II} ions, it is carried out by the linear combination with C_{4v} in 48% and O_h in 52% while for Cr^{III} ions they are in purely octahedral symmetry.

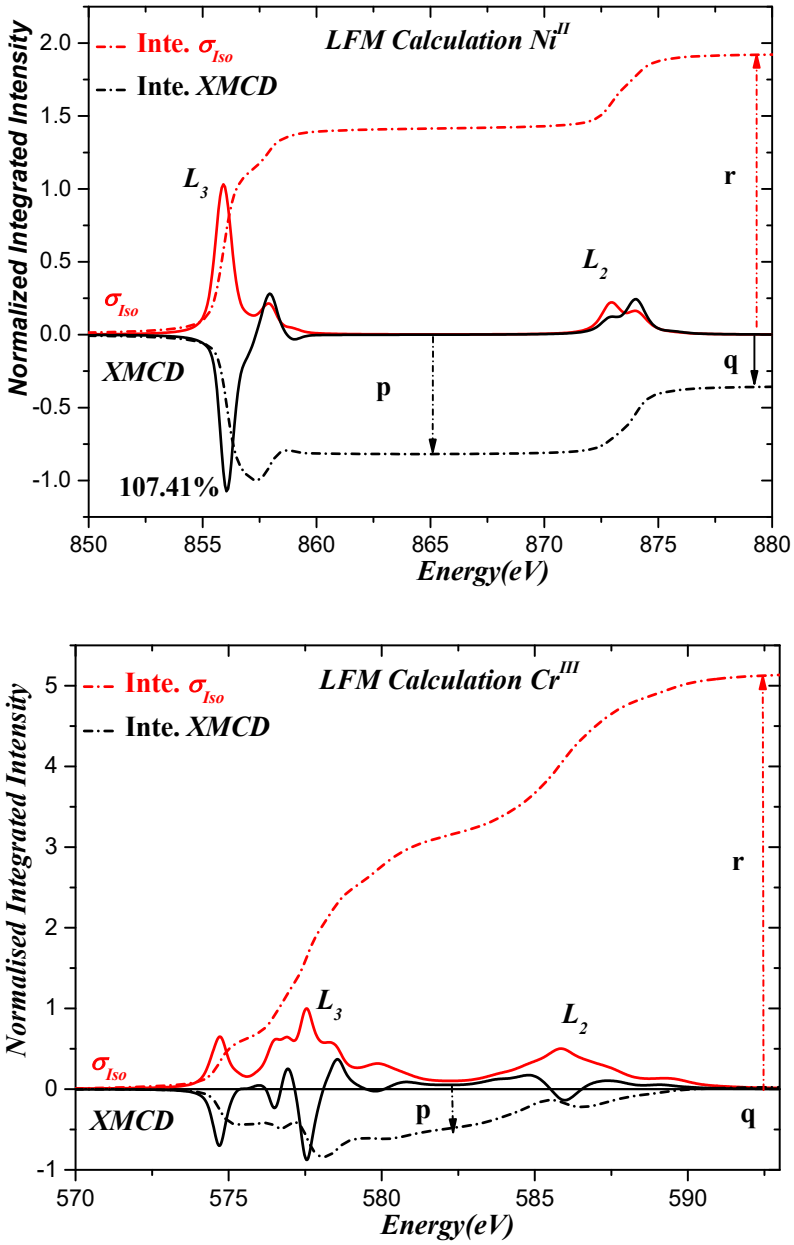

Figure II-4. The assumed interfacial structures among CsNiCr[6] NPs, water molecules and HOPG. The bond length of Cr^{III}—CN is around 4.3 Å, the Ni^{II}—OH_2 is 2.3 Å, the bond distance between two oxygen atoms connecting by two hydrogen bonds is 4.5 Å, the H—O------H is 2.76 Å, the N-----H is 2.27 Å, the bond length of Ni^{II}—CN—Cr^{III} (or Cr^{III}—CN—Ni^{II}) is 5.0 Å and the radius of cesium ion is 1.67 Å.

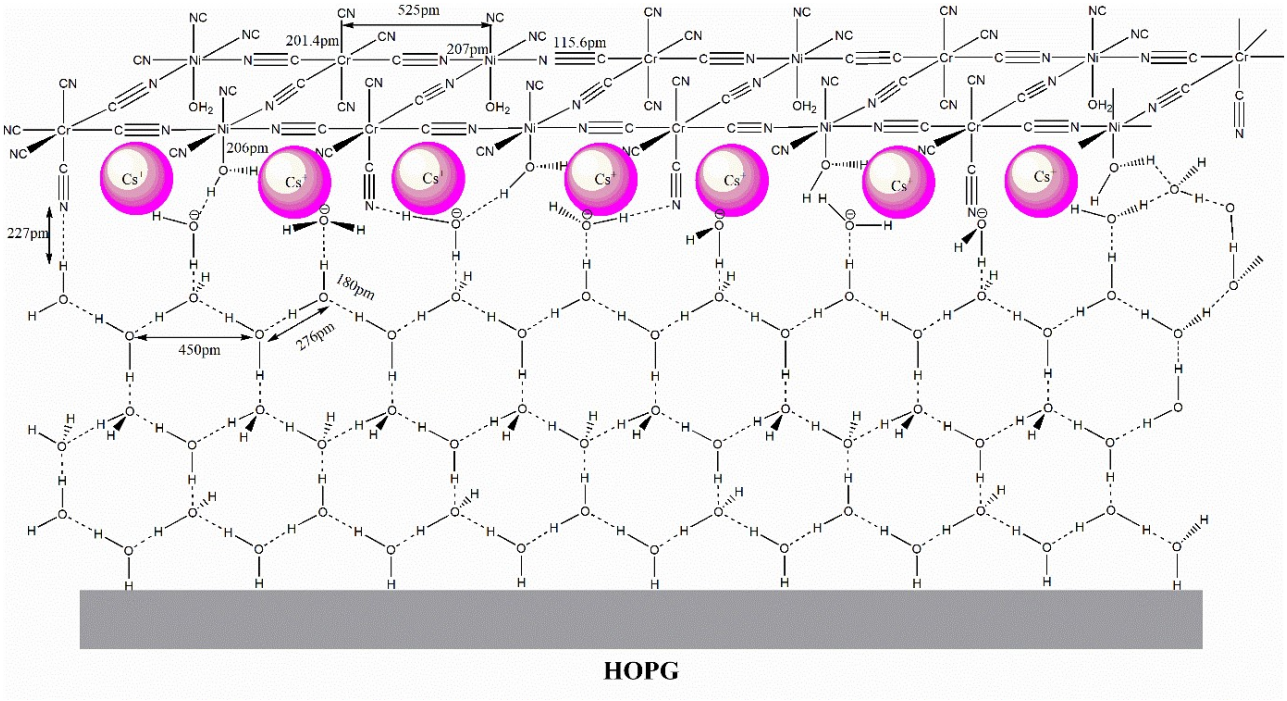

APPENDIX- III

Figure III-1. Calculated spectra of HS using LFM calculations in O_h symmetry.

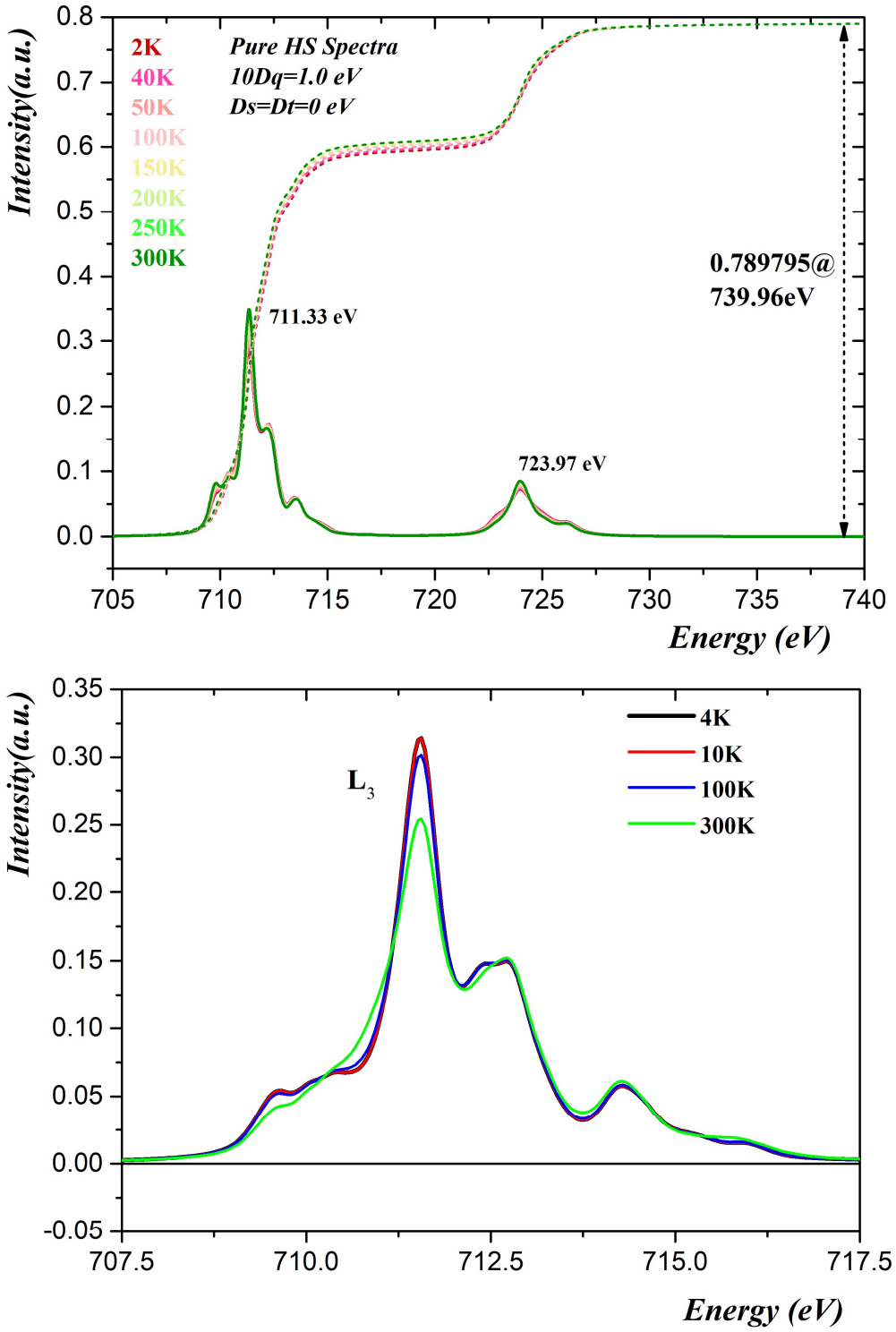

Figure III-2. Calculated spectra of LS using LFM calculations in O_h symmetry.

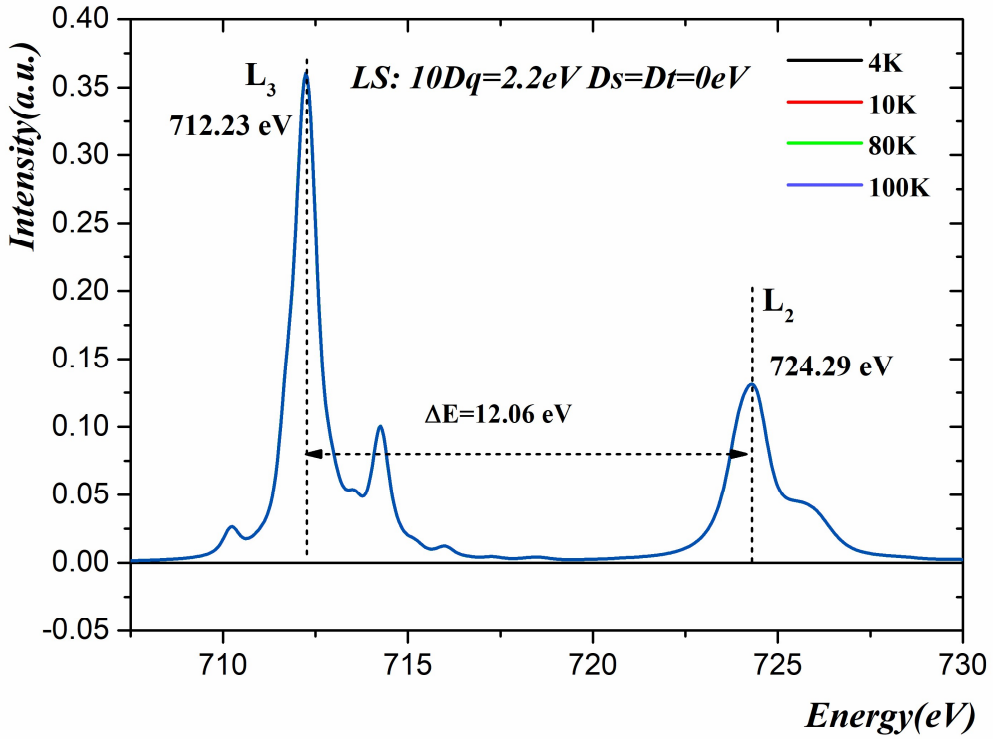

Figure III-3. Calculated XAS spectra for HS and LS at $L_{2,3}$ edges as reference using LFM calculations in O_h symmetry.

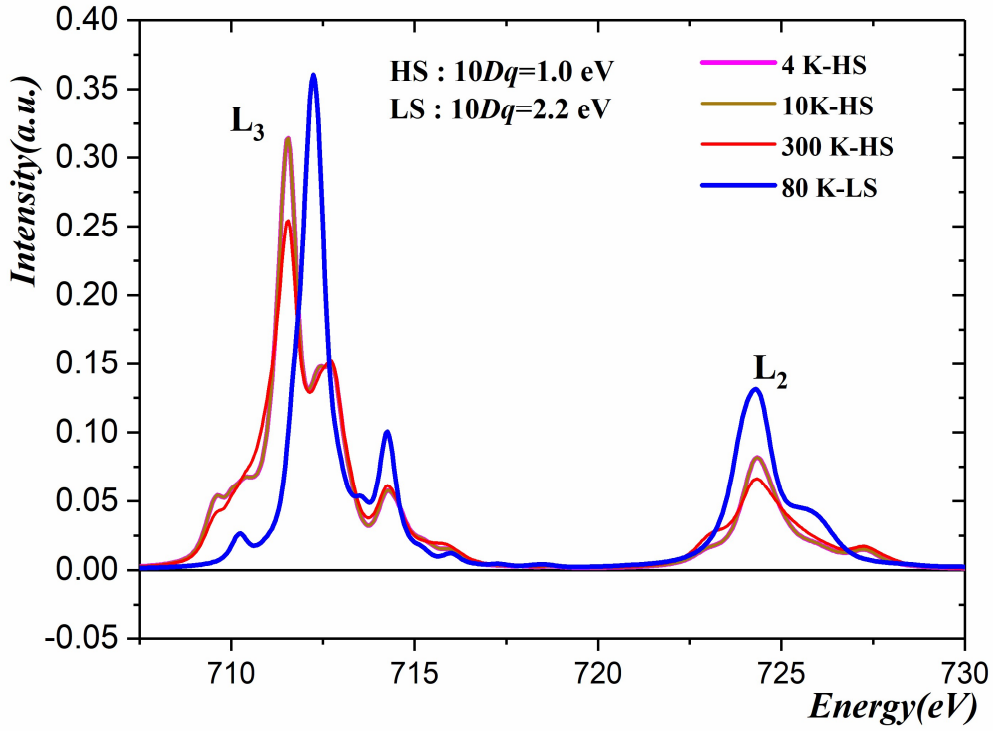

Figure III-4. Comparisons of STM images between before light and after light. The exposure time of light is 10 seconds.

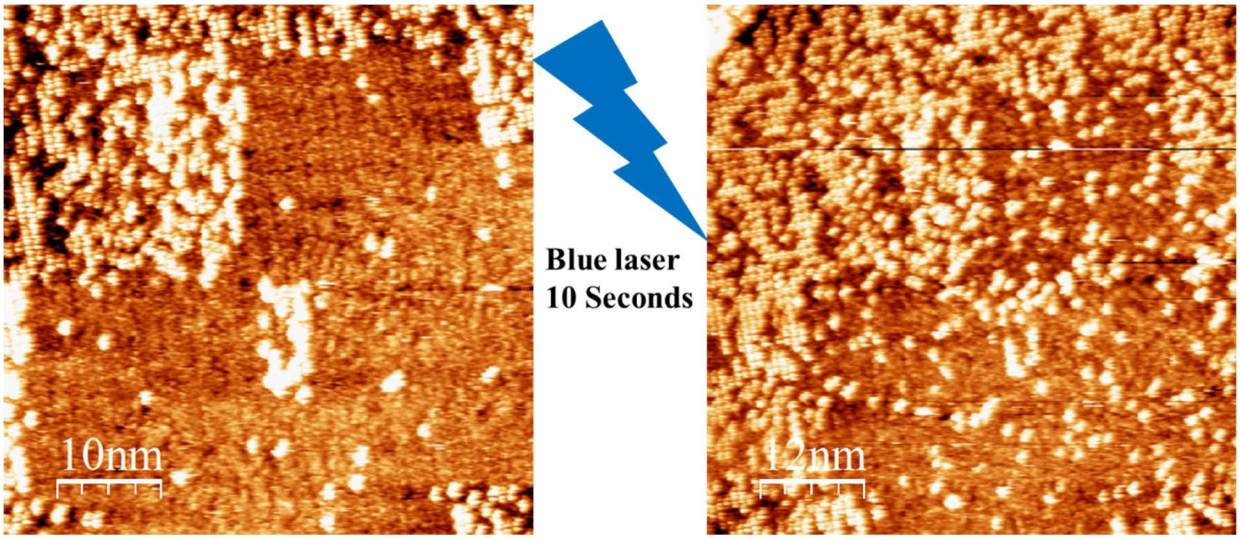

Note: STM images are measured at 4 K under the illumination of blue light. The size of each image is 30.00 x 30.00 nm2, tunneling voltage is 0.30 V, the tunneling current is 20.00 pA and the energy is 1mW. This figure is used to make a comparative analysis with the figure in **Chapter 4** ***(Figure 4-15)***

Figure III-5. Complete dynamic SCO behavior of Fe^{II}-SCO@Au at 4 K.

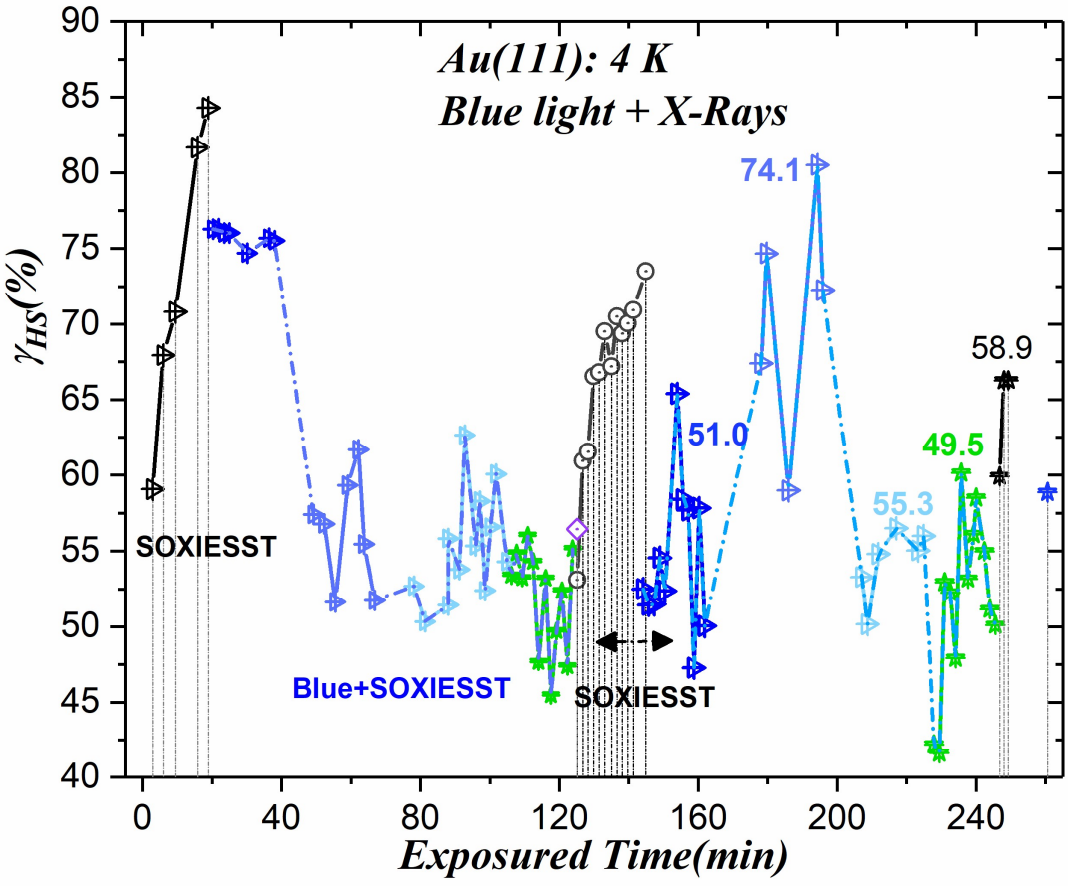

Figure III-6. Comparison among simulated spectra using linear fits based one experimental XAS spectra under the blue light illumination recorded at 4 K.

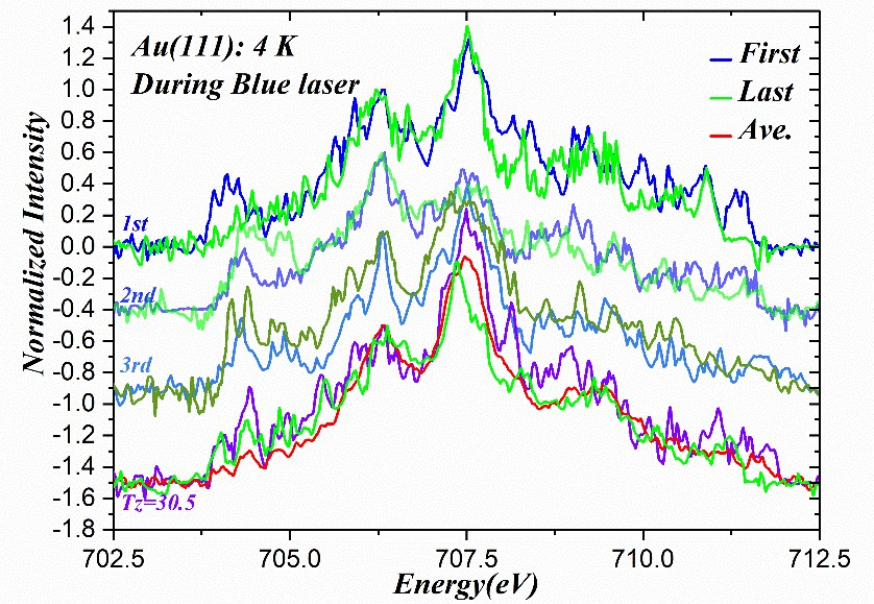

Note : In the figure, only the first, average and last measurements are taken into account to express the distinct differences observed before/during and after the illumination of blue light (405nm).

Figure III-8. Time evolution of HS fraction vs exposure time, with the illumination of blue (405nm) or red (635 nm) light.

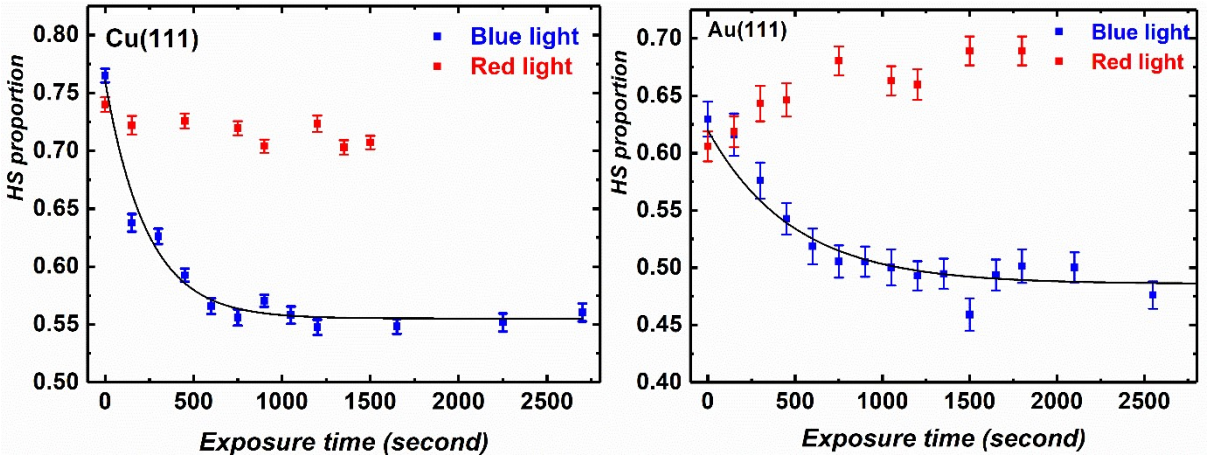

Note: In these two figures, HS fraction are estimated without using unit "1". All values of HS fraction are extracted from XAS spectra. The black lines are the exponential decay fits. Up-panel is for the sample of 0.6± 0.15ML on Cu(111) and down-panel is for the sample of 0.5± 0.1ML on Au(111)

Figure III-7. Comparison among XAS spectra obtained from experiments under the illumination of blue light recorded at 4 K and simulated ones obtained from linear fits using pure HS and LS.

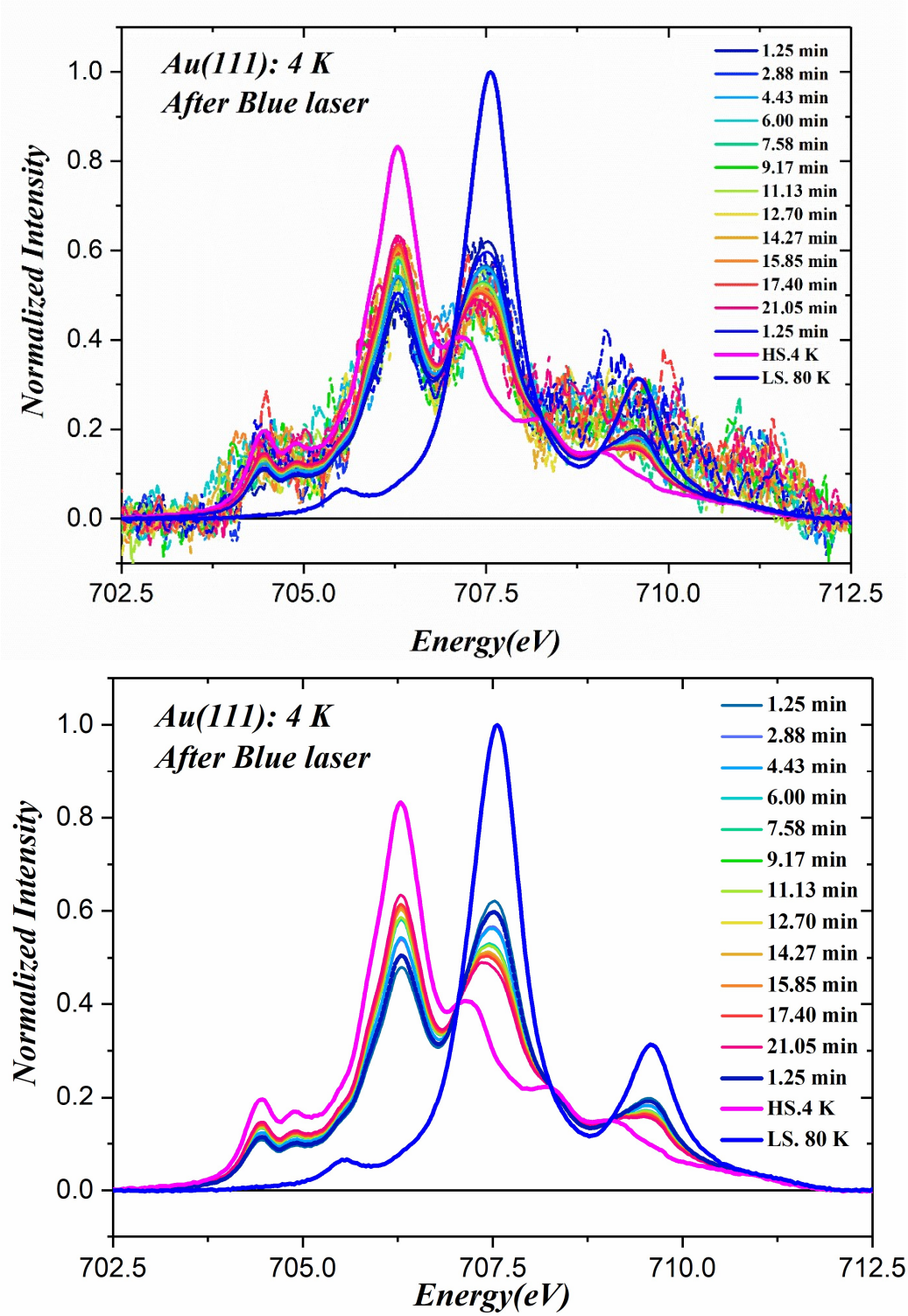

Note: Spectral evolution in the process after blue light only under the exposure of X-Rays: up-panel is the one estimated experimentally while down-panel is the one estimated theoretically.

Figure III-9. Comparison among XAS spectra obtained from experiments under the illumination of red light recorded at 4 K and simulated ones obtained from linear fits using pure HS and LS.

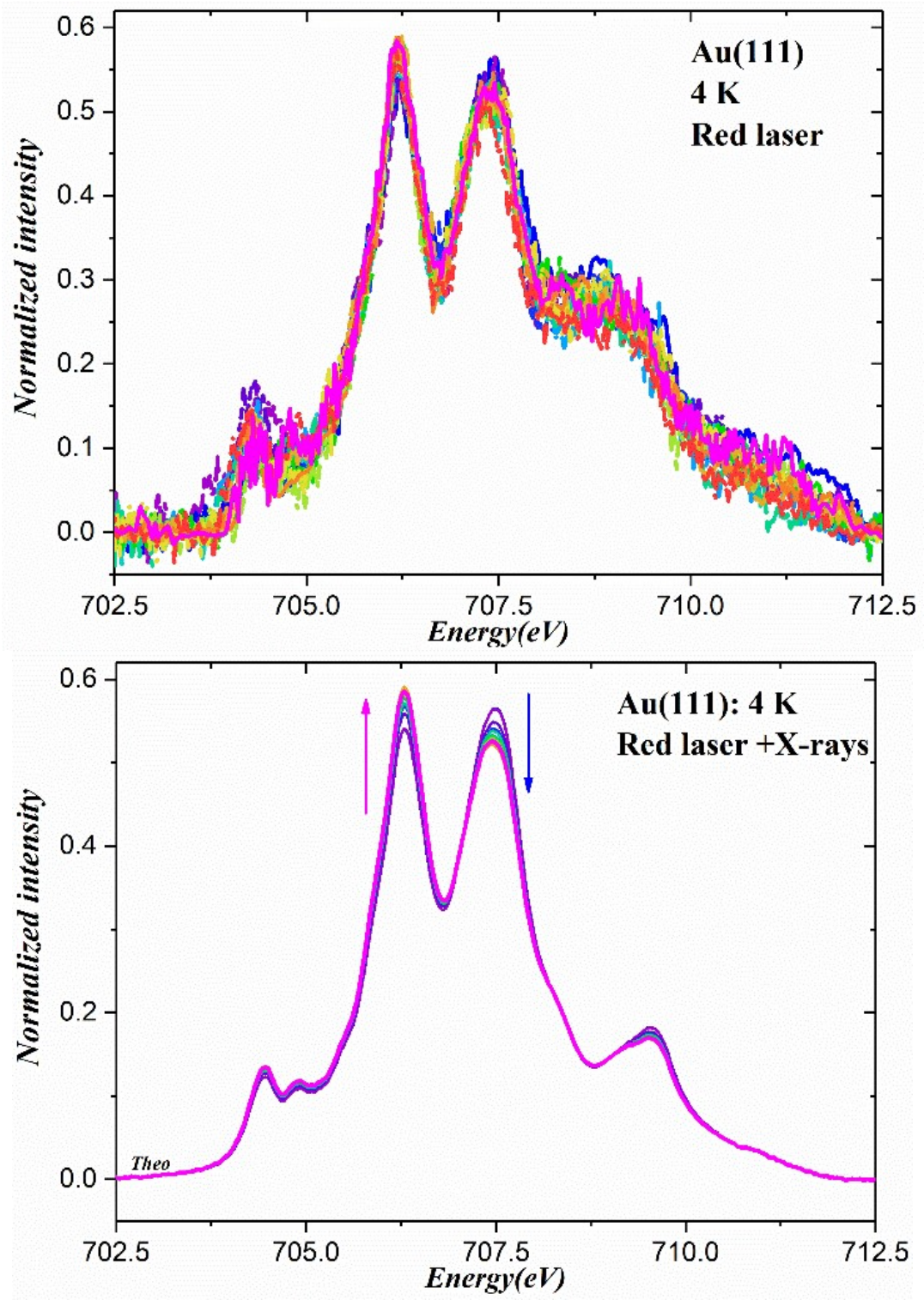

Note: Spectral evolution in the process after blue light only under the exposure of X-Rays: up-panel is the one estimated experimentally while down-panel is the one estimated theoretically.

université PARIS-SACLAY | ÉCOLE DOCTORALE Sciences chimiques : molécules, matériaux, instrumentation et biosystèmes

Titre : Matériaux magnétiques à base moléculaire assemblés sur des substrats métalliques: spectroscopie expérimentale d'absorption des rayons X et calcul du multiplet de champ de ligands.

Mots-clés: matériaux moléculaires, surfaces métalliques, spectroscopie d'absorption des rayons X, calculs multiplets en champ de ligands, nanoparticules de coordination, transition de spin

Résumé. Les travaux de recherche concernent l'étude des propriétés magnétiques des nanoparticules de coordination et de complexes à transition de spin assemblés en monocouches sur différents substrats métalliques par spectroscopie d'absorption des rayons X (XAS) aux seuils $L_{2,3}$ des atomes métalliques. Nous utilisons le dichroïsme magnétique circulaire des rayons X (XMCD) et le dichroïsme naturel linéaire des rayons X (XNLD). La simulation des données expérimentales est réalisée par la méthode des multiplets en champ de ligands (LFM). Cette thèse est divisée en deux parties.

La première partie vise à étudier l'anisotropie magnétique des nanoparticules magnétiques de coordination assemblées en une monocouche sur du graphite pyrolytique hautement orienté. Les mesures XAS, XNLD et XMCD révèlent la présence d'une anisotropie électronique et magnétique par l'ouverture d'une boucle d'hystérèse magnétique à basse température. En combinant les données expérimentales avec les calculs LFM, nous proposons un modèle structural de la surface des particules qui permet de rendre compte de l'anisotropie électronique et magnétique due à l'interface nanoparticules/vide.

Dans la deuxième partie, on étudie la transition de spin thermique et photo-induite de complexes de Fe(II) assemblés en sous-monocouches sur des substrats métalliques. Les calculs LFM et les données expérimentales permettent de démêler les différents effets que les paramètres externes (température, rayons X, lumière bleue et rouge) induisent sur la nature et l'ampleur de la transition de spin. Une transition "anormale" de l'état haut spin vers l'état bas spin, induite par la lumière bleue est découverte et analysée comme étant due à une interaction à l'interface entre les molécules et les substrats métalliques, cette interaction apportant l'énergie nécessaire à cette transition.

Title: Magnetic molecular-based materials assembled on metallic substrates: experimental X-ray absorption spectroscopy and ligand field multiplet calculations.

Keywords: molecular materials, metallic surfaces, X-ray absorption spectroscopy, ligand field multiplet calculations, coordination nanoparticles, spin crossover

Abstract. This thesis is focused on the investigation of the magnetic properties of magnetic nanoparticles and spin crossover complexes assembled as monolayers on different metallic substrates by X-ray Absorption Spectroscopy (XAS) at the $L_{2,3}$ edges of the metal atoms. We use X-ray Magnetic Circular Dichroism (XMCD) and X-ray Natural Linear Dichroism (XNLD) to do so. The simulation of the experimental data is carried out by Ligand Field Multiplet (LFM) calculations. This thesis is divided into two parts.

The first part aims at studying the magnetic anisotropy of Prussian blue analog magnetic coordination nanoparticles that were assembled as a single layer on Highly Oriented Pyrolytic Graphite. XAS, XNLD and XMCD measurements disclose the presence of electronic and magnetic anisotropy by the opening of a magnetic hysteresis loop at low temperature. Combining experimental data with LFM calculations, we propose a structural model of the surface of the particles that allows accounting for electronic and magnetic anisotropy and that is proposed to be due to the single layer/vacuum interface.

In the second part, thermal and light-induced spin crossover behavior of Fe(II) containing molecules have been assembled as a submonolayer on metallic substrates. Complementary LFM calculations and experimental XAS data allow unravelling the nature and the magnitude of the spin crossover as a function of the external stimuli (temperature, X-rays, blue and red light). An anomalous blue light effect allowing a crossover at low temperature from the high to low spin states is discovered and analyzed as being due to the interface between the molecules and the metallic substrates.